The Relation between the Deposition Process and the Structural, Electronic, and Transport Properties of Magnetron Sputtered Doped ZnO and $Zn_{1-x}Mg_xO$ Films

D i s s e r t a t i o n

zur Erlangung des akademischen Grades

d o c t o r r e r u m n a t u r a l i u m

(Dr. rer. nat.)

im Fach Physik

eingereicht an der

Mathematisch-Naturwissenschaftlichen Fakultät I

der Humboldt-Universität zu Berlin

von

Diplom-Physiker André Bikowski

Präsident der Humboldt-Universität zu Berlin

Prof. Dr. Jan-Hendrik Olbertz

Dekan der Mathematisch-Naturwissenschaftlichen Fakultät I

Prof. Stefan Hecht, Ph.D.

Gutachter/innen: 1. Prof. Dr. Recardo Manzke

2. Dr. Klaus Ellmer

3. Prof. Dr. Marius Grundmann

Tag der mündlichen Prüfung: 4. Juni 2014

Abstract

Doped ZnO (zinc oxide) and $Zn_{1-x}Mg_xO$ belong to the material class of transparent conductive oxides (TCOs). These materials are characterized by a high optical transmittance accompanied by a low electrical resistivity that makes them crucial for a wide field of technological applications nowadays. In thin film solar cells, TCOs are employed as transparent and conductive window layers, whose quality is essential for the realization of high power conversion efficiencies. The field is not only of technological significance but also of scientific interest, since most of the basic effects governing the film properties in correlation with the use of different dopant elements, alloys, or the deposition techniques and parameters are not yet fully understood. Therefore, it is of great importance to clarify the relation between these parameters to be able to deliberately decrease the resistivity while maintaining a high optical transmittance – especially for ZnO as a contact material in thin film solar cells.

In this thesis, the relation between the structural, electronic, and charge carrier transport properties of doped ZnO and $Zn_{1-x}Mg_xO$ films has been investigated in detail. A main focus was the study of the influence of the deposition process and the deposition parameters on the structural and the resulting electronic properties of the films for the application as front contact window layers in thin film solar cells. The objective was to clarify the above mentioned relations, which allows to derive solutions for a deliberate improvement of the layer properties. For the investigation, thin films deposited by magnetron sputtering at substrate temperature between ~30 °C and 500 °C with different plasma excitation frequencies in the range of DC to 27.12 MHz were used. The characterization of the electronic properties was mainly performed by means of resistivity, Hall-effect, and Seebeck-coefficient measurements, while the structural properties were primarily determined by X-ray diffraction.

The investigations showed that the charge carrier transport in doped polycrystalline and epitaxial ZnO and $Zn_{1-x}Mg_xO$ layers is dominated by ionized impurity scattering and grain boundary scattering. The grain boundary scattering has been characterized by a model, which has been derived to describe the charge carrier transport over grain boundaries in semiconductors of arbitrary degeneracy. A comparison of the transport properties of the polycrystalline and epitaxial films confirmed the dominance of the grain boundary scattering even for a very low number of grain boundaries present in the material. Furthermore, this scattering is mainly caused by the segregation of the dopant material to the grain boundaries. Hence, for practical applications, the grain boundary scattering could only be reduced by lowering the amount of dopant material in the films.

The influence of the most important deposition parameters on the electronic and structural properties was explained by a model derived on the basis of a comparison of ion energy distributions measured for the magnetron sputtering process with the resulting film properties. According to this model, the properties of the films are mainly influenced by the formation of electrically active acceptor-like oxygen interstitial (O_i) defects at low deposition temperatures T_{sub}, which lead to a partial compensation of the extrinsic donor. At higher T_{sub}, the formation of secondary phases or defect complexes, in which the dopant is also electrically inactive, prevails. Additionally, the generally lower free carrier concentrations in the $Zn_{1-x}Mg_xO$:Al films can be explained as a result of a stronger compensation of the extrinsic dopant due to a stronger bombardment of the growing films. Concluding

from the model, the structural and electronic properties of the films can be improved by reducing the maximal energy of the bombarding ions. This is, for example, possible by increasing the plasma excitation frequency.

The investigation of the influence of different dopants on the structural, electronic, and optical properties of the films confirmed the suitability of the group III elements Al and Ga as dopants. Furthermore, experimental proof for the group III element doping model in ZnO, where the dopants are assumed to occupy Zn lattice sites, was found by X-ray absorption spectroscopy measurements. The distribution of the dopant element in the films, however, is highly inhomogeneous, which has been shown by energy dispersive X-ray spectroscopy and atom probe tomography measurements. Especially in the interface region to the substrate, a thick layer with a strong enrichment of the dopant material was detected, which can be attributed to the formation of a Zn-depleted nucleation layer. In this layer, the dopant material is mainly present in the form of electrically inactive metal-oxide compounds. The indications for a stronger phase segregation in the $Zn_{1-x}Mg_xO$:Al films in comparison to the ZnO:Al films were attributed to the possible formation of additional secondary phases, for instance $MgAl_2O_4$. A feasible solution to inhibit the growth of such an interface layer would be the use of buffer layers or adequate process parameters at the initial stages of the film formation.

Eventually, the $Zn_{1-x}Mg_xO$:Al films were employed as front contact window layers with the goal to increase the efficiency by an improved band alignment in wide-gap chalcopyrite thin film solar cells. Although the $Zn_{1-x}Mg_xO$:Al films prepared in this work are of similar quality in comparison to the ZnO:Al films and different approaches were tried, for example the preparation of the solar cells without buffer layer and using alternative buffer layers, it was not yet possible to increase the open circuit voltage and hence the efficiency by the use of $Zn_{1-x}Mg_xO$ as window layer significantly. There is still a substantial need for further research.

Kurzfassung

Dotierte ZnO- und $Zn_{1-x}Mg_xO$-Schichten gehören zu den transparenten leitfähigen Oxiden. Diese Materialien weisen eine hohe optische Transparenz bei gleichzeitig niedrigem elektrischem Widerstand auf, weshalb sie heutzutage für eine Vielzahl von technologischen Anwendungen von entscheidender Bedeutung sind. In Dünnschichtsolarzellen werden transparente leitfähige Oxide als leitfähige Fensterschichten benutzt, deren Qualität für das Erreichen von hohen Effizienzen eine wesentliche Rolle spielt. Auch wissenschaftlich ist das Feld von großem Interesse, da eine Vielzahl von grundlegenden Mechanismen, die die Eigenschaften der Schichten mit den verwendeten Parametern verknüpfen, nicht umfassend verstanden sind. Solche Parameter sind zum Beispiel die Art und Menge der Dotier- und Legierungsmaterialien sowie die Abscheidungsmethoden und -bedingungen. Aus diesem Grund ist es von großer Bedeutung, den Zusammenhang zwischen diesen Parametern systematisch zu untersuchen, um die Schichten zielgerichtet verbessern zu können und damit den elektrischen Widerstand zu senken, ohne die optische Transparenz negativ zu beeinflussen.

In dieser Dissertation wurde die Beziehung zwischen den strukturellen-, elektronischen- und Ladungstransporteigenschaften von dotierten ZnO- und $Zn_{1-x}Mg_xO$-Schichten eingehend studiert. Der Schwerpunkt dieser Arbeit lag dabei auf der Untersuchung des Einflusses der Prozessparameter auf die strukturellen und die damit verknüpften elektronischen Eigenschaften der transparenten leitfähigen Oxide, welche als leitfähige Fensterschichten in chalkopyritbasierten Dünnschichtsolarzellen angewendet werden sollen. Das Ziel war es, die oben genannten Zusammenhänge weiter aufzuklären, wodurch sich anschließend Ansätze für eine zielgerichtete Verbesserung der Schichteigenschaften ableiten lassen. Für die Untersuchungen wurden Schichten mittels Magnetronsputterns bei Substrattemperaturen im Bereich von circa 30 °C bis 500 °C mit verschiedenen Plasmaanregungsfrequenzen, von Gleichspannung bis 27.12 MHz, abgeschieden. Die Charakterisierung der elektrischen Eigenschaften erfolgte hauptsächlich durch Widerstands-, Hall-Effekt- und Seebeck-Koeffizient-Messungen, während die strukturellen Eigenschaften überwiegend durch Röntgendiffraktometrie bestimmt wurden.

Die Untersuchungen zeigten, dass der Ladungsträgertransport in polykristallinen und epitaktisch gewachsenen dotierten ZnO- und $Zn_{1-x}Mg_xO$-Schichten von ionisierter Störstellenstreuung und Korngrenzenstreuung dominiert ist. Zur Charakterisierung der Streuung an den Korngrenzen wurde ein Modell erarbeitet, welches in der Lage ist, den Ladungstransport über Korngrenzen in Halbleitern mit beliebiger Entartung zu beschreiben. Des Weiteren ging aus einem Vergleich der Transporteigenschaften zwischen den polykristallinen und epitaktisch gewachsenen Schichten hervor, dass die Streuung an Korngrenzen in den Schichten auch dann dominant ist, wenn die Anzahl der Korngrenzen drastisch reduziert wird. Außerdem wird sie hauptsächlich durch die Ausscheidung des Dotanden an den Korngrenzen verursacht. Für eine praktische Anwendung der transparenten leitfähigen ZnO-Schichten kann daher der Einfluss der Streuung an den Korngrenzen auf den elektrischen Transport nur dadurch verringert werden, dass die Menge des Dotiermaterials in der Schicht reduziert wird.

Der Einfluss der wichtigsten Abscheidungsparameter auf die elektrischen und strukturellen Eigenschaften konnte mit Hilfe eines Modells erklärt werden, welches auf der Basis eines Vergleichs von Ionenenergieverteilungen im Magnetronsputterprozess mit den resultierenden Schichteigenschaften entwickelt wurde. Gemäß diesem Modell sind die Schichteigenschaften bei niedrigen Abscheidungstemperaturen hauptsächlich durch ein Ionenbombardement bestimmt, welches die

Bildung von akzeptorartigen Sauerstoffzwischengitterdefekten (O_i) hervorruft, die einen Teil der extrinsischen Elektronen kompensieren. Bei höheren Abscheidungstemperaturen ist die Bildung von sekundären Phasen oder Defektkomplexen, in denen der Dotand ebenfalls elektrisch inaktiv ist, dominierend. Die niedrigeren Ladungsträgerkonzentrationen in den $Zn_{1-x}Mg_xO$:Al-Schichten können damit als Folge eines stärkeren Bombardements mit hochenergetischen Ionen erklärt werden. Aus dem Modell folgt außerdem, dass die strukturellen und elektrischen Eigenschaften der transparenten leitfähigen Oxide durch eine Verminderung der maximalen Energien der bombardierenden Ionen verbessert werden können. Praktisch lässt sich das durch eine höhere Plasmaanregungsfrequenz für die Abscheidung erreichen.

Untersuchungen des Einflusses verschiedener Dotiermaterialien auf die strukturellen, elektrischen und optischen Eigenschaften der Schichten zeigten, dass Ga und Al die effizientesten Dotanden der Gruppe III sind. Darüber hinaus konnte mit Hilfe von Röntgenabsorptionsspektroskopie-Messungen ein experimenteller Beleg dafür gefunden werden, dass Dotanden der Gruppe III auf Zn-Gitterplätzen eingebaut werden. Allerdings offenbarten energiedispersive Röntgenspektroskopie- und Atomsonden-spektroskopie-Messungen eine stark inhomogene Verteilung der Dotanden in der Schicht. Speziell an der Grenze zwischen Substrat und Schicht befindet sich eine vergleichsweise dicke Übergangsschicht mit einer starken Anreicherung des Dotiermaterials. Diese Anreicherung wird vermutlich durch die Bildung einer Zn-armen Kondensationsschicht hervorgerufen, in der das Dotiermaterial bevorzugt in der Form von sauerstoffreichen, elektrisch inaktiven Verbindungen vorliegt. Die Hinweise auf eine stärkere Ausscheidung von Fremdphasen in den $Zn_{1-x}Mg_xO$:Al-Schichten im Vergleich zu den ZnO:Al-Schichten wurden der möglichen zusätzlichen Bildung von $MgAl_2O_4$ zugeschrieben. Eine Methode, die Bildung dieser Schicht zu unterdrücken, könnte die Verwendung von Keimschichten beziehungsweise speziell angepassten Prozessparametern in der Anfangsphase der Schichtbildung sein.

Abschließend wurden die $Zn_{1-x}Mg_xO$:Al-Schichten als transparente leitfähige Fensterschichten für die verbesserte Bandanpassung zur Effizienzsteigerung von Chalkopyrit-Dünnschichtsolarzellen mit großer Bandlücke eingesetzt. Es zeigte sich, dass die $Zn_{1-x}Mg_xO$:Al-Schichten ebenfalls als Fensterschicht einsetzbar sind, es allerdings zunächst trotz verschiedener Ansätze, die die Herstellung der Solarzellen ohne Pufferschicht und alternative Pufferschichten aus Zn(O,S) beinhalteten, nicht möglich war, die Leerlaufspannung und damit die Effizienz der Solarzelle durch den Einsatz von $Zn_{1-x}Mg_xO$:Al wesentlich zu erhöhen. An dieser Stelle gibt es noch erheblichen Forschungsbedarf.

List of Important Symbols and Abbreviations

α	Optical absorption coefficient
β	Non-parabolicity parameter or integral breadth
ΔE	Energy difference between conduction band edges for alloy scattering
ΔE_c	Conduction band offset
ΔE_D	$= E_c - E_D$, difference between donor level energy and conduction band minimum
ΔE_t	$= E_c - E_t$, difference between trap state energy and conduction band minimum
ε_∞	High-frequency dielectric constant
ε_s	Static dielectric constant
η	Fermi energy measured from the band edge in units of the thermal energy kT or solar cell power conversion efficiency
θ	Diffraction angle
λ	Wavelength
μ^{Hall}, μ_n, μ	Hall mobility of the electrons
μ_p	Hall mobility of the holes
$\mu_{d,n}$, μ_d	Drift mobility of the electrons
μ^{opt}	Electron mobility determined by optical measurements
μ_{LO}^{Hall}	Hall mobility associated with longitudinal-optical phonon scattering
μ_{ac}^{Hall}	Hall mobility associated with acoustical mode phonon scattering
μ_{piezo}^{Hall}	Hall mobility associated with piezoelectric scattering
μ_{ii}^{Hall}	Hall mobility associated with ionized impurity scattering
μ_{GB}^{Hall}	Hall mobility associated with grain boundary scattering
μ_{alloy}^{Hall}	Hall mobility associated with alloy scattering
μ_{disl}^{Hall}	Hall mobility associated with dislocation scattering
ν	Frequency of the light
ρ	Electrical resistivity or space charge
σ	Electrical conductivity
τ	Mean free time
$\langle \tau \rangle$	Averaged mean free time
ω	Angular frequency of the light
ω_p	Plasma frequency
a	a-axis lattice parameter or grain boundary width
A	Optical absorbance
c	c-axis lattice parameter
c_{ij}	Elastic constants
c_l	Average longitudinal elastic constant
c_{ref}	Value for the c-axis lattice parameter of a reference powder
d	Film thickness
d_{cryst}	Crystallite size
$D_{0,Al}$	Diffusion prefactor for aluminium
$D_{0,Oi}$	Diffusion prefactor for oxygen interstitial defects
E	Electron energy
$\langle E \rangle$	Averaged energy of negative ions reaching the substrate surface
E_{ac}	Deformation potential
E_{Al}	Activation energy for the diffusion of aluminium
E_B	Potential barrier height
E_c	Energy of the conduction band minimum
E_{c0}	Energy of the conduction band minimum in the undepleted region
E_D	Energy level of the donors
E_D^0	Donor level energy for low free carrier concentrations
E_F	Fermi energy
E_g	Band gap energy
E_{Oi}	Activation energy for the diffusion of oxygen interstitial defects

E_{ph}	Photon energy
E_t	Energy level of the electron traps at the grain boundaries
E_U	Urbach energy
E_v	Energy of the valence band maximum
$\mathscr{F}_{1/2}(\eta)$	Fermi-Dirac integral of the order 1/2
FF	Fill factor
$g(E)$	Number of states per unit volume
$g_D(E)$	Number of donor states per unit volume
$g_n(E)$	Number of electron states per unit volume
H	Full width at half maximum
H_ω	Rocking curve full width at half maximum
$\hbar\omega_0$	Energy of the longitudinal-optical phonon
I_{sc}	Short-circuit current
j	Current density
j_{th}	Thermionic emission current density
k	Electron wave vector
K	Scherrer constant
L	Lateral grain size
L_d	Diffusion length
m^*,m_n^*	Effective electron mass
m_0^*	Effective electron mass at the conduction band bottom
m_c^*, $m_{c,n}^*$	Conductivity effective electron mass
$m_{c,p}^*$	Conductivity effective hole mass
m_d^*, $m_{d,n}^*$	Density of states effective electron mass
$m_{d,p}^*$	Density of states effective hole mass
m_p^*	Effective hole mass
M_{Zn}	Metal atom on zinc lattice site
n	Free electron concentration
n_0	Free electron concentration in the undepleted region
n_a	Average free electron concentration in the grain
n_D	Concentration of occupied localized donor states
N	Number of atoms per unit volume
N_A^-	Concentration of ionized acceptors
N_c	Effective density of states at the conduction band minimum
N_D	Concentration of donors
N_D^+	Concentration of ionized donors
N_{disl}	Concentration of dislocations
N_i	Concentration of ionized impurities
N_t	Concentration of electron traps at the grain boundaries
N_v	Density of states at the valence band maximum
O_i	Oxygen interstitial defect
p	pressure or free hole concentration
$P_{\parallel,\perp}$	Averaged piezoelectric electro-mechanical coupling coefficient
r_H	Hall coefficient factor
R	Resistance or optical reflectance
R_H	Hall constant
S	Seebeck coefficient
T	Temperature or optical transmittance
T_{avg}	Average transmittance in the visible spectral region (400 nm to 800 nm)
T_{sub}	Substrate temperature during the deposition
V	Voltage
V_{fl}	Floating potential
V_{oc}	Open-circuit voltage
V_{pl}	Plasma potential
V_t	Target voltage
w	Width of the space charge region
x	Fraction of the alloy component
y	Scattering exponent
Y	Ion intensity
Z	Charge of impurities in units of the elementary charge
Zn_i	Zinc interstitial defect

AFM	Atomic force microscopy
APT	Atom probe tomography
AZO	Al-doped ZnO (ZnO:Al)
CVD	Chemical vapour deposition
DC	Direct current
DFT	Density-functional theory
EDX	Energy-dispersive X-ray spectroscopy
FTO	Fluorine-doped tin oxide (SnO_2:F)
HZB	Helmholtz-Zentrum Berlin für Materialien und Energie GmbH
ITO	Tin-doped indium oxide (In_2O_3:Sn)
JCPDS	Joint Committee on Powder Diffraction Standards
MS	Magnetron sputtering
PLD	Pulsed laser deposition
XRD	X-ray diffraction
XAS	X-ray absorption spectroscopy
PPM	Plasma process monitor
RBS	Rutherford backscattering spectrometry
RF	Radio frequency
SEM	Scanning electron microscopy
SIMS	Secondary ion mass spectrometry
TCO	Transparent conductive oxide
TEM	Transmission electron microscopy

Physical Constants

ε_0	Vacuum permittivity ($8.854 \cdot 10^{-12}$ F/m)
c	Speed of light ($2.998 \cdot 10^{8}$ m/s)
e	Elementary charge ($1.602 \cdot 10^{-19}$ C)
h	Planck's constant ($6.626 \cdot 10^{-34}$ Js)
$\hbar$	$h/(2\pi)$
k	Boltzmann constant ($1.381 \cdot 10^{23}$ J/K)
m_e	Free electron mass ($9.109 \cdot 10^{-31}$ kg)

Contents

1. Introduction

ZnO and $Zn_{1-x}Mg_xO$ belong to the class of transparent conductive oxides (TCOs). TCOs are a unique class of materials, because they exhibit both, transparency and electronic conductivity, simultaneously.[1] Usually, conductive materials, such as metals, are not transparent, while transparent materials, such as insulators, are not conductive. Transparent conductive oxides combine these two properties due to their large band gap ($\geq$ 3 eV), leading to the transparency in the visible spectrum of the light, and a low effective mass of the electrons, which can be attributed to the high dispersion and the s-type character of the conduction band, explaining the high conductivity.[2,3]

Since the first report of CdO, being transparent and conductive simultaneously, by Bädeker[4] in 1907, many different materials have been investigated and various applications found. Nowadays, TCOs are used for example as architectural glass coatings, in flat-panel displays, as electrochromic mirrors and windows, as defrosting windows, for static dissipation, in touch-panel controls, for electromagnetic shielding, or as front contact windows in solar cells.[5] The various applications of the TCOs impose different requirements on the materials, which led to the investigation of a great many of different transparent conductive oxide compounds. Some important properties of TCO materials and their applications are listed in Table 1.1.

Table 1.1: Properties relevant to TCO materials and their applications. The table is adapted from Reference 6.

General criteria	sustainable materials, sustainable processing, cost, availability, ease of application
Opto-electronic criteria	transparency in the visible spectrum, infrared transparency, conductivity, carrier concentration, mobility, suitability to flexible electronics, work function
Processing criteria	deposition temperatures and conditions, annealing stability, chemical stability, etchability, interfacial chemistry, surface states, temperature sensitivity, atmospheric sensitivity

Today, of technological importance are almost exclusively doped In_2O_3, SnO_2, and ZnO.[7] While tin-doped indium oxide (ITO) is nearly the sole TCO used in flat panel displays, which can be attributed to its high conductivity and good chemical etchability, fluorine-doped tin oxide (FTO) is mainly employed as low emissivity coating due to its suitable plasma wavelength and excellent durability and low cost. FTO is also applied as a front electrode in solar cells, where the thermal stability and the low cost are determining.[5] However, in comparison to ITO, it has a much lower conductivity, which reduces the achievable efficiencies. Therefore, as a cost effective alternative to ITO and due to its higher conductivity in comparison to FTO, increasingly doped ZnO is used in front contact window layers. As a bulk material, ZnO is already applied to a large extend for the production of gum, cement, as a catalyst, as a gas sensor, as white pigment in colours, and as a component of varistors.[8]

The research on ZnO has mainly been driven by its application in surface acoustic wave devices and its prospective use as a wide band gap semiconductor for light emitting devices and for transparent and

high temperature electronics.[9] Furthermore, the interest on ZnO has been triggered by reports on p-type conductivity, diluted ferromagnetic properties, and considerable progress in nanostructure fabrication. Nevertheless, many of the critical issues for the applications of ZnO have not yet been solved. Especially for the application of ZnO as a transparent conductive window material in solar cells, the development of a cost efficient deposition process and the optimization of the electronic and optical properties are still an active field of research.

The different thin film solar cell technologies established nowadays impose different requirements on the TCO window layers and the deposition processes. All of these requirements have in common that the production costs shall be low while the resulting TCO needs to have a transparency as high as possible and a resistivity as low as possible, which is a prerequisite for high power conversion efficiencies of the solar cells. Up to now, tin-doped indium oxide offers the best balance between a low electrical resistivity and a high optical transparency,[10] but indium is a rare material and leads to high production costs. These costs can be reduced significantly by employing cheaper raw materials. Zn, for example, is roughly 300 times less expensive in comparison to In, and Al-doped ZnO offers only slightly worse electronic properties in comparison to ITO. Yet, the reason for the difference in the electronic properties is not clear, and the aim is to improve the doped ZnO to be competitive with the ITO. It is known already, that the electronic properties of the TCOs are closely related to their structural properties such as the incorporation of the dopants, the density of crystallographic defects, the presence of grain boundaries, and the grain boundary trap densities. These properties in turn are strongly dependent on the deposition parameters. Nevertheless, even though ZnO, CdO, In_2O_3, and SnO_2 are investigated for a very long time now, some of the fundamental relations between the deposition parameters and the structural as well as the electronic properties are not yet understood, and hence the optimization of the material properties is mostly performed by trial and error, which is not satisfying and needs to be addressed.

Among the different thin film solar cell technologies, chalcopyrite solar cells have the great advantage that the band gap of the chalcopyrite-based absorber layer can be varied by changing the stoichiometry of the film. This allows for a tuning of the band gap to the optimal value of approximately 1.5 eV (see for example Reference 11 page 88) for the absorption of the spectrum of the sunlight. Still, high efficiencies can only be obtained when the alignment of the energy bands of the absorber material and the front contact window layer is optimized. Otherwise, losses in form of low open circuit voltages and, in consequence, low efficiencies are encountered. While the band edges of the absorber material can easily be tuned, this is more difficult for the window layer. One approach is to tune the band gap of the ZnO by isovalent ion substitution. Alloying ZnO with MgO, for example, increases the band gap energy from 3.24 eV to 4.20 eV for values of $x = 0$ and 0.46 in $Zn_{1-x}Mg_xO$, respectively, by replacing Zn^{2+} ions by Mg^{2+} ions without segregation of the MgO phase.[12] However, alloying ZnO leads to a deterioration of the electronic, structural, and optical properties of the TCO, which is unfavourable for the application as a front contact window layer in solar cells. Therefore, the origin of the deterioration of the properties must be investigated to be able to realize a proper band alignment while at the same time minimizing the deterioration of the film properties. This is especially important to achieve high efficiencies in solar cells but also vital for other applications of the band gap tuned TCOs.

In this work, the relation between the structural properties on the one hand and the electronic properties as well as the electronic transport on the other hand for doped ZnO and $Zn_{1-x}Mg_xO$ films will be investigated and compared. It is the aim to gain a deeper understanding of this relationship, which enables to relate the deposition process and the deposition parameters to the structural properties and the resulting electronic properties of the films. This will provide a basis for the deliberate improvement of the TCO layers for the application as window layers in thin film solar cells

as well as for other applications. This work has been realized within the framework of an AiF (‘Arbeitsgemeinschaft industrieller Forschungsvereinigungen “Otto von Guericke” e.V.’) project aiming for the optimization of the surface and interface properties between transparent conductive electrodes and the photovoltaic active layer of chalcopyrite wide-gap thin film solar cells.

A brief introduction to the basic properties of ZnO and the fundamental physics for the understanding of the discussion of the electronic properties of the films with a special emphasis on the charge carrier scattering mechanisms in semiconductors will be provided in Chapter 2. Additionally, the magnetron sputtering process and fundamental aspects of solar cells will be reviewed, before the methods of analysis and the realization of the experiments are elucidated in Chapter 3. All techniques used throughout this work will be mentioned, but only the techniques frequently employed for the investigation of the film properties will be considered in detail. In Chapter 4, the crystalline growth of the ZnO films will be characterized in dependence of the deposition parameters and the substrate type. These results form the basis for the discussion of the relation between the structural properties and the electronic transport in Chapter 5. In this chapter, the dominant scattering mechanisms will be determined and a model, derived for the consistent description of the charge carrier scattering in degenerate semiconductors, will be applied to the ZnO. These results are used in Chapter 6, where the relation between the deposition process and the structural as well as electronic properties is further investigated. The role of high-energetic particle bombardment of the growing films, typical for magnetron sputtering, is discussed, and a model explaining its influence on the electronic properties of the films is developed. In Chapter 7, the influence of the doping on the structural, electronic, and optical properties of ZnO films is elucidated. The efficiency of different dopant elements is investigated and the distribution of the Al atom in the films determined. The results are going to give further insight into the relation between the deposition parameters and the electronic properties of the films and allow to deduce possible routes for the deliberate improvement of doped ZnO films for the application as TCOs. Chapter 8 shortly summarizes the results of the first experiments using $Zn_{1-x}Mg_xO$:Al front contact window layers with improved band alignment to $Cu(In,Ga)S_2$ wide-gap chalcopyrite absorber layers performed with Jonas Schulte. Finally, the thesis will conclude with a short summary of the main results and a brief outlook in Chapter 9.

2. Fundamentals

In this chapter, fundamental aspects of transparent conductive ZnO, which provide the basis for the discussion in the following chapters, will be reviewed. First, the basic properties of ZnO are going to be outlined. Then, after a short introduction to the most important formulae dealing with the band theory of semiconductors, the dominant scattering mechanisms in ZnO will be presented. Eventually, the most commonly used preparation technique for the ZnO, magnetron sputtering, and the application of ZnO:Al films in chalcopyrite solar cells will briefly be discussed. For a more thorough and detailed insight into the fundamental aspects of transparent conductive oxides, the reader is referred to the textbooks (see References 1, 13, and 14).

2.1 Zinc Oxide

ZnO, which is already investigated since 1912, is especially interesting due to its piezoelectricity that led to a first application of ZnO as a thin layer for surface acoustic wave devices.[9] Another driving force for the research on ZnO is its prospective use as a wide band gap semiconductor for light emitting devices and for transparent or high temperature electronics. The field of application of major interest for this investigation, however, is the application of ZnO as a transparent conductive electrode in thin film solar cells. Different requirements have to be fulfilled for that application:[9]

- high transparency in the visible and near-infrared spectral region,
- ability to dope the material to produce films with a low resistivity ($< 10^{-3}$ Ωcm),
- possibility to deposit the material on large areas at low substrate temperatures,
- possibility for preparation of structured surfaces for light trapping,
- low material costs, nontoxicity, and abundance,

which is feasible using Al-doped ZnO prepared by magnetron sputtering. In the following, a brief overview of the structural, electronic, and optical properties of ZnO, mainly based on References 1, 13, and 14, will be provided.

2.1.1 Crystalline Structure

Zinc oxide crystallizes in the hexagonal wurtzite structure, the zinc blende structure, and the rocksalt structure. While the thermodynamically stable phase under ambient conditions is that of wurtzite symmetry, ZnO exhibits the rocksalt structure at high pressures or when it is alloyed with a high amount of Mg. The structure of the wurtzite ZnO, which has been determined by Bragg in 1914,[9] is depicted in Figure 2.1 on page 6.

The structure belongs to the space group $P6_3mc$ and consists of two interpenetrating hexagonal close packed sublattices, each of which consists of one type of atom. The anions in this tetrahedral coordination are surrounded by four cations, and vice versa. The bulk lattice parameters reported in literature for ZnO in this structure are $c = 0.52066$ nm and $a = 0.32498$ nm (JCPDS 36-1451). The corresponding values for thin films, however, strongly depend on the doping and the deposition

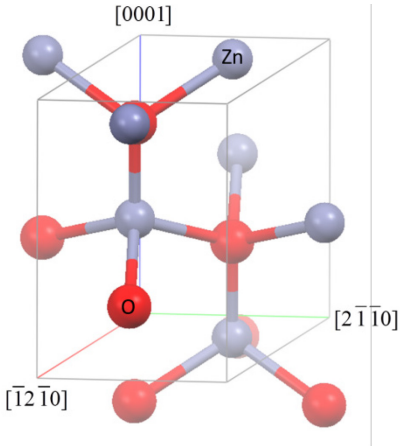

Figure 2.1: Structure model of wurtzite ZnO. The grey balls represent zinc atoms, while the red balls denote the oxygen atoms.

conditions of the ZnO. This wurtzite crystal structure does not exhibit an inversion symmetry along the c-axis, which leads to polar planes consisting only of Zn atoms ((0001) plane) or O atoms ($(000\bar{1})$ plane). The difference between these planes becomes especially obvious in the etching behaviour of the two planes. Since furthermore the Zn-O bonds are primarily ionic, the planes perpendicular to the c-axis consist of positively charged Zn and negatively charged O atoms. Together with the lack of inversion symmetry, this gives rise to a strong piezoelectric behaviour in ZnO.

2.1.2 Electronic Properties

In the tetrahedrally bonded II-VI semiconductor ZnO, the cation and anion s- and p-orbitals form sp^3-hybrids, whose overlap leads to bonding and antibonding combinations. In consequence, the conduction band of ZnO is mostly composed of Zn 4s electrons, while the valence band is dominated by O 2p states. The band gap of ZnO has a direct character and a value of 3.4 eV. The band structure of ZnO has also been calculated by density-functional theory (DFT) models, which confirm that the valence band maximum and the conduction band minimum both occur at the Γ point, meaning that ZnO is a direct semiconductor. The results are shown in Figure 2.2.

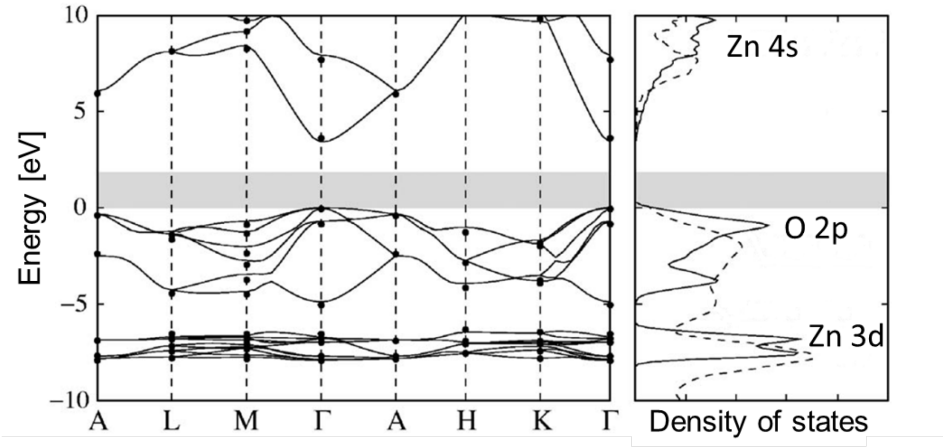

Figure 2.2: Band dispersion of bulk ZnO in the wurtzite structure obtained from density-functional theory calculations within the generalized-gradient approximation including self-interaction corrections (GGA+U) adapted from Reference 15. The conduction band states have been shifted to the experimental band gap. On the right side, solid lines represent the calculated density of states, while dashed lines show the experimental data. The grey area indicates the calculated band gap.

For low free carrier concentrations, for instance in undoped ZnO, the conduction band can be approximated parabolically. For the application of ZnO as a transparent conductive oxide, on the other hand, high free carrier concentrations are needed, which lead to strong deviations from the parabolic

approximation for free carrier concentrations above $n \approx 10^{20}\,\mathrm{cm}^{-3}$. This has for example been investigated by Young et al.[16] and will be discussed in detail later.

To achieve the low resistivity at room temperature, needed for the application of ZnO as a transparent conductive oxide, two different approaches can be used: the creation of intrinsic donors by lattice defects or the introduction of extrinsic dopants.

Intrinsic Doping

If ZnO single crystals are grown without the addition of extrinsic dopants, the resistivities are in the order of $0.1\ldots10^3\,\Omega\mathrm{cm}$, which can be attributed to an n-type intrinsic doping.[7] The intrinsic doping is caused by electrically active defects, which constitute deviations from the ideal structure due to the displacement or removal of lattice atoms. For a long time, it was believed that oxygen vacancies are the dominant intrinsic donors. This hypothesis was supported by annealing experiments, where an increase of the free carrier concentration for annealing under reducing conditions and a decrease of the free carrier concentration for annealing under oxidizing conditions, was observed. Recent theoretical and experimental studies, however, showed that interstitial Zn is the dominant donor-like defect in ZnO.[17,18] According to density-functional-theory calculations, the interstitial Zn (Zn_i) occupies the octahedral site in the wurtzite structure and induces a state with two electrons above the conduction band minimum thus contributing to the intrinsic n-type doping.

Another likely cause of unintentional doping discussed in literature is hydrogen. It is present in the growth environment of most deposition techniques used to produce ZnO, for instance vapour-phase transport, chemical vapour deposition, hydrothermal growth, laser ablation, and sputtering, and is known to act as a dopant in ZnO.[17] The role of hydrogen co-doping in ZnO:Al and $Zn_{1-x}Mg_xO$:Al will be discussed more detailed in Section 7.2.

The lowest resistivities obtained by intrinsic doping are still not suitable for the application of ZnO as a transparent conductive oxide. Furthermore, the optical transmittance is decreased for increasing Zn excess and the high conductivity is not stable. During heat treatments in air, for example, the conductivity decreases by orders of magnitude, which is unfavourable for a TCO and can only be circumvented by extrinsic doping.[19,20]

Extrinsic Doping

Extrinsic doping of ZnO is mostly performed by the addition of group III elements, which results in an n-type doping. The first investigations of the doping of ZnO are reported in the 1950s, where the effect of the addition of B_2O_3, Al_2O_3, Ga_2O_3, and In_2O_3 was examined. The result was an increase of the conductivity by orders of magnitudes. Generally, it is assumed that the group-III dopants are built in onto Zn lattice sites (M_{Zn}), contributing the additional electron, which is not required for the bonding, to the conduction band. According to Thomas[21], this can be described by the following equation

$$M_2O_3 \Leftrightarrow 2M_{Zn}^{+} + 2O_O + 2e^{-} + \frac{1}{2}O_2, \tag{2.1}$$

where O_O represents an O^- ion at a normal oxygen lattice site. Since this introduces additional states in the band gap, which are in the case of Al, Ga, and In only 59 meV, 54.5 meV, and 63.2 meV below the conduction band minimum,[22] respectively, the free carrier concentration at room temperature can be increased by orders of magnitude. Yet, not only doping with group III elements was reported, but other elements such as Si, Y, Sc, F, V, S, Ge, Ti, Zr, and Hf have been used as well.[23-25] Indeed, free carrier concentrations of more than $n \approx 1.5\cdot10^{21}\,\mathrm{cm}^{-3}$ have been achieved by extrinsic doping of ZnO. For such high free carrier concentrations, the electronic states introduced by the dopants form an impurity band, which overlaps with the conduction band of the ZnO and leads to an ionization energy of the

dopants equal to zero. The semiconductor is then referred to as degenerately doped. Degenerate semiconductors exhibit conductivities comparable to those of metals, and the free charge carriers can be described similar to the free electrons in metals.

The introduction of the dopants does not only increase the free carrier concentration but also changes the crystalline structure of the films. To reduce the effect of the dopant on the lattice, its ionic radius should not differ too much from that of the Zn ion. The influence of Al, Ga, In, and Al + H on the electronic, structural, and optical properties of ZnO will be elaborated in Chapter 7 of this work.

A competing process to the extrinsic doping is the formation of secondary phases or defect complexes containing the dopant material in an electrically inactive state. The formation of such compounds should be avoided. This, however, can be difficult. In Al-doped ZnO, for instance, the formation of electrically inactive Al_2O_3 or $ZnAl_2O_4$ is promoted by large negative values of the enthalpy of formation of these secondary phases.[26,27] The influence of the formation of secondary phases on the electronic properties of the films will be a major aspect of this work.

2.1.3 Optical Properties

Transparent conductive oxides are characterized by a high optical transmittance in the visible (400 nm to 800 nm) and parts of the near-infrared (800 nm to 2500 nm) spectral region. The optical properties of ZnO are a direct result of the electronic properties and have been investigated in the spectral region between 200 nm and 2500 nm in this work. Figure 2.3 shows the transmittance *T*, reflectance *R*, and absorbance *A* of a typical ZnO:Al film.

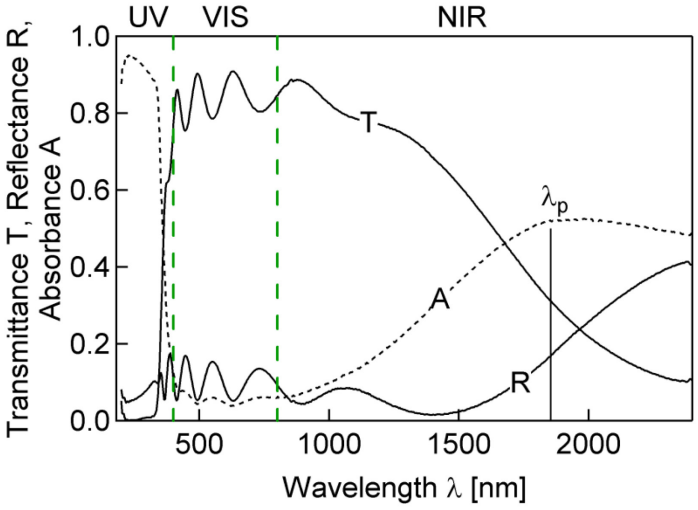

Figure 2.3: Transmittance *T*, Reflectance *R*, and Absorbance *A* (calculated using *R* + *T* + *A* = 1) of a typical ZnO:Al layer with a high free carrier concentration ($n = 3.4 \cdot 10^{20}$ cm^{-3}).

The optical properties of the ZnO in the ultraviolet spectral region ($\lambda < 400$ nm, see Figure 2.3 'UV') are dominated by a strong absorption. This absorption is caused by the excitation of electrons from the valence band into the conduction band of the semiconductor and occurs for wavelengths smaller than a certain value λ_g. In undoped ZnO single crystals, this wavelength corresponds to the band gap energy according to Planck's relation

$$\lambda_g = \frac{hc}{E_g}, \tag{2.2}$$

where h is Planck's constant, c is the speed of light, and E_g is the band gap energy of the ZnO. For a band gap energy of E_g = 3.4 eV, the wavelength λ_g is approximately 365 nm. For TCO materials,

which usually exhibit band gap energies above 3 eV, this absorption edge is generally in the ultraviolet region, which explains their transparency for longer wavelengths.

The doping of a semiconductor influences the optical band gap. Mainly, an increase of the optical band gap with increasing free carrier concentration is observed. If the Fermi level is increased due to the higher free carrier concentration, the photons need to have a higher energy to excite the electrons from the valence band into the unoccupied states above the Fermi level. This effect is called the Burstein-Moss shift,[28,29] which was used by Burstein and Moss independently from each other to explain their experimental results for InSb. The increase of the optical band gap due to the Burstein-Moss shift can be calculated according to[30]

$$\Delta E_{\mathrm{g}}^{BM} = \frac{\hbar^2}{2}\left(3\pi^2 n\right)^{\frac{2}{3}}\left(\frac{1}{m_{\mathrm{n}}^*}+\frac{1}{m_{\mathrm{p}}^*}\right), \tag{2.3}$$

where m_{n}^* and m_{p}^* are the effective masses of the electrons and holes, respectively. The effective masses are important for the Burstein-Moss shift, because the transitions from the valence band to the conduction band occur nearly without a change in the wave number of the electrons k. This is due to the much smaller wave vector of the light $k = 2\pi/\lambda$ in comparison to the momentum of the electrons at the Fermi energy $k_{\mathrm{F}} = (3\pi^2 n)^{\frac{1}{3}}$ (using $E_{\mathrm{F}} = \frac{\hbar^2}{2m_{\mathrm{n}}^*}(3\pi^2 n)^{\frac{2}{3}}$ and $E_{\mathrm{F}} = \frac{\hbar^2 k_{\mathrm{F}}^2}{2m_{\mathrm{n}}^*}$).

Although the increase of the band gap due to the Burstein-Moss effect is dominant, highly doped semiconductors also exhibit effects narrowing the band gap. This can be attributed to the interaction of the electrons with the charged dopant atoms and the production of electron-hole pairs in absorption experiments, which lead to a downward shift of the conduction band and an upward shift of the valence band.[30-32] While the Burstein-Moss shift can be observed easily and is therefore often used in the literature to explain the increased optical band gap due to the doping, the band gap narrowing is not very well investigated. Some theoretical models have at least been discussed by Sernelius et al.[32], Hamberg and coworkers[30], and Abram et al.[33].

When the wavelength of the photons is below λ_{g}, the energy is not sufficient to excite electrons from the valence band to the conduction band (see Figure 2.3 'VIS'). The energy cannot be absorbed and is thus transmitted, which results in a high average transmittance of the films in the visible and near-infrared region (approximately 400 nm to 1000 nm). Depending on the film thickness, the transmittance and reflectance show oscillations caused by the interference of the incoming light and the light reflected from the interface between the film and the substrate. For TCOs, the optical transmittance of the layer stack composed of the film and the substrate is usually above 80 %. Their transmittance is reduced by several effects: the reflection of the light at the interfaces in the layer stack, the absorption due to defects, which induce states in the band gap, and the absorption caused by free carriers.

In the near-infrared region above wavelengths of roughly 1000 nm (see Figure 2.3 'NIR'), the optical properties of the ZnO are mostly characterized by an increase of the absorption and the reflectivity. This is caused by the contribution of the free charge carriers. For a TCO, the electrons are generally regarded as quasi-free and can therefore be described by the classical Drude theory for metals. According to this theory, the real part of the dielectric constant $\mathrm{Re}\{\varepsilon\}$ can be written as[34]

$$\mathrm{Re}\{\varepsilon\} = \varepsilon_\infty - \frac{ne^2}{\varepsilon_0 m_{\mathrm{n}}^* \omega^2}, \tag{2.4}$$

where ε_∞ is the high-frequency dielectric constant, n is the free carrier concentration, e is the elementary charge, ε_0 is the vacuum permittivity, m_n^* is the electron effective mass, and ω is the angular frequency of the light. The resonance of the free electron gas is then described by the plasma frequency ω_p, which is obtained for $\mathrm{Re}\{\varepsilon\} = 0$,

$$\omega_p = \sqrt{\frac{ne^2}{\varepsilon_\infty \varepsilon_0 m_n^*}}. \tag{2.5}$$

For wavelengths much smaller than the plasma wavelength $\lambda_p = 2\pi c/\omega_p$, the light can travel through the material mostly undisturbed. For wavelengths in the region of λ_p, an increasing amount of the radiation is absorbed, while for wavelengths larger than the plasma wavelength, the real part of the dielectric constant becomes negative and, in consequence, the plasma reflective.[34] The plasma wavelength is marked in Figure 2.3 on page 8 using $n = 3.4 \cdot 10^{20}$ cm^{-3}, $\varepsilon_\infty = 3.74$ and $m_n^* = 0.28 m_e$ (see Reference 22, m_e: free electron mass).

If the free carrier concentration is very high ($n \gtrsim 10^{21}$ cm^{-3}), the plasma frequency is shifted into the visible spectral region. Therefore, the free carrier concentration is fixed as the plasma frequency has to be adjusted to the specific application of the transparent conductive oxide. For a further decrease of the resistivity, the mobility of the free carriers has to be increased. This has been shown to improve the near-infrared transparency of the materials as well.[35] Figure 2.4 presents a simulation of the optical properties of a doped ZnO film for a free carrier concentration of $n = 3.4 \cdot 10^{20}$ cm^{-3} and different charge carrier mobilities. The effective mass was assumed to be $m_n^* = 0.28 m_e$ and the simulation was performed using the program WVASE32 by Wollam, Inc., which will be described more detailed in Section 3.3.

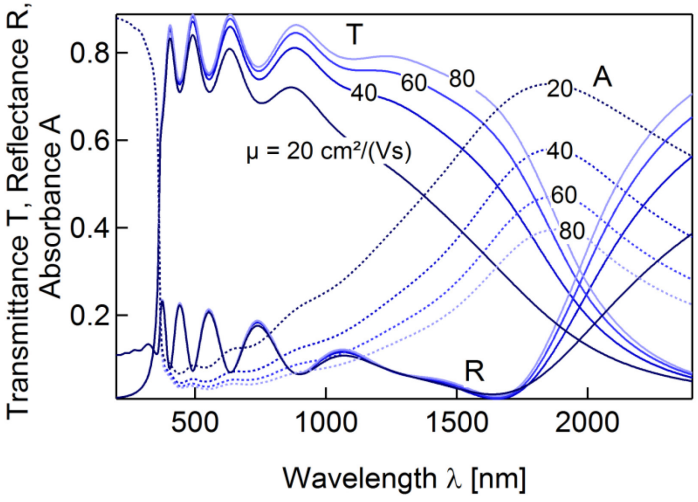

Figure 2.4: Transmittance T, reflectance R, and absorbance A for a semiconductor with a free carrier concentration $n = 3.4 \cdot 10^{20}$ cm^{-3} and charge carrier mobilities between μ = 20 cm²/(Vs) and 80 cm²/(Vs). The effective mass and the high-frequency dielectric constant are assumed to be $m_n^* = 0.28 m_e$ and $\varepsilon_\infty = 3.74$, respectively. The optical data has been simulated using an Adachi oscillator[36] for the band-to-band transitions and a Drude oscillator for the plasmon absorption in the near-infrared spectral region.

The simulation clearly shows the improvement of the transmittance in the near-infrared region for increased charge carrier mobilities. This increased transmittance T is due to a reduced absorbance A.

2.1.4 $Zn_{1-x}Mg_xO$ Alloys

ZnO can be alloyed with a variety of elements. The main purpose is to tailor the band gap, which is especially interesting for optimizing the device performance of optoelectronic devices that incorporate TCO contacts.[37] Furthermore, it can be used to improve the band alignment in solar cells. Mainly investigated are the oxides of Be, Mg, Ca, and Cd. As can be inferred from the band gaps, alloying of ZnO (E_g = 3.4 eV) with BeO (E_g = 10.6 eV), MgO (E_g = 7.8 eV), and CaO (E_g = 7.0 eV) could be used to extend the band gap, while CdO (E_g = 2.3 eV) should decrease the band gap of ZnO.[7]

Since Mg^{2+} ions are assumed to occupy Zn lattice sites and the tetrahedral ionic radius[38] of Mg^{2+} (57 pm) is quite comparable to that of Zn^{2+} (60 pm), a wide range of solubility of Mg in the ZnO lattice is expected.[39] Hence, it is a very promising material for the band gap engineering of ZnO. Ohtomo et al.[40] were the first to report the growth of $Zn_{1-x}Mg_xO$ films. They prepared the films on c-sapphire substrates by pulsed laser deposition with a Mg content up to $x = 0.46$. Although the solubility limit of MgO in ZnO under thermodynamic equilibrium conditions is only 4 mol.%,[40] a solid solution exhibiting the ZnO wurtzite structure was observed up to $x = 0.33$, which resulted in an increase of the band gap energy from 3.29 eV to 3.99 eV at room temperature. Apparently, the films constitute a metastable wurtzite structure. Park et al.[39] reported single phase MOCVD (metal-organic chemical vapour deposition) grown films up to $x = 0.49$ with a band gap of up to 4.3 eV, and Minemoto et al.[12] prepared single phase $Zn_{1-x}Mg_xO$ films by radio-frequency magnetron sputtering with $x \leq 0.46$ and a band gap increase of nearly 1 eV.

An overview of the literature data of the band gap energies of $Zn_{1-x}Mg_xO$ films was given by Ellmer.[7] This data, together with other literature data for the band gap energy of $Zn_{1-x}Mg_xO$ is shown in Figure 2.5.

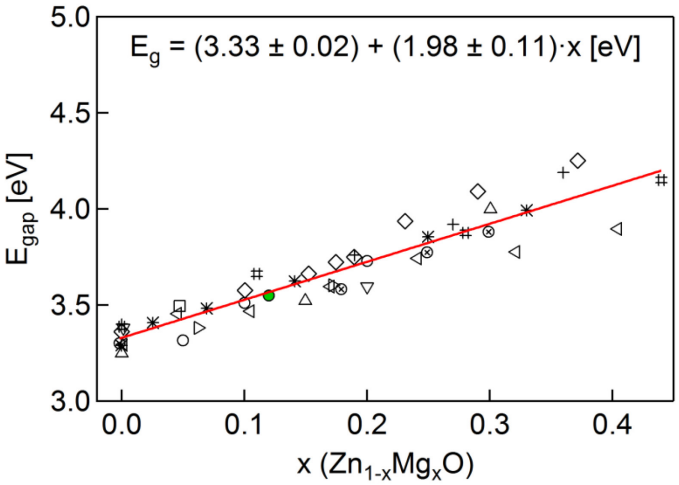

Figure 2.5: Band gap energies of $Zn_{1-x}Mg_xO$ as a function of the Mg content. The data presented is based on a compilation by Ellmer.[7] The following sources have been used: Cohen et al.[41] (circles), Ellmer and Vollweiler[42] (squares), Glatzel et al.[43] (triangles up), Kang et al.[44] (triangles down), Matsubara et al.[45] (triangles left), Minemoto et al.[12] (triangles right), Muthukumar et al.[46] (otimes), Ohtomo et al.[40] (stars), Schmidt-Grund et al.[47] (diamonds), Teng et al.[48] (plusses), Wu et al.[49] (crosses), and this work (filled circle). The solid red line shows a linear fit to the data.

Ellmer determined $E_g = 3.32 + 2.2x$ [eV] for the nearly linear relationship between the Mg content and the band gap energy, fitting the data of Ohtomo et al.[40], which is in good agreement with the result of the fit performed for the whole dataset presented here. The relation between the band gap energy and the Mg content with the uncertainty of the linear fit in Figure 2.5 is given by $E_g = (3.33 \pm 0.02) + (1.98 \pm 0.11) \cdot x$ [eV].

The introduction of Mg into the ZnO lattice leads to a reduction of the c-axis lattice parameter and an increase of the a-axis lattice parameter,[39,40,49] while the cell volume $(1.5\sqrt{3}a^2c)$ is rather constant due to the similar ionic radii of Zn^{2+} and Mg^{2+}.[40] Additionally, an increase of the full width at half maximum of the (0002) X-ray diffraction peaks is observed, which can be attributed to a decrease in the crystalline quality of the ZnO with increasing Mg incorporation.[39]

Investigations of Al-doped $Zn_{1-x}Mg_xO$ films show an increase of the resistivity with increasing Mg content,[37,41,45] which is caused by a decreasing free carrier concentration and a decreasing mobility of the free carriers. Matsubara et al.[45], for instance, observed an increase of the resistivity in their films prepared by pulsed laser deposition by a factor of roughly 30 when increasing the Mg content from $x = 0$ to $x = 0.42$. This was accompanied by a decrease of the free carrier concentration from $7 \cdot 10^{20}$ cm^{-3} to $1.5 \cdot 10^{20}$ cm^{-3} and a decrease of the free carrier mobility from 30 cm²/(Vs) to 5 cm²/(Vs). Similar effects have also been found by Cohen et al.[41] for their direct-current reactive magnetron sputtered $Zn_{1-x}Mg_xO$:Al films ($0 < x < 0.2$). Possible explanations for the decrease of the free carrier

concentration are the formation of Mg-Al-O compounds, where the Al dopant is electrically inactive, an increase of the formation energy of the heterovalent dopant defects (Al_{Zn}), and changes of the formation energies of the intrinsic point defects.[37,41] Furthermore, Cohen et al.[41] proposed an increase of the free-electron mass, which they found for increasing Mg content, to lead to a decreasing doping efficiency. Additional charge carrier scattering mechanisms due to the incorporation of the Mg in the lattice are also discussed as a reason for the reduced mobility.[37,45] However, only few groups are investigating the structural, optical, and electronic properties of doped $Zn_{1-x}Mg_xO$:Al films for the application as TCO in detail, which is why the effects are not yet fully understood. The charge carrier scattering of the $Zn_{1-x}Mg_xO$:Al films will be discussed in detail in Chapter 5.

2.2 The Band Theory of Semiconductors

In this section, fundamental aspects of the band structure and the doping of semiconductors will be presented as a basis for the discussion of the different scattering mechanisms of the charge carriers and the effects of the doping on the properties of ZnO. Since the aspects of solid state physics for doped and undoped semiconductors are elucidated in numerous textbooks, the following section will only provide a brief review based on References 50-53.

2.2.1 Band Structure

The complete theoretical quantum mechanical description of the band structure of a solid material with the Schrödinger equation is a many-body problem that contains a number of variables larger than the number of atoms in the material. This problem can only be solved using simplifications such as the Born-Oppenheimer and the single-electron approximation.

In the Born-Oppenheimer approximation, also called the adiabatic approximation, the crystal Hamiltonian is subdivided into an electronic and an atomic (or ionic) part. Taking into account the large differences in the speed of motion of the light electrons and the heavy ions, the electron wave function is then determined by the instantaneous position of the ions and the ionic wave function is determined by the averaged electron field. Eventually, the lattice structure is given as the minimum of the total energy. In the single-electron approximation, a single electron in the field of the remaining electrons, which is assumed to be known, is considered. From the probability of the presence of the single electron in the energy levels, the potential of the other electrons can be determined. This results in a self-consistent, iterative description of the electron system.

Based on the single-electron approximation and the translational symmetry of the crystal lattice, it can be inferred that the solutions of the Schrödinger equation

$$\hat{\boldsymbol{H}}\psi(\boldsymbol{r}) = E\psi(\boldsymbol{r}) \tag{2.6}$$

have the form

$$\psi_{\boldsymbol{k}}(\boldsymbol{r}) = e^{i\boldsymbol{k}\cdot\boldsymbol{r}}\boldsymbol{u}_{\boldsymbol{k}}(\boldsymbol{r}), \tag{2.7}$$

known as Bloch's theorem. In these equations, $\hat{\boldsymbol{H}}$ is the Hamiltonian, the energy eigenvalue E is the energy of the electron, $\psi(\boldsymbol{r})$ is the wave function of an arbitrary electron, $\boldsymbol{u}_{\boldsymbol{k}}(\boldsymbol{r})$ is a periodic function with the periodicity of the potential field in the crystal lattice, and $\boldsymbol{k}$ is an arbitrary real vector, which characterizes the wave function $\psi_{\boldsymbol{k}}(\boldsymbol{r})$ and can be identified with a momentum as $\hbar\boldsymbol{k}$ (bold letters represent vectors). For every $\boldsymbol{k}$ in the first Brillouin zone, a discrete quantity of wave functions,

numbered by ν, exists. Hence, the energy eigenvalues are dependent on ν and $\boldsymbol{k}$. Those energy eigenvalues that belong to an arbitrary $\boldsymbol{k}$ for a certain ν are called energy band; the entirety of $E_\nu(\boldsymbol{k})$ is called band structure.

2.2.2 Density of States and Effective Mass

The number of states per unit volume in an energy interval is given by the integral in the k-space over a surface of constant energy

$$g(E) = \frac{1}{4\pi^3} \sum_{\upsilon} \oint_{E_\upsilon(\boldsymbol{k})=E} \frac{d\boldsymbol{S}}{\left|\nabla_{\boldsymbol{k}} E_\upsilon(\boldsymbol{k})\right|}, \tag{2.8}$$

where $d\boldsymbol{S}$ is the area element in the k-space on the iso-energy surface $E = E_\nu(k)$ in the direction of $\nabla_{\boldsymbol{k}} E_\upsilon(\boldsymbol{k})$.

Critical points, where

$$\nabla_{\boldsymbol{k}} E_\upsilon(\boldsymbol{k})\big|_{\boldsymbol{k}=\boldsymbol{k}_0} = 0, \tag{2.9}$$

contribute significantly to the density of states. For a single band, these so-called van Hove singularities represent extremes or saddle points. Close to a critical point, a parabolic expansion of the energy

$$E_\upsilon(\boldsymbol{k}) = E_\upsilon(\boldsymbol{k}_0) + \frac{\hbar^2}{2m_\upsilon(\boldsymbol{k}_0)} \left(\boldsymbol{k} - \boldsymbol{k}_0\right)^2 \tag{2.10}$$

with the tensor of the effective mass at the critical point $\boldsymbol{k}_0$

$$\left\{ \frac{1}{m_\upsilon(\boldsymbol{k}_0)} \right\}_{ij} = \frac{1}{\hbar^2} \frac{\partial^2}{\partial k_i \partial k_j} E_\nu(\boldsymbol{k}) \bigg|_{\boldsymbol{k}=\boldsymbol{k}_0} \tag{2.11}$$

is possible. The tensor is symmetric and can be diagonalized to

$$\frac{1}{m_\upsilon(\boldsymbol{k}_0)} = \begin{pmatrix} \frac{1}{m_1^*} & 0 & 0 \\ 0 & \frac{1}{m_2^*} & 0 \\ 0 & 0 & \frac{1}{m_3^*} \end{pmatrix}. \tag{2.12}$$

Expression (2.10) is then given by

$$E_\upsilon(\boldsymbol{k}) = E_\upsilon(\boldsymbol{k}_0) + \frac{\hbar^2}{2} \sum_{i=1}^{3} \frac{1}{m_i^*} (k_i - k_{0i})^2. \tag{2.13}$$

Despite the replacement of the free electron mass m_e by the effective mass m_i^*, this is the same relation between the momentum $\boldsymbol{k}$ and the energy E compared to a free electron in the case of $\boldsymbol{k}_0 = \boldsymbol{0}$.

Using this approximation for the energy of the electrons, the density of states close to the conduction band minimum can be calculated and is given by

$$g_n(E) = 2\pi \left(\frac{2m_{d,n}^*}{h^2}\right)^{\frac{3}{2}} \sqrt{E - E_C} \qquad \text{for } E > E_C, \tag{2.14}$$

where E_c is $E(\boldsymbol{k}_0)$ for a specific ν and $m_d^* = (M^2 m_1^* m_2^* m_3^*)^{1/3}$ is the density of states effective mass of the charge carriers (the index 'n' in Equation (2.14) indicates the values for electrons). M denotes the number of energy minima at the critical point. The corresponding formulae for the holes can be found in the textbooks.

2.2.3 Undoped Semiconductors

For temperatures equal to zero, the electronic states are occupied for energies smaller than the Fermi energy E_F, while they are empty for higher energies. For non-zero temperatures, the states are filled according to the Fermi-Dirac distribution

$$f(E) = \frac{1}{1 + e^{\frac{E - E_F}{kT}}}, \tag{2.15}$$

where k is the Boltzmann constant and T is the absolute temperature. $f(E)$ is the probability that for a given temperature T a state is occupied by an electron. With $f(E)$, the concentration of the electrons in the conduction band is given by

$$n = 2\int_{E_c}^{\infty} g_n(E) f(E) \mathrm{d}E. \tag{2.16}$$

The relation between the Fermi-Dirac distribution, the density of states, and the occupied states is shown in Figure 2.6.

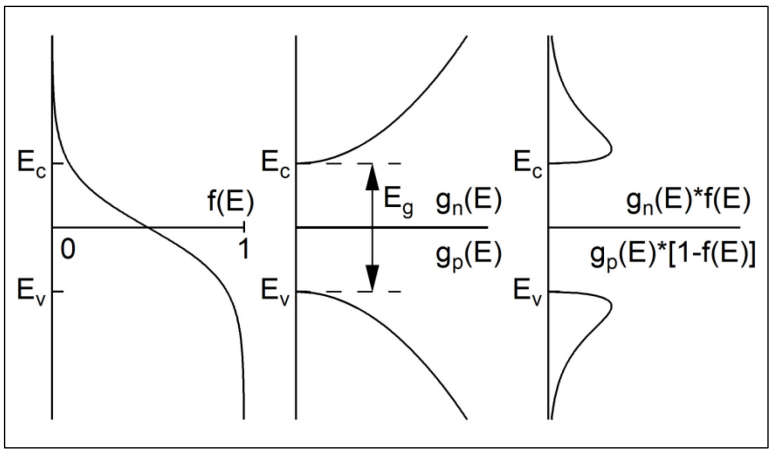

Figure 2.6: Fermi-Dirac distribution (*left*), density of states (*centre*), and occupied states (*right*) as a function of the energy.

Substituting $\eta = (E_F - E_c)/(kT)$ in Equation (2.16) yields

$$n = \frac{2}{h^3}(2\pi m_{d,n}^* kT)^{\frac{3}{2}} \frac{2}{\sqrt{\pi}} \int_0^{\infty} \frac{\sqrt{\varepsilon}}{1 + e^{\varepsilon - \eta}} \mathrm{d}\varepsilon = N_c \mathscr{F}_{1/2}(\eta), \tag{2.17}$$

where $\mathscr{F}_{1/2}(\eta)$ is the Fermi-Dirac integral of the order 1/2 and N_c is the effective density of states at the conduction band bottom. For $\eta \ll -1$ or $E_c - E_F \gg kT$, the Fermi-Dirac distribution can be approximated by the Boltzmann distribution, which means $\mathscr{F}_{1/2}(\eta) \approx e^{\eta}$. In this case

$$n \approx N_c e^{\frac{E_F - E_c}{kT}}, \tag{2.18}$$

and the semiconductor is called non-degenerate. In an intrinsic semiconductor without defects, every electron in the conduction band stems from the valence band and therefore $n = p$ holds, where p is the hole concentration described by similar equations. Solving $n = p$ for the Fermi energy in a non-degenerate semiconductor yields

$$E_F = \frac{E_v + E_c}{2} + \frac{kT}{2}\ln\left(\frac{N_v}{N_c}\right), \tag{2.19}$$

where E_v is the valence band maximum, $N_v = 2/(h^3)(2\pi m_{d,p}{}^* kT)^{3/2}$, and $m_{d,p}{}^*$ is the density of states effective mass of the holes. For zero temperature, the Fermi energy of the intrinsic semiconductor is in the middle of the band gap. When the temperature is raised, the Fermi energy shifts upwards. This can be attributed to the smaller effective mass of the electrons in comparison to that of the holes in ZnO.

2.2.4 Doped Semiconductors

The concentration of electrons in the conduction band at room temperature can be increased by orders of magnitude by doping of the semiconductor. As this work deals exclusively with n-type doping of ZnO, only the donor-like dopants will be discussed. Usually, the donor levels are some 10 meV below the conduction band minimum and can easily be ionized at room temperature. Figure 2.7 schematically shows the energy band scheme of a doped semiconductor.

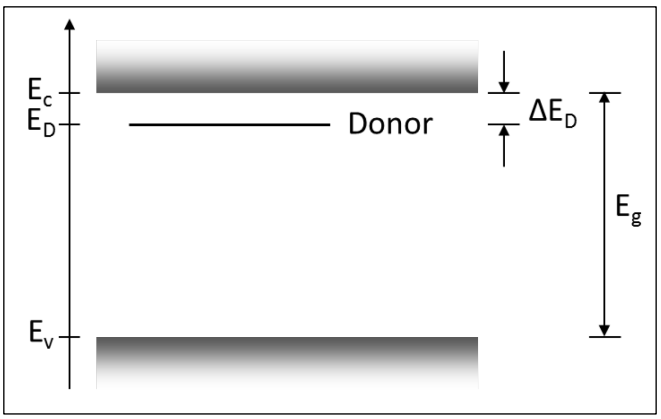

Figure 2.7: Schematic band diagram of a doped semiconductor.

For small impurity concentrations, the energy of the impurity states is adequately described by a δ-function.[54] In this case, their density of quantum states is given by

$$g_D(E) = N_D \delta(E - E_D), \tag{2.20}$$

where N_D is the concentration of the impurities. This is a very rough model, because for very high carrier concentrations, the impurities form a band which merges with the conduction band. This has for example been taken into account by Morgan[55] or Kuźmicz[56]. Since the integrals can mostly be solved analytically and the basic dependences can be described reasonably well when using the δ-shaped impurity state distribution, the discussion will be limited to this case. The concentration of the free electrons in the conduction band is then given by[56]

$$n = \int_{E_c}^{\infty} \frac{[g_n(E) + g_D(E)]}{1 + e^{\frac{E - E_F}{kT}}} dE \tag{2.21}$$

with the density of states of the electrons $g_n(E)$ (see Equation (2.14)). The concentration of occupied localized impurity states is

$$n_D = \int_{-\infty}^{E_C} \frac{g_D(E)}{1 + \frac{1}{2} e^{\frac{E - E_F}{kT}}} dE. \tag{2.22}$$

Neglecting the concentration of acceptors and the contribution of intrinsic electron hole pairs, the charge neutrality condition $n + N_A{}^- = p + N_D{}^+$ reduces to $n \approx N_D{}^+$, and hence the total donor

concentration is given by $N_D = n + n_D$. N_D^+ and N_A^- denote the concentration of ionized donors and acceptors, respectively. Using this relation and Equations (2.21) and (2.22), the ratio of ionized to neutral dopant atoms is given by

$$\frac{N_D^+}{N_D} = 1 - \frac{1}{1 + \frac{1}{2} e^{\frac{E_D - E_F}{kT}}} = \frac{1}{1 + 2e^{\eta + \frac{\Delta E_D(N_D^+)}{kT}}}, \qquad (2.23)$$
$$N_D^+ = N_c \mathscr{F}_{1/2}(\eta),$$

for $E_D < E_c$, which is the case for carrier concentrations below approximately 10^{18} cm^{-3} as will be shown in Section 5.2.2. $\Delta E_D = E_c - E_D$ is the energetic position of the dopant levels with respect to the conduction band edge. Using Boltzmann statistics, Equation (2.23) can be solved for the Fermi energy, which yields

$$E_F = \frac{E_D + E_c}{2} + \frac{kT}{2} \ln\left(\frac{N_D}{2N_c(T)}\right) \qquad (2.24)$$

as long as $kT \ll E_c - E_D$. For zero temperature, the Fermi energy is now in the middle between the donor energy level and the conduction band minimum.

Following Pearson and Bardeen[57], Debye and Conwell[58], as well as Hagemark and Chacka[59], the ionization energy of the dopants can be approximated as a function of the ionized dopant concentration by

$$\Delta E_D = E_D^0 - \alpha N_D^{+\frac{1}{3}}, \qquad (2.25)$$

where E_D^0 is in the order of 55 meV (see References 22 and 60) and $\alpha \approx 5 \cdot 10^{-8}$ eV/cm to account for $\Delta E_D = 0$ for $N_D^+ \approx 10^{18}$ cm^{-3}. For Energies $\Delta E_D \leq 0$ ($E_D \geq E_c$), $n_D = 0$ and the ionization rate equals 100 % within this model. When the Boltzmann statistics cannot be applied, the Fermi-Dirac integral can be approximated by $\mathscr{F}_{1/2}(\eta) = \frac{1}{e^{-\eta} + 0.27}$ in the range of $-\infty < \eta < 1.3$ and $\mathscr{F}_{1/2}(\eta) = \frac{4}{3\sqrt{\pi}}\left(\eta^2 + \frac{\pi^2}{6}\right)$ for $\eta > 0.8$ with an error smaller than 3 %.[61,62] η, on the other hand, has been approximated to a high accuracy by Nilsson[63,64] as a function of the free carrier concentration $\frac{n}{N_c} = \mathscr{F}_{1/2}(\eta) =: u$

$$\frac{E_F - E_c}{kT} = \eta \approx \frac{u}{1 - u^2} + \frac{\left(\frac{3\sqrt{\pi}u}{4}\right)^{\frac{2}{3}}}{1 + \left[0.24 + 1.08\left(\frac{3\sqrt{\pi}u}{4}\right)^{\frac{2}{3}}\right]^{-2}}, \qquad (2.26)$$

which is valid for $\eta > -5$ with $\left|\eta - \eta_{approx}\right| < 0.006$.

Figure 2.8 on page 17 shows the ratio of the concentration of ionized donors to the total donor concentration N_D^+/N_D, according to Equation (2.23) for $E_D < E_c$ and $N_D^+/N_D = 1$ for $E_D > E_c$, as a function of the impurity concentration for $T = 295$ K and $m_{d,n}^* = 0.28 m_e$.

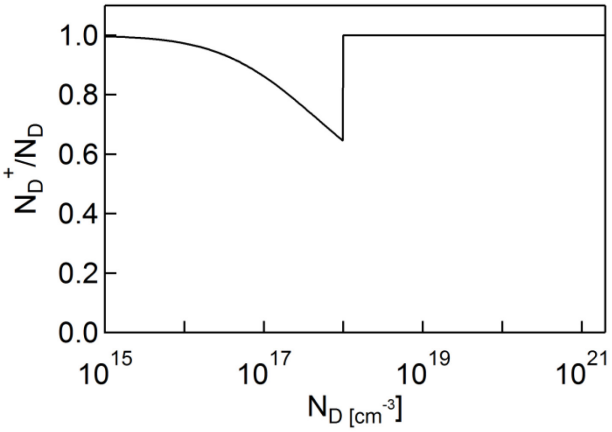

Figure 2.8: Calculated ratio of the concentration of ionized donors to the total donor concentration N_D^+/N_D as a function of the total donor concentration. For $n < 10^{18}$ cm^{-3}, Equation (2.23) was used (T = 295 K, $m_{d,n}^* = 0.28m_e$), while for degenerate conditions, $N_D^+/N_D = 1$ holds.

The step is caused by the (inappropriate) δ-shape of the energy level of the impurities. For a Gaussian distribution of the energy levels of the impurities, the notch in the ionization rate is smooth as it is shown by the calculations performed for doped Si by Kuźmicz[56]. Still, even from this simple calculation, it becomes apparent that there is an impurity concentration range in the transition region between the non-degenerate and the degenerate state, where the dopants are not completely ionized. This has also been observed experimentally.[56] It can be concluded that the approximation of completely ionized donors, which will be used in most of the models for the charge carrier scattering mechanisms, is appropriate for small and large impurity concentrations, while it is only roughly fulfilled in the partially degenerate case. Askerov (see Reference 52 page 34) proposed the following limits: $\eta < 4$ for the non-degenerate case, $-4 < \eta < 10$ for a partially degenerate state, and $\eta > 10$ for highly degenerate conditions. For a given η or free carrier concentration, this determines which approximations have to be applied within the models for the electronic transport.

2.3 Charge Carrier Scattering Mechanisms

Charge carriers, such as electrons or holes, can be described as a superposition of Bloch waves traveling through a solid.[65] In an ideal single crystal, these waves can, in principle, travel undisturbed through the material. The interaction with the ions of the solid is incorporated in the Bloch solution. However, real materials exhibit crystallographic defects, which lead to scattering of the wave packet. Such scattering can be described with the help of the mean free time τ – the average time between two scattering events. With the help of Ohm's law ($\boldsymbol{j} = \boldsymbol{\sigma E}$), under the assumption that the scattering randomizes the electron velocity, and for a constant applied electric field, the drift mobility of the charge carriers can be related to the scattering time by

$$\mu_{d,n} = \frac{e\langle\tau\rangle}{m_{c,n}^*}, \tag{2.27}$$

where e is the elementary charge and $m_{c,n}^*$ is the conductivity effective mass of the electrons. The conductivity effective mass for ellipsoidal constant energy surfaces is given by $\frac{1}{m_c^*} = \frac{1}{3}\left(\frac{1}{m_1^*} + \frac{1}{m_2^*} + \frac{1}{m_3^*}\right)$, which results from the fact that a symmetrical distribution of anisotropic valley conductivities results in an isotropic full conductivity composed of the conductivities in the different directions in the crystal (see Reference 51 page 268). If only one band with spherical constant energy surfaces is assumed to be contributing to the conduction, the difference between the density of

states effective mass m_d^* and the conductivity effective mass m_c^* vanishes. This is the case for the derivation of the scattering mechanisms that will be discussed in the following. Hence, the index 'd' or 'c' denoting the density of states or conductivity effective mass will be omitted. Furthermore, in this thesis, solely the charge transport of electrons is investigated, and the index 'n' denoting the electron effective mass is therefore redundant. The same applies for the electron mobility μ_n, whose index will be spared in the following as well. Since the density of states effective mass and the conductivity effective mass for electrons in ZnO are similar,[16] the distinction between m_c^* and m_d^* will not only be omitted for the discussion of the scattering mechanisms, but throughout the rest of the thesis, and m^* will be used to denote the effective mass of the electrons.

In Hall measurements both, magnetic fields and electric fields, are used. The drift mobility then slightly differs from the mobility of the carriers determined by the Hall experiment, which can be expressed in terms of the relaxation time τ for weak magnetic fields B ($\mu_d^2 B^2 \ll 1$) by (see for example Reference 51 page 285)

$$\mu^{\mathrm{Hall}} = \frac{e\langle\tau\rangle}{m_c^*}\frac{\langle\tau^2\rangle}{\langle\tau\rangle^2} = r_H \mu_d. \tag{2.28}$$

The value $\langle\tau^s\rangle$ is given for non-degenerate semiconductors by

$$\langle\tau^s\rangle = \frac{\int_0^\infty x^{\frac{3}{2}} e^{-x} \tau^s(x)\mathrm{d}x}{\int_0^\infty x^{\frac{3}{2}} e^{-x}\mathrm{d}x} \tag{2.29}$$

with the dimensionless variable $x = E/(kT)$ and for degenerate semiconductors by

$$\langle\tau^s\rangle = \left[\tau(E_F - E_c)\right]^s. \tag{2.30}$$

Hence, $r_H = 1$ for degenerate semiconductors (see Reference 51 page 261 and following). Assuming that the scattering events are independent from each other, the total probability of scattering $\mathrm{d}t/\tau$ in a small unit of time $\mathrm{d}t$ is the sum of the probabilities for the single scattering mechanisms $\mathrm{d}t/\tau_i$, and in consequence (see for example Reference 65 page 22 and following) the following expression holds:

$$\frac{1}{\tau} = \sum_i \frac{1}{\tau_i} \propto \frac{1}{\mu} = \sum_i \frac{1}{\mu_i}, \tag{2.31}$$

which is known as Matthiessen's rule. For non-degenerate conditions, this is only an approximation, but for degenerate semiconductors, the relation is exact. If different types of charge carriers contribute to the electrical conduction, they may have different mobilities, which has to be taken into account for the conductivity

$$\sigma = e(n\mu_n + p\mu_p), \tag{2.32}$$

where n and μ_n are the carrier concentration and the mobility of the electrons and p and μ_p are the concentration and the mobility of the holes, respectively.

The scattering in semiconductors and its influence on the free carrier concentration and the charge carrier mobility were subject to investigations for a long time now. Huge efforts have been made to understand the scattering mechanisms more detailed and various formulae have been derived to describe the scattering mechanisms. The following subsections will give an overview of the most important scattering mechanisms required for the discussion of the electronic transport in ZnO films,

abstracted from the vast amount of literature dealing with this topic. For a more detailed background on the scattering mechanisms in semiconductors, the reader is referred to References 22, 50-52, and 66.

2.3.1 Phonon Scattering

Optical Phonon Scattering

Optical phonon scattering occurs in polar semiconductors with partially ionic bonding and can be attributed to the dipole electric moment induced by the displacement of atoms, which strongly interacts with electromagnetic waves (light). Devlin calculated the optical Hall mobility for non-degenerate semiconductors and $kT \ll \hbar\omega_0$ (see Reference 59)

$$\mu_{LO}^{Hall} = r_{H,LO}\Phi\frac{e}{2\alpha\omega_0 m^*}\left(e^{\frac{\hbar\omega_0}{kT}} - 1\right), \tag{2.33}$$

where α, the polaron coupling constant, is given by

$$\alpha = \left(\frac{1}{\varepsilon_\infty} - \frac{1}{\varepsilon_s}\right)\frac{\sqrt{m^* e^2}}{4\pi\varepsilon_0\hbar\sqrt{2\hbar\omega_0}}. \tag{2.34}$$

ε_s is the static dielectric constant, ε_∞ is the high-frequency dielectric constant, m^* is the effective mass of the charge carriers, and $\hbar\omega_0$ = 72 meV (see Reference 67) is the energy of the longitudinal-optical phonon in ZnO. $r_{H,LO}$ is the correction factor for the Hall mobility of the longitudinal-optical modes and $r_{H,LO}\Phi$ is a slowly varying function of the temperature, usually assumed to be equal to 1.

For degenerate conditions, there is hardly any formula given in literature. At least, Askerov (see Reference 52 page 141) calculated the scattering time for degenerate conditions under the assumption $E \ll \hbar\omega_0$ (E: energy of the electrons), which, however, is unfortunately also violated for carrier concentrations above $n \approx 10^{19}$ cm^{-3}. From that, the mobility was determined to be

$$\mu_{LO,deg}^{Hall} = \frac{e}{4\alpha\omega_0 m^*}\left(e^{\frac{\hbar\omega_0}{kT}} + 1\right), \tag{2.35}$$

which is very similar to Equation (2.33). Figure 2.9 shows the Hall mobility as a function of the temperature for polar-optical phonon scattering in non-degenerate and degenerate ZnO ($m^* = 0.28m_e$).

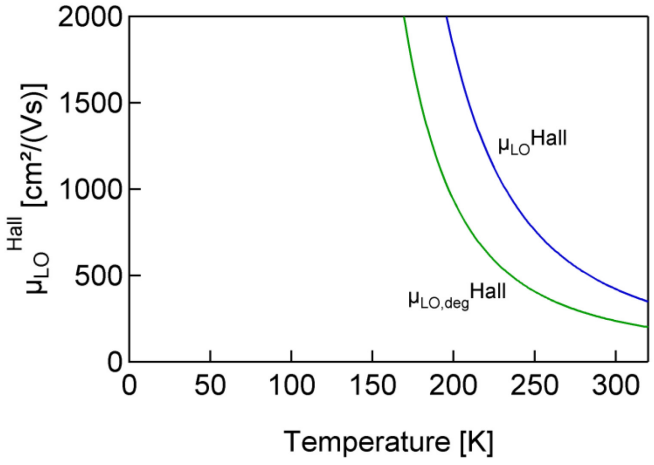

Figure 2.9: Hall mobility μ_{LO}^{Hall} as a function of the temperature for the polar-optical phonon scattering for non-degenerate ZnO (blue) and degenerate ZnO (green). $m^* = 0.28m_e$.

The dominance of the polar-optical phonon scattering is increasing with increasing temperature and it is independent of the free carrier concentration.

Acoustical Phonon Scattering

The deformation potential or acoustical mode scattering is caused by the displacement of atoms, which leads to local compressions and extensions in the crystal analogous to those occurring when acoustical waves propagate through the crystal, and hence to local energetic shifts of the band edges. Bardeen and Shockley[68] determined the acoustical mode scattering mobility in non-degenerate semiconductors

$$\mu_{ac}^{Hall} = r_{H,ac} \frac{\sqrt{8\pi}\hbar^4 c_l e}{3E_{ac}^2 m^{*\frac{5}{2}} (kT)^{\frac{3}{2}}}, \tag{2.36}$$

where $r_{H,ac} = 3\pi/8$ (see for example Reference 22) is the correction factor for the Hall mobility of the acoustical mode scattering, E_{ac} is the energy shift of the conduction band per unit dilation (deformation potential), and c_l is the average longitudinal elastic constant that can be calculated for ZnO from the elastic constants c_{ij} by

$$c_l = \frac{(8c_{11} + 4c_{13} + 3c_{33} + 8c_{44})}{15} \tag{2.37}$$

with c_{11} =203 GPa, c_{13} = 105 GPa, c_{33} = 207 GPa, c_{44} = 43 GPa.[22] The deformation potential is not very well known. In the literature, the values for E_{ac} in ZnO scatter from 1.4 eV to 31.4 eV.[22]

For degenerate conditions, using τ as in Reference 68 and employing $E_F = \hbar^2/(2m^*)(3\pi^2 n)^{2/3}$, which is valid for highly degenerate semiconductors, the mobility is given by (see also Reference 69)

$$\mu_{ac,deg}^{Hall} = \frac{\pi\hbar^4 c_l e}{2^{\frac{1}{2}} E_{ac}^2 m^{*\frac{5}{2}} (kT)} (E_F - E_C)^{-\frac{1}{2}} = \frac{\left(\frac{\pi}{3}\right)^{\frac{1}{3}} \hbar^3 c_l e}{E_{ac}^2 m^{*2} (kT) n^{\frac{1}{3}}}. \tag{2.38}$$

Figure 2.10 shows the acoustical mode scattering for non-degenerate and degenerate ZnO as a function of the temperature and the free carrier concentration for different values of the deformation potential E_{ac}.

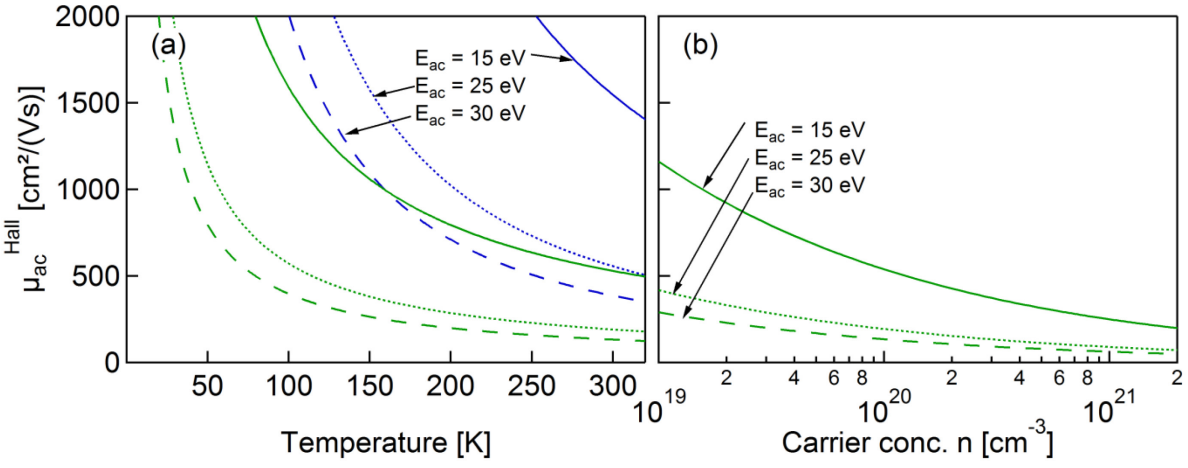

Figure 2.10: Hall mobility μ_{ac}^{Hall} as a function of the temperature T (a) and the free carrier concentration n (b) for acoustical phonon scattering in non-degenerate (blue) and degenerate (green) ZnO. $n = 1 \cdot 10^{20}$ cm^{-3} (a), T = 295 K (b), $m^* = 0.28 m_e$, solid line: E_{ac} = 15 eV, dotted line: E_{ac} = 25 eV, dashed line: E_{ac} = 30 eV.

The dominance of the acoustical mode phonon scattering is increasing with increasing temperature for both, the non-degenerate as well as the degenerate case. For degenerate conditions, the acoustical phonon scattering further limits the mobility for increasing free carrier concentrations.

2.3.2 Piezoelectric Scattering

The piezoelectric scattering is caused by the electric field associated with acoustical phonons. It occurs only in piezoelectric materials and depends on the electro-mechanical coupling coefficient *P*. For most materials, this coupling coefficient is in the order of 10^{-3}, while ZnO exhibits values of about 0.2...0.4, leading to strong piezoelectric scattering.[22] Zook[70] calculated (see also References 22 and 71)

$$\mu_{\text{piezo}}^{\text{Hall}} = r_{\text{H,piezo}} \frac{16\sqrt{2\pi}\hbar^2 \varepsilon_s \varepsilon_0}{3eP_{\perp,\parallel}^2 \sqrt{m^{*3} kT}}, \tag{2.39}$$

where $P_{\parallel,\perp}$ is the averaged piezoelectric electro-mechanical coupling coefficient for electrical transport parallel or perpendicular to the c-axis and $r_{\text{H,piezo}} = 45\pi/128$. According to Rode[71], $P_{\perp} = 0.21$ and $P_{\parallel} = 0.36$ for ZnO. Figure 2.11 shows the Hall mobility corresponding to piezoelectric scattering in ZnO using $\varepsilon_s = 8.34$ and $m^* = 0.28 m_e$.

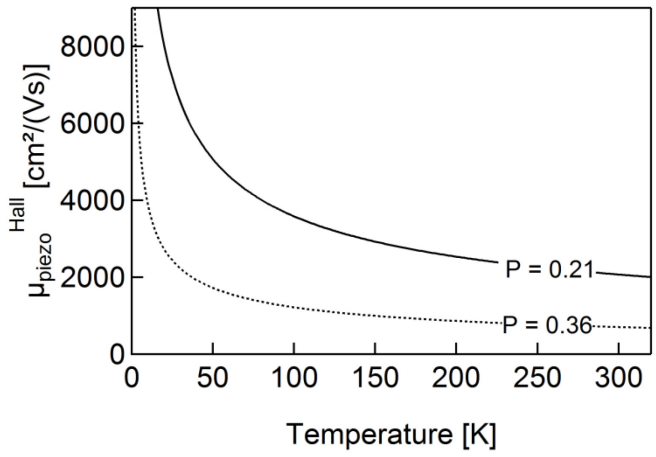

Figure 2.11: Hall mobility $\mu_{\text{piezo}}^{\text{Hall}}$ as a function of the temperature *T* corresponding to the piezoelectric scattering mode for carrier transport perpendicular to the c-axis (solid line, $P_{\perp} = 0.21$) or parallel to the c-axis (dotted line, $P_{\parallel} = 0.36$) in ZnO. $\varepsilon_s = 8.34$, $m^* = 0.28 m_e$.[22]

The mobilities obtained for the piezoelectric mode scattering for charge carrier transport perpendicular to the c-axis, which is mostly the case in sputtered ZnO, are much larger in comparison to those of the longitudinal-optical or acoustical phonon scattering modes. Hence, piezoelectric scattering is of minor importance. Remarkable is that the piezoelectric scattering leads to an anisotropy of the mobility in ZnO, which, however, becomes apparent only at low temperatures and low doping concentrations.[72]

2.3.3 Ionized Impurity Scattering

The ionized impurity scattering describes the scattering of free carriers at the Coulomb potential of ionized impurity atoms (dopants) or defects. First works treated the ionized impurity scattering using a screened Coulomb potential for the ionized impurity atoms.[73,74] Using this approximation, Brooks and Herring derived in the 1950s

$$\mu_{\text{ii}}^{\text{BH}} = \frac{128\sqrt{2\pi}\left(\varepsilon_0 \varepsilon_s\right)^2 \left(kT\right)^{\frac{3}{2}}}{m^{*\frac{1}{2}} N_i Z^2 e^3 \left[\ln\left(\frac{24 m^* \varepsilon_0 \varepsilon_s \left(kT\right)^2}{n e^2 \hbar^2}\right)\right]} \tag{2.40}$$

for the mobility of the free carriers in the non-degenerate case.[75] In Equation (2.40), *n* is the carrier concentration, N_i is the ionized impurity concentration, and *Z* is the charge of the impurities in units of *e*. Later, Chattopadhyay and Queisser[75] reviewed the problems of the theories and their subsequent

refinements in 1981 and compared them to experimental data of elemental and compound semiconductors.

For degenerate semiconductors, the ionized impurity scattering has been treated first by Shockley[76] for the scattering at the truncated Coulomb potential. He obtained

$$\mu_{ii}^{\mathrm{Hall,Sh}} = \frac{3\left(\varepsilon_0\varepsilon_s\right)^2 h^3}{Z^2 m^{*2} e^3} \frac{1}{\ln\left[1+\left(\frac{3^{\frac{2}{3}}\pi^{\frac{1}{3}}\varepsilon_0\varepsilon_s h^2 n^{\frac{1}{3}}}{2m^* e^2}\right)^2\right]}. \tag{2.41}$$

A truncated Coulomb potential is, however, physically not very appropriate. Dingle[77] used a screened Coulomb potential to describe the ionized impurity scattering and calculated (see also Reference 78)

$$\begin{aligned} \mu_{ii}^{\mathrm{Hall,Di}} &= \frac{3\left(\varepsilon_0\varepsilon_s\right)^2 h^3}{Z^2 m^{*2} e^3} \frac{n}{N_i} \frac{1}{F_{ii}(\xi)}, \\ F_{ii}(\xi) &= \ln\left(1+\xi\right) - \frac{\xi}{1+\xi}, \\ \xi &= \left(3\pi^2\right)^{\frac{1}{3}} \frac{\varepsilon_0\varepsilon_s h^2 n^{\frac{1}{3}}}{e^2 m^*}, \end{aligned} \tag{2.42}$$

with $E_F = \hbar^2/(2m^*)(3\pi^2 n)^{2/3}$ for the scattering of the free carriers in degenerate semiconductors, where F_{ii} is the screening function.

In the case of a fully ionized semiconductor, the free carrier concentration equals the concentration of ionized impurities ($n = N_i$). Otherwise, charge neutrality requires $N_D^+ = n + N_A^-$.[79,80] Accordingly, the concentration of scattering centres is then given by $N_i = N_D^+ + N_A^- = n + 2N_A^-$. With respect to the value of ξ, there is some ambiguity in the literature: Dingle[77], Zakrzewska et al.[80], Zawadzki[78], and Chattopadhyay and Queisser[75] reported the screening parameter ξ as it is given above. Look[81] ($\xi' = 1/2 \cdot \xi$) and Pisarkiewicz[79] ($\xi' = \xi/\pi$) gave slightly different values, although Pisarkiewicz explicitly referenced the work of Zakrzewska. Since the majority of the authors reported ξ as given in Equation (2.42), this value will be used for further evaluation of the ionized impurity scattering.

Disagreements between theory and experiment – especially for degenerate semiconductors the theoretically predicted mobilities were too high – could be reduced by taking into account the non-parabolicity of the conduction band. In this case, the effective mass is treated as a function of the electron energy in the conduction band,

$$m^* = m_0^*\left(1 + 2\beta\left(E - E_C\right)\right), \tag{2.43}$$

where β is the non-parabolicity parameter. Using the Fermi energy as the energy of the electrons and employing the approximation for $\eta = (E_F - E_c)/(kT)$ by Nilsson (Equation (2.26)), an analytical expression for the effective mass as a function of the free carrier concentration can be given:

$$\frac{m^*}{m_0^*} = 1 + 2\beta kT \left[\frac{\ln\left(\frac{n}{N_C}\right)}{1-\left(\frac{n}{N_C}\right)^2} + \frac{\left(\frac{3}{4}\sqrt{\pi}\frac{n}{N_C}\right)^{\frac{2}{3}}}{\left(\left(0.24 + 1.08\left(\frac{3}{4}\sqrt{\pi}\frac{n}{N_C}\right)^{\frac{2}{3}}\right)^{-2} + 1\right)} \right]. \tag{2.44}$$

Figure 2.12 shows a fit of this formula to the data of the density of states effective mass in ZnO:Al as a function of the free carrier concentration of Young et al.[16].

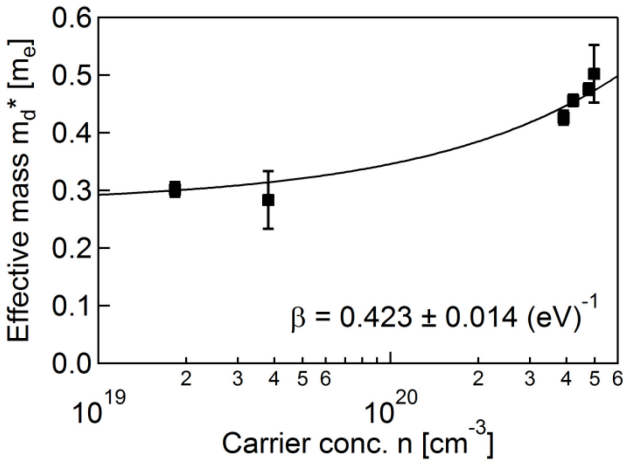

Figure 2.12: Density of states effective mass m_d^* as a function of the free carrier concentration n (the data were taken from Reference 16). The solid line represents a fit according to Equation (2.44), using $m_0^* = 0.28m_e$ and $T = 295$ K, which yields $\beta = 0.423 \pm 0.014$ (eV)$^{-1}$.

This value is in good agreement with the rule $\beta \approx 1/E_g$, which yields in the case of ZnO approximately 0.3 eV^{-1} for β.[22] A screening function for the degenerate case and a non-parabolic band has been derived by Zawadzki[78]:

$$
\begin{aligned}
F_{ii}(\xi,\xi_1) &= \ln(\xi+1) - \frac{\xi}{1+\xi} - \frac{\xi_1}{2}\left(3-\frac{\xi_1}{2}\right)f_1 + \frac{3}{2}\left(\frac{\xi_1}{2}\right)^2 f_2, \\
f_1 &= 1 + \frac{1}{\xi+1} - \frac{2}{\xi}\ln(\xi+1), \\
f_2 &= 1 - \frac{4}{\xi} - \frac{2}{\xi(\xi+1)} + \frac{6}{\xi^2}\ln(\xi+1), \\
\xi_1 &= 1 - \frac{m_0^*}{m^*}.
\end{aligned}
\tag{2.45}
$$

This expression has later been simplified by Pisarkiewicz[79] to

$$
F_{ii}(\xi,\xi_1) = \left[1 + \frac{4\xi_1}{\xi}\left(1-\frac{\xi_1}{8}\right)\right]\ln(\xi+1) - \frac{\xi}{1+\xi} - 2\xi_1\left(1-\frac{5}{16}\xi_1\right). \tag{2.46}
$$

Figure 2.13 shows the ionized impurity scattering for ZnO for the different models using $m_0^* = 0.28m_e$, $T = 295$ K, $\varepsilon_s = 8.34$, and $N_i = n$ (ξ according to Equation (2.42)).

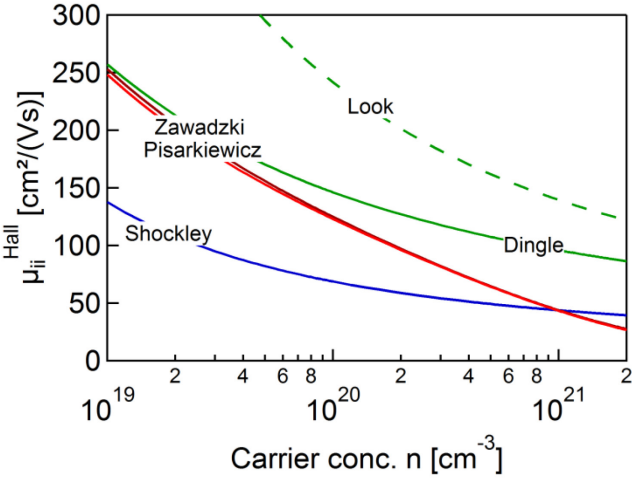

Figure 2.13: Hall mobility μ_{ii}^{Hall} as a function of the free carrier concentration n for ionized impurity scattering in degenerate semiconductors according to different authors. Various approximations are shown: Shockley[76] (blue): truncated Coulomb potential (Equation (2.41)), Dingle[77] (green, solid): screened Coulomb potential (Equation (2.42)), Look[81] (green, dashed): screened Coulomb potential with a different screening parameter, Zawadzki[78] (brown): screened Coulomb potential and non-parabolic conduction band (Equations (2.45) and (2.42)), Pisarkiewicz[79] (red): screened Coulomb potential and non-parabolic conduction band ('simplified Zawadzki', Equations (2.46) and (2.42)).

When comparing these results with experiments, the ionized impurity scattering mobility is still too high. Klaassen[82] interpreted the low mobilities of the charge carriers in highly doped single crystals by scattering at clusters of ionized impurities. Indeed, it can be argued that the scattering centres are not statistically distributed anymore for very high carrier concentrations and must therefore be described by clusters with an effective charge higher than $Z = 1$ and a concentration $N_i' = N_i/Z$. Figure 2.14 shows the effect of an increasing Z on the mobility for very high carrier concentrations ($n = N_i$).

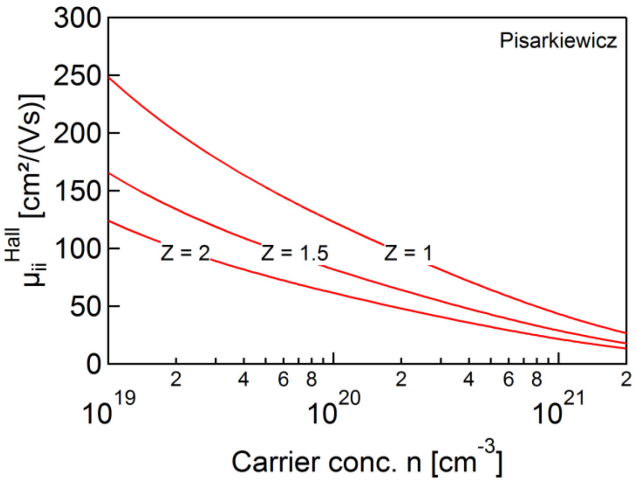

Figure 2.14: Carrier mobility μ_{ii}^{Hall} as a function of the carrier concentration n derived for a non-parabolic conduction band according to Equation (2.42) using the screening function given in Equation (2.46) for different values of the effective charge of the scattering centres Z (in units of e).

For increasing effective charge of the impurity clusters, the mobility is reduced, which is in better agreement with the experimental values as will be shown in Section 5.1.

2.3.4 Grain Boundary Scattering

Polycrystalline materials exhibit grain boundaries, which give rise to additional scattering mechanisms such as grain boundary scattering. This mechanism describes the scattering of the free carriers at potential barriers created in the conduction and valence band at the grain boundaries. A first comprehensive treatment of the effect was given by Seto[83] in 1975. His model is related to the work of Petritz[84] (1956) and Kamins[85] (1971). Later, various extensions of the model have been published, which will be presented, together with Seto's model, in the following. The treatise will again be restricted to n-type semiconductors and, initially, to the non-degenerate case. Nevertheless, the dependences will be shown for carrier concentrations in the degenerate regime as well, because some of the models have also been used to interpret experimental data of degenerately doped semiconductors, although they are only valid in the non-degenerate case as will be elucidated in Section 5.2.

Seto's Model

Seto assumed that the polycrystalline material is composed of identical crystallites having a lateral size L and that the dopant atoms of only one type are uniformly distributed with a concentration of N_D and totally ionized. The mobile carriers in the depletion region are neglected. Furthermore, Seto presumed a concentration of N_t ($[N_t] = cm^{-2}$) electron traps at the grain boundaries located at the energy E_t, and he used an abrupt depletion approximation, which means (see also Figure 2.15 on page 25)

$$\rho(x) = \begin{cases} eN_D, & \left|x - \frac{L}{2}\right| < w \\ 0, & \text{else.} \end{cases} \tag{2.47}$$

In this equation, ρ is the space charge in a region with the width w (valid for $0 < x < L$).

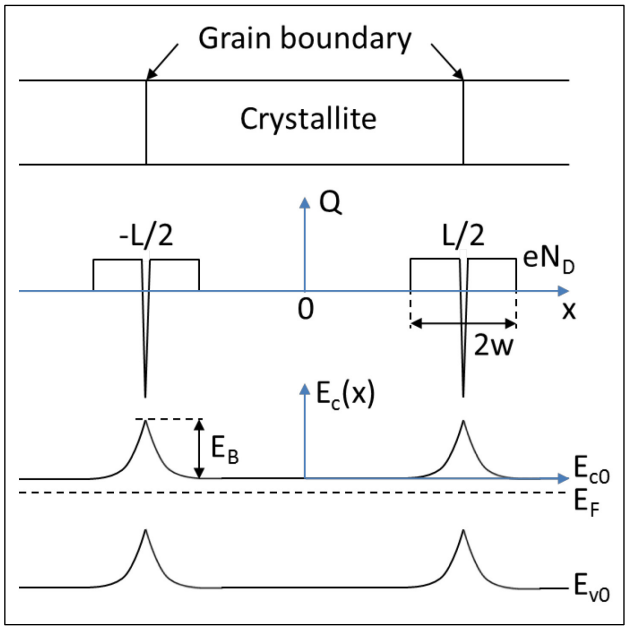

Figure 2.15: (*top*) Structure model for the polycrystalline semiconductor, (*centre*) charge distribution in the grains and at the grain boundaries, (*bottom*) energy band structure of the n-type polycrystalline material. The figure is adapted from Reference 83.

Integrating Poisson's equation $\Delta\phi(x) = -\frac{\rho}{\varepsilon_s \varepsilon_0}$ twice (restricting the problem to one dimension) and using $E_c(x) = E_{c0} - e\phi(x)$ as well as the boundary conditions $\frac{d\phi(x)}{dx} = 0$ for $x = L/2 - w$ and $E_c(L/2 - w) = E_{c0}$, $E_c(x)$ is given by

$$E_c(x) = \begin{cases} \frac{e^2 N_D}{2\varepsilon_s \varepsilon_0}\left(\left|x - \frac{L}{2}\right| - w\right)^2 + E_{c0}, & \left|x - \frac{L}{2}\right| < w \\ E_{c0}, & \text{else.} \end{cases} \tag{2.48}$$

The barrier height can then be derived by

$$E_B = E_c\left(\frac{L}{2}\right) - E_c(0) = \frac{e^2 N_D}{2\varepsilon_s \varepsilon_0} w^2. \tag{2.49}$$

According to Seto, two situations have to be distinguished depending on the crystallite size and the carrier concentration: for $LN_D < N_t$, the whole grain is depleted and the traps are partially filled and for $LN_D > N_t$, only part of the grain is depleted and the traps are completely filled. For the first situation, $w = L/2$, and hence the barrier height is given by

$$E_B = \frac{e^2 L^2 N_D}{8\varepsilon_s \varepsilon_0}, \tag{2.50}$$

which means the barrier height is linearly increasing with increasing impurity concentration. For $LN_D > N_t$, when all the traps are filled, the charge neutrality condition in the depleted region reduces to $2N_D w = N_t$, leading to

$$E_B = \frac{e^2 N_t^2}{8\varepsilon_s \varepsilon_0 N_D}. \tag{2.51}$$

In this case, the barrier height is decreasing proportional to $1/N_D$. The maximum barrier height is obtained for $LN_D = N_t$.

The electronic transport over a sufficiently thick grain barrier can be modelled by a double Schottky barrier,[86,87] where the applied voltage decreases the barrier height for the transport in one direction and

increases it for the transport in the other direction. The resulting current in the approximation of pure thermionic emission over the barrier between two crystals, 1 and 2, is given by[87]

$$j_{\mathrm{th}} = j_{1\to 2} - j_{2\to 1} = n_0 e\left(\frac{kT}{2\pi m^*}\right)^{\frac{1}{2}} e^{-\frac{E_\mathrm{B}}{kT}}\left(e^{\frac{V_1}{kT}} - e^{-\frac{V_2}{kT}}\right), \tag{2.52}$$

where $V_1 + V_2 = V$ is the applied voltage and n_0 is the carrier concentration in the bulk of the crystallite (undepleted region). For small voltages $qV \ll kT$, Equation (2.52) reduces to

$$j_{\mathrm{th}} = n_0 e^2\left(\frac{1}{2\pi m^* kT}\right)^{\frac{1}{2}} e^{-\frac{E_\mathrm{B}}{kT}} \cdot V, \tag{2.53}$$

which is a linear current voltage relation and similar to the expression used by Seto, despite the fact that the average free carrier concentration n_a instead of the free carrier concentration in the bulk of the crystallite n_0 (the undepleted region) is used in Setos formula. It is important to note the difference between n_0 and n_a, which depends on the impurity concentration, trap state concentration, crystallite size, and temperature. Although the interpretation of the Hall measurements is open to several doubts,[88,89] there is some theoretical evidence that the carrier concentration obtained by Hall measurements is directly related to the average free carrier concentration within the crystallite n_a.[85,90-92] In the non-degenerate case, the average free carrier concentration is given by the spatial average over the locally changing free carrier concentration $n(x)$ in the grain[83,88]

$$\begin{aligned} n_\mathrm{a} &= n_0\left[\left(1-\frac{2w}{L}\right)+\frac{1}{eL}\left(\frac{2\pi\varepsilon_0\varepsilon_\mathrm{s}kT}{N_\mathrm{D}}\right)^{\frac{1}{2}}\mathrm{erf}\left[\left(\frac{e^2N_\mathrm{D}w^2}{2\varepsilon_0\varepsilon_\mathrm{s}kT}\right)^{\frac{1}{2}}\right]\right] \\ &= n_0\left[\left(1-\frac{2w}{L}\right)+\frac{w}{L}\left(\frac{\pi kT}{E_\mathrm{B}}\right)^{\frac{1}{2}}\mathrm{erf}\left[\sqrt{\frac{E_\mathrm{B}}{kT}}\right]\right]. \end{aligned} \tag{2.54}$$

For degenerate conditions, the integrals cannot be solved analytically. However, for very high carrier concentrations, the depletion region is small compared to the grain size, and the average and the bulk carrier concentration become similar. Figure 2.16 shows the ratio of the average to the bulk carrier concentration for $N_\mathrm{t} = 10^{13}$ cm^{-2} and $L = 50$ nm for Seto's model (blue line) and the model of Baccarani et al.[88] (green lines), which will be discussed next.

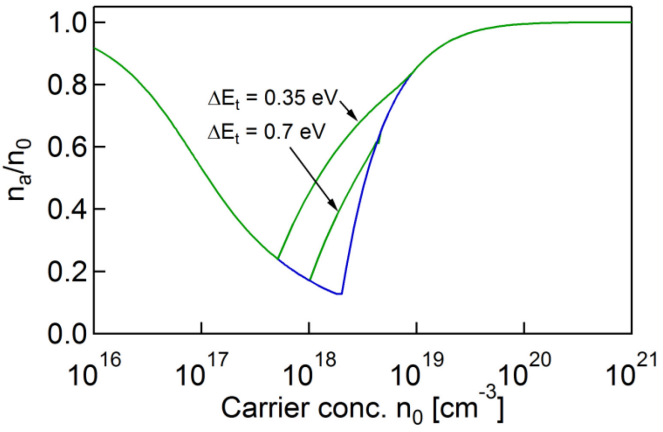

Figure 2.16: Ratio of the average free carrier concentration n_a to the bulk free carrier concentration in the undepleted region n_0 as a function of the bulk free carrier concentration n_0 shown for the model of Seto (blue) and the model of Baccarani and coworkers[88].

Apparently, when the potential barriers at the grain boundaries are high, which is the case for strong depletion of the grains ($n_0 \approx 10^{17}...10^{18}$ cm^{-3} in Figure 2.16), the average carrier concentration is much

smaller in comparison to the bulk carrier concentration. However, this effect has to be neglected if the models are used in a fit procedure, because the formulae cannot be expressed in a closed form otherwise.

Employing $\sigma = Lj_{th}/V$ and $\sigma = en_a\mu$, an effective mobility for the scattering of charge carriers at the grain boundaries can be derived

$$\mu_{GB}^{Hall} = \left(\frac{n_0}{n_a}\right)\frac{eL}{\sqrt{2\pi m^* kT}}e^{-\frac{E_B}{kT}}, \tag{2.55}$$

that reduces to

$$\mu_{GB,Seto}^{Hall} = \frac{eL}{\sqrt{2\pi m^* kT}}e^{-\frac{E_B}{kT}} \tag{2.56}$$

in Seto's model, because he used n_a instead of n_0 in Equation (2.53). Figure 2.17 shows the potential barrier height E_B and the effective Hall mobility μ_{GB}^{Hall} for different trap densities at the grain boundaries N_t.

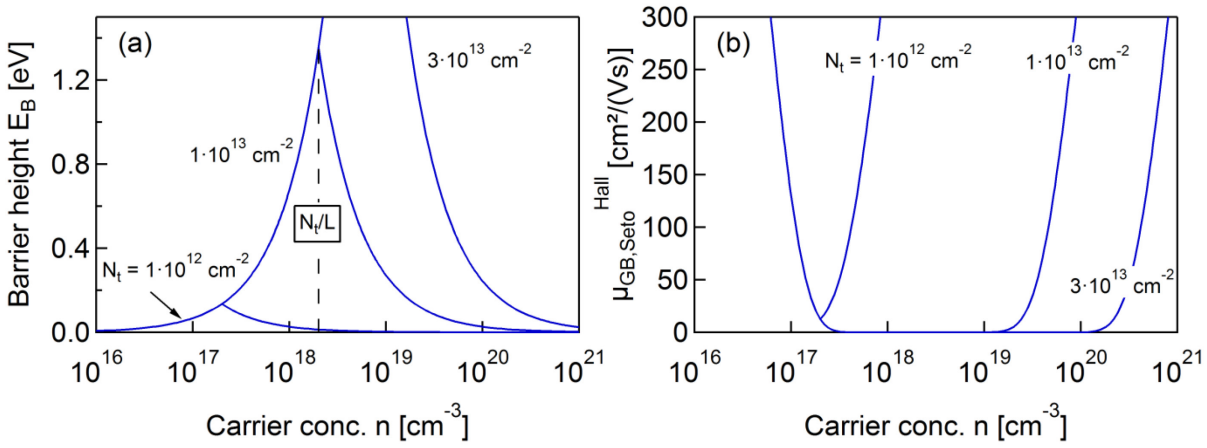

Figure 2.17: (a) Potential barrier height E_B in ZnO calculated according to the model of Seto[83] as a function of the carrier concentration $n = N_D = N_D^+$ (for different values of the trap density at the grain boundaries N_t). $m^* = 0.28m_e$, $\varepsilon_s = 8.34$, $L = 50$ nm, $T = 295$ K. (b) Hall mobility $\mu_{GB,Seto}^{Hall}$ as a function of the free carrier concentration for the trap densities shown in (a).

The maximal potential barrier heights vary from roughly 0.1 eV to some eV. Increasing the trap density at the grain boundaries N_t shifts the potential barrier maxima to higher free electron concentrations n and increases their maximal height. Decreasing the crystallite size shifts the potential barriers to the right in Figure 2.17 (a) as well but leads to smaller maximal heights. For $n = N_t/L$, when the potential barriers exhibit their maximum, the effective Hall mobility of the charge carriers is strongly reduced by the grain boundary scattering (see Figure 2.17 (b)).

Baccarani's Model

The model of Seto does not include a situation, where the trap states are only partially filled while the depletion region does not extend over the whole grain. In 1978, Baccarani et al.[88] improved the model for the intermediate range of impurity concentrations by including this case for trapping states at a single energy E_t as well as trapping states with a continuous energy distribution within the gap. Since the formulae in Baccarani's model cannot be expressed in a closed form and are therefore not applicable to a fit procedure, the discussion will be limited to the basic ideas. For monoenergetic trapping states ($g_t(E) = N_t\delta(E - E_t)$), Baccarani and coworkers used the electrical neutrality condition

$$2N_D w = \frac{N_t}{1+\frac{1}{2}e^{\frac{E_t+E_B-E_F}{kT}}} = \frac{N_t}{1+\frac{1}{2}e^{\frac{E_B-\Delta E_t}{kT}-\eta}} \tag{2.57}$$

with $\Delta E_t = E_c - E_t$, the barrier height according to Equation (2.49), and $w = L/2$, to derive a specific impurity concentration (using $\eta = -\ln(N_c/N_D)$)

$$N^*_{D,Bacc} = \frac{8\varepsilon_s\varepsilon_0}{e^2L^2}\left(\Delta E_t - kT\ln\left(\frac{N_C}{N^*_{D,Bacc}}\right) + kT\ln\left[2\left(\frac{N_t}{N^*_{D,Bacc}L}-1\right)\right]\right), \tag{2.58}$$

which has to be solved iteratively. For $N_D < N_D^*$, the crystallites are entirely depleted and the effective mobility and the potential barrier height are similar to those in Setos model for $LN_D < N_t$ (only that Seto used the average carrier concentration inside the grain for the thermionic emission current). For $N_D^* < N_D < N_D^{**}$, the crystallites are partially depleted, but in contrast to Setos model, the traps are not completely filled. For this case, the barrier height can be calculated by eliminating w in Equations (2.49) and (2.57). The result,

$$E_B = \Delta E_t - kT\ln\left(\frac{N_C}{N_D}\right) + kT\ln\left[2\left(\frac{N_t e}{\sqrt{N_D 8\varepsilon_s\varepsilon_0 E_B}}-1\right)\right], \tag{2.59}$$

must again be solved iteratively. For $E_B(N_D^{**}) = \frac{e^2N_t^2}{8\varepsilon_s\varepsilon_0 N_D^{**}}$, Equation (2.59) loses validity, and hence, for $N_D > N_D^{**}$, the following equation for the barrier height holds:

$$E_B = \frac{e^2N_t^2}{8\varepsilon_s\varepsilon_0 N_D}, \tag{2.60}$$

which is again equal to the result of Seto. Figure 2.18 on page 29 shows the potential barrier height at the grain boundary and the effective mobility for different N_t, L, and ΔE_t calculated according to the models of Seto (blue lines) and Baccarani and coworkers (green lines). For this illustration, the difference between n_a and n_0 has been neglected for Seto's model.

For small trap state densities, both models lead to the same potential barrier height (for $N_t < N_D^*/L$). With increasing concentration of trap states N_t, however, the maximal potential barrier height increases strongly according to Seto's model, while it is limited by the trap state energy ΔE_t in the model of Baccarani et al. For very high carrier concentrations, on the other hand, the barrier width becomes very small in both models. When it is in the range of some nm thickness only, tunnelling of the carriers through the potential barriers will become more probable. The tunnelling, which was neglected in the models of Seto and Baccarani et al., has been treated by Garcia-Cuenca and coworkers[93,94].

Garcia-Cuenca's Model

In 1985, Garcia-Cuenca et al.[93,94] extended the models of Seto and Baccarani et al. by introducing a finite boundary width to take into account tunnelling effects. Additionally, their model is one of the first to describe the grain boundary scattering for degenerate conditions as well, because they did not simplify the thermionic emission current using Boltzmann statistics. In Figure 2.19 on page 30, a schematic band diagram for their model is shown.

They used trapping states located at a single energy E_t and the abrupt depletion approximation and calculated a barrier height in the boundary region

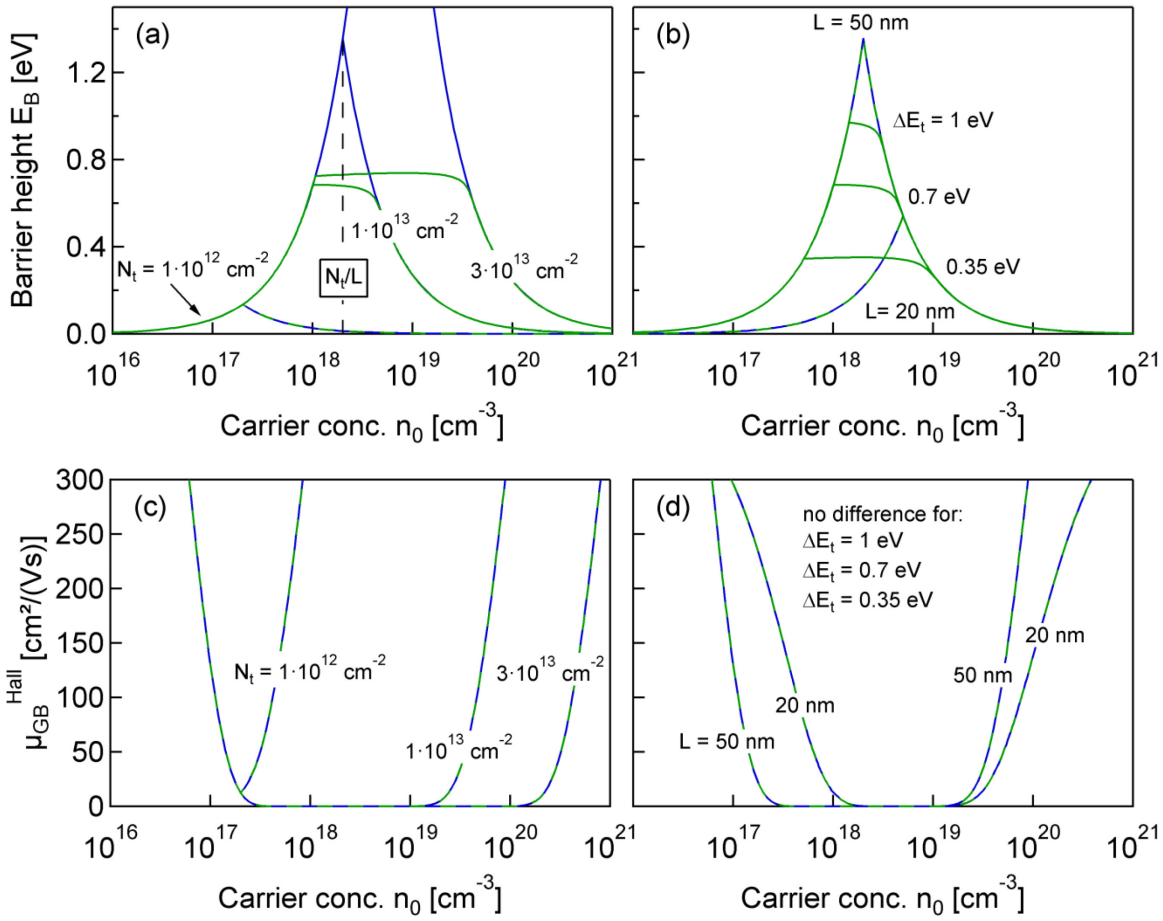

Figure 2.18: Potential barrier height E_B (*top*) in ZnO calculated according to the models of Seto[83] (blue) and Baccarani et al.[88] (green) as a function of the free carrier concentration in the bulk of the grains n_0 for different values of the trap density at the grain boundaries N_t (*left*: L = 50 nm, ΔE_t = 0.7 eV (see Reference 96)), different trap state energies ΔE_t and different lateral grain sizes L (*right*: $N_t = 1\cdot10^{13}$ cm^{-2}). $m^* = 0.28m_e$, $\varepsilon_s = 8.34$, T = 295 K. Also shown is the Hall mobility μ_{GB}^{Hall} (*bottom*) as a function of the free carrier concentration for the trap densities, trap state energies, and grain sizes shown in (a) and (b). The difference between n_a and n_0 was neglected for Seto's model.

$$E_B' = E_B\left[1+\frac{a}{w}\right], \tag{2.61}$$

where E_B is the barrier height in the depletion region and a is the half width of the grain boundary. Reasonable values for the grain boundary width $2a$ are in the range of a few nm.[95] In principle, Garcia-Cuenca et al. used the same scheme to determine the model parameters as Baccarani and coworkers did. However, they substituted N_D by $N_D - n_a$ in Equations (2.50) and (2.57). This yields with $w = L/2$

$$\left(N_{D,GC}^* - n_a\right) = \frac{8\varepsilon_s\varepsilon_0}{e^2L^2}\left(1+\frac{2a}{L}\right)^{-1}\left(\Delta E_t - kT\ln\left(\frac{N_C}{N_{D,GC}^*} - 0.27\right) + kT\ln\left[2\left(\frac{N_t}{L(N_{D,GC}^* - n_a)} - 1\right)\right]\right) \tag{2.62}$$

for the limit between the total and the partial depletion case. Furthermore, they assumed $2a \ll L$ ($\rightarrow E_B \approx E_B'$), which will, because of the small grain sizes, not be done here. In Equation (2.62), $\eta = -\ln(N_c/N_D - 0.27)$ has been used, which is valid within an error of 3 % for $\eta < 1.3$. Since $\eta \leq 1.3$ for $N_D \leq 7\cdot10^{18}$ cm^{-3}, this approximation is sufficient for the determination of $N_{D,GC}^*$. For $N_D > N_{D,GC}^*$, Garcia-Cuenca et al. consequently used the neutrality condition (2.57) with E_B' instead of E_B and obtained

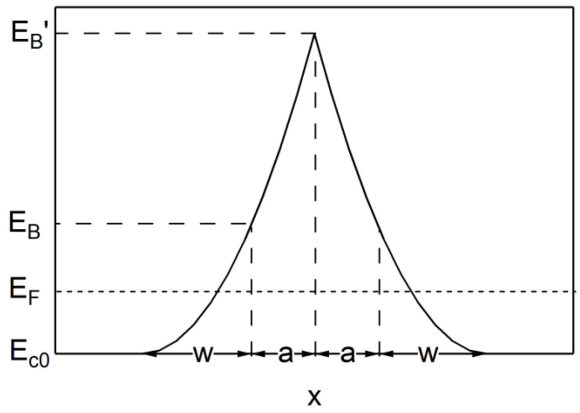

Figure 2.19: Schematic band diagram for the model of Garcia-Cuenca and coworkers[93,94] adapted from Reference 93.

$$E_B^{'} = \Delta E_t + kT\eta + kT\ln\left[2\left(\frac{N_t}{N_D a\left(\sqrt{1+\frac{E_B^{'} 8\varepsilon_s\varepsilon_0}{e^2 N_D a^2}}-1\right)}-1\right)\right], \tag{2.63}$$

which converges to Equation (2.59) for a → 0. When all the traps are filled ($N_D < N_{D,GC}^{*}$) or when Equation (2.63) loses its validity ($N_D > N_{D,GC}^{**}$), they calculated E_B' according to Equation (2.61) with E_B as in Equation (2.49) and $w = L/2$ or $w = N_t/(2N_D)$, respectively. Therefore, their model for the barrier height is the same as the model of Baccarani et al., except that they determine the impurity concentration limit between the whole and the partial depletion case slightly different and that the potential barrier height is scaled with $(1 + a/w)$. Figure 2.20 shows the potential barrier heights E_B' for different values of the width of the grain boundary $2a$ (neglecting n_a in Equation (2.62) and using $\eta = -\ln(N_c/N_D - 0.27)$ in Equation (2.63)).

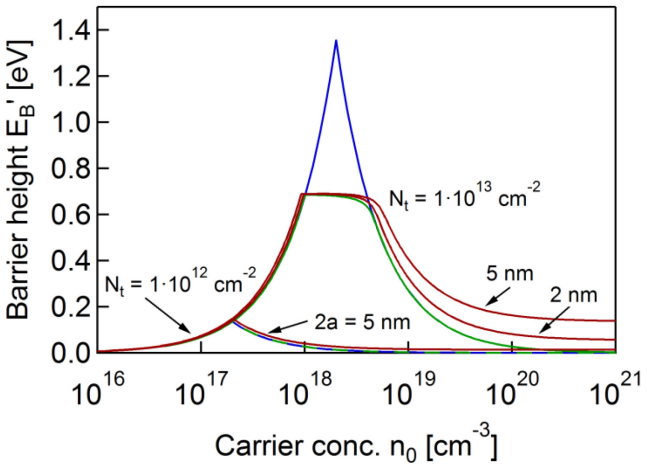

Figure 2.20: Potential barrier height E_B in ZnO calculated according to the models of Seto[83] (blue), Baccarani et al.[88] (green), and Garcia-Cuenca et al.[93,94] (brown) as a function of the free carrier concentration in the bulk of the grains n_0 for different values of the trap state density at the grain boundaries N_t and different grain boundary widths $2a$. L = 50 nm, ΔE_t = 0.7 eV,[96] m^* = 0.28m_e, ε_s = 8.34, T = 295 K.

The most important extension, however, is the introduction of a tunnelling current in the conductivity $\sigma = Lj/V$. Under the assumption of small bias voltages $qV \ll kT$ and using the WKB (Wentzel-Kramers-Brillouin) approximation, the effective mobility for scattering at grain boundaries according to Garcia-Cuenca et al.[93,94] is given by

$$\mu_{GB,GC}^{Hall} = \frac{eLN_C}{n_a kT\sqrt{2\pi m^* kT}}\left(\int_{E_C}^{E_B+E_C} f(E)e^{-\alpha_1}\mathrm{d}E + \int_{E_B+E_C}^{E_B^{'}+E_C} f(E)e^{-\alpha_2}\mathrm{d}E + \int_{E_B^{'}+E_C}^{\infty} f(E)\mathrm{d}E\right), \tag{2.64}$$

where

$$f(E) = \frac{1}{1 + e^{\frac{E - E_C}{kT} - \eta}} \tag{2.65}$$

and

$$\alpha_1 = \frac{4\pi}{h}\left(2m^*\right)^{\frac{1}{2}}\left[(a+w)(E_B - E)^{\frac{1}{2}} - \frac{wE}{E_B^{1/2}}\ln\left(\frac{E_B^{1/2} - (E_B - E)^{1/2}}{E^{1/2}}\right) + \left(\frac{aw}{E_B}\right)^{\frac{1}{2}}(E_B' - E)\sin^{-1}\left(\frac{aE_B}{w(E_B' - E)}\right)^{\frac{1}{2}}\right],$$

$$\alpha_2 = \frac{2\pi^2}{h}\left(2m^*\right)^{\frac{1}{2}}\left(\frac{aw}{E_B}\right)^{\frac{1}{2}}(E_B' - E). \tag{2.66}$$

The first and the second term in Equation (2.64) correspond to quantum-mechanical tunnelling currents and the last term is the contribution from the thermionic emission. Figure 2.21 shows the effective mobility contributions from the tunnelling and the thermionic emission currents as a function of the free carrier concentration n_0 for different grain boundary widths $2a$ using a trap state energy of $\Delta E_t = 0.7\text{eV}$ (adapted from Reference 96). For carrier concentrations n_0 above approximately $7 \cdot 10^{18}$ cm^{-3} ($\eta \approx 1.3$), $\eta = \sqrt{\left(\frac{n_0}{N_C}\frac{3\sqrt{\pi}}{4}\right)^{\frac{4}{3}} - \frac{\pi^2}{6}}$ has been applied, which is correct with an error smaller than 3 % in the range of $\eta > 0.8$.[61,62]

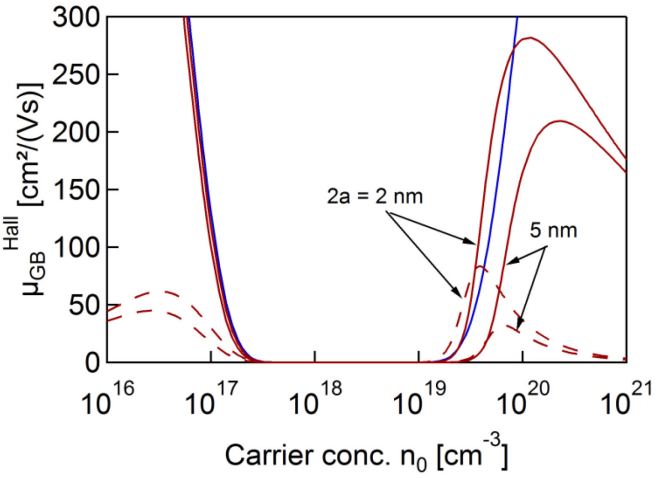

Figure 2.21: Contributions of the thermionic emission current (solid brown lines) and the tunnelling currents (dashed brown lines) to the Hall mobility μ_{GB}^{Hall} as a function of the carrier concentration n_0 for different grain boundary widths $2a$ calculated according to the model of Garcia-Cuenca et al.[93,94]. For comparison, the effective mobility according to Seto's model is also shown. The difference between n_a and n_0 has been neglected for Seto's model. L = 50 nm, ΔE_t = 0.7 eV, $m^* = 0.28m_e$, ε_s = 8.34, T = 295 K, N_t = 10^{13} cm^{-2}.

Comparing the mobilities related to the thermionic emission of the models of Seto (non-degenerate, blue lines in Figure 2.21) and Garcia-Cuenca et al. (degenerate, brown lines), the influence of the degeneracy on the mobility as a function of the free carrier concentration becomes apparent. The main difference is the decreasing mobility for very high carrier concentrations in the degenerate case caused by the $1/n_a$ dependence of the Hall mobility. Beyond that, the Hall mobility corresponding to the tunnelling currents remains mostly below the Hall mobility related to the thermionic emission current. This is expected since the tunnelling can only be significant when the potential barriers at the grain boundaries are narrow and high. However, the barriers are wide when they are high and when their width decreases for increasing free carrier concentration, their height is also strongly reduced. Hence, it is justified to neglect the tunnelling currents as it was intentionally done by Seto.

Seto Model for Arbitrary Degeneracy

The preceding overview provides the basis to derive a model to fit the experimental transport data for semiconductors of arbitrary degeneracy. As shown, the improvements of Baccarani et al. in comparison to Seto's model are not leading to different effective mobilities. Only the maximum barrier height was decreased in a certain free carrier concentration range, in which the effective mobility of the carriers is negligible anyway. The tunnelling currents introduced by Garcia-Cuenca and coworkers are mostly smaller compared to the thermionic emission current and do not significantly alter the results obtained by Seto as well. Yet, the most important point is that their model is able to describe non-degenerate as well as degenerate semiconductors. However, their formulae cannot be expressed in a closed form, making that model inapplicable to a fit procedure for the experimental data. Hence, in the following, an extended Seto model, valid for arbitrary degeneracy but still applicable to a fit procedure, will be derived on the basis of the formulae given by Garcia-Cuenca et al.

Ignoring the tunnelling currents and solving the integral for the thermionic emission current in Equation (2.64) using E_B instead of E_B' (a = 0), the effective mobility for non-degenerate and degenerate conditions is determined by

$$\mu_{\mathrm{GB,arbdeg}}^{\mathrm{Hall}} = \frac{eLN_C}{n_a\sqrt{2\pi m^* kT}} \ln\left(1 + e^{-\left(\frac{E_B}{kT} - \eta\right)}\right), \tag{2.67}$$

which is consistent with the effective mobility for arbitrary degeneracy in the case of thermionic field emission given by Weis.[97] Choosing

$$\begin{aligned} \eta &= -\ln\left(\frac{N_C}{n_0} - 0.27\right) && \text{for } 0 < n_0 < 6\cdot 10^{18}\ \mathrm{cm^{-3}}, \\ \eta &= \sqrt{\left(\frac{n_0}{N_C}\frac{3\sqrt{\pi}}{4}\right)^{\frac{4}{3}} - \frac{\pi^2}{6}} && \text{for } 6\cdot 10^{18}\ \mathrm{cm^{-3}} < n_0 < \infty, \end{aligned} \tag{2.68}$$

and

$$\begin{aligned} E_B &= \frac{e^2 L^2 n_0}{8\varepsilon_s\varepsilon_0} && \text{for } Ln_0 < N_t, \\ E_B &= \frac{e^2 N_t^2}{8\varepsilon_s\varepsilon_0 n_0} && \text{for } Ln_0 > N_t, \end{aligned} \tag{2.69}$$

according to Seto' model, and neglecting the difference between n_0 and n_a, the model remains reasonably simple and can be used to fit the experimental data. The main improvement in comparison to Seto's model becomes obvious for the temperature dependence of the effective mobility $\mu(T)$: Although Seto's model explains the Hall mobility as a function of the free carrier concentration $\mu(n)$ reasonably well, it cannot explain the temperature independence of the effective mobility of the degenerately doped films investigated here. The extended Seto model for arbitrary degeneracy, on the other hand, can explain both, $\mu(T)$ and $\mu(n)$. Figure 2.22 on page 33 shows the difference between the effective mobility of the classical Seto model and the effective mobility of the model for arbitrary degeneracy.

While the differences in the qualitative trend of $\mu(n)$ between the classical Seto model and the model for arbitrary degeneracy are rather small, the contrast in the temperature dependence is striking. In fact, the Hall mobility as a function of the temperature of the classical Seto model does not change significantly for varying trap densities and free carrier concentrations, whereas the temperature

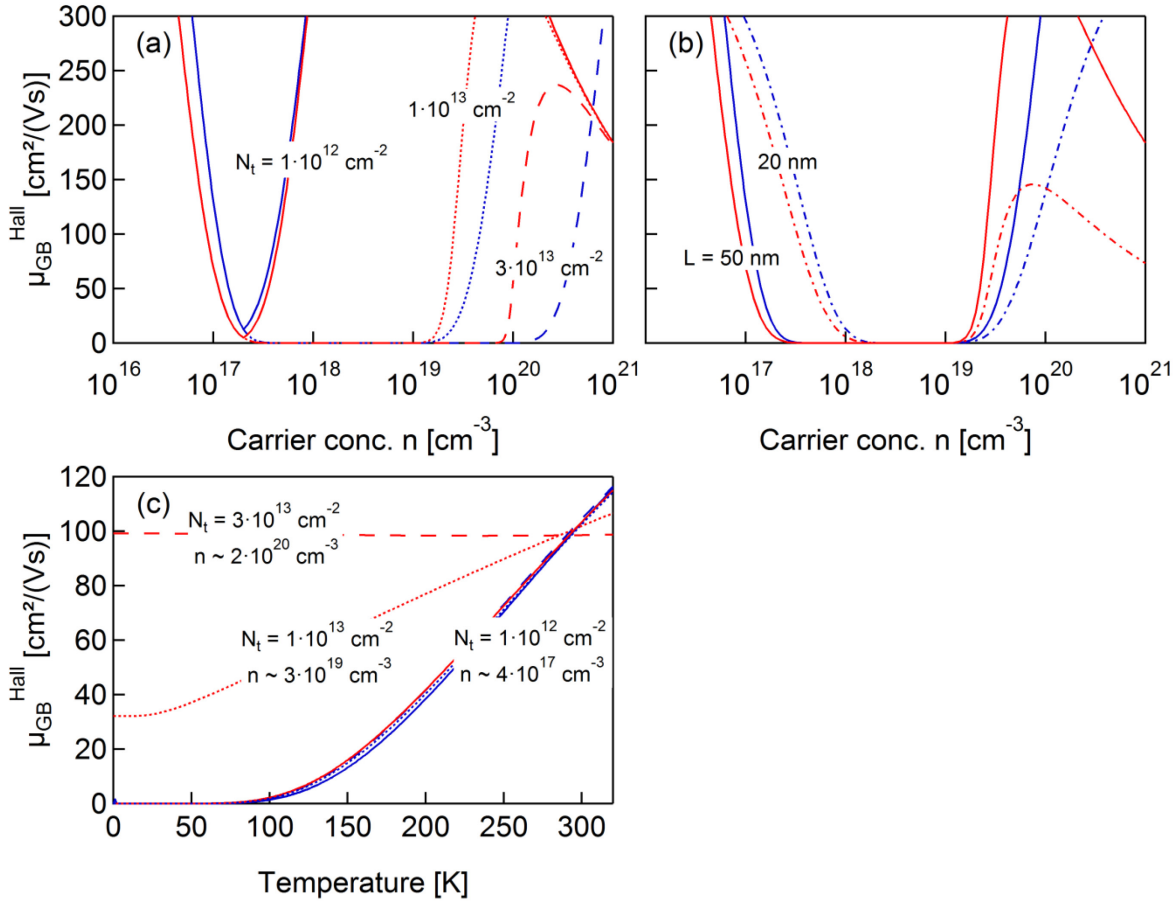

Figure 2.22: Comparison of the effective mobility μ_{GB}^{Hall} as a function of the carrier concentration n (*top*) and the temperature T (*bottom*) between the classical Seto model (blue) and the extended Seto model for arbitrary degeneracy (red) for different trap densities N_t (*left*, L = 50 nm) and lateral grain sizes L (*right*, N_t = 1·10^{13} cm^{-2}). *Left*: solid lines: N_t = 1·10^{12} cm^{-2}, dotted lines: N_t = 1·10^{13} cm^{-2}, dashed lines: N_t = 3·10^{13} cm^{-2}. *Right*: solid lines: L = 50 nm, dash-dotted lines: L = 20 nm.

dependence of the effective mobility of the model for arbitrary degeneracy nearly vanishes for high free carrier concentrations. This is in accordance with the experimental observations and will be discussed in detail in Section 5.2.2.

With respect to the formulae, the temperature independence for high carrier concentrations can be explained as follows: η is proportional to $1/T$ (as can be inferred from Equation (2.68) with $N_c \propto T^{3/2}$). Since $\eta kT \gg E_B$ in the exponential term in Equation (2.67) for high n, this expression becomes large and the '1' as well as $E_B/(kT)$ can be neglected. The logarithm can then be calculated and yields approximately η. Together with $T^{1/2}$ in the denominator and $N_c \propto T^{3/2}$, this yields a prefactor in front of the η proportional to T, which means η multiplied by this prefactor, and hence the effective mobility, is temperature independent.

2.3.5 Alloy Scattering

Alloy scattering is caused by the periodic modulation of the lattice potential due to the (homogeneous) incorporation of atoms, which are different from the host material. Nordheim[98] presented one of the first models dealing with alloy scattering in metals in 1931. Later, the alloy scattering had to be used to describe the transport in ternary III-V semiconductor compounds, such as $Ga_{1-x}In_xAs$, $Al_{1-x}Ga_xAs$ and $GaAs_{1-x}Sb_x$. Based on the work of Nordheim, Brooks derived the following expression for the drift mobility in a non-degenerate semiconductor for scattering due to the disorder:[99,100]

$$\mu_{\text{alloy}} = \frac{(2\pi)^{\frac{1}{2}} e\hbar^4 N}{3m^{*\frac{5}{2}} \sqrt{kT}\, x(1-x)(\Delta E)^2}, \tag{2.70}$$

where N is the number of atoms per unit volume, x is the fraction of the alloy component, and ΔE is the energy difference between the conduction band edges of the pure materials. To obtain the Hall mobility, this equation has to be multiplied by $\langle \tau_{\text{alloy}}^2 \rangle / \langle \tau_{\text{alloy}} \rangle^2 = r_{\text{H,alloy}} = 3\pi/8$. Figure 2.23 shows the Hall mobility for alloy scattering for a linear interpolation between the values of the single materials (following Look et al.[101]), using $N_{\text{ZnO}} \approx 7 \cdot 10^{22}\,\text{cm}^{-3}$ (determined by X-ray reflectivity (XRR) measurements), $N_{\text{MgO}} \approx 1.07 \cdot 10^{23}\,\text{cm}^{-3}$ (see Reference 102), $m^*_{\text{ZnO}} = 0.28 m_e$, $m^*_{\text{MgO}} = 0.35 m_e$ (see Reference 103), and $\Delta E = 2.7$ eV (see Reference 104) as a function of the composition and the temperature for different scattering potentials ΔE.

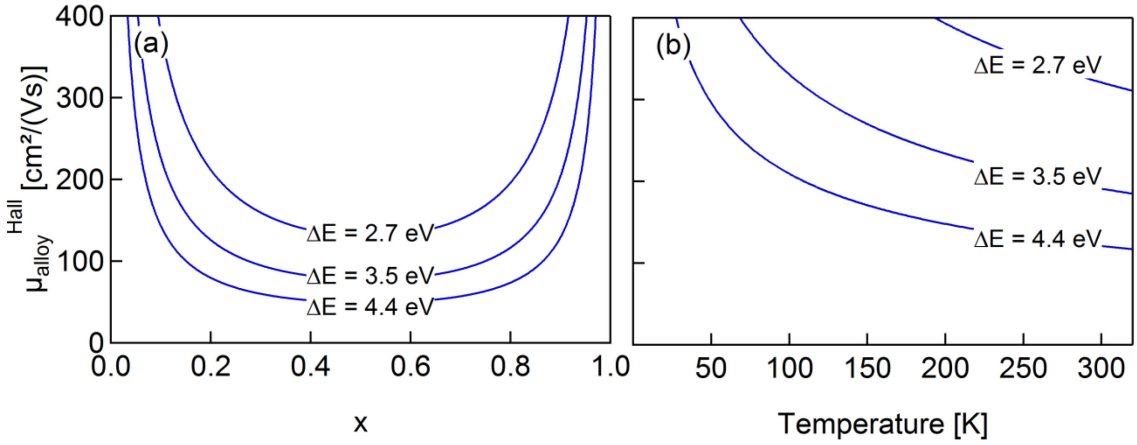

Figure 2.23: Hall mobility of the charge carriers for alloy scattering $\mu_{\text{alloy}}^{\text{Hall}}$ calculated according to the Brooks formula (2.70) with $r_{\text{H,alloy}} = 3\pi/8$ using a linear interpolation between the material parameters. (a) shows the Hall mobility as a function of the composition x (T = 295 K), while (b) presents the carrier mobility as a function of the temperature T (x = 0.12).

For alloy compositions in the range of $x \approx 0.5$, the Hall mobility is strongly decreased in comparison to the pure materials. Additionally, the dominance of the alloy scattering is increasing with increasing temperature.

Equation (2.70) was derived using

$$\frac{1}{\tau_{\text{alloy}}} = \frac{\sqrt{2}\nu_a x(1-x)(\Delta E)^2 m^{*\frac{3}{2}}}{\pi\hbar^4} E^{\frac{1}{2}}, \tag{2.71}$$

averaging over $\tau(E)$ by applying Equation (2.29), and inserting $\nu_a = 1/(N/2)$, where ν_a is a cation volume used as the cut-off radius for the effective scattering range. The choice of the cut-off radius is rather arbitrary,[105] which explains the various slightly different formulae in the literature (see for example References 91, 101, and 105-108). However, the uncertainty introduced by the choice of the cut-off radius is small in comparison to the uncertainty caused by the scattering potential. Many models, including the band gap difference, the electron affinity difference, and the electronegativity difference, have been proposed for the alloy scattering potential ΔE. However, it is not known exactly, which model is the most realistic one.[109]

From Equation (2.71), using Equations (2.30) and (2.27) as well as $E = E_F - E_c = \hbar^2/(2m^*)(3\pi^2 n)^{2/3}$, the Hall mobility for alloy scattering for degenerate conditions can be derived:

$$\mu_{\text{alloy,deg}}^{\text{Hall}} = \frac{e\hbar^3 N\left(\frac{\pi}{3}\right)^{\frac{1}{3}}}{2m^{*2}n^{\frac{1}{3}}x(1-x)(\Delta E)^2}. \tag{2.72}$$

It is independent of the temperate but does depend on the free carrier concentration. Figure 2.24 shows the alloy scattering as a function of the free carrier concentration for different ΔE and $x = 0.12$.

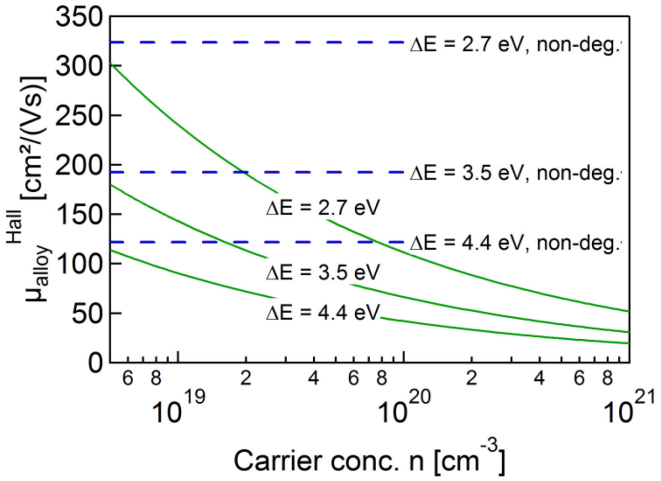

Figure 2.24: Hall mobility of the free charge carriers $\mu_{\text{alloy}}^{\text{Hall}}$ as a function of their concentration according to the alloy scattering model for degenerate ZnO (blue) compared to the carrier mobility for non-degenerate ZnO (blue, dashed lines) for different values of the scattering potential ΔE. $T = 295$ K, $x = 0.12$.

The mobilities calculated using the models for the alloy scattering for degenerate and non-degenerate conditions coincide for $n \approx 4 \cdot 10^{18}$ cm^{-3}. For higher carrier concentrations, the mobility of the degenerate semiconductors is decreasing and therefore well below the values of the non-degenerate semiconductors. Since $\mu_{\text{alloy,deg}}^{\text{Hall}} < 100$ cm²/(Vs) is easily possible, this scattering process can have a strong impact on the charge carrier mobility for alloyed samples with high free carrier concentrations.

2.3.6 Dislocation Scattering

The scattering of charge carriers at dislocations is likely due to the fact that polycrystalline materials exhibit a high concentration of dislocations (see Section 4.1). However, this scattering process is rarely used to interpret the transport data of polycrystalline semiconductors, which can mainly be attributed to the lack of data for the dislocation densities.[22] In non-degenerate semiconductors, the scattering at charged dislocations leads to a mobility given by[22,50,110]

$$\mu_{\text{disl}}^{\text{Hall}} = r_{\text{H,disl}} \frac{30\sqrt{2\pi}(\varepsilon_s\varepsilon_0)^{\frac{3}{2}}a^2\sqrt{nkT}}{e^2 f^2\sqrt{m^*}N_{\text{disl}}}, \tag{2.73}$$

where a is the distance between acceptor centres along the dislocation line, f ($0 \le f \le 1$) is the occupation number of these acceptors, and N_{disl} is the dislocation density. According to Pödör, the Hall factor is $r_{\text{H,disl}} = 3\pi/8$.[110] In degenerate semiconductors, the scattering of the carriers at charged dislocations can be calculated using[81]

$$\mu_{\text{disl,deg}}^{\text{Hall}} = \frac{4 \cdot 3^{\frac{2}{3}} ec^2 n^{\frac{2}{3}}}{\pi^{\frac{8}{3}}\hbar N_{\text{disl}}}\left[1 + \frac{2 \cdot 3^{\frac{1}{3}}\pi^{\frac{8}{3}}\hbar^2\varepsilon_0\varepsilon_s n^{\frac{1}{3}}}{e^2 m^*}\right]^{\frac{3}{2}}, \tag{2.74}$$

where c is in the order of a lattice constant. Figure 2.25 shows the dislocation scattering as a function of the free carrier concentration and the temperature assuming 0.5 nm for the parameters a and c and $f = 1$.

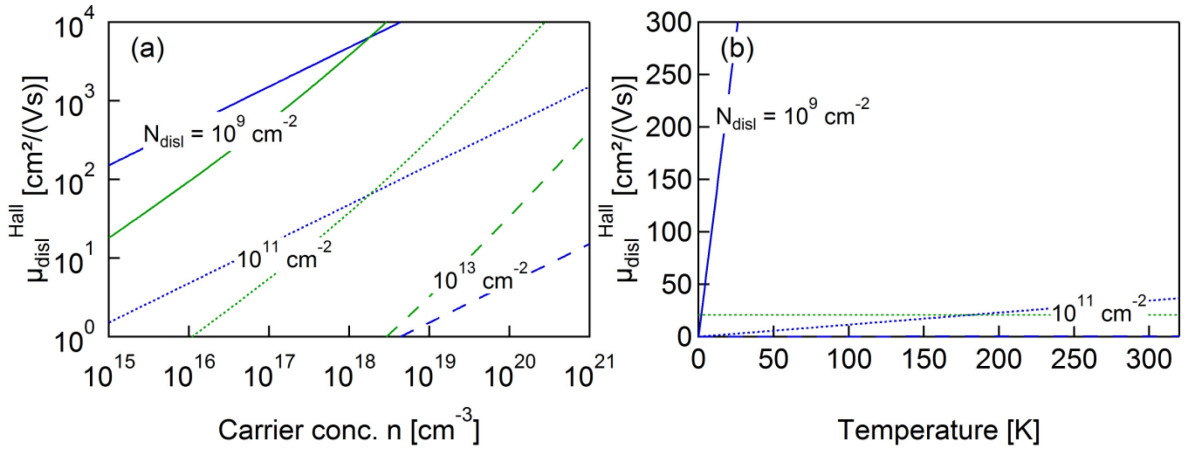

Figure 2.25: (a) Hall mobility μ_{disl}^{Hall} of the charge carriers as a function of the free carrier concentration n according to the model for the dislocation scattering in non-degenerate (blue) and degenerate (green) ZnO for different dislocation densities N_{disl} (T = 295 K). (b) Temperature dependence of the dislocation scattering ($n = 5 \cdot 10^{17}$ cm^{-3}). solid line: $N_{disl} = 10^9$ cm^{-2}, dotted line: $N_{disl} = 10^{11}$ cm^{-2}, dashed line: $N_{disl} = 10^{13}$ cm^{-2}. $a = c = 0.5$ nm, $f = 1$, $\varepsilon_s = 8.34$, $m^* = 0.28 m_e$.

For non-degenerate as well as degenerate conditions, the dominance of the dislocation scattering is increasing with decreasing free carrier concentration. The absolute values of μ_{disl}^{Hall}, however, depend strongly on the order of magnitude of the dislocation density N_{disl}. Since values for N_{disl} between 10^6 cm^{-2} and 10^{12} cm^{-2} have been determined for epitaxial and polycrystalline films in this work, respectively, (see Section 4.2) a large uncertainty is introduced. This complicates the application of the dislocation scattering model.

While the dislocation scattering is temperature independent in degenerate semiconductors, it is proportional to the temperature in non-degenerate semiconductors. Hence, for non-degenerate conditions, the dislocation scattering can become dominant at low temperatures.

2.4 Magnetron Sputtering

The sputtering process was observed for the first time in the 1850s in experiments with glow discharges.[111] In these experiments, a darkening of the glass wall of the discharge tube near the cathode was found, which was caused by the deposition of metallic films. The term ‘sputtering’ refers to the ejection of atoms from a solid target material by the impact of high-energetic species. This sputter deposition process belongs to the class of physical vapour deposition processes and is distinguished by a high versatility.

In 1936, Penning[112] performed experiments on the influence of an axial magnetic field on a gas discharge between coaxial cylinders and found a significant increase of the discharge current at a constant discharge voltage and a strongly decreased minimal pressure for the discharge.[111] This so-called magnetron sputter process became technically relevant only in the 1970s, when the planar magnetron was invented. Today, magnetron sputtering is used for the preparation of films in various fields such as metallic films for reflectors or back contacts, oxidic and nitridic films for optical and protective coatings or transparent contacts, infrared-reflective films for low-emissivity coating, and hard coatings for tools. The broad field of application is mainly due to the fact that compact films with

a very good homogeneity can be prepared at a high deposition rate on large areas at low substrate temperatures. This can mostly be attributed to the much higher energy input into the film in comparison to thermally excited deposition methods such as evaporation or chemical deposition methods, which opens up the possibility to tailor the film properties by adjusting the energy input. However, there are also disadvantages of the magnetron sputtering process. The targets can be expensive and the target usage is rather low. Furthermore, the process control can be very complicated. In the following, the basic principle of the sputtering process will be described and the different modes of sputtering, used for the preparation of the films in this investigation, presented. In literature, numerous articles and textbooks dealing with the basic principles of magnetron sputtering can be found. A good overview can be obtained from References 111 and 113-116, which also provided the basis for this section.

2.4.1 Principles of the Sputtering Process

Magnetron sputtering is a high vacuum deposition process, where ions from the process gas are accelerated onto a solid target (cathode) leading to the sputtering of the target material. The process gas is usually an inert gas – Ar. Subsequently, the sputtered atoms travel to the substrate and condensate there. The ions originate from a confined plasma in front of the target. The confinement is realized by magnets behind the target with a magnetic field locally parallel to the cathode, which leads to a trapping of the electrons onto cycloidal paths in the crossed electrical and magnetic fields in front of the target and hence to a very high ionization efficiency. The principal setup together with the potential distribution for a direct-current (DC) excited discharge is shown in Figure 2.26.

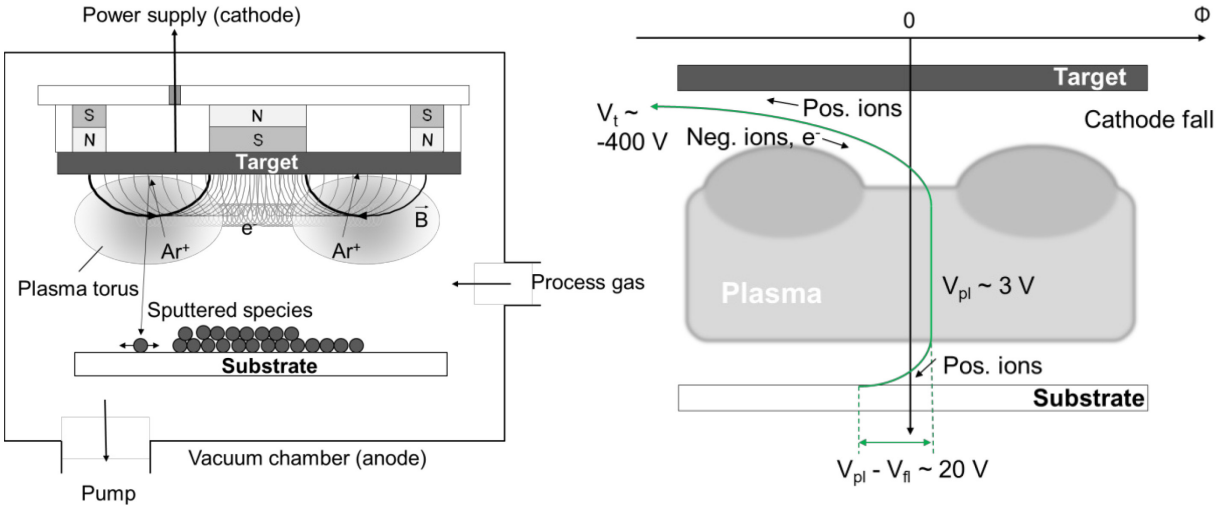

Figure 2.26: *Left*: Schematic representation of the planar magnetron sputter configuration (after References 114 and 117). *Right*: Potential distribution between the target and the substrate in the case of direct-current (DC) sputtering adapted from Reference 113.

The ions are initially formed by a variety of sources, one of which is cosmic radiation. Subsequently, the released electrons are accelerated in the electric field, hit other atoms as well as the electrodes, and produce more electrons and ions leading to an avalanche. The consequent potential distribution between the target and the substrate is essential for the sputtering and the deposition of the film. The positive ions, mostly process gas ions, are accelerated by the potential difference between the plasma and the cathode in the direction of the target, where they lead to the emission of neutral particles, secondary electrons, and secondary ions, to the desorption of gases, or to the emission of radiation. Additionally, the incident particles can be reflected or implanted in the target.

The most important process for the magnetron sputtering, however, is the sputtering of the target atoms. The impact of particles with energies of several hundred eV leads to a collision cascade, which eventually causes the emission of mostly neutral target atoms. There is a threshold energy for sputtering that is approximately equal to the heat of formation of the target material. Above this threshold, the sputtering yield, defined as the ratio between the number of emitted atoms and incoming ions, increases approximately linear with the incident ion energy and mass. The emitted atoms then have energies in the range of some eV, which is much higher in comparison to the thermal energy of the particles in evaporation processes and explains the ability to prepared dense films at low temperatures with a good adhesion to the substrate by the sputter deposition.

2.4.2 Sputtering Modes

There are mainly two different sputtering modes: the direct-current sputtering and the radio-frequency sputtering. For sputtering in the direct-current mode, the plasma is excited by a constant (DC) voltage, usually in the range of 300 V to 800 V. In this case, the plasma is essentially sustained by secondary electrons emitted from the cathode and the acceleration of the electrons in the cathode sheath. Therefore, large target voltages are necessary, because the electron emission increases only linearly with the ion velocity. The DC plasma excitation is mostly used for metallic targets or targets with a sufficiently high conductivity. If the conductivity is not high enough, local charging up effects of the target surface can occur, which eventually are transferred into an arc discharge if the field strength for a dielectric breakdown is reached. This can lead to local target melting that can damage the target substantially. However, modern DC power supplies are equipped with sophisticated arc detection circuits. For even higher resistivities of the target (semiconductors, ceramics, or insulators), the target is charged up and the discharge vanishes, eventually. This effect can be circumvented when using the radio-frequency (RF) sputtering mode.

In the RF sputtering mode, a high-frequency voltage with a sufficiently high amplitude is superimposed to the constant voltage. This prevents the charge built-up, because the target will be neutralized by fast electrons in every second half wave when its potential is positive. One major advantage of this mode is the possibility to sputter low conductive compound materials, for example ZnO, without the use of reactive gases. This leads to more stable and reproducible processes. The frequency of the superimposed voltage is usually 13.56 MHz, but mid-frequency sputtering (10...200 kHz) and sputtering with 27.12 MHz is also routinely performed. Figure 2.27 shows the target voltage of a 13.56 MHz discharge as a function of time.

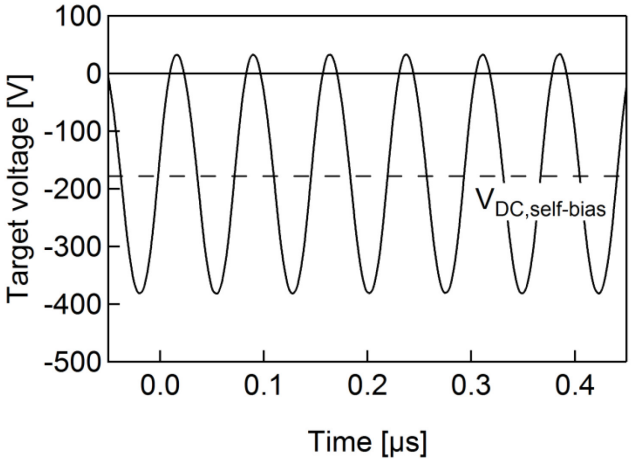

Figure 2.27: Target voltage as a function of time for a 13.56 MHz RF plasma discharge measured using a ZnO:In target. The dotted line denotes the DC self-bias voltage.

In contrast to the DC discharge, the RF plasma is mainly sustained by the ionization caused by the oscillatory motion of the electrons in the plasma body. Since the electrons are able to follow the oscillating electric field, while the ions are not significantly affected due to their large inertia, this ionization process is much more effective in comparison to the excitation by non-oscillating secondary electrons. In consequence, an RF discharge exhibits lower DC self-bias target voltages. However, the magnetic confinement of the electrons in the RF discharge is less effective, because the target does not act as a cathode, but as an anode, during the positive half-cycle. This leads to a higher plasma density in front of the target. The altered distribution of the plasma is also reflected in a different erosion of the target.

The low discharge voltage in the case of RF sputtering causes a threshold power for sputtering of approximately 10 W. Above these values, the deposition rate is mostly proportional to the discharge power. Comparing both sputtering modes, the DC process yields deposition rates that are a factor of 1.5 to 2 higher in comparison to RF excitation when using the same power. This can be attributed to the higher target voltage (ion energy) in the DC process.

Although the RF sputtering mode allows to sputter ceramic materials, the process technology is more complex. Since alternating fields and currents occur, impedance matching is necessary to suppress losses due to inductive and capacitive reactances. Furthermore, RF radiation is produced, RF electromagnetic interference occurs, and parasitic plasma generation within the deposition chamber is facilitated by the low requirements for sustaining the plasma.

2.4.3 Film Formation

The quality of the resulting films depends on a variety of parameters: external parameters such as the working pressure, the discharge power, and the substrate temperature as well as plasma parameters such as the ion energy, the electron temperature, and the ion-to-neutral ratio. Thornton performed pioneering work on the description of the growth process in sputtered coatings in dependence of the external parameters. He divided the growth process into three steps.[118] First, the sputtered species has to be transported to the substrate. This process is mainly influenced by the pressure in the process chamber. For higher pressures, the incoming particles have lower energies due to scattering, leading to a decrease of the adatom mobility, which is crucial for the second step.[119] The second step involves the adsorption of the sputtered species on the substrate or the growing film, their diffusion over the surface, and their incorporation into the coating or the removal by evaporation or sputtering. Finally, the atoms move to the energetically most favourable positions by processes such as bulk diffusion. These processes are mainly influenced by the substrate temperature.

The species, which contribute to the energy input into the growing film, are electrons and ions from the plasma, neutral particles that contribute to the film growth, and neutral particles of the sputtering gas(es). To reduce the bombardment by electrons, the substrates are usually kept at floating potential. This potential is slightly negative in the case of DC sputtering and established at the substrate due to the different mobilities of ions and electrons. Especially important for this investigation, however, are high-energetic species formed during the sputtering process. Particles with the highest energies are reflected atoms (neutralized ions) and negative ions.[120] Since these particles can have energies far above the formation energy of defects in ZnO, they have a strong impact on the structural properties of the films. The effects of high-energetic negative ion bombardment and other process parameters on the electronic and structural properties of the films will be elucidated in Chapter 6.

2.5 Transparent Conductive Oxides in Solar Cells

As already pointed out, transparent conductive oxides are not only used in applications such as flat panel displays, architectural glass coatings, organic light emitting diodes, or touch panel controls, but also in thin film photovoltaics. In thin film solar cells, the transparent conductive oxides are used as window layers to transport the charge carriers to the electrodes without hindering the light from reaching the absorber layers. Since this work is closely related to the application of the transparent conductive ZnO in chalcopyrite thin film solar cells, and especially the investigations on the $Zn_{1-x}Mg_xO$:Al are motivated by the prospect of increasing the efficiency of wide-gap chalcopyrite solar cells by improving the band alignment between the front contact and the absorber layer of the solar cell, this section will be used to provide a short introduction into the basics of solar cells in general and wide-gap chalcopyrite thin film solar cells in particular. Special emphasis will be given to the band alignment between the window layer and the absorber layer. For more detailed information, the reader is referred to the textbooks in References 11 and 121-124, which this section is based on.

2.5.1 Basic Aspects

Becquerel[125] was the first to observe the photovoltaic effect in 1839. This effect is defined as 'the emergence of an electric voltage between two electrodes attached to a solid or liquid system upon shining light onto this system'.[121] The following requirements have to be fulfilled to convert light into electrical energy:

(i) The incoming light has to be absorbed to generate electron-hole pairs.

(ii) The electron-hole pairs must be mobile and have to have a sufficiently high lifetime.

(iii) The electron-hole pairs must be separated by internal electric fields.

(iv) The separated charge carriers must be extracted by electrodes.

The realization of these 4 requirements determines the efficiency of the solar cell, which is defined as the ratio of the generated electric power of the solar cell to the incoming power of the light

$$\eta = \frac{I_m V_m}{P_{light}} = \frac{FF \cdot I_{sc} V_{oc}}{P_{light}}, \tag{2.75}$$

where FF is the fill factor, I_{sc} is the short circuit current, V_{oc} is the open circuit voltage, and P_{light} is the power of the illumination. I_{sc} is obtained when the illuminated solar cell is short-circuited, which means when the voltage is zero. The open circuit voltage V_{oc} is obtained when the current is zero. The generated electric power of a solar cell depends on the load resistor. For the determination of the efficiency, the optimal value for the load resistor, leading to the highest efficiency, is chosen. This is the so-called working point of the solar cell.

For the direct conversion of light into electrical energy, a semiconductor is necessary. The band gap of the absorber material is a limiting factor for the efficiency of the solar cell. In a very simplified picture, only those photons with an energy larger than the band gap energy E_g can produce an electron-hole pair. Every photon with an energy higher than the band gap energy will then excite the electron or the hole in states that are deeper in the valence or conduction band. The electron and the hole will relax to the band edges within picoseconds and the additional energy will be released in form of thermal energy. If the energy of the photons is smaller than the band gap energy, they will not be absorbed and thus not be used for the generation of electricity. The ratio of the used energy to the energy of the incident light in this simple model is called 'ultimate efficiency'.[126] Because of the two opposed effects, there is a maximum of the efficiency as a function of the band gap energy of the

absorber material. For the ultimate efficiency, this maximum is reached for a band gap energy of 1.1 eV (see Figure 2.28) if the incident light is approximated by black-body radiation at $T = 6000$ K according to Planck's law.

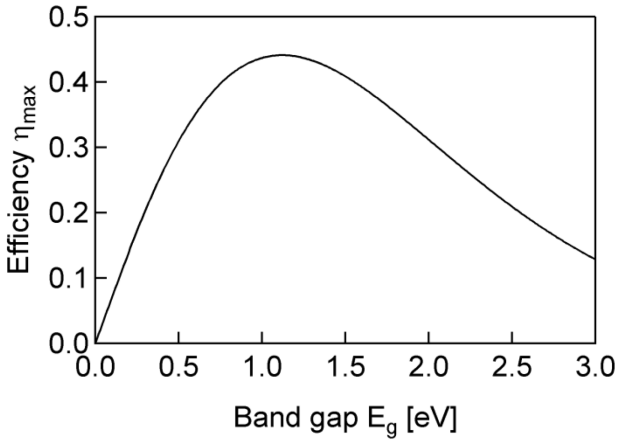

Figure 2.28: Ultimate efficiency η_{max} as a function of the band gap energy E_g of the semiconducting absorber layer derived using Equation (2.8) in Reference 126 and approximating the incident light by black-body radiation at $T = 6000$ K according to Planck's law.

In practice, however, the solar cell also has a certain temperature and a part of the electron-hole pairs recombines before reaching the electrodes. This reduces the limit for the efficiency and shifts the optimal value of the band gap to higher energies of approximately 1.5 eV (see for example Reference 11 page 88).

2.5.2 Chalcopyrite Thin Film Solar Cells

The term chalcopyrite, originally used for the $CuFeS_2$ mineral that crystallizes in the tetragonal system, was adapted to the ternary compounds $CuInSe_2$, $CuInS_2$, $CuGaSe_2$, or the multinary compound $Cu(In,Ga)(S,Se)_2$ in solar cells, which exhibit the same crystalline structure.[127] Although the crystalline structure of these materials is rather complicated, it became obvious that the material is very flexible with respect to the process conditions, because the electronic properties are not very much affected by deviations from the stoichiometry.[128] A main advantage of the chalcopyrite materials is the tunable band gap that can be altered in the range of roughly 1 eV to 2.5 eV by changing the stoichiometry of the films. Hence, it is possible to adjust the band gap to the optimal value in the range of 1.5 eV, which is not feasible with other technologies. A cross section of a chalcopyrite thin film solar cell is shown in Figure 2.29.

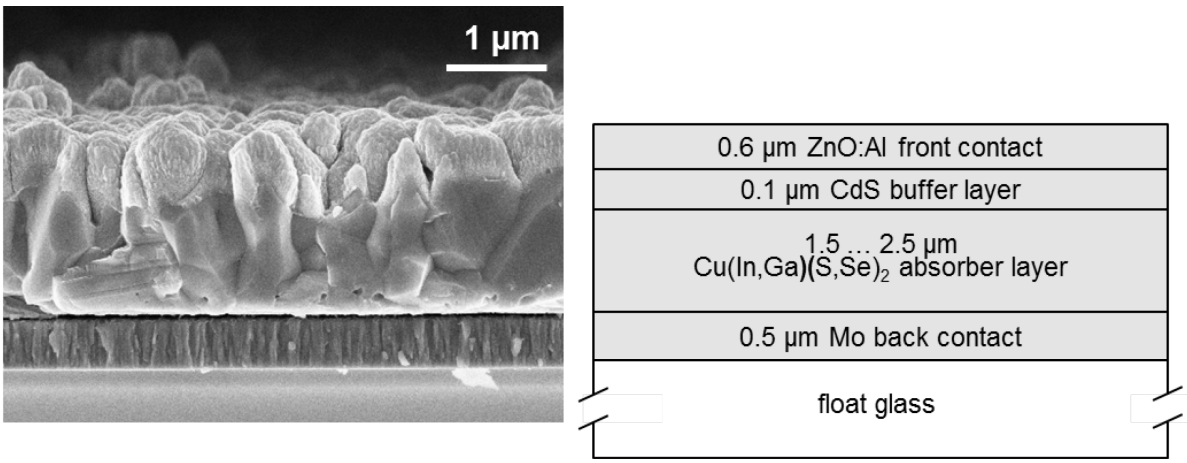

Figure 2.29: Left: Cross-sectional scanning electron microscopy image of the layer stack of the reactively magnetron co-sputtered solar cell.[129] *Right*: Schematic representation of the layer stack.

Typically, the solar cell is prepared on soda lime glass, which also serves as a source for the doping of the absorber layer with sodium.[128] The back contact is realized using a Mo layer and the transparent conductive front electrode is made of Al-doped ZnO. The window layer (front contact) consists of an intrinsic layer in contact to the CdS buffer layer and a highly conductive top layer. The role of the intrinsic layer is not completely clear. It has been shown that the cell process becomes more reproducible when using the intrinsic layer, whereas the efficiency is not affected. Furthermore, the devices seem to be more stable during damp-heat stress tests. Between the front electrode and the absorber layer, a buffer layer composed of CdS is inserted. Without the buffer layer, the performance of the solar cell is significantly lower. Yet, the effect of the buffer layer is not completely understood as well. It can increase the efficiency by reducing reflection losses but also decrease the efficiency due to light absorption and carrier recombination. For chalcopyrite solar cells it has been found that the buffer layer electronically passivates the absorber surface and preserves a high carrier lifetime.[123] Additionally, it acts as a diffusion barrier. Because of the toxicity of the Cd, there are attempts to replace the CdS buffer layer by non-toxic abundant materials, for example Zn(O,S) or $Zn_{1-x}Mg_xO$.

Nowadays, the highest efficiencies are reached with $Cu(In,Ga)(Se,S)_2$ chalcopyrite absorber layers with a low Ga and S content. The world record efficiency reported by the 'Zentrum für Sonnenenergie- und Wasserstoff-Forschung (ZSW)' in 2011 is $\eta = 20.3\,\%$ for a $Cu(In,Ga)Se_2$ solar cell. However, the band gap in the range of 1.1 eV is not optimally suited for the absorption of the spectrum of the sunlight. Therefore, wide-gap chalcopyrites with $E_g \approx 1.5$ eV are investigated to achieve higher efficiencies. But still, despite their more suitable band gap energy, the efficiencies obtained with these materials are actually lower in comparison to the chalcopyrites with a low Ga and S content. This is mainly caused by lower open circuit voltages in comparison to those values expected from their larger band gap (see Figure 2.30)

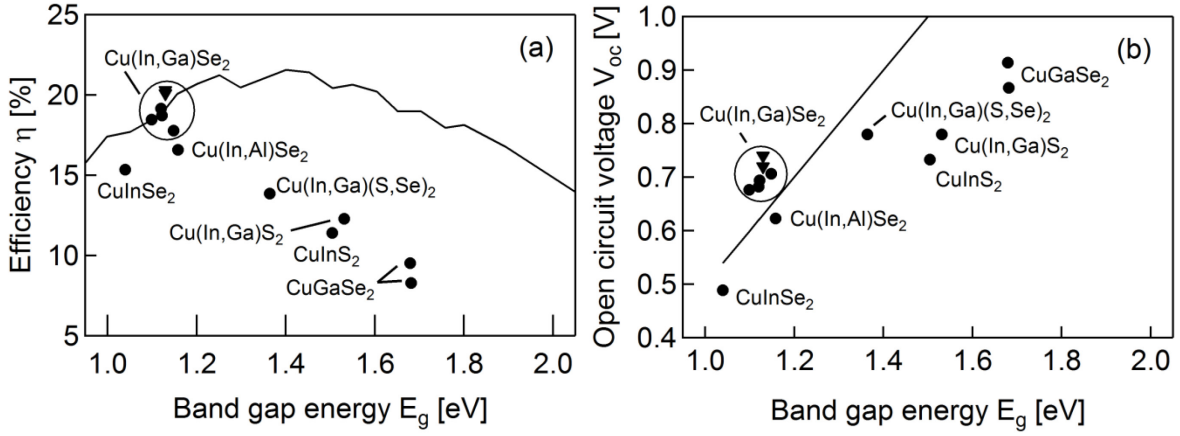

Figure 2.30: (a) Highest published efficiencies η of chalcopyrite solar cells as a function of the band gap energy E_g. (b) Open circuit voltages V_{oc} of the cells shown in (a). The solid lines represent an extrapolation of the recombination properties of the $Cu(In,Ga)Se_2$ solar cells toward higher and lower band gap energies. The figure has been adapted from Reference 124. Values from Jackson et al.[130] for $Cu(In,Ga)Se_2$ solar cells (triangles) have been added.

The physical origin of this effect has not clearly been identified yet. Actually, there are several possible explanations. There is for example a variety of difficulties in the preparation of high efficiency solar cells that have been solved and understood for the alloys with a low band gap after a long research effort. Apparently, these solutions cannot readily be applied for the wide-gap chalcopyrites. Additionally, slight changes in the grain boundary properties, the interface properties of the front and back contact, or the defect chemistry may sum up to the significantly degraded performance.

One crucial point referring to the interface properties of the front contact is an unfavourable energy band alignment, which wide-gap chalcopyrites may exhibit.[131] Device simulations have shown that the

low open circuit voltage is related to the conduction band offset between the window, the buffer, and the absorber material, and interface recombination at the absorber/buffer interface. Figure 2.31 shows the principal energy band alignment that can be encountered for a normal chalcopyrite solar cell and a wide-gap chalcopyrite solar cell.

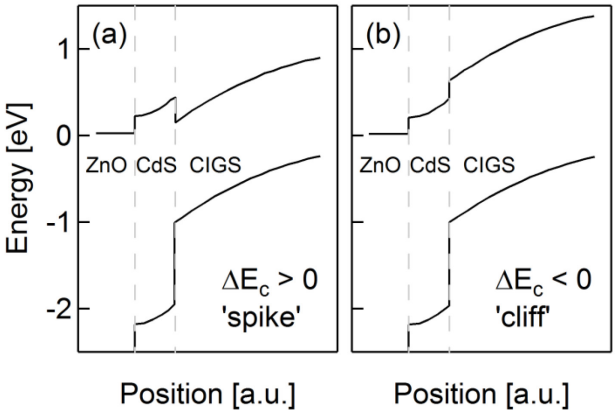

Figure 2.31: Conduction and valence band edge alignment of the window, the buffer, and the absorber layer for a solar cell with an absorber layer with a small band gap (a) and with a large band gap (b). The data has been taken from Reference 132.

The main difference is the conduction band offset, which is either positive, $\Delta E_c > 0$ ('spike'), or negative, $\Delta E_c < 0$ ('cliff'). Simulations performed by Gloeckler and Sites[132] for $Cu(In,Ga)Se_2$ with a changing conduction band offset ΔE_c from positive values to negative values have shown that the open circuit voltage increases mainly linearly when the recombination at the CdS/absorber interface is not taken into account. This would be expected for the wide-gap chalcopyrites due to the increasing band gap of the absorber layer. If, however, recombination processes at the CdS/absorber interface are taken into account, the situation changes: the open circuit voltage increases until approximately $\Delta E_c = 0$ is reached. But for further increase of the conduction band minimum, which means for $\Delta E_c < 0$ when the band structure exhibits a cliff between the CdS and the absorber, the open circuit voltage V_{oc} remains constant. Because of the decrease of the short circuit current I_{sc} with increasing band gap, the efficiency decreases, and hence the low open circuit voltages and efficiencies of the wide-gap chalcopyrites shown in Figure 2.30 can tentatively be explained.

The aim for wide-gap chalcopyrite solar cells is therefore to introduce a conduction band offset ΔE_c at the interface to the absorber in the range of 0 eV to 0.4 eV. This can be realized by using different window and absorber materials, which exhibit a higher conduction band minimum. A suitable material for the window layer is for example $Zn_{1-x}Mg_xO$. As already pointed out, the band gap of this material can be shifted in a wide range. Additionally, this band gap shift is mostly due to an increase of the conduction band minimum.[133] $Zn_{1-x}Mg_xO$ is especially interesting, because it can be used as an alternative buffer layer. Actually, efficiencies over 16 % have been achieved using $Zn_{1-x}Mg_xO$ instead of CdS in $Cu(In,Ga)Se_2$ solar cells (see Reference 123 page 271). A possible layout employing $Zn_{1-x}Mg_xO$ as alternative buffer and window layer is shown in Figure 2.32.

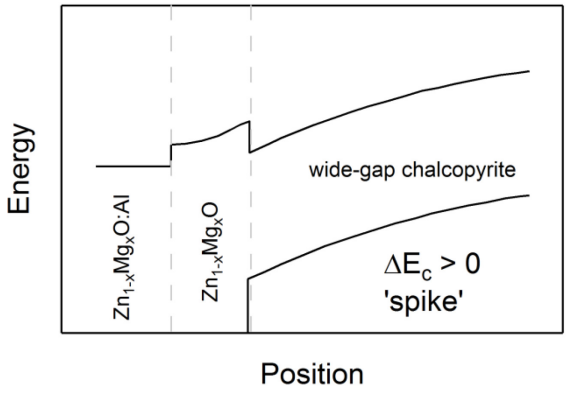

Figure 2.32: Schematic band diagram of a suitable layout for a wide-gap chalcopyrite solar cell using a window layer based on $Zn_{1-x}Mg_xO$ adapted from Reference 131.

3. Methods of Analysis and Realization of Experiments

In this chapter, the techniques used for the preparation and the analysis of the samples will briefly be introduced. First, the sample preparation will be described with a focus on the sample type, the cleaning procedure, and the deposition conditions. Subsequently, the characterization techniques employed for the analysis of the structural, electronic, and optical properties of the doped ZnO and $Zn_{1-x}Mg_xO$ films will be reviewed, which is going to constitute the major part of this chapter. The structural properties have mainly been investigated by X-ray diffraction and transmission electron microscopy, the electronic properties by resistivity, Hall-effect, and Seebeck-coefficient measurements, and the optical properties by measurements of the transmittance and reflectance. Additionally, the techniques used for the determination of the chemical composition of the films, Rutherford backscattering spectrometry, and the distribution of the elements in the films, atom-probe tomography, will shortly be presented. Since many different methods have been employed to characterize the properties of the films, the scope of this chapter is to give only a short introduction to the basic principles of the measurement techniques and the parameters used for the investigations.

3.1 Thin Film Deposition

3.1.1 Substrates and Substrate Cleaning

For the majority of the experiments, polished borosilicate glass substrates with a size of 10 x 10 x 1 mm³ were used to prepare polycrystalline films. The borosilicate glass substrates are characterized by a high thermal and chemical resistance, a high transparency, a good surface quality, and by a low sodium content (below 3 at.%)[134]. Prior to the deposition, the glass substrates have been cleaned in an ultrasonic bath for 5 min in isopropanol. Afterwards, the substrates were rinsed with deionized water to ensure that no organic material is left on the surface and blown dry with nitrogen. For the experiments related to the radial distribution of the film properties (see Section 6.2), 10 x 70 x 1 mm³ borosilicate glass substrates were employed.

Especially for the determination of the optical properties of the $Zn_{1-x}Mg_xO$:Al films, substrates with a larger band gap were required. For this purpose, the films were prepared on quartz glass with a size of 10 x 10 x 1 mm³. The quartz glass consists of SiO_2 (> 99.99 wt.%) and contains other elements only as impurities.

In this work, the epitaxial growth of undoped and doped ZnO and $Zn_{1-x}Mg_xO$ was investigated as well. Epitaxial films were prepared on a-sapphire $(11\bar{2}0)$, c-sapphire (0001), r-sapphire $(01\bar{1}2)$, or ZnO (0001) single crystals. The sapphire single crystals were delivered by Crystec GmbH (Berlin) and the ZnO single crystals were obtained from Crystec GmbH and TokyoDenpa Co., Ltd. Only for the single crystalline substrates, a special surface conditioning procedure was used. Prior to the deposition, they were annealed in the vacuum chamber ($p < 10^{-6}$ mbar) for 40 min, before the desired deposition temperature was adjusted and levelled for 30 min. The films were then deposited on the Zn-terminated surface of the ZnO (0001) single crystals.

3.1.2 Film Growth

The majority of the films were prepared in a sputtering system equipped with a (pulsed) DC power generator PMP-1 by Advanced Converters, a 13.56 MHz RF generator RTX-600 combined with an ATX-600 matching network power supply by Advanced Energy, and a 27.12 MHz power generator CESAR RF 276 by Dressler. The pulsed DC sputtering was performed with a pulse frequency of 40 kHz and a pulse time of 15 µs.

The targets mainly used for this investigation were eroded 3 inch diameter ceramic ZnO/Al_2O_3 (98.4/1.6 mol.%) and $ZnO/MgO/Al_2O_3$ (88/10/2 mol.%) targets purchased from Cerac, Inc. with a purity of 4N5 and purchased from Kurt J. Lesker Company with a purity of 3N for the deposition of the Al-doped ZnO and $Zn_{1-x}Mg_xO$ films, respectively. For the sputtering of the Ga-doped ZnO films, an eroded ceramic ZnO/Ga_2O_3 target (98.7/1.3 mol.%) with a purity of 4N by Kurt J. Lesker Company has been employed, and for the deposition of the ZnO:In films, a new ZnO/In_2O_3 (98.4/1.6 mol.%) target with a purity of 4N purchased from FHR Anlagenbau GmbH was applied. The targets were mounted on a nearly balanced magnetron. The average discharge power was chosen to be 50 W, which resulted in an average target voltage of ~500 V for the DC sputtering (during the duty cycle), ~170 V for the 13.56 MHz RF sputtering, and ~90 V for the 27.12 MHz sputtering. For the depositions above substrate temperatures of ~30 °C, the samples were heated radiatively by a boron nitride encapsulated graphite heater by Boralectric. In this case, the substrate temperature was leveled for 15 min before the presputtering to ensure stable process conditions. Unless otherwise mentioned, the sputtering was performed in pure Ar (purity 5N) at a pressure of 0.27 Pa. The substrate-to-target distance was 61 mm and the base pressure of the chamber was $p < 10^{-6}$ mbar. The deposition rates at 300 °C were approximately 16 nm/min for DC sputtering, 12 nm/min for 13.56 MHz RF sputtering, and 6 nm/min for 27.12 MHz RF sputtering. They decrease by about a factor of 2 with increasing deposition temperature from ~30 °C to 500 °C. The influence of the deposition rates on the electrical and structural properties of the films has been examined for the RF sputtered films and no significant effect was found.

For the investigations of the radial distribution of the film properties, a different deposition chamber has been used. A schematic drawing of this chamber is shown in Figure 3.1.

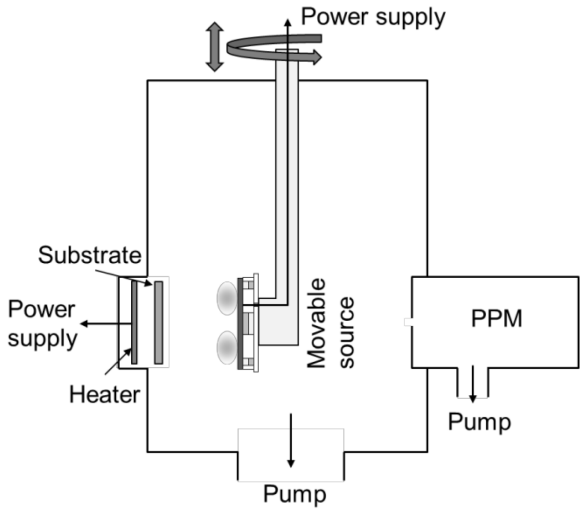

Figure 3.1: Schematic representation of the system used for the investigation of the radial distribution of the film properties. PPM denotes the plasma process monitor (Balzers, PPM 422). Important to note is the movable magnetron source, which allows for quasi-simultaneous plasma characterization and film deposition.

The parameters for the depositions in this chamber were chosen to be as similar as possible to the other depositions, which means a process pressure of 0.27 Pa and pure Argon were used. The substrate-to-target distance in this chamber was 60 mm and the substrate heating was performed by radiative heating with a boron-nitride encapsulated heater as well. The films were deposited at a

substrate temperature of 300 °C. For the DC excitation of the plasma, a power generator from Advanced Energy (MDX-1.5k) was applied, and the 13.56 MHz RF plasma excitation was performed with a Dressler CESAR RF 136 power supply. Since this chamber can only be equipped with 2 inch diameter targets, different targets had to be employed. The ZnO:Al films were deposited using a ceramic ZnO/Al_2O_3 target (95/5 mol.%) with a purity of 3N5 supplied by GfE Metalle und Materialien GmbH. The $Zn_{1-x}Mg_xO$:Al films have been deposited using a ceramic $ZnO/MgO/Al_2O_3$ target (85/10/5 mol.%) with a purity of 3N5 by the same manufacturer. The discharge power was again chosen to be 50 W, which resulted in an average target voltage of ~450 V and ~155 V for the DC and 13.56 MHz RF sputtering, respectively. The base pressure of the system was $p < 10^{-6}$ mbar.

3.2 Electrical Measurements

3.2.1 Resistivity Measurements

The resistivity of the samples was measured by the four-point-probe technique in the van-der-Pauw geometry. According to van der Pauw[135], the resistivity can be calculated by measuring the two resistances $R_{AB,CD}$ and $R_{BC,DA}$ and the thickness of the sample. The principal geometry for the measurements performed in this investigation is sketched in Figure 3.2.

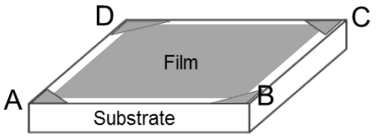

Figure 3.2: Sample geometry for the resistivity and Hall measurements based on the van-der-Pauw method.[135] The corners of the film are contacted with evaporated Ni/Au triangles.

The resistivity is then given by

$$\rho = \frac{\pi d}{\ln(2)} \frac{\left(R_{AB,CD} + R_{DC,DA}\right)}{2} f\left(\frac{R_{AB,CD}}{R_{BC,DA}}\right), \tag{3.1}$$

where $R_{AB,CD}$ is defined as the potential difference $V_D - V_C$ between the contacts D and C per unit current through the contacts A and B. The other resistances are defined accordingly. d is the film thickness and the function f satisfies the relation

$$\frac{R_{AB,CD} - R_{DC,DA}}{R_{AB,CD} + R_{BC,DA}} = f \cdot \operatorname{arcosh}\left(\frac{e^{\frac{\ln(2)}{f}}}{2}\right). \tag{3.2}$$

This relation has to be solved numerically or approximated. These formulae are only valid under the following circumstances:

(i) The contacts are at the circumference of the sample.

(ii) The contacts are sufficiently small.

(iii) The sample is homogeneous in thickness.

(iv) The sample does not have isolated holes.

For some of these requirements it is obvious that they are only partially fulfilled, but for others, the violation may not even be evident. The contacts, for example, are triangles with an edge length of about 1.5 mm. With respect to the size of the sample of 10 x 10 mm², this may already violate the rule about sufficiently small contacts. Furthermore, the sample thickness has a distribution due to the static

deposition (see Section 6.2), which perpetrates rule (iii). The last requirement may also be violated, because the films can have isolated regions with low conductivity due to the formation of non-conductive secondary phases. Juretschke et al.[136] quantified the effect of non-conductive inclusions in a conductive material on the measured resistivity ρ_m and Hall constant R_{Hm} and found for example for spherical inclusions (see also Reference 137)

$$\begin{aligned} \rho_m &= \frac{1+\varepsilon/2}{1-\varepsilon}\rho_0, \\ R_{Hm} &= \frac{1-\varepsilon/4}{1-\varepsilon}R_{H0}, \end{aligned} \tag{3.3}$$

where the index 'm' and the index '0' denote the measured and the true value, respectively, and ε is the fractional film volume occupied by the inclusions.

The measurement setup is home-built and consists of a current source (220), a voltmeter (DMM 196) and a Hall card (7065) by Keithley Instruments and is operated by a program using Igor Pro 5 (WaveMetrics, Lake Oswego, Oregon, USA). The Ni/Au contacts with a thickness of 10 nm and 150 nm, respectively, were deposited at the perimeter of the films to ensure ohmic contacts for the measurement. The film thickness was measured with a surface profilometer (Dektak 8, Veeco Instruments). To avoid influences of the surrounding, the sample holder was always covered with a lid. The setup also allows for temperature dependent measurements between room temperature and approximately 30 K. To cool the sample, a He cryostat (LTI 10) by Leybold was used. To minimize the heat flow between the sample and the cover for these measurements, an aluminium heat radiation shield was positioned between the sample and the cover and additionally the chamber was evacuated to a base pressure of $p < 10^{-5}$ mbar.

3.2.2 Hall-Effect Measurements

The measurement of the Hall coefficient $R_H = \dfrac{p\mu_p^2 - n\mu_n^2}{e\left(p\mu_p + n\mu_n\right)^2}$, where p and μ_p are the concentration and the Hall mobility of the holes, respectively, and n and μ_n are the concentration and the Hall mobility of the electrons, respectively, allows to determine the free carrier concentration in the sample. If the free electron concentration is much larger than that of the holes, which is the case for the samples investigated here, the Hall coefficient can be approximated by $R_H \approx -1/(en)$. When the conductivity has also been measured, it is possible to calculate the Hall mobility of the carriers $\mu_n = \sigma/(en)$. Since the charge carrier mobilities are almost exclusively determined by Hall measurements in this work, the index 'Hall' for the Hall mobilities will be omitted throughout the rest of this thesis, unless it is especially required. A detailed derivation of the formulae for the Hall effect can for example be found in References 50-52. Here, only a brief discussion of the basic effect will be given.

To measure the Hall effect, a current is driven through the sample, for example from contact A to C (see Figure 3.2 on page 47), which is exposed to a magnetic field oriented perpendicular to the sample surface. This exerts the Lorentz force $\boldsymbol{F}_L$ on the electrons in the sample and leads to an imbalance of charges perpendicular to the direction of the current. This introduces an electric field between the contacts B and D, which compensates the Lorentz force in the stationary case. Consequently, for weak magnetic fields, the following expression holds for electron transport:[138]

$$\boldsymbol{F}_L = -e\left(\boldsymbol{v}_d \times \boldsymbol{B}\right) - e\boldsymbol{E}_H = -e\left(\frac{1}{en}\boldsymbol{j} \times \boldsymbol{B}\right) - e\boldsymbol{E}_H = 0. \tag{3.4}$$

Since the magnetic field is perpendicular to the current, the cross product can be simplified and the current density can be expressed in terms of the current by $j = I/(bd)$, where b is the width and d is the thickness of the contributing part of the film. Defining further the product of the absolute value of the Hall electric field E_H and the sample width b as the Hall voltage U_H, the common relation

$$U_H = -\frac{1}{en}\frac{IB}{d} = R_H \frac{IB}{d} \tag{3.5}$$

is derived. A more precise calculation takes into account that the action of the magnetic field on the charge carriers leads to an electric field vector of the Hall field, which is tilted relative to the external electric field causing the current flow. This gives rise to the so-called Hall angle. In this case, the Hall coefficient is given by $R_H = -r_H/(en)$, with $r_H = \langle \tau^2 \rangle / \langle \tau \rangle^2$.

In the van-der-Pauw geometry, the Hall coefficient is determined by

$$R_H = \frac{\mu^{\text{Hall}}}{\sigma} = \frac{d}{B}\Delta R_{\text{BD,AC}}, \tag{3.6}$$

where $\Delta R_{\text{BD,AC}}$ is the change of the resistance $R_{\text{BD,AC}}$ induced by the magnetic field. It is important to note that the assumptions for the resistivity measurements also apply for the Hall measurements.

The Hall coefficient has been measured in the same setup as used for the resistivity measurements, employing the the van-der-Pauw geometry as well. The magnetic field was 0.86 T. With the available setup, also temperature dependent Hall-effect measurements were possible. Measuring $\mu(T)$ and $n(T)$ opens up the opportunity to determine the degeneracy of the doping of the semiconductor and the main mechanisms for the scattering of the charge carriers due to the specific temperature dependence of the scattering mechanisms. This will be deployed in Section 5.2.2.

3.2.3 Seebeck-Coefficient Measurements

The Seebeck effect, named after the physicist Thomas Johann Seebeck, is the occurrence of an electric field in a sample due to the presence of a temperature gradient. The Seebeck coefficient in the open circuit case (zero currents) is defined as the ratio between the potential difference and the temperature difference

$$S = -\frac{\nabla_r \Phi}{\nabla_r T}, \tag{3.7}$$

where $\nabla_r\Phi$ is the gradient of the electrochemical potential. It is positive when the majority of the charge transport is realized by holes and negative if the charge transport by electrons prevails.

The Seebeck coefficients were measured using a home-built setup. The material combination of the contacts was Ni/NiCr, and the measurements have usually been performed in the temperature range between 40 °C and 80 °C with a temperature difference of 10 K between the contacts. The potential difference is measured using the Ni contacts, while the temperature is determined at the same point using the Ni/NiCr thermocouple. Figure 3.3 on page 50 shows the principal setup for the measurement of the Seebeck coefficient.

Due to the sensitivity of the setup, the surrounding temperature in the laboratory had an influence on the measured values. To determine this effect, prior to every series of measurements, a Ni sample has been measured. It was found that the values increase or decrease by about ±2.5 µV/K depending on the average temperature in the laboratory.

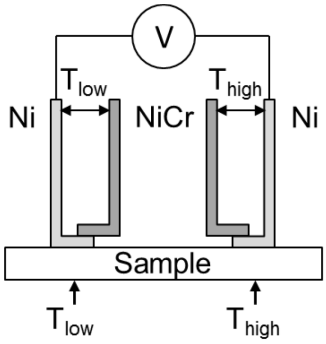

Figure 3.3: Schematic representation of the setup used for the measurements of the Seebeck coefficient. The figure is adapted from Reference 117 (page 79).

3.3 Optical Measurements

The optical characterization of the samples was performed by means of transmittance and reflectance measurements. This provides information about the optical band gap, the carrier concentration, the carrier mobility, and the thickness of the films. The optical reflectance and transmittance were determined with a Perkin Elmer Lambda 950 UV/VIS/NIR double-beam spectrophotometer in the wavelength range from 200 nm to 2500 nm with a step size of 3 nm. A 'VW'-setup has been used to ensure that the reflectance and transmittance were measured at the same position on the sample. Figure 3.4 shows a scheme of the 'VW'-setup.

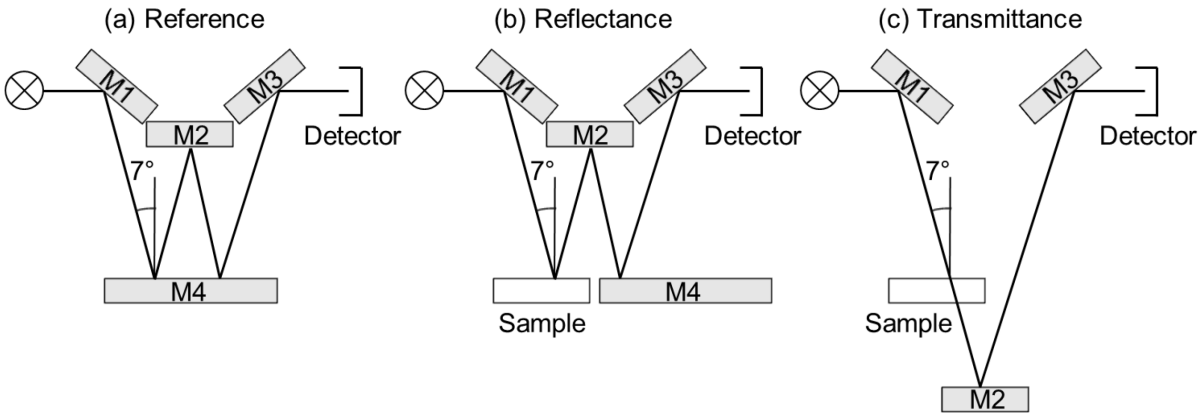

Figure 3.4: Schematic representation of the 'VW'-setup used for the reflectance and transmittance measurements.

First, using mirrors M1, M2, and M3 but no sample (setup as in Figure 3.4 (c)), the 100 % and 0 % intensity calibration is performed. Afterwards, the reflectance of mirror M4 is determined (Figure 3.4 (a)) as a reference for the reflectance measurements. Subsequently, the sample is inserted and the reflectance and transmittance are measured using the setups shown in Figure 3.4 (b) and (c), respectively. The reflectivity of the samples can then be calculated according to

$$R_s = \frac{R'_s}{\sqrt{R_{ref}}}, \tag{3.8}$$

where R'_s is the reflectance measured with the setup shown in Figure 3.4 (b), R_{ref} is the reflectance of mirror M4, and R_s is the reflectance of the sample.

The modelling of the optical properties of ZnO has for example been investigated in detail by Bundesmann et al.[139]. The simplest description of the band-to-band transitions in a semiconductor is based on a damped harmonic oscillator – the Lorentz oscillator. A more sophisticated model, typically

employed for ZnO, is the Adachi oscillator. It describes the dielectric function at the critical points of semiconductors for parabolic bands in 3 dimensions as a function of the photon energy E_{ph} by[36,139,140]

$$\varepsilon_{\text{Adachi}}(E_{\text{ph}} = \hbar\omega) = \varepsilon_\infty + \frac{A_0}{E_0^{-\frac{3}{2}}\chi_0(E_{\text{ph}})^2}\left[2 - \sqrt{1+\chi_0(E_{\text{ph}})} - \sqrt{1-\chi_0(E_{\text{ph}})}\right] \tag{3.9}$$

with $\chi_0 = (E + i\Gamma_0)/E_0$. A_0 and E_0 are the amplitude and the transition energy of the critical-point structures, while Γ_0 denotes the broadening. E_{ph} is the photon energy and ε_∞ is the high-frequency dielectric constant. The lowest band-to-band transitions in ZnO occur at the Γ point of the Brillouin zone and are typically associated with $3DM_0$-type critical-point structures – hence the index '0' in Equation (3.9).

The absorption due to plasmons in the near-infrared region is modelled using the well-known Drude ansatz. In this case, the dielectric function is derived from the equation of motion of the quasi-free electrons using a harmonically oscillating electric field. Combining this with the polarization due to the motion of the electron gas, the dielectric function according to the Drude model can be expressed in terms of the effective mass m^*, the free carrier concentration n, and the charge carrier mobility μ by

$$\varepsilon_{\text{Drude}}(E_{\text{ph}} = \hbar\omega) = \varepsilon_\infty - \frac{ne^2}{\varepsilon_0 m^*}\frac{\hbar^2}{E_{\text{ph}}^2 + \frac{iE_{\text{ph}}\hbar e}{m^*\mu}}, \tag{3.10}$$

where ε_0 is the static dielectric constant. For the analysis of the measured spectra, the Woollam Software WVASE32 version 3 (J.A. Wollam Co., Lincoln, Nebraska, USA) with the above mentioned models has been used. If the carrier concentration was too small, the absorption due to the plasmons was weak and the determined values had a large uncertainty. In consequence, only for the samples with the highest carrier concentrations, values for n and μ are presented in this work.

The complex index of refraction $\tilde{n} = n + i\kappa$ is related to the complex dielectric function by $\tilde{\varepsilon} = \varepsilon + i\varepsilon'' = (n + i\kappa)^2$, where n is the real part of the refractive index and κ is called the extinction coefficient. Therefore, $\varepsilon = n^2 - \kappa^2$ and $\varepsilon'' = 2n\kappa$. Using these expressions, the transmittance T and reflectance R can be determined as a function of the complex refractive index of the film and the substrate (see for example Reference 141 page 162 and following). Subsequently, T and R can be employed to determine the absorption coefficient $\alpha = 4\pi\kappa/\lambda$ the following way: Defining I_0 as the incoming light intensity, I_a as the absorbed intensity, and I_t and I_r as the transmitted and reflected light intensity, respectively, the absorbance A, transmittance T, and reflectance R can be calculated by

$$A = \frac{I_a}{I_0}, \quad T = \frac{I_t}{I_0}, \quad R = \frac{I_r}{I_0}. \tag{3.11}$$

From the fact that the sum of the reflected, absorbed, and transmitted light equals the incoming light intensity, the following relation can be deduced

$$A + T + R = 1. \tag{3.12}$$

Hence, if the light is transmitted through a plane parallel layer of thickness d only once, the transmittance is given by $T = (1 - R)\exp(-\alpha d)$. The transmittance is reduced by the portion of the reflected light at the first interface and the absorption in the material according to the law of Lambert and Beer. However, the light is also reflected at the second interface, and in consequence the transmitted portion is $(1 - R)^2\exp(-\alpha d)$. The reflected light will again be reflected at the first interface and a part of it will also be transmitted. This consideration can be continued and yields an infinite geometric series, which can be solved for T by

$$T = \frac{(1-R)^2 e^{-\alpha d}}{1-R^2 e^{-2\alpha d}} \approx (1-R)^2 e^{-\alpha d}. \tag{3.13}$$

The approximation is valid for sufficiently large absorption coefficients α and is quite commonly applied for transparent conductive ZnO. In this equation, the effect of the substrate is ignored. In a narrow sense, the reflectance and transmittance at the first interface (air/film) do not equal those at the interface to the substrate. From the approximated equation, the absorption coefficient as a function of the film thickness, the reflectance, and the transmittance can be calculated by

$$\alpha = \frac{1}{d} \ln\left(\frac{(1-R)^2}{T}\right). \tag{3.14}$$

Finally, the optical absorption can be used to determine the optical band gap. According to quantum mechanical calculations, the dependence of the absorption coefficient on the photon energy E_{ph} near the band gap can be expressed the following way (see for example Reference 51 page 573)

$$\alpha \propto \frac{1}{E_{ph}} (E_{ph} - E_g)^r, \tag{3.15}$$

where $r = 1/2$ and $r = 3/2$ for the allowed and forbidden transition in a direct semiconductor, respectively, and $r = 2$ for an allowed transition in an indirect semiconductor. Hence, by plotting $(\alpha h\nu)^r = (\alpha E_{ph})^r$ as a function of E_{ph} (Tauc plot), the band gap energy can be determined. In the case of ZnO, which is a direct semiconductor, the exponent $r = 1/2$ has to be used. The intersection of a linear fit to $(\alpha E_{ph})^{1/2}$ with the x-axis is then the optical band gap determined by the Tauc plot. Since the Tauc plot is frequently used in literature to determine the optical band gap, and the Adachi oscillator cannot take into account the effects of disordered, polycrystalline materials, it will also be used in this work to determine the optical band gap energy of the deposited films. This ensures comparability to the literature values.

3.4 Structural Measurements

3.4.1 X-Ray Diffraction

One of the main tools for the structural characterization of the samples in this investigation was X-ray diffraction (XRD). Due to their small wavelengths, X-rays can, according to the Rayleigh criterion, be used to analyse structures in the range of Ångströms. The X-ray diffraction is therefore suitable to analyse the crystalline quality, the crystallographic phases, and the lattice spacings in non-amorphous samples. A very detailed discussion of the technique, the working principle, and the basic phenomena can be found in Reference 142.

The method is based on the diffraction of X-rays at the lattice planes of the crystal. In a very simple model, this can be described by the Bragg equation

$$m\lambda = 2d \sin\theta, \tag{3.16}$$

where λ is the wavelength of the X-rays, d is the spacing of the corresponding lattice planes, θ is the diffraction angle, and m is an integer denoting the order of diffraction. Figure 3.5 on page 53 shows the principal setup for the X-ray diffraction.

In an ideal situation, the peaks observed in the diffractogram would be almost infinitely narrow. However, the peaks are shifted and broadened by various effects. A peak shift is observed if the lattice

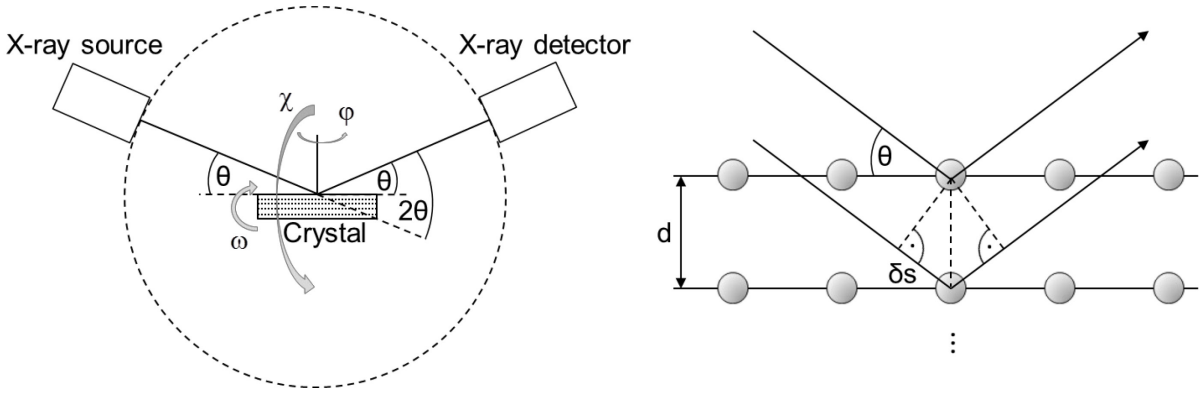

Figure 3.5: Schematic representation of the XRD setup (*left*) and the geometry for the X-ray diffraction at the atomic layers (*right*).

plane distance is changed homogeneously throughout the sample compared to a reference value. This may be due to stress in the films. Furthermore, if alloys are considered, the peak of the alloy is shifted with respect to the peaks of the single materials in correlation to the composition of the alloy. The broadening of the peaks can be symmetric or asymmetric with respect to the peak centre. The line width of the CuK_α radiation, the receiving slit, and any residual deficiency in focus give rise to symmetrical broadening, while deviations from the flat specimen surface, the axial divergence, and the transparency of the specimen produce asymmetrical line broadening. Additional broadening occurs for specimens containing structural defects.

The analysis of the diffraction data is usually performed by fitting the peaks in the diffraction patterns. To this end, different peak shape functions have been introduced. The most commonly used function is the pseudo-Voigt function, which is a weighted sum of a Gaussian and a Lorentzian line profile with the same full width at half maximum H (see Reference 143)

$$I_{\mathrm{pV}}(2\theta,\eta,H) = \eta L(2\theta,H) + (1-\eta)G(2\theta,H) = \\ = \eta \frac{\frac{2}{\pi H}}{1+\frac{4}{H^2}(2\theta-2\theta_0)^2} + (1-\eta)\frac{2}{H}\sqrt{\frac{\ln(2)}{\pi}}e^{-\frac{4\ln(2)}{H^2}(2\theta-2\theta_0)}. \tag{3.17}$$

Due to the instrumental broadening, even a diffractogram of an ideal single crystal would exhibit a certain peak width. Since this peak width is convoluted with the line broadening of the measured sample, it is necessary to determine the instrumental broadening and remove it from the measured line width of the sample. For this purpose, first the Gaussian and Lorentzian contributions to the instrumental broadening $H_{\mathrm{G,i}}$ and $H_{\mathrm{L,i}}$, respectively, are specified by the peak width of a reference material (usually LaB_6) with sufficiently large crystallites (~µm). Subsequently, the deconvolution of the peaks is performed as follows: according to the mathematical theory of convolution, the square of the breadth of two convoluted Gaussian functions can be calculated as the sum of the squares of the breadths of the contributing peaks (see for example Reference 142 page 635)

$$H_{\mathrm{G,m}}^2 = H_{\mathrm{G,s}}^2 + H_{\mathrm{G,i}}^2, \tag{3.18}$$

where $H_{\mathrm{G,m}}$ is the measured full width at half maximum of the peak and $H_{\mathrm{G,s}}$ is the breadth induced by the sample. For the Lorentzian part, it is simply the sum of the widths of the two contributing peaks

$$H_{\mathrm{L,m}} = H_{\mathrm{L,s}} + H_{\mathrm{L,i}}. \tag{3.19}$$

Together with the breadth of the measured peak and the results from the reference measurement for the instrumental broadening, the width of the sample peak H_{s} corrected for the instrumental broadening

can then be determined by the use of the following approximation for the full width at half maximum of the pseudo-Voigt peak[143]

$$H_s = (H_{G,s}^5 + 2.69269 H_{G,s}^4 H_{L,s} + 2.42843 H_{G,s}^3 H_{L,s}^2 + 4.47163 H_{G,s}^2 H_{L,s}^3 + 0.07842 H_{G,s} H_{L,s}^4 + H_{L,s})^{\frac{1}{5}}. \quad (3.20)$$

The integral breadth β, a value which is obtained as the width of a rectangle covering the same area as the peak and having the same height as the peak maximum, follows from the full width at half maximum H through[144]

$$\beta_{pV} = \frac{\frac{\pi H}{2}}{\eta + (1-\eta)\sqrt{\pi \ln(2)}}. \quad (3.21)$$

A quantification of the line broadening due to a finite crystallite size has first been proposed by Scherrer[145]. He calculated the crystallite size according to[146]

$$d_{cryst} = K\varepsilon = \frac{K\lambda}{\beta \cos(\theta)}, \quad (3.22)$$

where ε is the apparent crystallite size, d_{cryst} is the 'true' size, defined as the cube root of the crystallite volume, K is a dimensionless number in the order of unity known as the Scherrer constant, λ is the wavelength of the radiation, β is line broadening (in radians), and θ is the Bragg angle. In this case, it is assumed that the line broadening is only caused by the finite size of the crystals. However, there can also be strain in the films, which manifests in locally changing unit cell parameters and hence also in a broadening of the X-ray peak. To separate these effects, the different scattering angle dependences of these two broadening mechanisms are usually exploited in a Williamson-Hall plot. Unfortunately, this method is not applicable for the films investigated here because of their texture (see Chapter 4), which strongly limits the number of detectable peaks. Another method has been proposed by de Keijser[147], who argued that the finite crystallite size preferentially leads to a broadening with a Lorentzian peak shape and that the strain preferentially leads to a broadening with a Gaussian peak shape. But these assumptions are not well justified and the errors arising due to this method of interpretation are not clear. Therefore, in this work, the broadening by strain will be neglected and the crystallite size will be determined by the equation proposed by Scherrer using $K = 1$.

The X-ray diffraction analysis has also been employed to determine in-plane orientational relationships between substrates and epitaxially grown films. For this purpose, the diffractometer must be equipped with an Eulerian cradle, which allows for the positioning of the sample with arbitrary values of the angles θ, 2θ, χ, and φ. For the measurement, the crystalline film is oriented such that the Bragg condition is fulfilled for a plane that is not parallel to the substrate surface (see Figure 3.6).

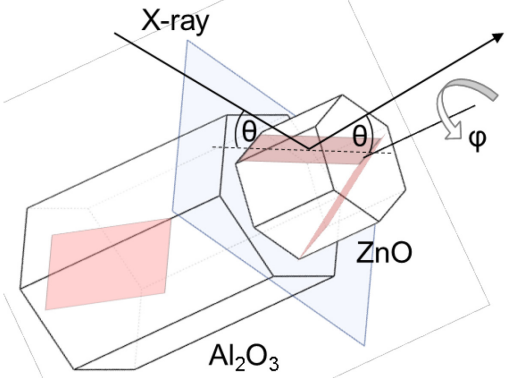

Figure 3.6: Schematic representation of the setup for the φ-scans to determine the in-plane orientation of single crystals. The hexagonal unit cells of the ZnO film and the Al_2O_3 substrate are shown. Examples of the $\{10\bar{1}1\}$ lattice plane family of the ZnO and the $\{20\bar{2}2\}$ lattice plane family of the c-sapphire substrate are marked. The plane between the ZnO and Al_2O_3 marks the substrate surface.

This can for example be the $(10\bar{1}1)$ plane of ZnO. Subsequently, a 360° φ-scan is performed. As the crystal is rotated around the axis perpendicular to the substrate surface, 6 peaks corresponding to the 6 equivalent planes of the $\{10\bar{1}1\}$ lattice plane family of ZnO will appear. Two of these planes are indicated in Figure 3.6. The same measurement is done for the c-sapphire substrate with the $\{20\bar{2}2\}$ lattice plane family. Finally, a comparison of the positions of the peaks in the two φ-scans reveals the in-plane orientational relationship between the epitaxial film and the single crystalline substrate. The orientational relationship of the films prepared on a-sapphire has been determined by performing a φ-scan of the $\{11\bar{2}3\}$ peak family of the substrate and the $\{10\bar{1}1\}$ peak family of the film. For the ZnO:Al films grown on the r-sapphire, the ZnO $\{21\bar{3}0\}$ peak family as well as the Al_2O_3 $\{20\bar{2}2\}$ peak family were used.

In order to determine the crystalline quality of the epitaxially grown films, rocking curve measurements were performed. To measure the rocking curve, the angle θ and the corresponding detector position 2θ were set to the Bragg angle of the plane parallel to the film surface. Subsequently, the sample orientation was varied by an angle Δω around its equilibrium position (see Figure 3.5 on page 53) while keeping the detector angle constant. The width of the resulting rocking curve is then assigned as a measure of the quality of the epitaxial growth.

To measure the θ-2θ scans of the heteroepitaxial and polycrystalline films, a PANalytical X'Pert Pro MPD using the Bragg-Brentano geometry and a tube voltage and current of 40 kV and 30 mA, respectively, was applied. The system had a 1D-detector ('PIXcel', PANalytical, Almelo, Netherlands) with an angular resolution in the range of the step size and no monochromator. A step size of 0.013° 2θ for a range from 25° to 80° 2θ and an integration time of 100 s per angular position resulted in a measurement time of 30 min for one spectrum. The XRD patterns were analyzed with the program Fullprof[148]. X-ray diffraction rocking curve measurements were performed with a Siemens D500 diffractometer for the heteroepitaxial and polycrystalline films and with a PANalytical X'Pert Pro MRD instrument equipped with a single crystal monochromator for the homoepitaxially grown films using the (0002) and $(11\bar{2}0)$ peaks of ZnO. To determine the in-plane orientation of the ZnO films, φ-scans have been performed with the Siemens D500, which was equipped with an Eulerian cradle. The θ-2θ scans of the homoepitaxial films were carried out with the PANalytical X'Pert Pro MRD. All X-ray instruments used CuK_α radiation.

3.4.2 Transmission Electron Microscopy

In transmission electron microscopy (TEM), a beam of electrons traversing the specimen is used to image the sample. The electrons have energies typically in the range of 80 keV to 400 keV, which allows to resolve features in the sample of sub-nm size. The principle of imaging is very similar to that of an optical microscope, but the lenses are electro or magnetostatic fields, the 'light' source is an electron gun, and the image plane is a fluorescent screen. A detailed description of the working principle, the limitations, and the parts of a transmission electron microscope can be found in Reference 149. A simplified model of the beam path in the transmission electron microscope used for this investigation is depicted in Figure 3.7 on page 56.

For the transmission electron microscopy investigation, a Carl Zeiss LIBRA 200FE microscope was employed. The electron source is a field emission gun operated at 200 kV. The 3 lens condensor system allows for a parallel and homogeneous illumination of the specimen. The system is equipped with an in-column energy filter, and for the imaging, a 2048 x 2048 pixel CCD camera (CCD: charge-coupled device) or a fluorescent screen is available. The electrons were usually zero-loss energy filtered to improve the contrast of the images.

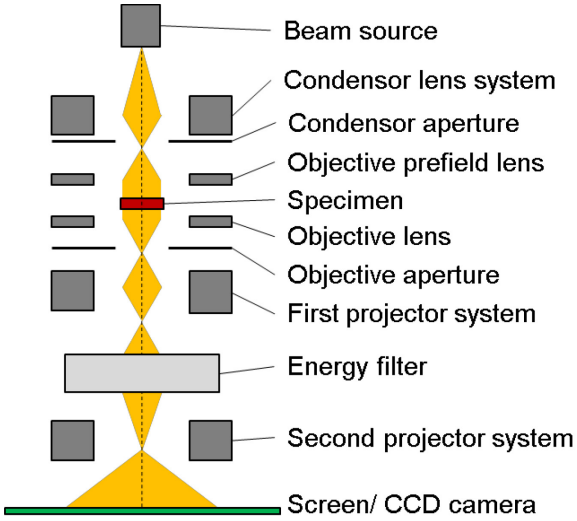

Figure 3.7: Schematic representation of the basic parts of the Carl Zeiss LIBRA 200FE transmission electron microscope with an integrated energy filter after Reference 150. The beam path is shown for parallel illumination in the TEM mode.

Additionally, the system is endued with an energy dispersive X-ray spectroscopy (EDX) setup by Thermo Fischer. For EDX measurements, the monochromatic electron beam excites the atoms in the specimen, which then emit X-rays with an energy characteristic for the different elements. This way, the composition of the sample can be determined locally resolved with a spot size of the beam below 1 nm. To analyse the spectra, the software NCC 2.2 (Thermo Fischer scientific, Waltham, Massachusetts, USA) was used.

The preparation of electron transparent cross sections of the films was performed by Ulrike Bloeck and Dr. Mythili Rengachari. It is realized the following way: first, the sample is cut and a sandwich of two film-and-substrate stacks is prepared with the help of a carbon-based epoxy glue. This sandwich is cut into smaller pieces, which are then mechanically thinned on both sides to a thickness of 5 µm to 10 µm. Afterwards, an ion milling process is applied, where the layer stack is bombarded with Ar^+ ions (5 kV, 2.5 mA) to reduce the thickness of the specimen to a few ten nm.

3.4.3 Scanning Electron Microscopy

In addition to the transmission electron microscopy investigations, cross sections of selected samples were examined by scanning electron microscopy. In scanning electron microscopy, a focussed electron beam is scanned over the specimen. In contrast to the transmission electron microscope, the backscattered or secondary electrons are used for the imaging and the acceleration voltages are smaller.

The cross sections have been prepared simply by breaking the samples. Beyond that, no special sample preparation was necessary.[149] The measurements were performed by Jonas Schulte and Man Nie with a LEO GEMINI 1530 operated with an accelerating voltage of 7 kV and a 60 µm aperture. The working distance was in the range of 3 mm to 4 mm, and an in-lens detector, arranged rotationally symmetric around the optical axis to detect the secondary electrons, has been applied.

3.4.4 X-ray Absorption Spectroscopy

For X-ray absorption spectroscopy (XAS) measurements, a monochromatic beam is directed onto the specimen and the absorption of the X-rays, or a signal proportional to that, is measured as a function of the energy (see Figure 3.8 on page 57). A more elaborated and detailed discussion of the basic principles of X-ray absorption spectroscopy than the following can be found for example in References 151 and 152.

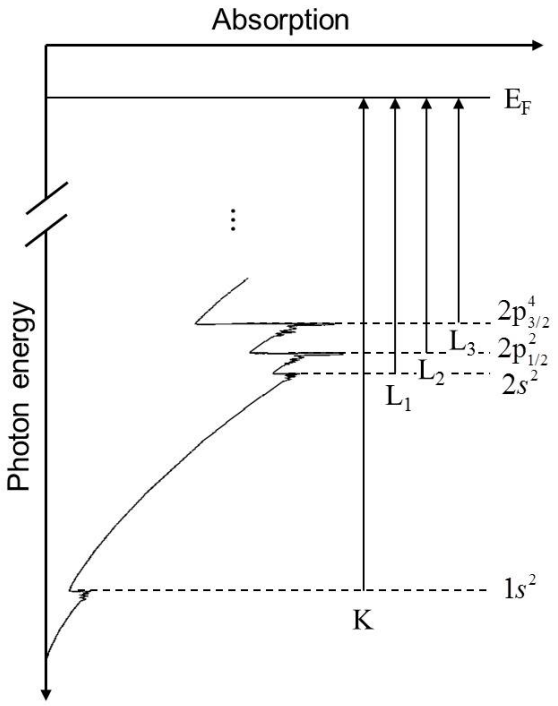

Figure 3.8: Schematic representation of the absorption coefficient as a function of the incident photon energy. Also shown is the relationship between the X-ray absorption edges (K, L_1, L_2, L_3) and the corresponding excitation of core electrons from the different core levels ($1s^2$, $2s^2$, $2p_{1/2}{}^2$, $2p_{3/4}{}^4$). The arrows show the threshold energy difference of the edges and E_F denotes the Fermi energy. The figure is adapted from Reference 152.

Most striking in Figure 3.8 is the step-like increase of the absorption at certain energies, called edges. These energies are characteristic for the different elements and reflect the excitation energy of inner-shell electrons. Hence, the absorption edge is related to a specific type of atoms present in the material and to a quantum-mechanical transition that excites particular atomic core-orbital electrons to free or unoccupied continuum levels.[152] The region between the edge and approximately 30 eV above the edge is called the X-ray absorption near edge fine structure (XANES) region, and the edge structures for energies beyond that value are the extended X-ray absorption fine structures (EXAFS). The XANES region can be used to obtain information about the formal oxidation state and the coordination chemistry, while the EXAFS region provides information about distances, coordination numbers, and the species of the neighbours of the absorbing atom. The information is contained in the characteristic features of the absorption edges, which are caused by the scattering of the photo-electron waves at the neighbouring atoms and the subsequent constructive or destructive interference with the photo-electron wave function at the absorbing atom. The two main mechanisms for the decay of the excited electrons are X-ray fluorescence and the Auger effect. Hence, these two effects yield signals, which are proportional to the absorption and can also be used for the X-ray absorption spectroscopy.

The XAS measurements were performed at the Synchrotron BESSY II in Berlin. The 'optics beamline' provided an energy range from roughly 20 eV to 2000 eV, allowing to investigate the Zn-L edge (L_3: 1022 eV), the Al-K edge (1560 eV), the Mg-K edge (1303 eV), and the O-K edge (543 eV).[153] The beamline is equipped with a plane-grating monochromator and optics with an energy resolution in the range of 0.5 eV for low energies (O-K edge) and 1.5 eV for higher energies (Al-K edge). At the sample, the X-ray beam is focused to a horizontal beam width of 300 µm. The measured signals were the partial fluorescence yield, detected by a Bruker XFlash 5010 fluorescence detector, and the total electron yield, measured as the sample drain current. The samples have been prepared on glassy carbon (Sigradur, HTW Hochtemperatur-Werkstoffe GmbH, Thierhaupten, Germany) to ensure a good electrical contact to the ground for the total electron yield measurement. The chamber is equipped with a load lock and the measurements were carried out under ultra-high vacuum conditions ($p < 5 \cdot 10^{-10}$ mbar).

3.4.5 Atom Probe Tomography

Atom probe tomography allows for a chemical analysis of the specimen on a nearly atomic scale. Individual atoms are removed from a tip-shaped sample by field evaporation, and subsequently the time of flight as well as the impact position on the detector are determined. From this data, the chemical species of the atoms and their geometric origin within the specimen can be inferred. A more detailed description of the atom probe technique for the analysis of thin films can for example be found in Reference 154. In this work, the atom probe tomography was used to investigate the spatial distribution of the dopant Al in a selected ZnO:Al film.

The ZnO:Al film has been deposited on a sharpened Mo tip without intentional heating using the same deposition conditions described earlier. Afterwards, 3D laser-assisted wide angle atom probe tomography (APT) measurements and the analysis of the raw data have been carried out by Dr. Nelia Wanderka in a local electrode APT built at the University of Münster. Details of the setup can be found in Reference 155. The field evaporation was realized with fs-pulses of a UV laser (λ = 343 nm, 200 kHz, 30 nJ/pulse) and the experimental parameters were set to maintain a detection rate of 0.02 to 0.04 ions per pulse. The measurements were performed in vacuum at a pressure below $p = 10^{-8}$ mbar, and the temperature of the tip was kept at 46 K. The raw data was analysed using the 3D data software developed by the Material Physics group at the University of Rouen.

3.4.6 Atomic Force Microscopy

The atomic force microscopy (AFM) is based on the determination of the forces between a sharp tip and the sample surface. The imaging is realized by measuring the interaction force through the deflection of a cantilever while scanning the tip over the surface of the sample. The signal is essentially based on interatomic repulsive forces of short-range nature and can be used to map the topography of the surface down to atomic dimensions. Basically, there are two modes of operation: In the static mode, the tip is very close to the surface and the static tip deflection is used as a feedback signal (also called contact mode). In the dynamic mode, the tip is oscillating at or close to its resonance frequency and the oscillating amplitude or frequency is used as a feedback signal, which is either influenced by long range forces (non-contact mode) or repulsive forces (tapping mode), depending on the distance between the sample surface and the tip. References 156 and 157 provide more information on the basic principles, the instrumentation, and the applications of atomic force microscopy.

The atomic force microscopy measurements were performed by Man Nie using an XE-100 AFM by Park Systems operated in the tapping mode with an etched Si tip with a tip radius around 10 nm and a force constant of 40 N/m. The data was analysed using the XEI software Version 1.7.6 supplied by the manufacturer of the AFM.

3.5 Other Techniques

3.5.1 Rutherford Backscattering Spectrometry

In Rutherford backscattering spectrometry (RBS), the amount and the energy of ions backscattered from a specimen is detected. The energy transfer from the projectile to the target atom can be calculated from collision kinematics. This provides information about the mass of the target atom. The probability of elastic collision can be calculated as well (scattering cross section) and allows for a

quantitative analysis of the atomic composition. The energy loss in a medium through inelastic interaction $S = -1/N \cdot dE/dx$, where S is the stopping cross section and N is the atomic density of the material, can also be treated and leads to the perception of depth. A more detailed survey of the basic concepts of RBS can be found in Reference 158. Figure 3.9 shows a typical RBS spectrum of a ZnO:Al layer on a carbon substrate.

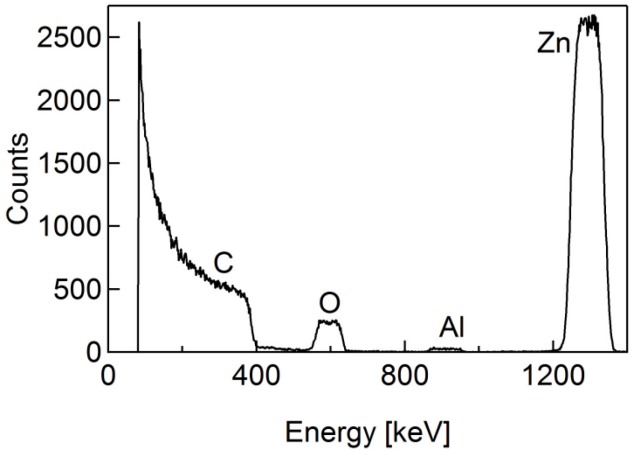

Figure 3.9: Rutherford backscattering spectrometry raw data obtained from a ZnO:Al film deposited at 300 °C. The measurement was performed at room temperature.

When the projectile, typically a He ion with an energy of some MeV, is backscattered from an atom at the surface of the film, it retains the energy $E_1 = k \cdot E_0$ and can be detected under a certain angle (E_0 is the initial energy of the projectile). The kinematic factor k depends on the mass of the projectile and the target atom as well as the scattering angle. Hence, the energy of the backscattered ion determines the type of the target atom from which it has been backscattered via the mass of the target atom. This defines the position of the peaks in the spectrum. If the projectile is not backscattered at the surface of the specimen but in a certain depth, it lost energy through inelastic interaction while travelling into the material and out of the material. Therefore, the energy will be lower in comparison to that of a projectile which has been backscattered at the surface. This explains the width of the peaks. The maximal peak width is then caused by the maximal depth/film thickness that limits the energy loss induced by travelling through the material. Eventually, the different heights of the peaks can be attributed to the distinct scattering cross sections that determine, together with the composition of the films, the probability of the scattering of the projectile at a certain target atom and hence the amount of backscattered ions.

The Rutherford backscattering spectrometry measurements were performed at an accelerator available at the 'Helmholtz-Zentrum Dresden-Rossendorf' using 1.7 MeV He ions at an incidence and scattering angle of 0° and 170°, respectively. The ions have been accelerated by an energy stabilized van-de-Graaff accelerator. The resolution of the Si surface barrier detector by Canberra was in the range of 15 keV and the charge collected with the detector, covering a solid angle of 3.18 msr, was 10 µC. For the RBS analysis, the films were deposited on glassy carbon (Sigradur) substrates to reduce the backscattering background. The analysis of the data was performed using the software SIMNRA version 6 by Dr. Matej Mayer from the 'Max-Planck-Institut für Plasmaphysik' in Garching, Germany.

3.5.2 Secondary Ion Mass Spectrometry

Secondary ion mass spectrometry (SIMS) has been employed to determine the absolute amount of hydrogen in the films, which could not be detected by RBS. For secondary ion mass spectrometry, the specimen is bombarded by ions with an energy in the range of 1 keV to 25 keV. The sputtered

secondary ions are then analysed with respect to their mass/charge ratio with a mass spectrometer, which allows to determine the elemental composition of the sample. Because of the erosion of the film due to the sputtering, a depth resolved signal is obtained. A detailed discussion of the secondary ion mass spectrometry has for example been performed by Arlinghaus and Hutter (see Reference 159 pages 86 to 121).

The SIMS measurements of the hydrogen content of the films have been realized by the company RTG Mikroanalyse GmbH in Berlin with a Cameca ims4f system using a primary ion beam of 14.5 keV Cs^+. In order to get rid of the high hydrogen background in the vacuum system of the SIMS apparatus, these samples were prepared with deuterium instead of hydrogen, where deuterium is expected to behave chemically in the same way as hydrogen. The absolute deuterium concentration was calibrated with ZnO:Al and $Zn_{1-x}Mg_xO$:Al films, implanted by deuterium with a dose of $1 \cdot 10^{15}$ cm^{-2}.

3.5.3 Plasma Process Monitoring

Characteristic properties of the species in the plasma were determined by plasma process monitor (PPM) measurements. The measurements were performed by Dr. Thomas Welzel with an energy-dispersive quadrupole ion mass spectrometer (Balzers PPM 422). The principal setup of the mass spectrometer is shown in Figure 3.10.

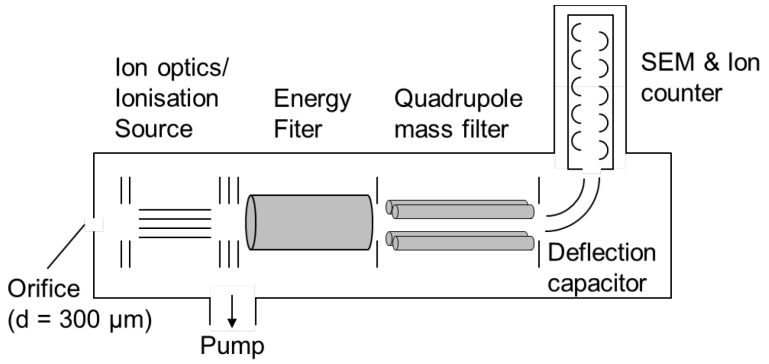

Figure 3.10: Schematic representation of the energy-dispersive quadrupole mass spectrometer Balzers PPM 422 for the plasma process monitor measurements. The figure is adapted from Reference 160.

The mass filter allows to detect specific types of ions, and the energy filter enables to investigate their energy distribution. The Balzers PPM 422 has a mass per charge number range from m/z = 1 u to 500 u and an energy range up to 500 eV. Directly after the films were deposited, the magnetron was rotated by 180° so that the PPM was placed opposite the magnetron target at a distance of 60 mm with its entrance orifice facing the target. Ion energy spectra were then measured radially resolved with 5 mm steps by moving the magnetron on a linear feedthrough (see Figure 3.1). The front electrode of the PPM with a 300 µm orifice was kept at floating potential. To Take into account the different focussing of the ions onto the instrument axis when entering the PPM, the energy spectra were multiplied by the square root of the ion energy to obtain the ion energy distribution functions (IEDFs).[160]

4. Growth of Zinc Oxide Thin Films

ZnO films can be grown by a great variety of deposition techniques such as metal-organic chemical vapour deposition (MOCVD),[161] spray pyrolysis,[162] reactive evaporation, arc-evaporation,[163] pulsed laser deposition (PLD),[164] or (reactive) magnetron sputtering.[9] These techniques have different advantages and disadvantages. In chemical vapour deposition and evaporation processes, for example, the species contributing to the film growth have only thermal energies, which means they will cause no damage to the growing film. The lowest resistivities, on the other hand, are usually obtained by plasma assisted processes like PLD or sputtering.[22] The main difference between the plasma assisted processes and the methods, where the species are thermally excited, is the much higher energy input into the film for ion-assisted processes. Especially for magnetron sputtered films, this leads to compact films with a good homogeneity even at low deposition temperatures.[113] Hence, the growth of the films and the resulting crystalline quality strongly depend on the method used for the deposition.[13] Moreover, they are influenced by the deposition parameters, such as the substrate type,[165] the deposition temperature and pressure,[166] the process gas type,[113] the substrate-to-target distance, the sputtering power, and the target voltage for magnetron sputtering alone. These parameters do not only influence the structural quality, but also the closely related electronic transport properties. It is therefore necessary to understand the relation between the deposition parameters and the resulting structural properties of the grown films. Furthermore, the dependence of the structural properties on the deposition parameters can be used to tailor the characteristics of the films. In this chapter, the crystalline quality of polycrystalline, heteroepitaxial, and homoepitaxial films prepared on different substrates using different deposition temperatures will be presented. These structural properties are a basis for the discussion of the charge carrier transport in the following chapter, where the lateral grain size, dislocation densities, or other values characterizing the crystalline quality are required to substantiate the theoretical models.

Results, presented in this chapter, have partly been published already in Reference [D] from the list in the appendix.

4.1 Polycrystalline Films

ZnO films deposited by magnetron sputtering on amorphous substrates or single crystalline substrates with an incommensurate interface fitting are polycrystalline, which means they exhibit crystals of varying size and orientation.[9] In the following, the results of the characterization of these polycrystalline films by means of electron microscopy, X-ray diffraction, and optical measurements will be presented.

4.1.1 Results of Electron Microscopy Measurements

Figure 4.1 on page 62 exemplarily shows transmission electron and scanning electron micrographs of ZnO:Al and $Zn_{1-x}Mg_xO$:Al films ($x \approx 0.12$) deposited on Si substrates at 300 °C.

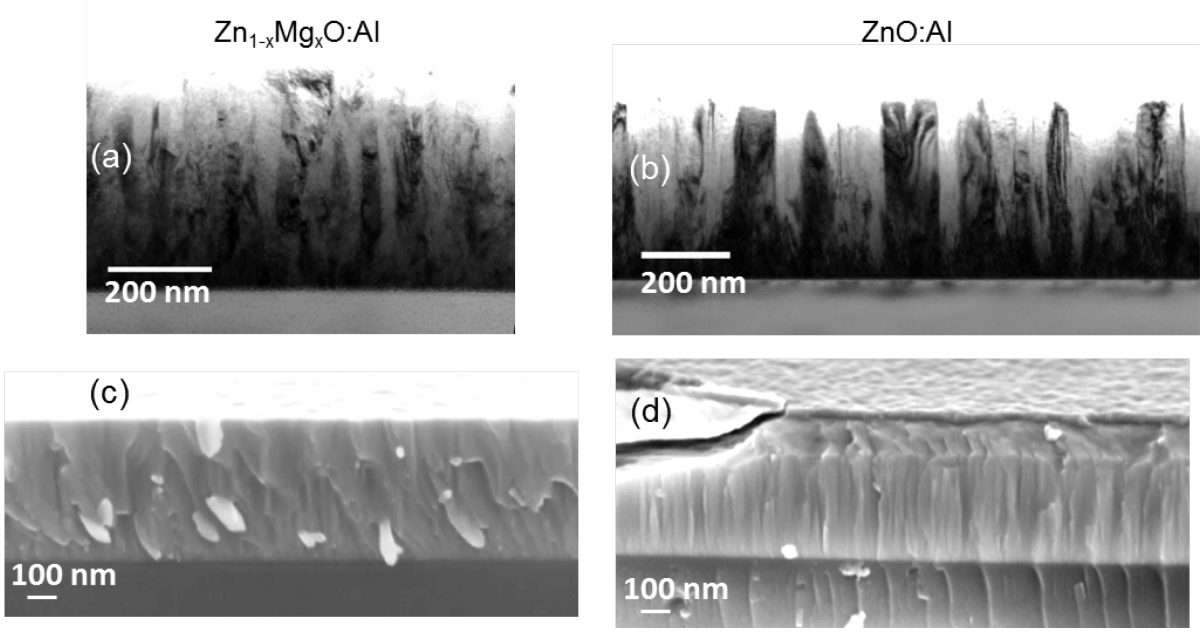

Figure 4.1: Transmission electron micrographs of the cross sections of a $Zn_{1-x}Mg_xO$:Al ($x \approx 0.12$) (a) and a ZnO:Al (b) film prepared at 300 °C on Si substrates. The images are zero-loss energy filtered and show only the unscattered electrons. (c) and (d) present scanning electron microscopy images of cross sections of the $Zn_{1-x}Mg_xO$:Al and the ZnO:Al film, respectively.

The grains are clearly distinguishable by the varying brightness, which is caused by an object aperture that filters out the scattered electrons. Hence, if the Bragg condition is fulfilled for a certain crystal, it appears dark, while it is bright if the electron has not been scattered. In the transmission electron micrographs, the changing contrast within the grains also indicates that the bulk of the grains is disturbed by crystallographic defects and strain. Comparing Figure 4.1 (a) and (b), the brightness in the $Zn_{1-x}Mg_xO$:Al films is changing on a much smaller length scale in comparison to the ZnO:Al films where whole grains fulfil the Bragg condition. This points to a lower structural quality of the $Zn_{1-x}Mg_xO$:Al films. In general, the films exhibit a columnar growth, which has been reported for magnetron sputtered ZnO by many authors (see for example References 113 and 167-169). This columnar growth is more pronounced in the ZnO:Al films in comparison to the $Zn_{1-x}Mg_xO$:Al films as can be inferred from both, the TEM and the SEM images. In fact, the columns have a width ranging from 50 nm to 150 nm for the ZnO:Al films and from 30 nm to 100 nm for the $Zn_{1-x}Mg_xO$:Al films. In outline, also a narrower width of the columns is observed in the interface region to the substrate, which means their width is slightly depth dependent. This is due to the formation of many nuclei, which lead to a fine-crystalline structure in the early stages of the film growth. Later, only the fastest growing crystallites remain and form larger crystals. Therefore, the crystallites have a conical shape.

Other plasma assisted processes induce the pronounced c-axis texture as well. Furthermore, also for thermally activated deposition methods like CVD, conditions have been found, which result in polycrystalline films with a columnar growth in a preferred orientation.[170] Generally, limited adatom diffusion and shadowing are assumed to be responsible for the columnar growth.[171,172] For magnetron sputtering, it is also possible to suppress this preferred orientation, for example by energetic oxygen bombardment as it was reported by Tominaga et al.[173].

4.1.2 Results of XRD Measurements

Since TEM cannot be used as a standard method to specify the crystalline quality due to the required effort for sample preparation, the crystalline quality has to be determined with a simpler technique, for instance with X-ray diffraction. With the 1-D X-ray detectors available today, a full diffractogram of

good quality can be measured within less than 30 min, which allows to examine a much larger number of samples. Figure 4.2 shows the diffractograms for a ZnO:Al and a $Zn_{1-x}Mg_xO$:Al film deposited under conditions comparable to those of the samples shown in Figure 4.1 (300 °C substrate temperature).

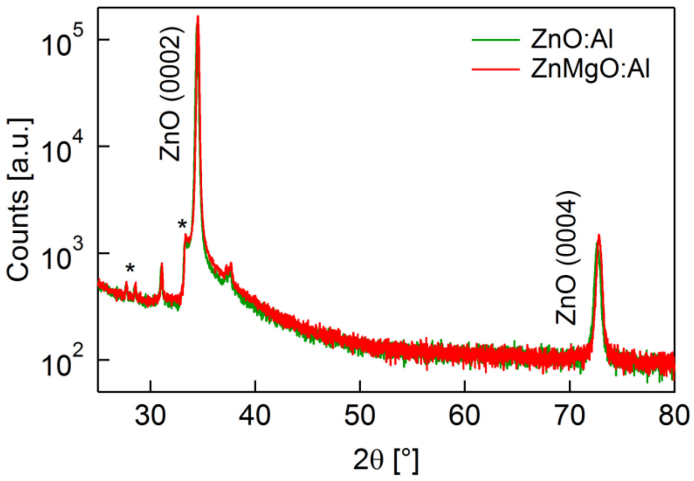

Figure 4.2: X-ray diffractograms of a ZnO:Al (green line) and a $Zn_{1-x}Mg_xO$:Al (red line) film prepared at 300 °C. The strongest peaks belong to the {0002} peak family. Because of a degradation of the X-ray source, also peaks from W-L_α lines are visible (*). The peaks at 31° correspond to the Cu-K_β lines and the peaks at 37° are caused by the Ni filter.

The XRD patterns only show peaks of the {0002} peak family of hexagonal ZnO (see JCPDS 36-1451), which is a result of the pronounced (0001) orientation of the lattice planes, because in contrast to a powder, where the crystallites have statistically distributed orientations, the crystals in the films are preferentially oriented with their c-axis perpendicular to the substrate surface. Therefore, the Bragg condition cannot be fulfilled for other lattice planes when using the symmetrical Bragg-Brentano geometry. Besides, due to the preferred orientation, measurements under grazing incidence, usually used to increase the signal intensity when measuring thin films by increasing the illuminated volume, cannot improve the signal quality of the films investigated here. On the contrary, the intensity is decreased when using grazing incidence, because the number of crystallites oriented with a shallow angle relative to the substrate surface is small, which can be attributed to the above mentioned film texture.

As already pointed out in Section 3.4.1, the line broadening due to the finite crystallite size cannot reliably be separated from the line broadening caused by strain due to the preferred orientation of the crystallites. Assuming only broadening owing to the finite crystallite size and using the equation derived by Scherrer[145] to determine the size of the crystallites from the corrected integral peak width, a crystallite size of (55 ± 5) nm and (67 ± 7) nm is determined for the ZnO:Al and the $Zn_{1-x}Mg_xO$:Al films shown in Figure 4.1 and Figure 4.2, respectively. These values derived from the (0002) peak of the X-ray diffraction patterns refer to a crystallite size parallel to the c-axis. Therefore, this size corresponds to a vertical crystallite size in the films. A comparison between the vertical grain sizes, visible in the scanning electron micrograph, where the grains extend mainly from the bottom to the top of the roughly 500 nm thick film, and those determined by the X-ray diffraction, shows a clear difference. This is not surprising since the crystallite size represents a volume of coherent scattering of the X-rays in the material that is reduced by crystallographic defects, for instance stacking faults, dislocations, grain boundaries, or voids (see Reference 174 page 19). In scanning electron microscopy, on the other hand, the grains and not the defects inside the grains are visible.

While the θ-2θ scans proved a strong (0001) out-of-plane orientation of the ZnO:Al and the $Zn_{1-x}Mg_xO$:Al films, the φ-scans of the films prepared on amorphous substrates showed that the crystals have no in-plane orientation, which distinguishes them from epitaxially grown films. Their c-axis is perpendicular to the substrate, but the crystallites are randomly rotated within the film plane.

This means that there is no preferred orientation of the a-axis as can be inferred from the continuous intensity distribution measured during the φ-scan of the $\{10\bar{1}1\}$ lattice plane family. The orientational relationship and a representative φ-scan are depicted in Figure 4.3.

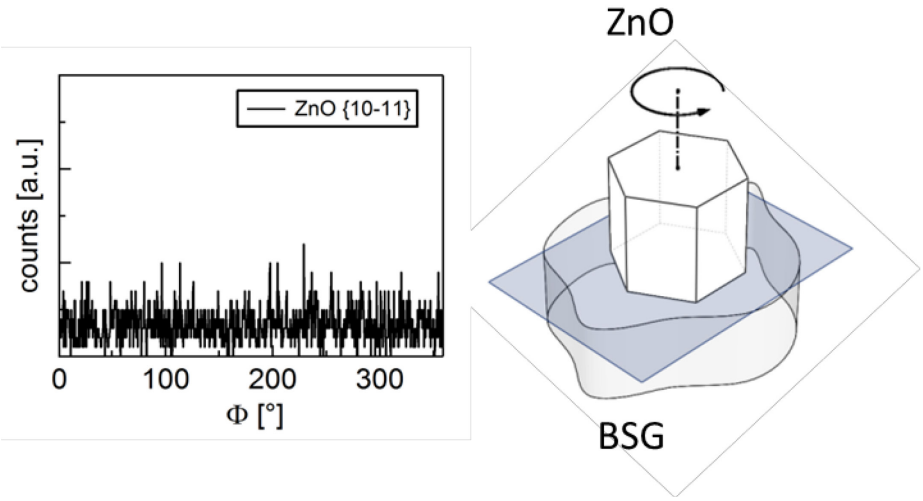

Figure 4.3: Representative φ-scan of a polycrystalline Al-doped ZnO film to determine the in-plane orientation (*left*) and a scheme of the orientational relationship between the substrate and the film (*right*). There is no in-plane orientation, which is denoted by the rotation of the crystallite around the c-axis.

Although rocking curve measurements are usually employed to determine the quality of the crystalline growth of epitaxial films, they were performed for the polycrystalline films for comparison as well. The parameter quantifying the quality of the crystalline growth is the width of the rocking curves. This value is mainly related to the dislocation density in the films, the finite size of the crystallites, and, if any, the tilt of the crystallites with respect to each other.[175] The results of the rocking curve measurements for the polycrystalline films are shown in Figure 4.4.

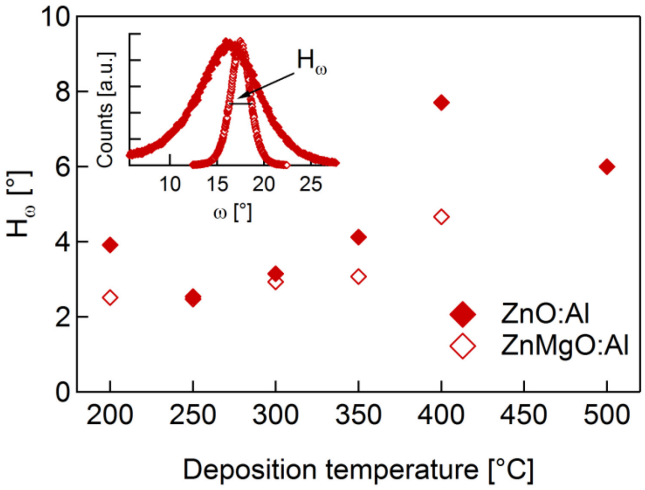

Figure 4.4: Rocking curve full width at half maximum H_ω for the polycrystalline ZnO:Al and $Zn_{1-x}Mg_xO$:Al films deposited at substrate temperatures between 200 °C and 500 °C. The rocking curves have been fitted using a Gaussian function. The inset exemplarily shows the narrowest and the widest measured rocking curve.

The full width at half maximum H_ω of the rocking curves of the polycrystalline films is in the range of 2.5° to 7.7°. The trend is basically the same for the ZnO:Al and $Zn_{1-x}Mg_xO$:Al films: There is a (slight) decrease of H_ω for deposition temperatures from 200 °C to 250 °C and an increase for higher deposition temperatures. In comparison to the ZnO:Al films, the $Zn_{1-x}Mg_xO$:Al films have a slightly lower H_ω, which points to a better orientation of the crystallites. A comparison to literature data is hardly possible, because the rocking curve measurements are mostly used to determine the structural properties of epitaxial films. At least, Kuppusami et al.[165] reported comparable values between 4° to 8° for their RF magnetron sputtered ZnO:Al films on glass substrates.

From the rocking curve half widths, the threading dislocation density of the ZnO films can be calculated. According to Ayers[175], the measured rocking curve full width at half maximum $H_{\omega,\mathrm{m}}$ can be approximated by

$$H^2_{\omega,\mathrm{m}}(hkl) = H^2_{\omega,\mathrm{L}}(hkl) + H^2_{\omega,\mathrm{i}}(hkl) + K_\alpha + K_\varepsilon \tan^2\theta \tag{4.1}$$

if the broadening due to specimen curvature and the intrinsic rocking curve width for the crystal is neglected. In this equation,

$$H^2_{\omega,\mathrm{L}} = \frac{4\ln(2)\lambda^2}{\pi L^2_\perp \cos^2\theta} \tag{4.2}$$

is the broadening caused by the finite crystallite size, $H_{\omega,\mathrm{i}}$ is the rocking curve broadening due to the instrument, and

$$\begin{aligned} K_\alpha &= 2\pi\ln(2) b^2 N_{\mathrm{disl}}, \\ K_\varepsilon &= 0.09 b^2 N_{\mathrm{disl}} \left|\ln(2\cdot 10^{-7}\,\mathrm{cm}\sqrt{N_{\mathrm{disl}}})\right| \end{aligned} \tag{4.3}$$

(for dislocations with screw character) are the angular broadenings due to the rotation at dislocations and the strain surrounding the dislocations, respectively. $L_\perp$ is the crystallite size perpendicular to the film surface (identified with the film thickness for the heteroepitaxial and polycrystalline films and the sample thickness for the homoepitaxial films), N_{disl} is the dislocation density, θ is the Bragg angle, b is the length of the Burgers vector, and λ is the wavelength of the X-rays. When $H_{\omega,\mathrm{L}}$ and $H_{\omega,\mathrm{i}}$ are subtracted from the measured broadening $H_{\omega,\mathrm{m}}$, the dislocation density can be determined by solving $K_\alpha + K_\varepsilon\tan^2\theta$ for N_{disl} iteratively. Similar to the works of Metzger et al.[176] and Chine et al.[177] on GaN, which is isostructural to ZnO, the c-axis lattice parameter is chosen as Burgers vector b_{ZnO} = 0.52066 nm for the calculation of the dislocation densities. The dislocation densities N_{disl} derived for the polycrystalline films are shown in Figure 4.5.

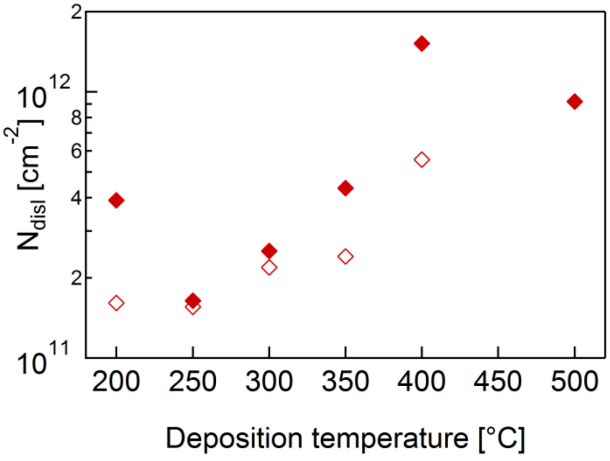

Figure 4.5: Threading dislocation densities N_{disl} determined from the rocking curves using Ayers[175] model.

The basic trend of the rocking curve half widths is reproduced for the dislocation densities, which are in the range of $1.6\cdot10^{11}$ cm^{-2} to $1.5\cdot10^{12}$ cm^{-2}. These values can be compared with only few literature data as well. Sagalowicz and Fox[178] reported dislocation densities in the order of 10^{12} cm^{-2} in their polycrystalline DC magnetron sputtered ZnO films. A more detailed interpretation of the dislocation densities will be performed together with the epitaxially grown films in Section 4.2.

4.1.3 Results of Optical Measurements

The disruption of the symmetry of the crystal, which is present for polycrystalline films due to grain boundaries and other crystallographic defects, splits degenerate electronic states into separate levels and leads to the formation of states in the band gap.[179,180] These states are referred to as Urbach tails and are detectable in optical absorption and emission spectra[180]. Usually, the band tail states are interpreted as a result of local disorder, but also fluctuations of the fundamental band gap, which can in principle occur on any length scale, give rise to tail-like absorption (see Reference 180 and references therein). In 1953, Urbach[181] introduced an empirical rule for the optical absorption coefficient α for electronic interband transitions in disordered solids. This rule can be expressed as

$$\alpha = \alpha_0 e^{\frac{h\nu}{E_U}}, \tag{4.4}$$

where α_0 is a proportionality constant and E_U is the Urbach energy, characterizing the slope of the exponential edge. Subsequent experimental studies showed that the Urbach absorption edge is a nearly universal property of disordered solids.[182] Figure 4.6 shows the Urbach plots of the polycrystalline ZnO:Al and $Zn_{1-x}Mg_xO$:Al films. The absorption coefficient α was determined using Equation (3.14).

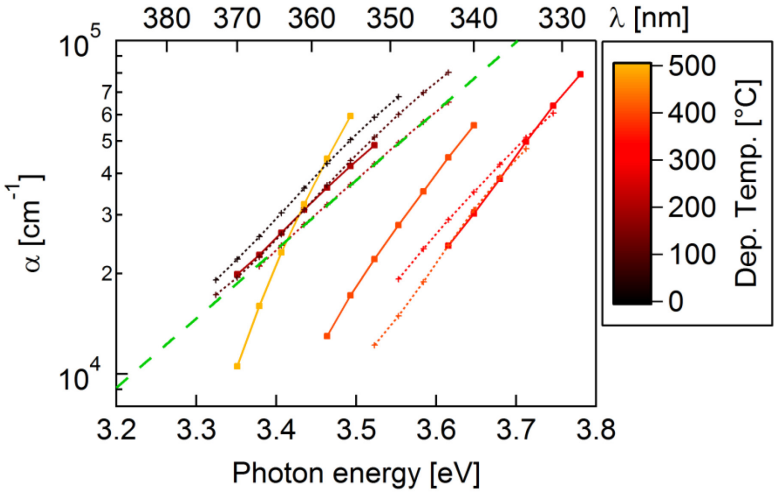

Figure 4.6: Urbach plots of ZnO:Al films (solid lines) and $Zn_{1-x}Mg_xO$:Al films (dotted lines) deposited at temperatures between ~30 °C and 500 °C as a function of the photon energy and the wavelength of the light. The dashed green line shows a fit to the data of the $Zn_{1-x}Mg_xO$:Al film deposited at 200 °C.

The logarithm of the absorption coefficient as a function of the energy of the light is not linear for all films. An interpretation with respect to the empirical Urbach rule is therefore less reliable for these films. Yet, a linear fit has been performed to the lower and higher end of these curves and the average of the two slopes has been assigned to the Urbach energy. The error is assumed to be one standard deviation from the average of these two values and hence higher in comparison to the errors of the samples for which only one line fit was necessary. The $Zn_{1-x}Mg_xO$:Al films for this measurement have been prepared on quartz glass under the same deposition conditions, because the Mg increases the band gap and shifts the absorption edge of the film into the region of the absorption edge of the borosilicate glass substrate, which makes an interpretation of the Urbach tails and the band gap energies impossible unless a substrate with a higher band gap energy is used, for instance quartz glass (fused silica). The results for the Urbach energies of the polycrystalline films are summarized in Table 4.1.

The Urbach energies of the ZnO:Al films are between 88 meV and 190 meV and hence slightly smaller compared to the values of the $Zn_{1-x}Mg_xO$:Al films, which are in the range of 135 meV to 207 meV. The higher Urbach energies of the $Zn_{1-x}Mg_xO$:Al films point to a higher local structural disorder. This is to be expected, since the introduction of the Mg introduces additional disorder. Generally, for both types of films, there is a distinct trend: At low deposition temperatures, the Urbach energy is rather high at values in the order of 200 meV, while for increasing deposition temperatures,

Table 4.1: Urbach energies of polycrystalline ZnO:Al and $Zn_{1-x}Mg_xO$:Al films determined by fitting Equation (4.4) to the absorption data. Some values are calculated by fitting this equation to the higher and lower end of the curves in Figure 4.6 to consider the nonlinear slope. The errors are then one standard deviation of the average of the two values obtained by the fit. For the other fits, the error represents the uncertainty of the single line fit.

	ZnO:Al	$Zn_{1-x}Mg_xO$:Al
T_{sub} [°C]	E_U [meV]	E_U [meV]
~30 °C		184 ± 8
100 °C		190 ± 12
200 °C	190 ± 10	207 ± 3
300 °C	143 ± 3	170 ± 15
400 °C	132 ± 8	135 ± 3
500 °C	88 ± 5	

the Urbach energies and therefore the local disorder decrease down to values in the range of 100 meV. This can be explained by an annealing out of defects caused by the deposition process, which will be discussed in detail in Chapter 6. Srikant and Clark[183] reported $E_U \approx 150$ meV for their as-deposited films prepared by pulsed laser deposition with 600 °C substrate temperature on fused silica. They were able to decrease the Urbach energy by approximately 40 meV due to an annealing at 800 °C, which they attributed to an annealing out of point defects as well. Dimova-Malinovska et al.[184] found Urbach energies of 100 meV, 120 meV, and 91 meV for deposition temperatures of 100 °C, 275 °C, and 500 °C, respectively, for their RF magnetron sputtered ZnO:Al films. These values are lower in comparison to the Urbach energies determined for the films investigated here, but they are in reasonable agreement and they follow the same trend with respect to the deposition temperature.

After having determined the properties, values, and parameters for the polycrystalline films, they can now be compared to the epitaxially grown ZnO:Al and $Zn_{1-x}Mg_xO$:Al layers.

4.2 Epitaxial Films

Epitaxial growth of ZnO films has already been reported in the 1960s. Rozgonyi and Polito[185], for example, grew ZnO films on sapphire substrates by DC sputtering and proved the epitaxial relation between the film and the substrate by reflection high-energy electron diffraction (RHEED). Although Rozgonyi and Polito accomplished the epitaxial growth using DC sputtering, the most common techniques to prepare epitaxial films nowadays are based on chemical vapour deposition, molecular beam epitaxy (MBE), or pulsed laser deposition.[186] Still, epitaxial films with a high structural quality can also be grown by magnetron sputtering. Kuppusami et al.[165], for example, reported heteroepitaxial growth on a-, c- and r-sapphire substrates with rocking curve full width at half maximum values as low as 0.8°. An even lower value (H_ω = 0.46°) was achieved by Matsubara and coworkers[187] for RF sputtered films on $LiNbO_3$ (0001) substrates. Moreover, homoepitaxial growth of ZnO by magnetron sputtering has been reported as well (see Reference 188 page 72). In general, however, only few of the vast number of papers on ZnO thin film growth by sputtering are dedicated to epitaxial growth.[189]

In this work, hetero- and homoepitaxial films have been deposited on a-sapphire $(11\bar{2}0)$, c-sapphire (0001), r-sapphire $(01\bar{1}2)$ and ZnO (0001) substrates at deposition temperatures ranging from 200 °C to 500 °C. The term homoepitaxial growth is, for simplicity, also used for the ZnO:Al and $Zn_{1-x}Mg_xO$:Al films, although there is a small lattice mismatch due to the Al and Mg in the films. In the following, the structural properties of the epitaxial films will be presented and compared to the polycrystalline films.

4.2.1 Results of TEM Measurements

Figure 4.7 shows transmission electron micrographs of ZnO:Al films grown either on a-sapphire or on a ZnO (0001) single crystal at 300 °C.

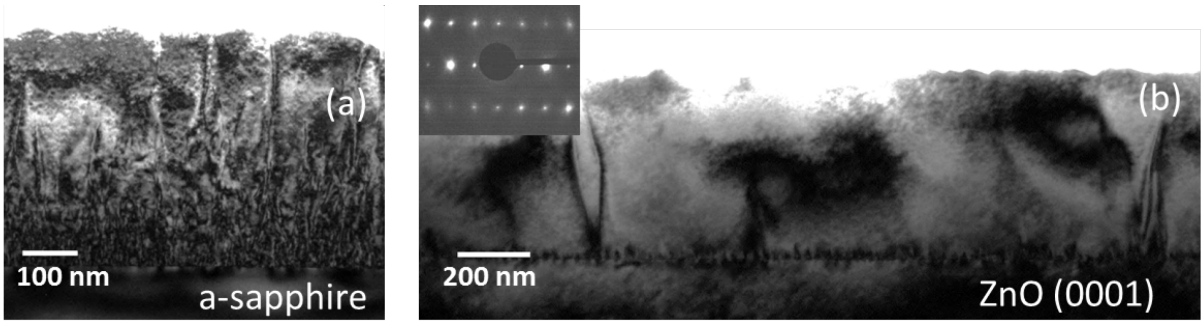

Figure 4.7: Transmission electron micrographs of the cross sections of a heteroepitaxial ZnO:Al film deposited on a-sapphire (a) and a homoepitaxial ZnO:Al film deposited on a ZnO (0001) single crystal (b), both prepared at 300 °C. The images were zero-loss energy filtered and show only the unscattered electrons. The inset in (b) shows the electron diffraction pattern of the homoepitaxial film.

For the heteroepitaxial film grown on the a-sapphire, a columnar growth is visible as well. However, not all of the structures in the film are grain boundaries, because (i) they end abruptly in the middle of the film and/or (ii) there is no change in brightness among the different columns. Additionally, there is again a higher density of defects in the lower part of the film, which can be inferred from the smaller distance between the structures in the transmission electron micrograph. The variations in brightness in the substrate region at the interface to the heteroepitaxial film can be related to defect induced strain fields (see for example Reference 149 page 289 and following). The structural quality of the homoepitaxial film, on the other hand, is much higher in comparison to that of the heteroepitaxial film. Yet, the interface between the substrate and the film is defective in both cases. The defects in the film grown on the ZnO (0001) single crystal are most likely dislocations to relief the strain between the ZnO:Al film and the substrate due to the still existent lattice mismatch. The average distance between two dark strain fields is roughly 50 nm. Assuming a lattice mismatch of $|a_{\mathrm{ZnO:Al}} - a_{\mathrm{ZnO}}|/a_{\mathrm{ZnO}} = \varepsilon \approx 1\,\%$, the equilibrium distance of the dislocations to compensate the strain induced by the lattice mismatch for an infinitely thick layer would be $d = b/\varepsilon \approx 30$ nm, where b is the Burgers vector for such dislocations (the Burgers vector is assumed to be in the order of a lattice distance in a-axis direction (JCPDS 36-1451: $a = 0.32498$ nm)).[190,191] This is in reasonable agreement with the distance between the structures in the TEM image at the interface and thus supports the hypothesis of misfit-dislocations. On the left side and on the right side of the section of the film shown in Figure 4.7 (b), vertical structures are visible. These may be dislocations or grain boundaries. The distance between these structures is in the range of 1.5 µm. It may be surprising to find grain boundaries in the homoepitaxially grown films, but investigations of Owen (see Reference 188 page 72 and following) also suggest the formation of grain boundaries in such films. He performed wet-chemical etching experiments on homoepitaxial ZnO:Al films grown by magnetron sputtering and found etching craters with dimensions in the range of a few µm. Since the used acid preferentially etches grain boundaries, this is in agreement with the distance between the structures visible in the TEM micrograph for the homoepitaxially grown film, which is an indication that these structures are grain boundaries.

4.2.2 Results of XRD Measurements

The orientational relationship of the epitaxial films has been determined by φ-scans as well. Nearly all heteroepitaxial films exhibit an explicit epitaxial relationship to the substrates as can be inferred from

the presence of narrow peaks from the grown films in the φ-scans. Exceptions were the $Zn_{1-x}Mg_xO$:Al films deposited at 500 °C on all substrates and deposited between 350 °C and 500 °C on r-sapphire. The orientational relationships determined for the heteroepitaxial films are shown in Figure 4.8.

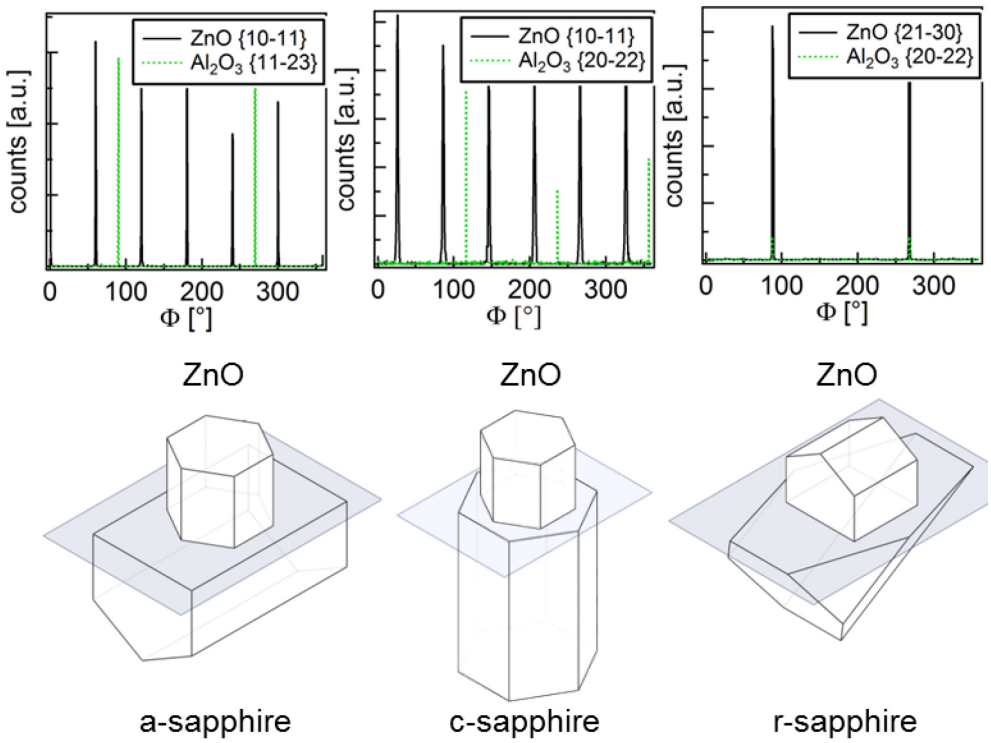

Figure 4.8: Representative φ-scans of the films (black, solid line) and substrates (green, dotted line) for heteroepitaxial ZnO:Al and $Zn_{1-x}Mg_xO$:Al films grown on a-,c-, and r-sapphire (*top*), and schemes of the orientational relationships between the substrates and the films for the heteroepitaxial samples (*bottom*).

The orientational relationships of the polycrystalline and heteroepitaxial films, depicted in Figure 4.3 and Figure 4.8, can be summarized by

- a-plane $(11\bar{2}0)$ sapphire: $(0001)<1120>_{ZnO} \| (11\bar{2}0)<0001>_{Al_2O_3}$
- c-plane (0001) sapphire: $(0001)<10\bar{1}0>_{ZnO} \| (0001)<11\bar{2}0>_{Al_2O_3}$
- r-plane $(01\bar{1}2)$ sapphire: $(11\bar{2}0)<0001>_{ZnO} \| (01\bar{1}2)<0\bar{1}11>_{Al_2O_3}$
- borosilicate glass substrate: preferred orientation $(0001)_{ZnO}$ || substrate surface. No in-plane orientation,

where <0001>, for example, denotes the direction along the c-axis. These orientational relationships agree with those reported in the literature.[192-194] For growth on c-sapphire, sometimes two types of in-plane rotation domains twisted by 30° are observed.[195] However, the occurrence of this effect depends on the type of substrate and on the deposition conditions and was not detected for the films investigated here.

To quantify the structural quality of the epitaxial films, rocking curve measurements of the (0002) and $(11\bar{2}0)$ diffraction peaks have been performed. Figure 4.9 (a) on page 70 compares the rocking curve full width at half maximum H_ω of the homo- and heteroepitaxial films as a function of the deposition temperature to those of the polycrystalline films.

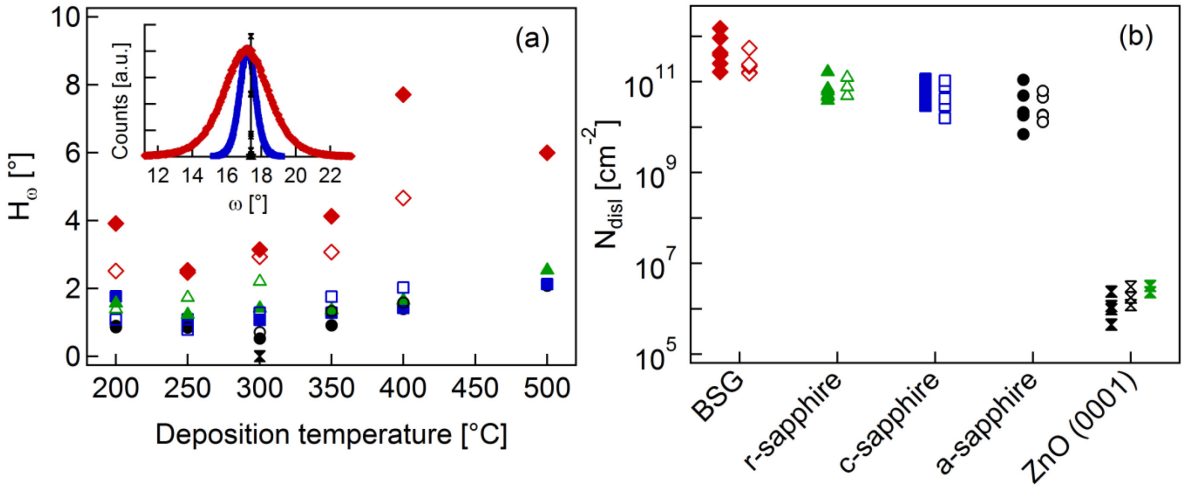

Figure 4.9: (a) Rocking curve full width at half maximum H_ω of the polycrystalline films (diamonds), the heteroepitaxial films grown on a-sapphire (circles), c-sapphire (squares), and r-sapphire (triangles), and the homoepitaxial (double triangles) ZnO:Al (full symbols) and $Zn_{1-x}Mg_xO$:Al (open symbols) films. The inset shows the rocking curves of a polycrystalline, a heteroepitaxial, and a homoepitaxial ZnO:Al film deposited at 300 °C. (b) Threading dislocation densities determined from the H_ω values using Ayers[175] model. ZnO films without Al doping deposited on ZnO (0001) single crystal substrates at 300 °C are denoted by green double triangles.

The full width at half maximum values of the rocking curves of the heteroepitaxial films (0.5° to 2.6°) and the homoepitaxial films (0.005° to 0.01°) are lower in comparison to those of the polycrystalline films (2.5° to 7.7°). For the heteroepitaxial films, the lowest rocking curve widths were obtained on a-sapphire at substrate temperatures between 250 °C and 300 °C. Such minima are observed for the polycrystalline films grown in the same temperature range on amorphous substrates as well. It seems, the mechanisms governing the crystalline quality as a function of the substrate temperature could be independent from the lattice mismatch. This might be explained by a dynamic equilibrium between the formation of defects due to an ion bombardment during the deposition process, the self-annealing of these defects at elevated deposition temperatures, and phase segregation, leading to an increase of the rocking curve full width at half maximum at $T_{sub} \geq 350$ °C, which will be discussed more detailed in Section 6.1.

There is not a clear trend, but the rocking curve widths of the heteroepitaxially grown $Zn_{1-x}Mg_xO$:Al films are generally larger in comparison to those of the ZnO:Al films for deposition temperatures $T_{sub} \geq 300$ °C. For lower deposition temperatures, the difference depends very much on the substrate type: The $Zn_{1-x}Mg_xO$:Al films grown on the c- and r-sapphire exhibit lower H_ω values ($H_{\omega,\text{c-sapphire}} = (1.087 \pm 0.005)°$, $H_{\omega,\text{r-sapphire}} = (1.395 \pm 0.006)°$) compared to the ZnO:Al films ($H_{\omega,\text{c-sapphire}} = (1.770 \pm 0.010)°$, $H_{\omega,\text{r-sapphire}} = (1.566 \pm 0.003)°$) grown on these substrates at 200 °C deposition temperature, while H_ω is almost equal for growth on a-sapphire. For deposition at 250 °C, on the other hand, only the $Zn_{1-x}Mg_xO$:Al film grown on the c-sapphire has a smaller $H_\omega = (0.795 \pm 0.005)°$ in comparison to the ZnO:Al ($H_{\omega,\text{c-sapphire,ZnO:Al}} = (1.105 \pm 0.005)°$). Incidentally, the errors of the H_ω values stem exclusively from the uncertainty of the Gaussian fit to the rocking curve. They are likely to be larger due to the remaining misalignment of the X-ray diffractometer and variations in the parameters during the deposition process. Table 4.2 on page 71 summarizes the results and compares them to literature data.

Ellmer et al.[42] and Kuppusami and coworkers[165] obtained rocking curve full width at half maximum values between 0.8° and 2.8° for their films magnetron sputtered on a-,c- and r-sapphire. These values are comparable to those determined in this investigation. Lorenz et al.[196] were able to prepare films with $H_\omega = 0.36°$ by PLD on c-sapphire substrates, which is slightly smaller than the lowest value of 0.5° obtained here. Most remarkable, however, are the low rocking curve half widths of the

Table 4.2: Comparison of the rocking curve full width at half maximum H_ω determined in this work with literature data for ZnO films grown on different substrates by various methods. RF-MS: radio-frequency magnetron sputtering, PLD: pulsed laser deposition, MBE: molecular beam epitaxy, BSG: borosilicate glass.

Substrate	Film	H_ω of the film	Method	Reference
a-sapphire	ZnO:Al	0.5°...2.1°	RF-MS	this work
	$Zn_{1-x}Mg_xO$:Al, $x \approx 0.12$	0.7°...1.6°	RF-MS	this work
	ZnO:Al	0.8°...2.3°	RF-MS	165
	ZnO:Al	1.1°...1.3°	RF-MS	42
c-sapphire	ZnO:Al	1.1°...2.1°	RF-MS	this work
	$Zn_{1-x}Mg_xO$:Al, $x \approx 0.12$	0.8°...2.0°	RF-MS	this work
	ZnO:Al	1.4°...2.6°	RF-MS	165
	ZnO:Al	1.6°...2.5°	RF-MS	42
	ZnO	0.06°	PLD	196
	ZnO:Ga	0.36°	PLD	196
r-sapphire	ZnO:Al	1.2°...2.5°	RF-MS	this work
	$Zn_{1-x}Mg_xO$:Al, $x \approx 0.12$	1.4°...n.a.	RF-MS	this work
	ZnO:Al	2.0°...2.8°	RF-MS	165
	ZnO:Al	1.9°...2.6°	RF-MS	42
BSG	ZnO:Al	2.5°...7.7°	RF-MS	this work
	$Zn_{1-x}Mg_xO$:Al, $x \approx 0.12$	2.5°...4.7°	RF-MS	this work
	ZnO:Al	4°...8°	RF-MS	165
ZnO	pure substrate	0.005°		this work
	ZnO:Al	0.005°...0.010°	RF-MS	this work
	$Zn_{1-x}Mg_xO$:Al, $x \approx 0.12$	0.007°...0.011°	RF-MS	this work
	ZnO	0.010°...0.011°	RF-MS	this work
	ZnO	0.006°...0.017°	PLD	197
	ZnO	0.006°...0.012°	PLD	198
	$Zn_{1-x}Mg_xO$, $0.05<x<0.44$	0.015°...0.063°	PLD	198
	ZnO (with buffer layer)	0.004°	MBE	199

homoepitaxial films. Lowest rocking curve full width at half maximum values of (0.0046 ± 0.0018)° and (0.0072 ± 0.0013)° were obtained for the ZnO:Al and $Zn_{1-x}Mg_xO$:Al film deposited at 300 °C on a ZnO (0001) single crystal, respectively. This is in the same order as the rocking curve full width at half maximums of 0.005° (in accordance with the datasheet value) of the TokyoDenpa ZnO (0001) single crystals used as substrates for the depositions. Lajn[197] and Lorenz[198] reported H_ω = 0.006° and H_ω = 0.009°, respectively, for homoepitaxial ZnO films prepared on ZnO (0001) single crystalline substrates by PLD, which corresponds to the values determined here.

The dislocation densities N_{disl}, determined from the rocking curve widths, are between $4.5 \cdot 10^5$ cm^{-2} and $3.2 \cdot 10^6$ cm^{-2} for the homoepitaxial films. For the heteroepitaxial films, significantly higher values, in the range from $7 \cdot 10^9$ cm^{-2} to $1.6 \cdot 10^{11}$ cm^{-2}, are calculated. The dislocation densities in the polycrystalline films ($1.6 \cdot 10^{11}$ cm^{-2} to $1.5 \cdot 10^{12}$ cm^{-2}) are again slightly higher compared to those of the heteroepitaxial films. In comparison to the ZnO:Al films, lower dislocation densities can only be obtained for the heteroepitaxial $Zn_{1-x}Mg_xO$:Al films when they are grown on c-sapphire substrates. On these substrates, a lowest value of $1.6 \cdot 10^{10}$ cm^{-2} is reached for the $Zn_{1-x}Mg_xO$:Al film prepared at T_{sub} = 250 °C, which is approximately half of the lowest dislocation density of $2.9 \cdot 10^{10}$ cm^{-2}

(T_{sub} = 300 °C) observed in the ZnO:Al films. In the homoepitaxial films, N_{disl} is generally lower by more than 4 orders of magnitude, which clearly shows the excellent crystalline quality of these layers. The homoepitaxial ZnO:Al films reach lower dislocation densities in comparison to the $Zn_{1-x}Mg_xO$:Al films. The lowest values obtained are $N_{disl} \approx 4.5 \cdot 10^5$ cm^{-2} and $N_{disl} \approx 1.2 \cdot 10^6$ cm^{-2}, respectively.

As already pointed out, the broadening of the rocking curves is mainly related to the dislocation density, the size of the crystallites, and the tilt of the crystallites. Usually, these parameters are assumed to be mainly influenced by the lattice mismatch between the film and the substrate.[165,193,194] Along the c-axis of the a-sapphire, a lattice mismatch of 0.05 % ($4a_{ZnO} \approx c_{Al2O3}$)[193] is calculated taking into account the reference values from JCPDS 36-1451 for the lattice constants of the ZnO films (a_{ZnO} = 3.2498 Å, c_{ZnO} = 5.2066 Å) and JCPDS 46-1212 for the sapphire substrates (a_{Al2O3} = 4.7587 Å, c_{Al2O3} = 12.9929 Å). Perpendicular to the c-axis in the plane of the film, the value is 2.4 % ($3a_{<10\text{-}10>ZnO} \approx 2a_{<10\text{-}10>Al2O3}$). An incommensurate interface fitting reduces the lattice mismatch for the c-sapphire to –1.4 % ($5a_{<10\text{-}10>ZnO} \approx 6a_{Al2O3}$)[165] along the <11$\bar{2}$0> direction of the substrate and approximately the same value perpendicular to that direction in the plane of the film ($5a_{ZnO} \approx 2a_{<10\text{-}10>Al2O3}$). On the r-sapphire, the lattice mismatch along the c-axis of ZnO and perpendicular to the c-axis in the plane of the film is 1.5 % ($3c_{ZnO} \approx a_{<0\text{-}111>Al2O3}$)[194] and –1.4 % ($5a_{<10\text{-}10>ZnO} \approx 6a_{Al2O3}$), respectively. From the calculated lattice mismatches, it is plausible that the heteroepitaxial films grown on the a-sapphire exhibit the highest structural quality. However, other correlations with the experimental data cannot be inferred. Furthermore, one has to take into account that the films investigated here are doped with Al and alloyed with Mg, which changes the lattice constants.[200,201] Also, the lattice constants of the sputtered films strongly depend on the deposition parameters, which means that the lattice mismatch is not exactly known, because the orientation of the films allows for measuring the lattice constants perpendicular to the substrate surface in the Bragg-Brentano geometry only. The peak intensity of the other lattice planes, on the other hand, was too low to determine the in-plane lattice parameters.

The lattice parameters of the axes perpendicular to the film surfaces of the polycrystalline and heteroepitaxial films and the grain sizes determined from the corresponding X-ray peaks are shown in Figure 4.10.

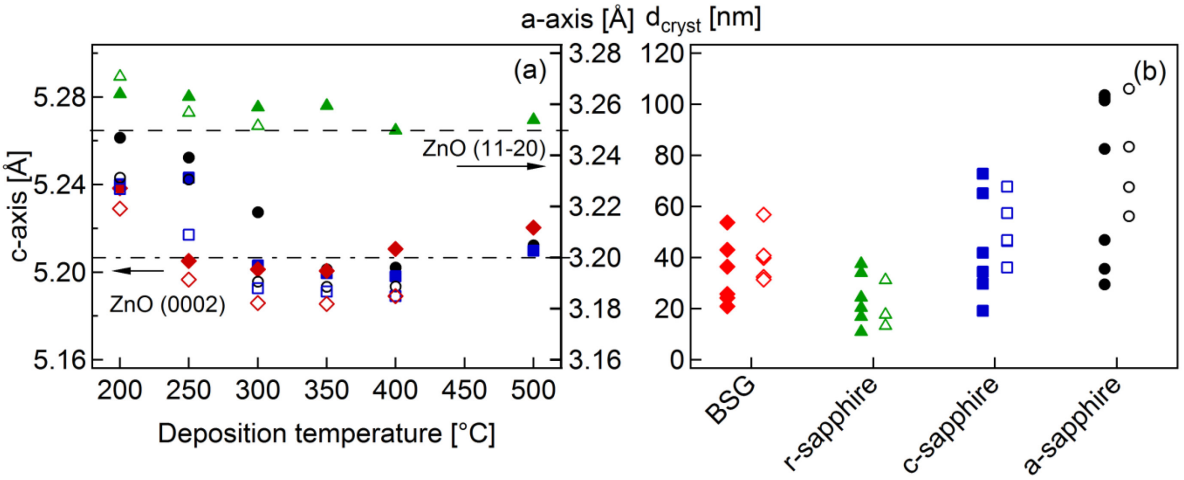

Figure 4.10: (a) c-axis (a-sapphire: circles, c-sapphire: squares, polycrystalline: diamonds) and a-axis (r-sapphire: triangles) lattice parameters for the heteroepitaxial and polycrystalline ZnO:Al (filled symbols) and $Zn_{1-x}Mg_xO$:Al (open symbols) films as a function of the deposition temperature. (b) Crystallite size d_{cryst} for the heteroepitaxial and polycrystalline films. For the homoepitaxial films, it was not possible to reliably determine a value for d_{cryst}.

The strongest elongation with respect to the ZnO powder reference value (c_{ref} = 0.52066 nm) is detected for the $Zn_{1-x}Mg_xO$:Al film deposited at 200 °C on r-sapphire ((0.65 ± 0.05) %) and the

ZnO:Al film deposited at 200 °C on a-sapphire ((1.05 ± 0.09) %). The smallest differences between the powder value and the c-axis lattice parameters are observed for the ZnO:Al and $Zn_{1-x}Mg_xO$:Al films deposited at 250 °C on glass ($c_{ZnO:Al}$ = (0.5205 ± 0.0004) nm, $c_{ZnMgO:Al}$ = (0.5197 ± 0.0004) nm). Generally, the c-axis lattice parameter is elongated for low deposition temperatures and decreases with increasing T_{sub}. For deposition temperatures above 300 °C, the lattice parameter is only slightly increasing. Interestingly, this trend is again observed in a very similar manner for the polycrystalline films. Obviously, the lattice matching at the substrate interface has indeed very little influence on the structural properties of the films. The elongation of the c-axis lattice parameters can hence also be related to the bombardment of the growing film with high-energetic particles leading to interstitial defects causing this tension independent of the substrate type (see Section 6.1). The same trend is observed for the a-axis lattice parameter of the films grown on the r-sapphire substrate. There, the lowest deviation (< 0.1 %) from the powder value of the a-axis is present for the $Zn_{1-x}Mg_xO$:Al film deposited at 300 °C and the ZnO:Al film deposited at 400 °C.

Figure 4.10 (b) shows the crystallite sizes perpendicular to the film surface determined from the θ-2θ scans for the heteroepitaxial and polycrystalline films. The values vary roughly between 10 nm and 100 nm depending on the substrate type and the deposition temperature. In general, the largest crystallite sizes were observed for deposition temperatures between 250 °C and 300 °C. With respect to the substrate type, the largest crystallite sizes are obtained for the films grown on a-sapphire (up to 110 nm) and the smallest crystallites sizes exhibited the films prepared on r-sapphire (down to 10 nm). Larger crystallite sizes in the $Zn_{1-x}Mg_xO$:Al films in comparison to those in the ZnO:Al layers were only observed for the films grown on glass ($d_{cryst,max,ZnMgO:Al} \approx 57$ nm, $d_{cryst,max,ZnO:Al} = 54$ nm) or a-sapphire substrates ($d_{cryst,max,ZnMgO:Al} \approx 106$ nm, $d_{cryst,max,ZnO:Al} = 103$ nm). The differences are, however, very small. It may be speculated that the change of the lattice parameter due to the incorporation of the Mg in the lattice facilitates the epitaxial growth on some substrate types in comparison to the ZnO:Al films. Additionally, for both materials, the effect of the variation of the lattice parameters with the deposition temperature may have an impact on the matching of the film to the substrate. Still, as already pointed out, the same substrate temperature dependence of the rocking curve widths can be observed for the polycrystalline films deposited on glass. For these films, no lattice match can occur at all. Therefore, the lattice mismatch is certainly not the only parameter that has to be used to interpret the rocking curve widths and by that the quality of the crystalline growth of the films.

4.2.3 Results of Optical Measurements

In order to examine the local disorder in the films more detailed, optical measurements have also been performed on the heteroepitaxial films to determine the Urbach energies. The results are shown in Figure 4.11 on page 74 and summarized in Table 4.3 on the same page. An analysis of the optical transmittance and reflectance data of the homoepitaxial films was not possible, because the optical band gap is either increased due to the doping with Al and/or due to the alloying with Mg. In consequence, the absorption of the ZnO single crystal substrate becomes significant at energies lower than those where the absorption edge of the ZnO:Al and $Zn_{1-x}Mg_xO$:Al films is located.

Figure 4.11 (a) shows the Urbach energies as a function of the deposition temperature for the films prepared on the different substrate types. The Urbach energies E_U span the range from roughly 50 meV to 210 meV. In general, E_U is decreasing with increasing deposition temperature, not only for the polycrystalline films but also for the heteroepitaxial films. Comparing the Urbach energies for the different substrate types, the lowest values are obtained for the films deposited on a-sapphire for both materials. On these substrates, the ZnO:Al films exhibit a lowest E_U of 54 meV and the $Zn_{1-x}Mg_xO$:Al

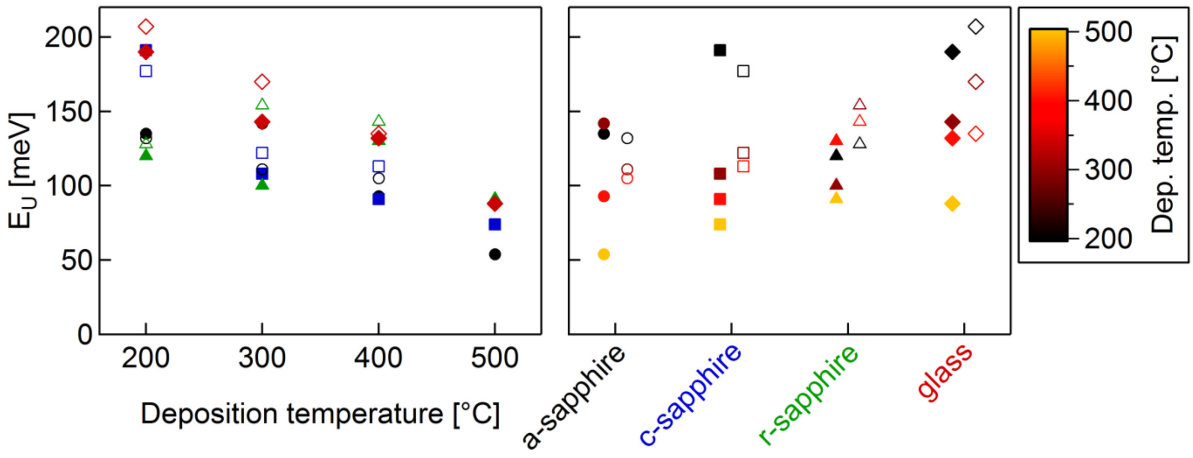

Figure 4.11: (a) Urbach energies E_U for the polycrystalline (diamonds) and heteroepitaxial (a-sapphire: circles, c-sapphire: squares, r-sapphire: triangles) ZnO:Al (filled symbols) and $Zn_{1-x}Mg_xO$:Al films (open symbols) deposited at different substrate temperatures between 200 °C and 500 °C. (b) Urbach energies as a function of the substrate type used for the film growth.

films show $E_U \geq 105$ meV. The highest values are, as expected, determined for the polycrystalline films. Although their structural quality is lower in comparison to the epitaxially grown films, the difference is not large. Even on glass, values of the Urbach energy as low as 88 meV for the ZnO:Al and 135 meV for the $Zn_{1-x}Mg_xO$:Al films are obtained for deposition at high temperatures. These values are only 1.6 and 1.3 times higher in comparison to the lowest Urbach energies determined for the heteroepitaxial films, respectively. Wei et al.[202] reported Urbach energies in the range of 90 meV to 130 meV for their pulsed laser deposited Ga-doped (1...3 at.%) $Zn_{1-x}Mg_xO$:Al films grown on c-sapphire substrates, which is lower in comparison to the values determined for the $Zn_{1-x}Mg_xO$:Al films here (110 meV to 180 meV). This can be explained by their smaller Mg content in the range of 2...3 at.% with respect to the whole compound, opposed to roughly 6 at.% for the films investigated here. Additionally, they used a substrate temperature of 650 °C, which is likely to further reduce the Urbach energies compared to lower deposition temperatures. An analysis of the Urbach tail of the TokyoDenpa ZnO (0001) single crystal yielded an energy $E_U = (30 \pm 3)$ meV. Although this is much lower in comparison to most of the values of the polycrystalline and heteroepitaxial films, it also shows that for example the ZnO:Al film grown on a-sapphire at $T_{sub} = 500$ °C with an Urbach energy of (54 ± 2) meV already has a very high local structural quality.

Table 4.3: Urbach energies E_U in meV for epitaxial ZnO:Al and $Zn_{1-x}Mg_xO$:Al films determined by fitting Equation (4.4) to the absorption data. Some values are calculated by fitting this equation to the higher and lower end of the curves in the Urbach plot to consider the nonlinear slope. The errors are then one standard deviation of the average of the two values obtained by the fit. For the other fits, the error represents the uncertainty of the single line fit.

	$Zn_{1-x}Mg_xO$:Al				ZnO:Al			
T_{sub} [°C]	a-sapphire	c-sapphire	r-sapphire	glass	a-sapphire	c-sapphire	r-sapphire	glass
200 °C	132 ± 2	177 ± 2	128 ± 2	207 ± 3	135 ± 20	191 ± 10	120 ± 2	190 ± 10
300 °C	111 ± 2	122 ± 2	154 ± 2	170 ± 15	142 ± 2	108 ± 3	100 ± 13	143 ± 3
400 °C	105 ± 2	113 ± 2	143 ± 4	135 ± 3	93 ± 2	91 ± 2	130 ±10	132 ± 8
500 °C					54 ± 2	74 ± 4	91 ± 13	88 ± 5

4.3 Chapter Conclusions

In conclusion, it has been shown that polycrystalline, hetero-, and homoepitaxial ZnO:Al and $Zn_{1-x}Mg_xO$:Al ($x \approx 0.12$) films can be grown by magnetron sputtering. The study revealed a strong preferred c-axis orientation of the polycrystalline films but no in-plane orientation. The c-axis of the heteroepitaxial films grown on the a- and c-sapphire substrates is perpendicular to the substrate surface as well, but these films exhibit a defined in-plane orientation. In the ZnO:Al and $Zn_{1-x}Mg_xO$:Al films grown on the r-sapphire substrate, on the other hand, the c-axis is parallel to the substrate surface. For all films, the crystalline quality has been quantified by rocking curve measurements, and in addition to that, dislocation densities have been calculated from the rocking curve widths using Ayers[175] model. It was found, that the crystalline quality of the films is strongly different for the various substrate types used for the deposition: While the polycrystalline films exhibited the lowest crystalline quality, the rocking curve widths and the Urbach energies were pointing to a slightly higher structural quality of the heteroepitaxial films and to an excellent quality compared to the other films and literature values for the homoepitaxial films grown on ZnO (0001). Mostly, the crystalline quality of the $Zn_{1-x}Mg_xO$:Al films was slightly lower in comparison to that of the ZnO:Al films, which can be related to the disorder induced by the Mg in the ZnO lattice.

Since charge carrier scattering can occur at crystallographic defects, the investigation of epitaxial films or single crystals yields valuable information about the impact of defects on the electronic transport, because in these materials, the number of grain boundaries and other crystallographic irregularities is significantly reduced. Hence, the results obtained in this chapter provide a basis for the investigation of the charge carrier transport, which will be discussed in the following chapter.

5. Charge Carrier Scattering in Zinc Oxide

Charge carrier scattering can be divided into two general processes: intrinsic scattering due to the band structure of the semiconductor and extrinsic scattering caused by dopants and charge carriers.[7] In single crystalline materials, the intrinsic scattering prevails for carrier concentrations below 10^{16} cm^{-3}, while the extrinsic ionized impurity scattering is limiting the transport for n > 10^{18} cm^{-3}.[7] When the arrangement of the atoms in the single crystal is disturbed, additional scattering of the charge carriers can occur, for example dislocation scattering, alloy scattering, and grain boundary scattering, which have been discussed in Section 2.3. Since the scattering of the free carriers leads to a reduction of their mobility, it is of great importance to understand the scattering mechanisms to suppress or reduce the scattering or to determine the theoretical limits for the optimization. Additionally, an increase of the mobility of the carriers will not only reduce the resistivity but also improve the optical properties of the transparent conductive oxide. In this chapter, the different scattering mechanisms will be discussed and the most important scattering mechanisms in the doped ZnO films determined. Furthermore, the model for the Hall mobility of the charge carriers in arbitrarily doped semiconducting films will be applied and examined more detailed.

Results, presented in this chapter, have partly been published already in References [A], [C], and [D] from the list in the appendix.

5.1 Scattering in Single Crystals – Literature Data

The first comprehensive study of the electronic transport in intrinsic and extrinsically doped single crystalline ZnO has been performed by Hutson[60] in the 1950s.[22] He measured the temperature dependent Hall effect and conductivity in the range of 55 K to 300 K and determined the electron concentration n and the Hall mobility μ. For carrier concentrations below 10^{17} cm^{-3}, he found a room temperature mobility in the range of 180 cm²/(Vs) for single crystalline ZnO needles, which decreased as the free carrier concentration was increased by intentional doping. These results are still valid today, but a quantitative description of the Hall mobility as a function of the free carrier concentration was required.

To model the electron mobility in doped Si as a function of the free carrier concentration in the range from $n \approx 10^{13}$ cm^{-3} to $n \approx 5 \cdot 10^{21}$ cm^{-3}, Masetti et al.[203] proposed a semi-empirical fit formula. They improved fit formulas for the electron mobility μ as a function of the free carrier concentration n for very high values of n by using[22,203]

$$\mu^{\mathrm{Ma}} = \mu_{\min} + \frac{\mu_{\max} - \mu_{\min}}{1 + \left(\frac{n}{n_{\mathrm{ref1}}} \right)^{\alpha_1}} - \frac{\mu_1}{1 + \left(\frac{n_{\mathrm{ref2}}}{n} \right)^{\alpha_2}}, \tag{5.1}$$

where $\mu_{\max}$ can be related to the physical quantity of the lattice mobility at low carrier concentrations, $\mu_{\min}$ is the ionized impurity mobility at high carrier concentrations, and $\mu_{\max} - \mu_1$ is the clustering mobility at very high carrier concentrations.[22] This model has also successfully been used to describe

the transport data of other single crystalline semiconductors.[22] Figure 5.1 shows a compilation of transport data for highly doped single crystals from the literature.

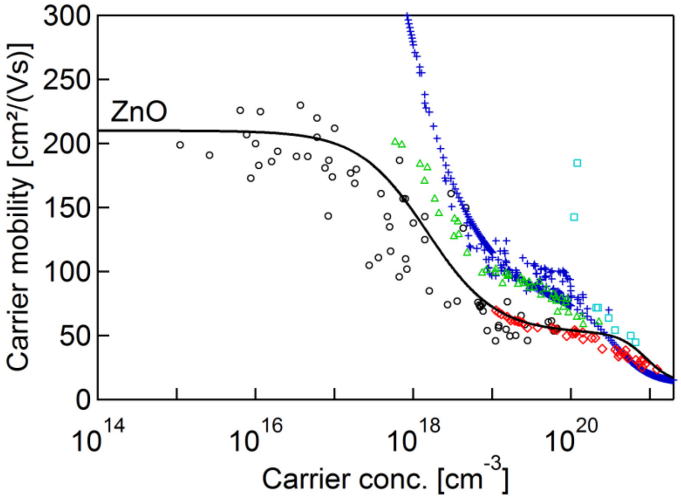

Figure 5.1: Carrier mobility as a function of the carrier concentration for different single crystalline semiconductors. The circles denote a compilation of data for ZnO (n-type) by Ellmer[204], the blue plus signs are data for Si:P (n-type) taken from Masetti et al.[203], Mousty and coworkers[205], Baccarani and Ostoja[206], Thurber et al.[207], and references therein. The red diamonds show the transport data of Si:B (p-type) taken from Masetti et al.[203] and Thurber et al.[208]. Also shown are the data for GaAs:C (p-type) by Chen (green triangles) and coworkers[209] and Ge:Ga (p-type) (light blue squares) by Impellizzeri et al.[210].

The semi-empirical Masetti formula is able to describe the data of the single crystalline ZnO quite accurately below $n \approx 10^{20}$ cm^{-3} (see the black line in Figure 5.1). At higher free carrier concentrations, there is no data available for the electronic transport in single crystalline ZnO. This will be discussed later together with the parameters of the Masetti formula for ZnO. The data of the other semiconductors shows in principle the same behaviour. Hence, the Masetti formula could also be used to describe the electronic transport of the GaAs or the Ge single crystals, but for these materials, the data covers only a narrow range of free carrier concentrations n thus making a reliable fit impossible.

The differences of the mobilities of the various semiconductors are largest for free carrier concentrations below approximately 10^{17} cm^{-3}. In this region, the mobility of the carriers is mainly limited by phonon scattering, which depends on the effective mass m^*, the static and high frequency dielectric constants ε_s and ε_∞, the energy of the longitudinal-optical phonon $\hbar\omega_0$, the average elastic longitudinal constant c_l, the deformation potential energy E_{ac}, and the piezoelectric coupling coefficient P. Since these parameters are not equal for the different materials, a difference in the lattice mobility for low carrier concentrations is expected. The lattice mobility of electrons in Si at room temperature is approximately 1420 cm²/(Vs),[203] while it is 3800 cm²/(Vs) for Ge, [211] 11000 cm²/(Vs) for GaAs,[212] and 210 cm²/(Vs) for ZnO. The hole mobilty at low carrier concentrations is roughly 470 cm²/(Vs) in Si,[203] 1820 cm²/(Vs) in Ge,[211] and 400 cm²/(Vs) in GaAs[213] (see Table 5.1).

Table 5.1: Lattice charge carrier mobilities of selected semiconductor materials.

	Lattice mobility [cm²/(Vs)]	
Material	**Electrons**	**Holes**
Si	1420	470
Ge	3800	1820
GaAs	11000	400
ZnO	210	

The Masetti formula fitted to the mobility data is only valid for room temperature. To calculate values for other temperatures, a theoretical description of the lattice scattering is required, which will be derived in the following.

5.1.1 Lattice Scattering

The most commonly used scattering mechanisms for the description of the lattice mobility in ZnO are the optical mode phonon scattering, the piezoelectric mode scattering, and the acoustical mode phonon scattering.[60,212,213]

For the optical mode phonon scattering, a value of $\mu_{LO}^{Hall} = 427$ cm²/(Vs) at $T = 295$ K is obtained for non-degenerate ZnO when using $m^* = 0.28 m_e$,[22] $\varepsilon_s = 8.34$,[22] $\varepsilon_\infty = 3.74$,[22] $\hbar\omega_0 = 72$ meV,[67] and Equation (2.33) from Section 2.3.1

$$\mu_{LO}^{Hall} = \frac{e}{2\left(\frac{1}{\varepsilon_\infty} - \frac{1}{\varepsilon_s}\right)\frac{\sqrt{m^* e^2}}{4\pi\varepsilon_0 \hbar\sqrt{2\hbar\omega_0}}\omega_0 m^*}\left(e^{\frac{\hbar\omega_0}{kT}} - 1\right). \tag{5.2}$$

The piezoelectric mode scattering in undoped single crystalline ZnO can, according to Equation (2.39) from Section 2.3.2, be calculated by

$$\mu_{piezo}^{Hall} = r_{H,piezo}\frac{16\sqrt{2\pi}\hbar^2\varepsilon_s\varepsilon_0}{3eP_{\perp,\parallel}^2\sqrt{m^{*3}kT}}. \tag{5.3}$$

Using the value $P_\perp = 0.21$,[22] the piezoelectric scattering mobility at room temperature is $\mu_{piezo}^{Hall} \approx 2100$ cm²/(Vs).

The acoustical mode scattering exhibits larger uncertainties, because the deformation potential E_{ac} is not very well known and scatters, as already pointed out, between 1.4 eV and 31.4 eV. Using Equation (2.36),

$$\mu_{ac}^{Hall} = r_{H_{ac}}\frac{\sqrt{8\pi}\hbar^4 c_l e}{3E_{ac}^2 m^{*\frac{5}{2}}(kT)^{\frac{3}{2}}} \tag{5.4}$$

and $E_{ac} = 1.4$ eV, a mobility $\mu_{ac}^{Hall} = 1.6\cdot10^5$ cm²/(Vs) is obtained ($c_l = 200.6$ GPa)[22]. By inserting $E_{ac} = 31.4$ eV instead, a value of $\mu_{ac}^{Hall} = 313$ cm²/(Vs) is determined. Since the parameters of the other scattering mechanisms are comparatively well known, E_{ac} can be determined by a fit to the lattice mobility of the ZnO. Applying the common approximation to Mathiessen's rule, $1/\mu = \Sigma(1/\mu_i)$, and adjusting the energy for the acoustic deformation potential E_{ac}, the lattice mobility of 210 cm²/(Vs) in ZnO can be described by $E_{ac} = 26$ eV. Values in this range have also been reported by Wagner and Helbig[72] (31.4 eV) for ZnO and Rode[214] for other II-VI compounds.

Using these three scattering mechanisms together with the adjusted deformation potential, a description of the lattice scattering for $n \lesssim 10^{17}$ cm^{-3} and a wide range of temperatures is available.

5.1.2 Ionized Impurity Scattering

Interestingly, the mobility values in the carrier concentration range above $n \approx 10^{20}$ cm^{-3} do not differ significantly for the various materials. There seems to be a universal mechanism limiting the mobility of the charged carriers for the different crystals in the same way. For single crystals, the dominant scattering mechanism in the carrier concentration range above 10^{18} cm^{-3} is ionized impurity scattering. The ionized impurity scattering can theoretically be described by Equation (2.42) (see Section 2.3.3)

$$\mu_{ii}^{Hall,Di} = \frac{3(\varepsilon_0\varepsilon_s)^2 h^3}{Z^2 m^{*2} e^3}\frac{n}{N_i}\frac{1}{F_{ii}(\xi)}. \tag{5.5}$$

In principle, the first expectation would be larger differences in the mobility at high free carrier concentrations, since these semiconductor crystals are distinct materials. However, the important parameters for the ionized impurity scattering are only the static dielectric constant ε_s and the effective mass m^*. These parameters are summarized in Table 5.2 for the different materials shown in Figure 5.1 on page 78.

Table 5.2: Effective masses and static dielectric constants of the different single crystalline semiconductor materials. The experimental and the theoretical ratio of the mobility of the charge carriers due to the ionized impurity scattering to the other materials $\mu_{ii,x}/\mu_{ii,ZnO}$ (x = Si, Ge, GaAs, ZnO) for $n = 10^{20}$ cm^{-3} are also presented. m_t^*: transversal effective mass, m_l^*: longitudinal effective mass, $m_{p,l}^*$: light hole effective mass, $m_{p,h}^*$: heavy hole effective mass, $m_{c,n}^*$: conductivity effective electron mass, $m_{c,p}^*$: conductivity effective hole mass, $m_{d,n}^*$: density of states electron effective mass, $m_{d,p}^*$: density of states hole effective mass.

Parameter	Si	Ge	GaAs	ZnO
$m_{d,n}^*$ [m_e]	$m_t^* = 0.19$, $m_l^* = 0.98$ [215]	$m_t^* = 0.082$, $m_l^* = 1.64$ [215]	0.067 [215]	0.24 – 0.31 [216]
$m_{d,p}^*$ [m_e]	$m_{p,l}^* = 0.16$, $m_{p,h}^* = 0.49$ [215]	$m_{p,l}^* = 0.044$, $m_{p,h}^* = 0.28$ [215]	$m_{p,l}^* = 0.082$, $m_{p,h}^* = 0.45$ [215]	0.31 – 0.59 [217]
$m_{c,n}^*$ [m_e]	0.26 [218]	0.12 [218]	0.067 [218]	$\approx m_n^*$ [16]
$m_{c,p}^*$ [m_e]	0.386 [218]	0.21 [218]	0.34 [218]	
ε_s	11.7 – 12.1 [219]	15.8 – 16.5 [220]	12.5 – 13.9 [221]	7.8 – 8.75 [222]
$\mu_{ii,x}/\mu_{ii,ZnO}$	1.8 (n-type)			1 (n-type)
(theory)	1.0 (p-type)	4.0 (p-type)	1.4 (p-type)	
$\mu_{ii,x}/\mu_{ii,ZnO}$	1.5 ± 0.4 (n-type)			1 (n-type)
(exp.)	0.95 ± 0.14 (p-type)	3.7 ± 1.6 (p-type)	1.4 ± 0.2 (p-type)	

Indeed, the parameters relevant for the ionized impurity scattering are all rather similar for the semiconductors shown in Figure 5.1. Furthermore, one has to take into account that the ionized impurity scattering leads to very low mobilities, which means that large relative differences are not leading to large absolute differences as it has been the case for the lattice mobility. Using the conductivity effective masses and the averaged values for ε_s given in Table 5.2, the theory for ionized impurity scattering predicts the following mobilities of the single crystalline materials shown in Figure 5.1 relative to the ZnO for a free carrier concentration of $n = 1 \cdot 10^{20}$ cm^{-3}: for n-type Si $\mu_{ii,Si}/\mu_{ii,ZnO} = 1.8$, for p-type Si $\mu_{ii,Si}/\mu_{ii,ZnO} = 1.0$, for p-type Ge $\mu_{ii,Ge}/\mu_{ii,ZnO} = 4.0$, and for p-type GaAs $\mu_{ii,GaAs}/\mu_{ii,ZnO} = 1.4$. The experimentally determined values are for n-type Si $\mu_{ii,Si}/\mu_{ii,ZnO} = 1.5 \pm 0.4$, for p-type Si $\mu_{ii,Si}/\mu_{ii,ZnO} = 0.95 \pm 0.14$, for p-type Ge $\mu_{ii,Ge}/\mu_{ii,ZnO} = 3.7 \pm 1.6$, and for p-type GaAs $\mu_{ii,GaAs}/\mu_{ii,ZnO} = 1.4 \pm 0.2$. There is a very good agreement between the theory and the experiment. Hence, the dominance of the ionized impurity scattering can explain the small differences in the mobility between Si, Ge, GaAs, and ZnO. For higher carrier concentrations, in the range above $n \approx 5 \cdot 10^{20}$ cm^{-3}, the Hall mobilities of the different materials are nearly equal. This equality cannot be explained by the simple ionized impurity model. Under the assumption that the material parameters still differ for such high free carrier concentrations, the scattering mechanism seems to become independent from the specific material properties. It appears this has not been discussed on the basis of theoretical models in the literature yet.

As already mentioned, no transport data exists for carrier concentrations above $n \approx 10^{20}$ cm^{-3} for the single crystalline ZnO. To fit the Masetti curve to ZnO anyway, the independence of the ionized impurity scattering from the crystallinity of the sample can be exploited. For this purpose, a compilation of the data of doped single crystalline ZnO (grey markers) and as-deposited heavily doped polycrystalline ZnO films (red markers) is shown in Figure 5.2 on page 81.

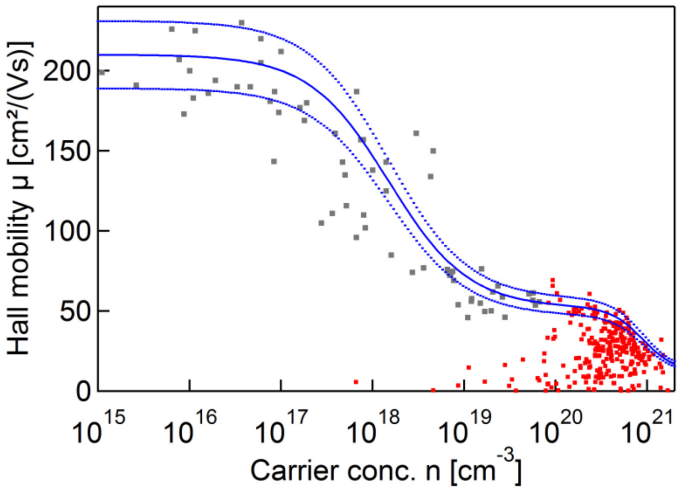

Figure 5.2: Hall mobility μ as a function of the free carrier concentration *n* for single crystalline ZnO (grey dots) and polycrystalline as-deposited films (red dots). The data for the single crystalline ZnO are a compilation by Ellmer[204] and the data for the polycrystalline films stem from Berginski et al.[223], Charpentier et al.[224], Cornelius and coworkers[225], Duenow et al.[226], Jäger et al.[227], Lorenz and coworkers[196], Nakada et al.[228], Nomoto et al.[229], Minami and coworkers[230], Suzuki et al.[231], Warzecha et al.[232], Yamada et al.[233], and this work. The blue solid line shows the Masetti formula with parameters adjusted to reproduce the μ(*n*) dependence of the experimental data. The dotted lines show ±10 % of the μ(*n*) values determined with the Masetti formula.

The data for the polycrystalline films covers the whole range between μ = 0 cm²/(Vs) and a certain maximum value that depends on the free carrier concentration. This is caused by grain boundary scattering, which can, for high trap densities at the grain boundaries or small crystallite sizes, be dominant also in the free carrier concentration range above 10^{20} cm^{-3}. The maximum mobility of the polycrystalline films is approaching the data of the single crystalline films. This upper limit of the mobility is, regarding the large number of data points, a good approximation for the limit of the mobility in heavily doped ZnO due to ionized impurity scattering. Figure 5.2 shows the results of the Masetti formula with parameters adjusted to reproduce the μ(*n*) dependence of the experimental data. The dotted lines show ±10 % of this curve. The parameters used in the Masetti formula are summarized in Table 5.3.

Table 5.3: Parameters used in the Masetti formula adjusted to the experimental data presented in Figure 5.2.

Parameter	ZnO
μ_{max} [cm²/(Vs)]	210
μ_{min} [cm²/(Vs)]	52
μ_1 [cm²/(Vs)]	40
n_{ref1} [cm^{-3}]	$1.5 \cdot 10^{18}$
n_{ref2} [cm^{-3}]	$9 \cdot 10^{20}$
α_1	1
α_2	2.5

These values are based on the work of Ellmer, who performed a similar fit using the same data for the single crystalline zinc oxide but only the data of Minami et al.[230] for the heavy doping regime.[204] The dotted lines show that a range of ±10 % can cover the scattering of the maximal values of the mobility for very high carrier concentrations properly.

Since the Masetti curve for ZnO is only valid for room temperature, it is also of interest for the heavy doping regime to have a theoretical description of the Hall mobility as a function of the free carrier concentration. The ionized impurity scattering for an uncompensated fully ionized ($N_i = n$), non-parabolic semiconductor with an effective charge of the ionized impurities of $Z = 1$ can be calculated using the $m^*(n)$ dependence determined for ZnO in Section 2.3.3 to take into account the non-parabolicity and $\varepsilon_s = 8.34$. When, furthermore, the mobility $\mu_{ii}^{Hall,Di}$ according to Equations (2.42), (2.44), and (2.46) is combined with the lattice mobility according to Mathiessen's rule, the results are

already close to the mobility values determined by the fit with Masetti's formula (compare the dashed dark-blue and the solid green line in Figure 5.3).

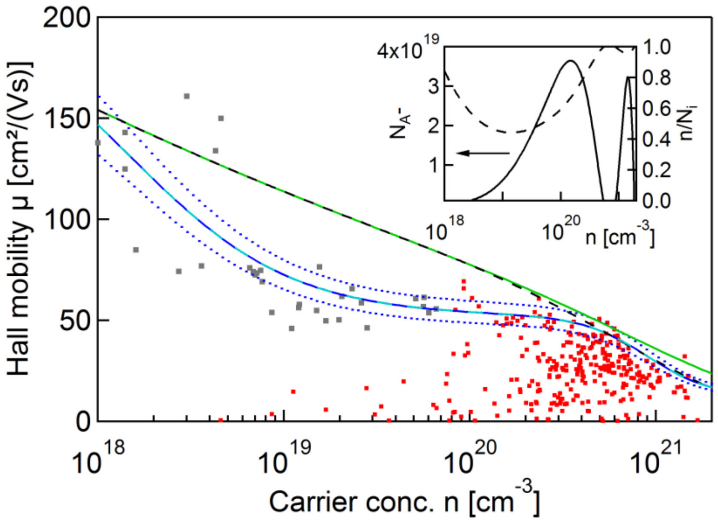

Figure 5.3: Hall mobility μ as a function of the free carrier concentration *n*. The dots show the experimental data and the dashed dark-blue line shows the Masetti curve adjusted to ZnO. The green solid line represents the theory of ionized impurity scattering combined with the lattice mobility for $Z = 1$. The black dashed line represents the combination of ionized impurity scattering and lattice scattering for linearly increasing effective charge of the impurities Z with $Z = 1$ for $n = 10^{20}$ cm^{-3} and $Z = 1.5$ for $n = 2 \cdot 10^{21}$ cm^{-3}. The dashed light-blue line illustrates the combination of ionized impurity scattering and lattice scattering taking into account trap states to correct for the differences between the theory and the Masetti curve for ZnO. The inset shows the electron trap concentration N_A^- (solid line) and the ratio n/N_i (dashed line).

Still, the calculated mobilities for the ionized impurity scattering are slightly too high. Two main deviations are observed: first, the theoretical formula cannot describe the low mobilities in the region below $n \approx 10^{20}$ cm^{-3}, and second, deviations are observed for the mobilities in the clustering region above $n \approx 10^{20}$ cm^{-3}. The clustering mobility can be modelled using a different effective charge of the ionized impurities Z. This effective charge Z is most likely dependent on the free carrier concentration. Assuming the simplest case, where the effective charge is increasing linearly with increasing free carrier concentration, the clustering mobility can be modelled using an increasing Z from 1 to 1.5 in the range from $n = 10^{20}$ cm^{-3} to $2 \cdot 10^{21}$ cm^{-3} (see black dashed line in Figure 5.3). Another variable parameter, which could explain the difference between the Masetti curve and the ionized impurity scattering, is the number of ionized impurities N_i. If acceptors are present in the material, N_i can be expressed as $N_i = n + 2N_A^-$ (see Section 2.3.3). This can be used to adjust N_A^- in a way that it corrects for the differences between the combined theoretical model (ionized impurity scattering and lattice mobility) and the Masetti curve for ZnO (yielding the dashed light-blue line in Figure 5.3). The resulting ratio between n and N_i is shown in the inset of Figure 5.3. In the region of $n \approx 10^{19}$ cm^{-3}, the ratio is reduced to roughly 0.4. For higher free carrier concentrations, the ratio approaches 1. N_A^- is then in the order of 10^{19} cm^{-3} for $n \approx 10^{19}$ cm^{-3} to 10^{21} cm^{-3}. Zakrzewska et al.[80] observed values for the ratio n/N_i in the range of 0.021 ($n = 3.8 \cdot 10^{18}$ cm^{-3}) and 0.462 ($n = 3.2 \cdot 10^{20}$ cm^{-3}) for their sputtered $CdIn_2O_4$ films. Chen and coworkers[234] attempted to determine a function $N_i = f(n)$ as well. They defined $f(n) = x \cdot n$, but the choice of this function is rather arbitrary. In agreement with the results presented here, their investigation also showed a lower carrier concentration n in comparison to the concentration of the ionized impurities N_i in In_2O_3:Sn and ZnO:Al.

5.2 Determining the Dominant Scattering Mechanisms

The description of the scattering in single crystals based on theoretical formulas derived in the preceding section allows to calculate the charge carrier mobility for temperatures other than room temperature in the materials without grain boundaries. This knowledge can now be used to separate the grain boundary scattering from other dominant scattering mechanisms in the polycrystalline films. First, the Hall mobility of the charge carries as a function of their concentration will be examined, and

subsequently the temperature dependence will be studied to consolidate and extend the results. Finally, the results will be compared to the outcomes of Seebeck-coefficient measurements.

5.2.1 Carrier Mobility as a Function of the Carrier Concentration

When ZnO films are deposited on amorphous substrates or substrates with an incommensurate interface fitting, they are polycrystalline and exhibit grain boundaries, which further limit the mobility of the charge carriers. Depending on the material, the deposition method, and the deposition parameters, this influence can become significant already below carrier concentrations of $n \approx 5 \cdot 10^{20}$ cm^{-3}. This decrease of the mobility is attributed to the formation of potential barriers in the conduction and valence band at the grain boundaries of the material, described quite good by the simple grain barrier model of Seto discussed in Section 2.3.4. Although it is only valid in the non-degenerate case, Seto's model has been widely used to interpret the mobility data of degenerate semiconductors as well.[225,235,236] The agreement between the model and the experimental data is surprisingly good even for very high carrier concentrations. Figure 5.4 (a) shows the Hall mobility μ as a function of the free carrier concentration n for polycrystalline ZnO:Al films prepared at substrate temperatures between ~30 °C and 500 °C using DC, 13.56 MHz, and 27.12 MHz plasma excitation frequency during sputtering. Also shown is the Masetti curve for single crystalline ZnO (solid line) and a fit using a combination of the Masetti curve for ZnO and grain boundary scattering according to Seto's model (dashed line). The dotted and dash-dotted lines represent dislocation scattering, which will be discussed later.

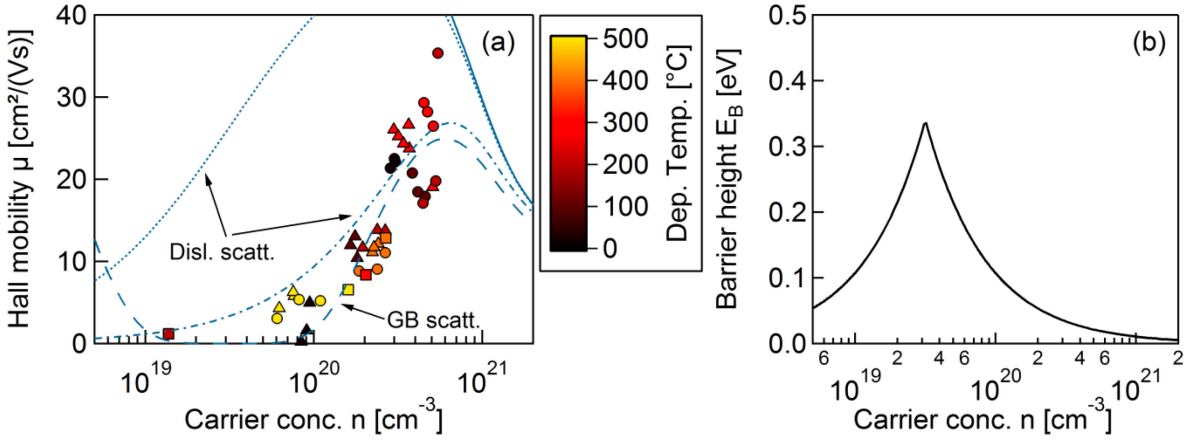

Figure 5.4: (a) Hall mobility μ of the free electrons as a function their concentration n. The markers show experimental data of the ZnO:Al films prepared using DC (squares), 13.56 MHz RF (triangles), and 27.12 MHz RF (circles) plasma excitation. The solid line depicts the mobility data for single crystalline ZnO, the dashed line represents a fit with the combined transport model taking into account the Masetti curve for ZnO and the grain boundary scattering according to the classical Seto model (Equation (2.55) with $n_0 = n_a = n$), and the dotted/dash-dotted lines show the combination of the Masetti curve for ZnO and dislocation scattering (dotted line: $N_{disl} = 1.5 \cdot 10^{12}$ cm^{-2}, dash-dotted line: $N_{disl} = 2 \cdot 10^{13}$ cm^{-2}). (b) Potential barrier height at the grain boundaries according to the classical Seto model.

In comparison to the mobility data of the single crystalline ZnO, the Hall mobility in the polycrystalline films is strongly decreased for free carrier concentrations below $5 \cdot 10^{20}$ cm^{-3}. The small deviation of the dashed line from the experimental data shows that the classical Seto model for grain boundary scattering is able to reproduce the trend of the experimental data very well, although it is not valid for such high free carrier concentrations. Still, from the fit, a lateral grain size $L = (6.3 \pm 1.3)$ nm and a trap density at the grain boundaries $N_t = (1.99 \pm 0.14) \cdot 10^{13}$ cm^{-2} can be determined. This lateral grain size is smaller in comparison to the width of the columns observed in the polycrystalline ZnO:Al films in the range of 50 nm to 150 nm (see Section 4.1). This can be explained by the single lateral

grain size used to fit the complete dataset. While the values determined from the SEM and TEM images stem from samples deposited at 300 °C with the best crystalline quality, the whole dataset of the electrical measurements contains also smaller crystallite sizes from other deposition temperatures. Furthermore, the grain size is depth dependent and 50 nm to 150 nm are the largest values. Using Seto's model as well, Ellmer[22] determined the trap densities for the $\mu(n)$ data reported by several authors and calculated values in the range of $N_t \approx 1.5 \cdot 10^{12}$ cm^{-2} for undoped ZnO grown by RF sputtering and $N_t \approx 3 \cdot 10^{13}$ cm^{-2} for DC sputtered ZnO:Al films. He found that the trap density was reduced when using RF sputtering instead of DC sputtering and that the lowest trap densities are achieved for magnetron sputtering onto substrates mounted perpendicular relative to the sputtering target and for pulsed laser deposited films. The experimental data of this investigation using DC as well as RF sputtering, on the other hand, can be described well by a single trap density when using the classical Seto model. A reason for this may be the strong dependence of the trap density on the dopant concentration (see Section 5.3), which was most likely not similar in the works on ZnO:Al examined by Ellmer. The maximum potential barrier height according to the model of Seto with N_t and L as determined above is ~0.3 eV for a free carrier concentration of $n \approx 3 \cdot 10^{19}$ cm^{-3} (see Figure 5.4 (b)).

The increasing free carrier mobility μ for increasing free carrier concentration n in the range of $n \approx 1 \cdot 10^{20}$ cm^{-3} to $5 \cdot 10^{20}$ cm^{-3} could in principle also be explained by the percolation conduction model. According to this model, local potential barriers are formed due to a statistical potential distribution around the conduction and valence band edge caused by the random distribution of the ions (for instance Al^{3+} or Zn^{2+} in ZnO:Al) in the material.[237,238] Usually, this model is applied to amorphous semiconductors like In-Ga-Zn-O (IGZO) compounds. Hence, this effect is less likely for the ZnO films investigated here, since these films are not amorphous but polycrystalline. In fact, the difference of the electronic transport between amorphous and single (poly) crystalline IGZO was already noted by Nomura et al. (see Figure 2 (b) in Reference 238). Another argument, supporting the grain boundary scattering model, can be derived from experiments performed by Steinhauser et al.[239]. They performed damp-heat tests on polycrystalline B-doped ZnO films and found a significant decrease of the Hall mobility of the charge carriers after the treatment, while the mobility determined by optical measurements was not changed. This means that the bulk of the crystallites still exhibited a high mobility, which would not be expected for a more homogeneous material like an amorphous semiconductor. This shows that the average electronic transport properties were not altered significantly and a mechanism, explaining the electronic transport on the basis of the random distribution of ions, is therefore not likely to be dominant.

Another possible scattering mechanism, describing the observed decrease of the mobility for carrier concentrations below $n \approx 5 \cdot 10^{20}$ cm^{-3}, is dislocation scattering (see Section 2.3.6), which may occur in polycrystalline materials exhibiting a high concentration of dislocations. The scattering of the carriers at charged dislocations in degenerate semiconductors is given by Equation (2.74)

$$\mu_{\mathrm{disl,deg}}^{\mathrm{Hall}} = \frac{4 \cdot 3^{\frac{2}{3}} e c^2 n^{\frac{2}{3}}}{\pi^{\frac{8}{3}} \hbar N_{\mathrm{disl}}} \left[1 + \frac{2 \cdot 3^{\frac{1}{3}} \pi^{\frac{8}{3}} \hbar^2 \varepsilon_0 \varepsilon_s n^{\frac{1}{3}}}{e^2 m^*} \right]^{\frac{3}{2}}, \tag{5.6}$$

where c is a length in the order of a lattice constant and N_{disl} is the dislocation density. The dislocation scattering for degenerate conditions combined with the scattering in the single crystalline ZnO is shown in Figure 5.4 (a) on page 83 as dotted and dash-dotted lines.

The agreement between the theoretical curves and the experimental data is again surprisingly good. For the $\mu(n)$ dependence of the dislocation scattering shown in Figure 5.4 (a), a value of $c = 0.52066$ nm and an effective mass of $m^* = 0.4 m_e$ has been used. The dislocation density N_{disl} was then set to

$2 \cdot 10^{13}$ cm^{-2} to adjust the theoretical curve to the experimental data (see the dash-dotted line in Figure 5.4). This value for N_{disl} is about a factor of 10 higher in comparison to the dislocation densities determined for the polycrystalline films, which exhibited highest values in the range of $1.5 \cdot 10^{12}$ cm^{-2} (the dislocation scattering for $N_{disl} = 1.5 \cdot 10^{12}$ cm^{-2} is represented by the dotted curve). However, neither for the degenerate case nor for the dislocation scattering in the non-degenerate case, which is proportional to √n, the carrier mobility will increase again when the carrier concentration falls beneath a lower limit. This effect is only observed for the grain boundary scattering, where the potential barrier height decreases when the free carrier concentration falls below N_t/L. This reduction of the Hall mobility in a limited range of the free carrier concentrations was, for example, reported for ZnO:Ga films epitaxially grown on $ScAlMgO_4$ substrates by Makino et al.[240]. It has also been observed for the films investigated here and will be discussed in Section 5.3. Yet, this cannot be used to reliably exclude the dislocation scattering as a reason for the reduced mobilities, because these films were epitaxially grown with a low dislocation density N_{disl} in the order of 10^6 cm^{-2}. For such low values of N_{disl}, the dislocation scattering does not decrease the mobility with respect to the single crystalline values. On the other hand, based on the damp-heat treatments, it could again be argued that the scattering centres are not homogeneously distributed in the bulk of the film and cannot be avoided, which points to extended defects like grain boundaries and not to dislocations.

Based on these considerations, the Hall mobility as a function of the free carrier concentration of the polycrystalline films will be modelled taking into account the fit to the transport data of the single crystalline ZnO with Masetti's formula and the grain boundary scattering. In Section 2.3.4, a simple model for the grain boundary scattering, based on the assumptions made in the Seto model but for arbitrary degeneracy, was presented. The Hall mobility according to this model is given by

$$\mu_{GB,arbdeg}^{Hall} = \frac{eLN_C}{n\sqrt{2\pi m^* kT}} \ln\left(1 + e^{-\left(\frac{E_B}{kT} - \eta\right)}\right), \tag{5.7}$$

where $\eta = (E_F - E_c)/(kT)$ is expressed by Equation (2.68), E_B has the same meaning as in the classical Seto model, and the differences in the average carrier concentration n_a and the carrier concentration in the non-depleted region of the grain n_0 are neglected to make this model applicable to a fit procedure to the experimental data. Figure 5.5 shows the data of the ZnO:Al films deposited with different plasma excitation frequencies (see also Figure 5.4) together with a fit using the combined transport model for arbitrary degeneracy. For comparison, the fit curve based on the classical Seto model is also shown.

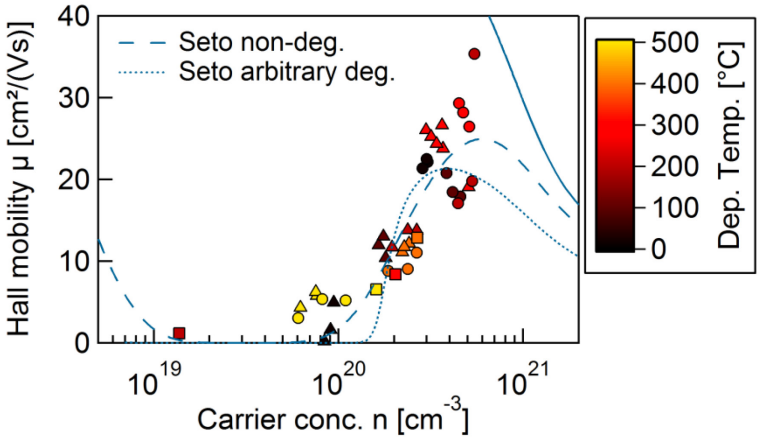

Figure 5.5: Hall mobility μ as a function of the free carrier concentration *n* for the ZnO:Al films deposited using DC (squares), 13.56 MHz (triangles), and 27.12 MHz (circles) plasma excitation frequency. The dashed line shows a fit to the experimental data with the combined transport model using the classical Seto formula for non-degenerate semiconductors, the dotted line depicts a fit using the combined transport model for arbitrary degeneracy ($N_t = (4.12 \pm 0.16) \cdot 10^{13}$ cm^{-2}, $L = (10.7 \pm 1.3)$ nm, $m^* = 0.4 m_e$).

The model for arbitrary degeneracy describes the trend of the experimental data less accurate in comparison to the classical model. This is caused by the strong increase of the simulated Hall mobility

with increasing free carrier concentration in the range between $n = 1 \cdot 10^{20}$ cm^{-3} and $n = 5 \cdot 10^{20}$ cm^{-3}. Since the Fermi level is strongly increasing in that range, the potential barriers at the grain boundaries are quickly surmounted and the steep slope of the mobility curve cannot significantly be altered, because the change of the height of the potential barrier with varying free carrier concentration has no influence on the electrons contributing to the conduction anymore. This limits the ability of the fit curve to approach the experimental data. The good agreement between the model for non-degenerate semiconductors (classical Seto model) and the experimental data, on the other hand, can be attributed to two effects: First, the error introduced by the fact that the Fermi level does not increase relative to the potential barriers in the conduction band is compensated by the decreasing potential barrier height with increasing free carrier concentration, and second, the classical Seto model has more degrees of freedom. In fact, the change of the potential barrier height with changing free carrier concentration and therefore the slope of the increase of $\mu(n)$ can be adjusted with two parameters in this model – N_t and L. In the model for arbitrary degeneracy, however, the increase is fixed by $E_F(n)$ according to Nilsson's formula. This also has an influence on the parameters determined from a fit with the model to the experimental data. The values determined for the trap density N_t in the ZnO:Al films deposited at different discharge frequencies using the model for arbitrary degeneracy are higher in comparison to those determined with the classical Seto model ($N_{t,arbdeg} = (4.12 \pm 0.16) \cdot 10^{13}$ cm^{-2}, $N_{t,non\text{-}deg} = (1.99 \pm 0.14) \cdot 10^{13}$ cm^{-2}).

Attempts to model the grain boundary scattering for arbitrary degeneracy have also been made by Prins et al.[241], Pisarkiewicz et al.[79], Lipperheide and coworkers[242], and Kajikawa et al.[243]. However, Prins et al., for example, did not give an explicit expression for the barrier height and kept it as a fit parameter. But for strong degeneracy, the potential barrier starts to correlate with the grain size, which means that it is not possible to determine these parameters independently from each other in their model. Pisarkiewicz and coworkers included the trap density at the grain boundaries as an acceptor concentration in the ionized impurity scattering and combined this with the classical Seto formula for the grain boundary scattering. But when the trap density is included in the ionized impurity scattering, this leads to a $\mu(n)$ dependence, which alone is able to explain the reduction of the Hall mobility with decreasing free carrier concentration below $n \approx 5 \cdot 10^{20}$ cm^{-3}. Since this is the same $\mu(n)$ dependence as it is modelled with the grain boundary scattering, the fit parameters of their combined model must be strongly correlated to each other and therefore unreliable as well. Furthermore, they introduced the acceptor density attributed to the trap states by $N_A^- = N_t/\delta$, with δ being the thickness of the grain boundary region. However, this acceptor density is only present at the grain boundaries and not homogeneously distributed in the films. Hence, this approach is questionable. Lipperheide et al. formulated a more sophisticated model that takes into account the relation between ballistic and diffusive transport, arbitrary degeneracy, and tunnelling currents, but the equations in this model are analytically very complex and therefore not applicable to a fit procedure. The model proposed by Kajikawa et al. cannot be used for a fit procedure for similar reasons. Therefore, the simple model for arbitrary degeneracy derived in this work is advantageous, since it can be applied to a fit procedure to the experimental data, does not only explain the Hall mobility as a function of the free carrier concentration but also as a function of the temperature, and contains almost no parameters correlated to each other, as will be shown in the next section.

Prior to that, the Hall mobility μ as a function of the free carrier concentration n for the $Zn_{1-x}Mg_xO$:Al films deposited at different temperatures using DC, 13.56 MHz, and 27.12 MHz plasma excitation frequency is compared to the ZnO:Al films in Figure 5.6 on page 87.

The Hall mobility of the electrons in the $Zn_{1-x}Mg_xO$:Al films is generally slightly lower in comparison to that of the ZnO:Al films. Furthermore, a fit with the combined transport model is not very reliable for $Zn_{1-x}Mg_xO$:Al, because the data points for the electronic transport above $n \approx 3 \cdot 10^{20}$ cm^{-3} are scarce.

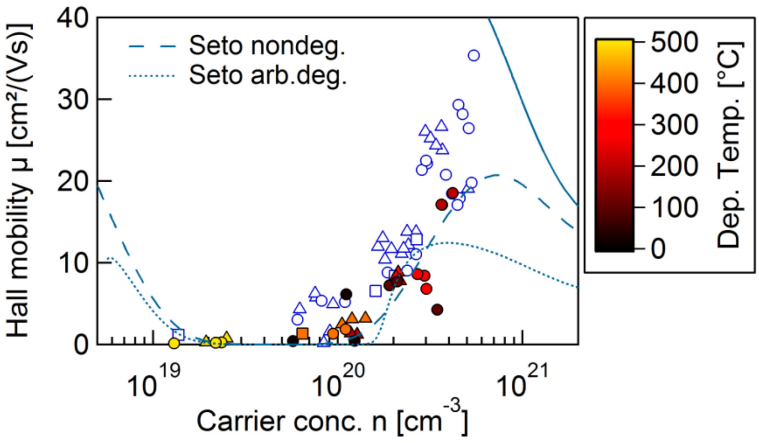

Figure 5.6: Hall mobility μ as a function of the free carrier concentration *n* for the $Zn_{1-x}Mg_xO$:Al films deposited between ~30 °C and 500 °C using DC (squares), 13.56 MHz (triangles), and 27.12 MHz (circles) plasma excitation frequency. The dashed line shows the fit to the experimental data with the combined transport model using the classical Seto formula for non-degenerate semiconductors and the dotted line depicts the fit using the combined transport model for arbitrary degeneracy ($N_t = (4.6 \pm 0.2)\cdot10^{13}$ cm^{-2}, $L = (5.4 \pm 0.6)$ nm, $m^* = 0.35 m_e$). For comparison, the data of the ZnO:Al films are also shown (open markers).

Nevertheless, using the combined transport model for the non-degenerate semiconductor (classical Seto model), a trap state concentration of $N_t = (2.32 \pm 0.11)\cdot10^{13}$ cm^{-2} for a lateral grain size of $L = (5.1 \pm 0.8)$ nm is determined. Employing the model for arbitrary degeneracy to fit the experimental data results in $N_t = (4.6 \pm 0.2)\cdot10^{13}$ cm^{-2} and $L = (5.4 \pm 0.6)$ nm. These values indicate a slightly larger trap density and lower lateral grain size in the $Zn_{1-x}Mg_xO$:Al films in comparison to the ZnO:Al layers. This may be explained by the additional segregation of Mg to the grain boundaries and a generally lower structural quality.

The essentially lower carrier mobility in the $Zn_{1-x}Mg_xO$:Al films can further be investigated by optical transmission and reflection experiments. In a Hall measurement, the current flows horizontally in the films over a great many of grain boundaries. In this case, the carrier mobility is strongly influenced by the potential barriers at the grain boundaries. In the optical measurements, on the other hand, the carriers are only slightly oscillating around their equilibrium positions, which means most of them do not cross the grain boundaries during such a measurement. The optically determined mobility values can therefore be interpreted as intragrain mobilities. Figure 5.7 shows the free carrier concentrations and mobilities for selected samples determined by Hall as well as by optical measurements (assuming $\varepsilon_\infty = 3.7$ and m^* adjusted to $n^{Hall} = n^{opt}$).

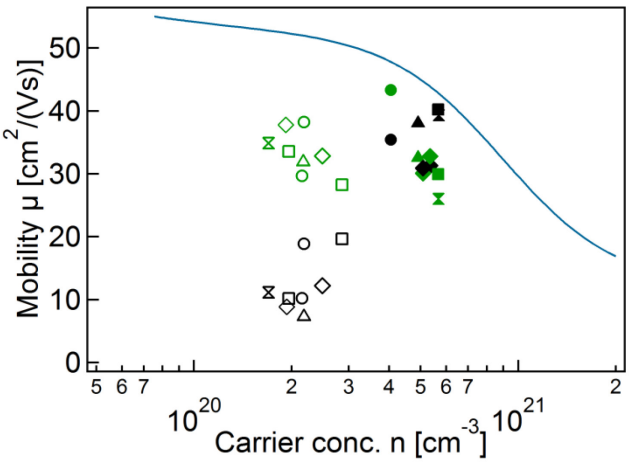

Figure 5.7: Hall mobility μ as a function of the free carrier concentration *n* for selected polycrystalline, heteroepitaxial and homoepitaxial ZnO:Al (filled symbols) and $Zn_{1-x}Mg_xO$:Al (open symbols) films determined by Hall and conductivity measurements (black symbols) as well as from the Drude absorption edge in the near infrared region (NIR) of the optical transmission and reflection spectra (green symbols). The different types of substrates and growth are denoted the following way: a-sapphire: circles, c-sapphire: squares, r-sapphire: triangles, polycrystalline: diamonds, homoepitaxial: double-triangles. The optical data have been fitted using an Adachi oscillator[36] for the band-to-band transitions and a Drude oscillator for the plasmon absorption in the NIR (assuming $\varepsilon_\infty = 3.74$ (see References 22 and 244) and m^* adjusted to $n^{Hall} = n^{opt}$).

For the ZnO:Al films, displayed by filled symbols, the optical (green symbols) and electrical (black symbols) measurements yield nearly the same mobility values ($\mu^{opt} = (32 \pm 6)$ cm²/(Vs), $\mu^{Hall} = (36 \pm 4)$ cm²/(Vs)). This is caused by the high free carrier concentration leading to a limitation of the electronic transport by ionized impurity scattering and not by grain boundary scattering. For the

$Zn_{1-x}Mg_xO$:Al films (open symbols), on the other hand, the optically determined mobility values are higher compared to the values determined by the electric measurements (μ^{opt} = (33 ± 4) cm²/(Vs), μ^{Hall} = (12 ± 5) cm²/(Vs)). This is further proof that grain boundary scattering occurs in these samples. Furthermore, even inside the grains, the mobility is well below the values determined for the single crystalline ZnO (see solid line in Figure 5.7). This clearly points to the occurrence of an additional scattering mechanism, which is not related to grain boundary scattering, phonon scattering, or ionized impurity scattering and is only caused by the Mg in the $Zn_{1-x}Mg_xO$:Al films. To account for the reduced mobility determined by the optical measurement, the additional scattering mechanism must limit μ to a value of (90 ± 30) cm²/(Vs).

Alloy scattering in degenerate semiconductors, caused by the periodic modulation of the lattice potential due to the incorporation of an alloy element, is a plausible candidate. It is described by Equation (2.72),

$$\mu_{\text{alloy,deg}}^{\text{Hall}} = \frac{e\hbar^3 N\left(\frac{\pi}{3}\right)^{\frac{1}{3}}}{2m^{*2}n^{\frac{1}{3}}x(1-x)(\Delta E)^2}, \tag{5.8}$$

where N is the number of atoms per unit volume, x is the fraction of the alloy component, and ΔE is the energy difference between the conduction band edges of ZnO and MgO. A value of 86 cm²/(Vs) for the alloy scattering is calculated when linearly interpolating between the values for the single materials and using $N_{ZnO} \approx 7 \cdot 10^{22}$ cm^{-3} (determined XRR measurements), $N_{MgO} \approx 1.07 \cdot 10^{23}$ cm^{-3} (see Reference 102), $m^*_{ZnO} = 0.28m_e$, $m^*_{MgO} = 0.35m_e$ (see Reference 103), $x = 0.12$, and $\Delta E = 2.7$ eV (see Reference 104), and a free carrier concentration of $n = 2.2 \cdot 10^{20}$ cm^{-3}. The error, however, is large, which can be attributed to the uncertainties of the material parameters. ΔE, for example, has also been reported to be 1.7 eV (wurtzite) or 3.3 eV (rocksalt)[245,246] depending on the assumed crystal structure of the single MgO phase. Still, the calculated value fits well to the 90 cm²/(Vs) determined for the additional scattering mechanism by the optical measurements. Using the above mentioned mobility to include the alloy scattering in the model for μ(n) in $Zn_{1-x}Mg_xO$:Al, a trap density $N_t = (4.5 \pm 0.3) \cdot 10^{13}$ cm^{-2} and a lateral grain size L = (6.0 ± 0.9) nm are determined for the grain boundary scattering. This is within the errors of the values found without alloy scattering.

Another possible explanation for the lower mobility of the charge carriers in the $Zn_{1-x}Mg_xO$:Al films could be an increased effective mass of the electrons. Cohen et al.[41] found an increasing value for the reduced effective mass $1/m^* = 1/m_n + 1/m_p$ with increasing Mg content in their reactively DC sputtered $Zn_{1-x}Mg_xO$:Al,In films, which they attributed to an increase of the free electron mass. Assuming a constant hole effective mass of $m_p^* = 0.59m_e$, their free electron mass increased from $0.26m_e$ for $x = 0.05$ via $0.33m_e$ for $x = 0.1$ to $0.43m_e$ for $x = 0.2$. This results in a possible increase of a factor of roughly 1.3 for the films investigated here ($x \approx 0.12$). Neglecting a change of the scattering mechanisms, this would, according to $\mu = e\langle\tau\rangle/m^*$, reduce the mobility of the carriers by the same factor 1.3. The ratio between the optically determined mobility of the free carriers in the $Zn_{1-x}Mg_xO$:Al in comparison to the single crystalline ZnO, however, is roughly 1.6 ± 0.2. It could be possible that both effects, the alloy scattering and the increase of the effective electron mass, are contributing to the reduction of the mobility of the free carriers. Unfortunately, the available data is too limited to reliably quantify the contribution of both effects.

5.2.2 Carrier Mobility as a Function of the Temperature

In non-degenerate semiconductors, the scattering mechanisms have different temperature dependences. This enables to determine the dominant scattering mechanisms in the material by performing temperature dependent Hall and conductivity measurements. In degenerate semiconductors, on the other hand, the scattering mechanisms such as ionized impurity scattering, alloy scattering, and dislocation scattering are temperature independent. Still, temperature dependent Hall measurements can be used to further investigate the scattering mechanisms even for degenerate semiconductors. Such measurements have been performed in the temperature range between approximately 35 K and 295 K. Figure 5.8 shows the resulting free carrier concentrations n and Hall mobilities μ of the ZnO:Al and $Zn_{1-x}Mg_xO$:Al films.

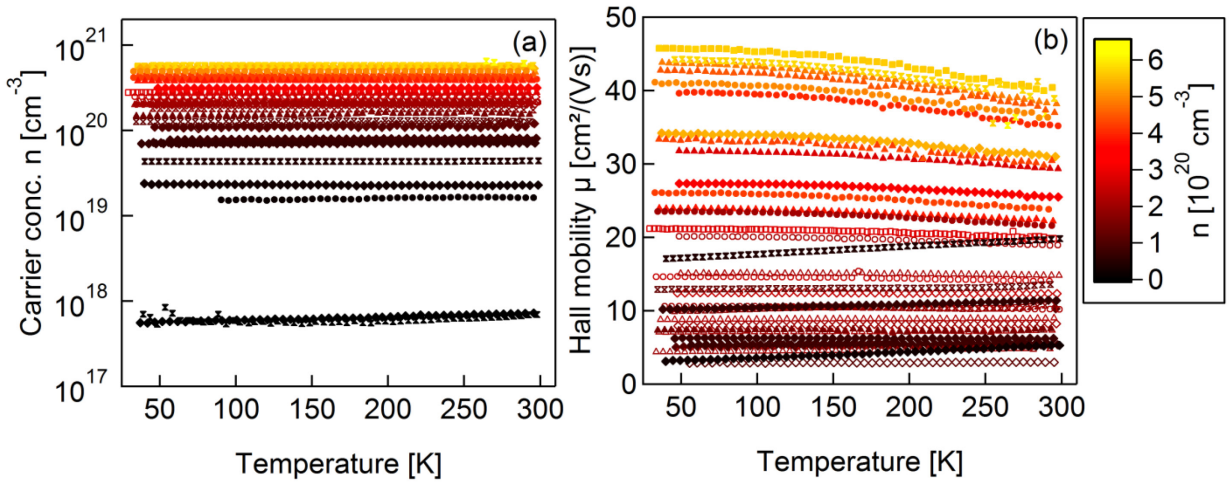

Figure 5.8: (a) Carrier concentration n as a function of the temperature T determined by Hall measurements on selected polycrystalline and epitaxial ZnO:Al and $Zn_{1-x}Mg_xO$:Al samples. (b) Hall mobility as a function of the temperature for the samples presented in (a).

The temperature dependent Hall measurements reveal no significant dependence of the free carrier concentration on the temperature for all films with carrier concentrations higher than $n \approx 5 \cdot 10^{17}$ cm^{-3}. This proves that the Al-doped ZnO and $Zn_{1-x}Mg_xO$ films are degenerately doped semiconductors with an ionization energy of the dopants equal to zero. The Hall mobilities as a function of the temperature, on the other hand, exhibit a very general trend: The films with a high carrier concentration above $n \approx 2 \cdot 10^{20}$ cm^{-3} show an increasing Hall mobility with decreasing temperature. This points to an influence of phonon scattering, since this is the only scattering mechanism expected in the ZnO films with a temperature dependence even in the case of degenerate doping (see Section 2.3.1). For carrier concentrations below $n \approx 4 \cdot 10^{19}$ cm^{-3}, a decreasing Hall mobility with decreasing temperature is determined. This suggests a temperature-activated process like grain boundary scattering. For intermediate carrier concentrations, no temperature dependence of the Hall mobility is observed, which means all dominant scattering mechanisms must be temperature independent in that range.

In the following, the various scattering mechanisms in ZnO will be examined more detailed. Usually, a fit model is established according to Mathiessen's rule using all relevant scattering mechanisms. However, this is not feasible here, because the scattering mechanisms have the same, namely no, temperature dependence, and hence it is not possible to distinguish between them in a fit to the experimental data. Therefore, the different scattering mechanisms will be discussed individually to decrease the number of parameters to still be able to extract valuable information from the temperature dependent Hall measurements.

Piezoelectric Scattering

The piezoelectrically limited mobility in the non-degenerate ZnO is in the range of 2100 cm²/(Vs) at 300 K and thus much higher in comparison to the values of 50 cm²/(Vs) determined for the samples investigated here. For a degenerate material, the piezoelectric scattering is even less compared to a non-degenerate material at any given temperature.[247] Consequently, the piezoelectric scattering does not have to be considered as a dominant scattering mechanism in the ZnO:Al and $Zn_{1-x}Mg_xO$:Al films.

Alloy Scattering

The alloy-scattering limited mobility caused by the Mg in the ZnO films is in the range of 90 cm²/(Vs) as determined by the optical measurements. This scattering mechanism is temperature independent in degenerate semiconductors. Hence, it is not possible to extract any additional information from the temperature dependent Hall measurements. The alloy scattering in the $Zn_{1-x}Mg_xO$:Al films will therefore be taken into account as a temperature independent constant of 90 cm²/(Vs).

Ionized Impurity Scattering

The ionized impurity scattering is temperature independent as well. Additionally, it can only be detected without the influence of grain boundary scattering in the films with the highest carrier concentrations (see for example Figure 5.4 on page 83). At 295 K the electronic transport in these films is further limited by phonon scattering, which can be inferred from the increasing Hall mobility with decreasing temperature. Conveniently, the optical mode phonon scattering and the acoustical mode phonon scattering are proportional to $e^{1/T}$ and 1/T, respectively, which means the dominance of the phonon scattering is reducing with decreasing temperature. Therefore, the mobility of the samples with the highest carrier concentrations at the lowest temperatures is neither significantly influenced by grain boundary scattering nor by phonon scattering. In consequence, under these conditions, the ionized impurity scattering can be determined. For the sample with a carrier concentration of $n = 5.7 \cdot 10^{20}$ cm^{-3}, a value of $\mu_{ii}^{Hall} = 46$ cm²/(Vs) is obtained at $T = 35$ K.

For lower free carrier concentrations, it is more difficult to obtain values for the pure ionized impurity scattering. To solve this problem, the Masetti curve for the single crystalline ZnO, which mainly describes the ionized impurity scattering and the lattice (phonon) scattering in that range of free carrier concentrations, can be employed to determine values for the pure ionized impurity scattering. To separate the ionized impurity scattering from the lattice scattering, the fit with the variable acceptor concentration for the ionized impurity scattering to the Masetti curve for ZnO is used (see the light-blue dashed line in Figure 5.3 on page 82). In this model, the lattice scattering has been combined with the pure ionized impurity scattering as a constant $\mu_{latt} = 210$ cm²/(Vs). Additionally, the acceptor concentration N_A^- has been adjusted to fit the Masetti curve for ZnO. Excluding the lattice scattering, a semi-empirical value for the mere ionized impurity scattering based on the Masetti curve is obtained; 'semi-empirical', because the adjusted acceptor concentration is included. The values for the pure semi-empirical ionized impurity scattering in comparison to the values for the single crystals taking also into account the lattice scattering (Masetti curve for ZnO) are shown in Figure 5.9 on page 91.

Using these semi-empirical values for the ionized impurity scattering without the lattice scattering, a mobility value of $\mu_{ii,semi\text{-}emp}^{Hall} = 54$ cm²/(Vs) is calculated for the sample with the highest carrier concentration. Taking into account, that the mobility at room temperature for this sample is also slightly below the curve for the single crystalline material (see the filled black square in Figure 5.7 on page 87), which means that there is a contribution of grain boundary scattering, the semi-empirical value for the ionized impurity scattering is in reasonable agreement with the experimental value of 46 cm²/(Vs). Therefore, the semi-empirical model for the ionized impurity scattering will be used to

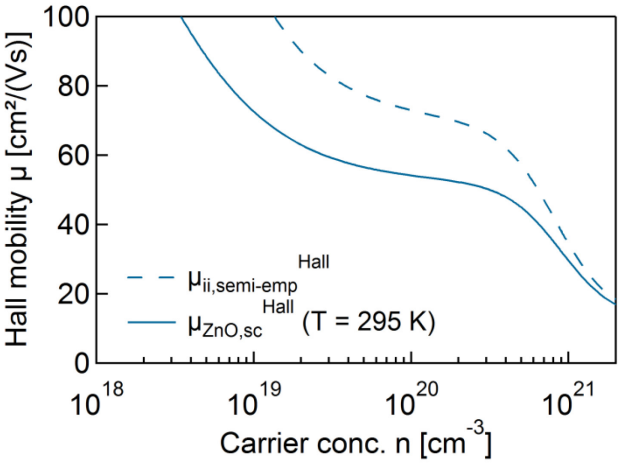

Figure 5.9: Semi-empirical ionized impurity scattering mobility $\mu_{ii,semi\text{-}emp}^{Hall}$ without lattice scattering (dashed line) taking into account compensating acceptors in comparison with the mobility determined by the fit with the Masetti formula to the transport data of single crystalline ZnO (solid line). The compensating acceptor density has been determined by fitting the combined model consisting of the theoretical formula for the ionized impurity scattering (Equations (2.42), (2.44), and (2.46)) and the lattice mobility μ_{latt} = 210 cm²/(Vs) to the Masetti curve for the experimental ZnO data.

calculate the mobility values for the ionized impurity scattering of the samples with lower free carrier concentrations for the following discussion.

Phonon Scattering

As mentioned earlier, the phonon scattering is only detectable in the samples with the highest carrier concentrations and mobilities. In this investigation, these are the ZnO:Al films. Hence, for the initial discussion, the alloy scattering can be neglected. Mathiessen's rule for fitting the mobility of these samples can be written as

$$\frac{1}{\mu} = \frac{1}{\mu_{const}} + \frac{1}{\mu_{LO,deg}^{Hall}} + \frac{1}{\mu_{ac,deg}^{Hall}}, \tag{5.9}$$

where $\mu_{LO,deg}^{Hall}$ is the longitudinal-optical phonon scattering according to Equation (2.35), $\mu_{ac,deg}^{Hall}$ is the acoustical phonon scattering according to Equation (2.38), and μ_{const} is a temperature independent contribution of the ionized impurity scattering and the grain boundary scattering to describe the values for the lowest temperatures. Using ε_∞ = 3.74, ε_s = 8.34, and m^* according to the fit of the data of Young et al. (see Section 2.3.3), the energy of the longitudinal-optical phonon $\hbar\omega_0$ and the deformation potential energy for the acoustical phonon scattering E_{ac} as well as the dominance of both scattering mechanisms can be determined by using $\hbar\omega_0$, E_{ac}, and μ_{const} as fit parameters. Yet, it has to be kept in mind that the formula for the optical phonon scattering has been derived under an assumption, which is violated for carrier concentrations above $n \approx 10^{19}$ cm^{-3}. But since no other formula for arbitrary degeneracy is available, this inconsistency must be neglected here, assuming that the deviations are not too severe. Figure 5.10 shows the experimental data together with the fit curves.

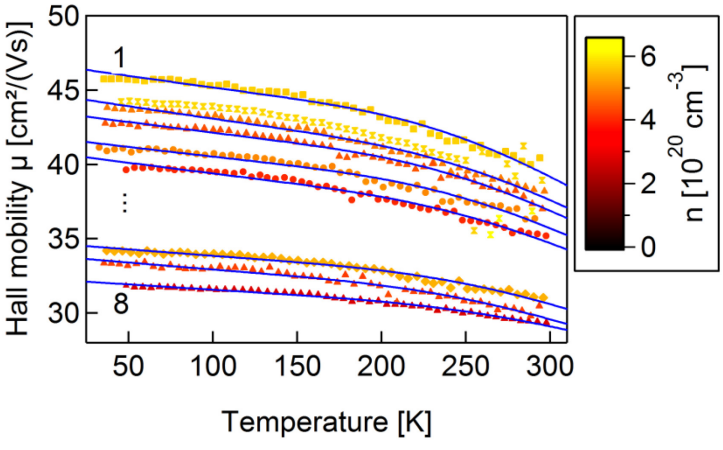

Figure 5.10: Fitted Hall mobility μ as a function of the temperature *T*. The model consists of a combination of a temperature independent term, the acoustical phonon scattering, and the longitudinal-optical phonon scattering for degenerate conditions according to Mathiessen's rule. Fit parameters were $\hbar\omega_0$, E_{ac}, and the temperature independent term, while *n*, ε_s, ε_∞, and m^* have been kept constant.

The results of the fits are summarized in Table 5.4.

Table 5.4: Parameters determined by and used for the fits of the phonon scattering model to the temperature dependent Hall mobility.

Fitnumber	n [10^{20} cm^{-3}]	m^* [m_e]	μ_{const} [cm²/(Vs)]	E_{ac} [eV]	$\hbar\omega_0$ [meV]
1	5.7	0.49	46.78 ± 0.13	7.0 ± 0.2	124 ± 2
2	4.8	0.47	44.79 ± 0.10	8.15 ± 0.18	126 ± 2
3	4.4	0.46	43.61 ± 0.10	8.0 ± 0.2	122 ± 2
4	4.9	0.47	41.86 ± 0.11	7.6 ± 0.3	124 ± 3
5	4.0	0.45	40.87 ± 0.12	8.9 ± 0.3	125 ± 3
6	5.3	0.48	34.74 ± 0.08	7.2 ± 0.3	127 ± 3
7	4.2	0.45	33.89 ± 0.12	8.6 ± 0.4	122 ± 4
8	2.8	0.41	32.30 ± 0.05	9.2 ± 0.3	128 ± 3
Average				8.1 ± 0.8	125 ± 2

The average value determined for the energy of the longitudinal-optical phonon is $\hbar\omega_0 = 125 \pm 2$ meV. This is in the same order as the value of $\hbar\omega_0 = 72$ meV determined by Damen et al.[67] by Raman scattering in ZnO single crystals and Sahoo et al.[248] in ZnO nanoparticles. The deformation potential energy for the acoustical phonon scattering is $E_{ac} = (8.1 \pm 0.8)$ eV, which is within the range of 1.4 eV reported by Solbrig[249] and 31.4 eV reported by Wagner and Helbig[72] but lower in comparison to the value determined by the fit to the data of the single crystalline ZnO for low free carrier concentrations of $E_{ac} = 26$ eV. Rode[214] reviewed the literature data for other II-IV compounds such as CdS, CdSe, CdTe, ZnS, ZnSe, and ZnTe and found values ranging from $E_{ac} = 9.5$ eV for CdTe and ZnTe to 14.5 eV for CdSe and ZnSe, which are closer to the 8.1 eV determined here.

Since the values of the fit parameters are all roughly in the same range for the different samples, it will be assumed that the phonon scattering of all samples of the temperature dependent Hall measurements can be described by these values. Therefore, in the following discussion, the phonon scattering will be calculated using the average values determined for E_{ac} and $\hbar\omega_0$ and the corresponding free carrier concentrations and effective masses. Unfortunately, all $Zn_{1-x}Mg_xO$:Al films exhibit strong alloy and grain boundary scattering, which means the phonon scattering is not detectable in these samples. Hence, it must be assumed that the parameters determined for the phonon scattering in the ZnO:Al films are also valid for the $Zn_{1-x}Mg_xO$:Al films.

Grain Boundary Scattering

Based on the investigation of the Hall mobility as a function of the free carrier concentration at room temperature, it became clear that the reduced mobility in the samples with a lower carrier concentration is mainly caused by grain boundary scattering. Still, especially the samples with a mobility below 30 cm²/(Vs) exhibit almost no temperature dependence of the mobility. As already pointed out, this means all dominant scattering mechanisms are temperature independent. Since grain boundary scattering is a dominant scattering mechanism, this behaviour cannot be explained by the classical Seto model for grain boundary scattering. In this model, the mobility is always decreasing with reducing temperature. Werner[250] also found curved Arrhenius plots of the conductivity, which means a deviation from the exponential activation of the mobility as a function of the temperature. He modelled this by introducing a variation of the average grain boundary potential barrier height. This, however, can lead to divergent mobilities for very low temperatures, and the basic formula is still only valid for non-degenerate semiconductors. Hence, it is no solution for the samples investigated here. The model derived for arbitrary degeneracy, on the other hand, can be used to explain the temperature independent Hall mobility as an effect of grain boundary scattering as will be shown below.

Since the parameters for the other scattering mechanisms have been determined, the only scattering mechanism left with variable parameters is the grain boundary scattering. In the following, the temperature dependent Hall mobility data will be fitted using

$$\frac{1}{\mu} = \frac{1}{\mu^{\text{Hall}}_{\text{ii,semi-emp}}} + \frac{1}{\mu^{\text{Hall}}_{\text{LO,deg}}} + \frac{1}{\mu^{\text{Hall}}_{\text{ac,deg}}} + \left(\frac{1}{\mu^{\text{Hall}}_{\text{alloy,deg}}} \right) + \frac{1}{\mu^{\text{Hall}}_{\text{GB,arbdeg}}}, \tag{5.10}$$

where $\mu^{\text{Hall}}_{\text{ii,semi-emp}}$ will be calculated according to the semi-empirical model for the ionized impurity scattering, $\mu^{\text{Hall}}_{\text{LO,deg}}$ and $\mu^{\text{Hall}}_{\text{ac,deg}}$ will be modelled using the average values determined by the fit of the data of the samples with a high mobility, and, if necessary, the alloy scattering will be included as well. The grain boundary scattering will be calculated using the free carrier concentration of the samples as determined by the Hall measurements and the effective mass according to the fit of the data of Young et al. (see Section 2.3.3). Since for high free carrier concentrations, the Hall mobility is proportional to the ratio of the lateral grain size L and the trap density N_t, which means these parameters are correlated, an increase of the lateral grain size L will lead to an increase of the constant value of the Hall mobility, while a decrease of the trap density N_t will do the same and vice versa. Consequently, these parameters cannot be fitted separately. It is therefore assumed that the films have a lateral grain size of 10 nm, and hence the trap density is the only fit parameter. Figure 5.11 shows the results of the fits.

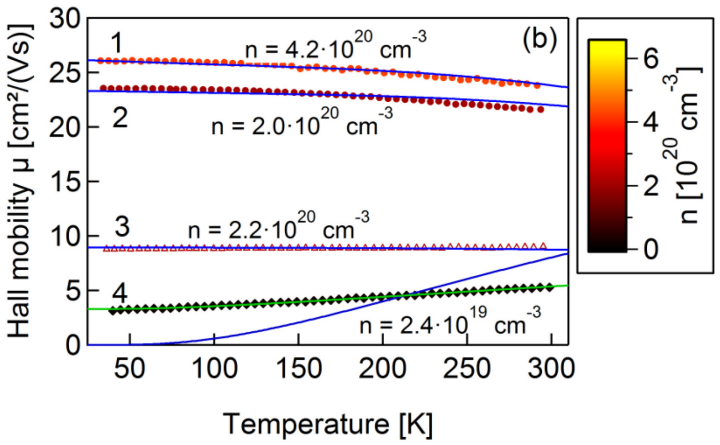

Figure 5.11: Fits of the Hall mobility μ as a function of the temperature *T* according to Equation (5.10) for selected ZnO:Al and $Zn_{1-x}Mg_xO$:Al films. The blue lines show the curves using the carrier concentration determined by the Hall measurements, the green line shows a fit with a variable free carrier concentration.

For high free carrier concentrations in the range of 10^{20} cm^{-3}, the temperature independent Hall mobility can be described by the combined transport model and specifically the grain boundary scattering for arbitrary degeneracy very well. The trap densities determined for the curves '1', '2', and '3' are $N_t = 2.1 \cdot 10^{13}$ cm^{-2}, $3.2 \cdot 10^{13}$ cm^{-2}, and $4.8 \cdot 10^{13}$ cm^{-2}, respectively. The errors of the fits are very small since the trap density is the only adjustable parameter and are therefore not given. For the sample with the lowest carrier concentration ('4'), a slight temperature activation of the Hall mobility is observed. This temperature dependence, however, is less strong than the theory predicts with the carrier concentration determined by the Hall measurement, $n = 2.4 \cdot 10^{19}$ cm^{-3}, and can therefore not be fitted properly (see the blue line for fit '4' in Figure 5.11). An appropriate fit is only possible when using n as additional fit parameter (see the green line in Figure 5.11). A carrier concentration of $n = 1.3 \cdot 10^{20}$ cm^{-3} and a trap density of $N_t = 3.9 \cdot 10^{13}$ cm^{-2} is then obtained. Obviously, the theoretical model is able to predict the temperature dependence of the Hall mobility, only the dependence on the free carrier concentration is not correct yet.

This is not surprising, because, according to the theory, the Fermi level is equal to the conduction band bottom at a free carrier concentration of $N_c \approx 3.6 \cdot 10^{18}$ cm^{-3}. This cannot be correct for the samples investigated here since there is no temperature dependence of the carrier concentration even for

samples with n as low as $6 \cdot 10^{17}$ cm^{-3}. These films are obviously also degenerately doped. If a lower value for N_c is assumed, the less strong temperature activation of the Hall mobility, which is an effect of the increased Fermi level, will be shifted to lower free carrier concentrations. In this case, the theoretical model should be able to describe the temperature dependence of the Hall mobility for low carrier concentrations as well. A curve identical to the green line in Figure 5.11 for the temperature dependence of the Hall mobility of the sample with a low free carrier concentration can be obtained for the correct carrier concentration if the value of N_c is multiplied by a factor of 0.18, which has been determined using a variable fit factor in the formula for N_c. Taking this into account, the semiconductor is degenerate for free carrier concentrations above $n \approx 6.5 \cdot 10^{17}$ cm^{-3}. This is then no longer in contradiction to the measured temperature dependence of the free carrier concentration. Using this value for N_c in the combined transport model to determine an average value for the grain size L and the trap density at the grain boundaries N_t from the $\mu(n)$ data yields the same general shape of the curves as shown in Figure 5.5 on page 85 and Figure 5.6 on page 87 for the ZnO:Al and $Zn_{1-x}Mg_xO$:Al films but $N_t = (6.9 \pm 0.2) \cdot 10^{13}$ cm^{-2} with $L = (17 \pm 2)$ nm (using an average $m^* = 0.4m_e$) and $N_t = (7.8 \pm 0.6) \cdot 10^{13}$ cm^{-2} with $L = (10 \pm 2)$ nm (for $m^* = 0.35m_e$), respectively. For both materials, the trap densities at the grain boundaries as well as the lateral grain sizes are higher in comparison to the fit with the theoretical value for N_c.

This shows the ability of the model for arbitrary degeneracy to explain the main trends of the experimental data. However, with respect to the $\mu(n)$ dependence, the assumption of a single lateral crystallite size and a single trap density for all films is oversimplifying, since the data can only be reproduced qualitatively. The temperature dependence of the Hall mobility, on the other hand, can be described very well by the model for the grain boundary scattering for arbitrary degeneracy, whereas this would not be possible with the classical Seto model. Yet, exact absolute values for the lateral grain sizes and the trap densities cannot be determined, because these parameters are correlated to each other in the fit. To extract the trap densities, the lateral grain size needs to be known with a much higher accuracy. Further complicating is the distribution of the grain sizes and their variation throughout the depth of the film.

Although the grain boundary scattering limits the mobility drastically, no significant temperature dependence or temperature activation can be observed. This may be surprising, but within the model, this temperature independence can be explained by the fact that the Fermi energy lies above the maxima of the potential barriers. Still, one could argue that the potential barriers should have no influence at all in this case. But yet, the Hall mobility is decreased. A qualitative explanation is the following: At higher temperatures, the electrons have an energy distribution around the Fermi energy with the result that not all states below the Fermi energy are occupied and therefore a part of the electrons, which contribute to the conduction, are hindered from moving due to the potential barriers that penetrate this region (see Figure 5.12).

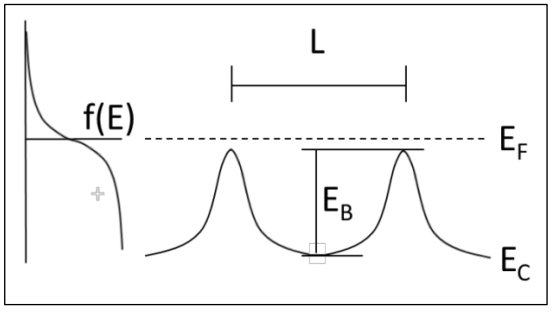

Figure 5.12: One dimensional schematic representation of the energy band diagram of a grain with potential barriers at the grain boundaries. Also indicated is the Fermi-Dirac distribution *f*(*E*) for temperatures above 0 K.

This reduces the Hall mobility of the free carriers in comparison to a material without grain boundaries to an effective mobility $\mu_{eff} < \mu_{sc}$. When the temperature decreases, the difference between the

conduction band bottom and the Fermi energy $E_F - E_c = \eta kT$ as well as the potential barrier height E_B remain constant (see also Section 2.3.4), while the distribution of the electrons contributing to the conduction around E_F narrows, which would in the first moment lead to the expectation that the effective mobility should increase. However, the density of states at the conduction band bottom N_c decreases at the same time, so that the overall number of electrons contributing to the conduction is reduced. Due to the specific temperature dependence of the terms, this effect cancels out, and hence the effective Hall mobility remains constant and therefore at a low value even for very low temperatures.

The results for the parameters of the different scattering mechanisms based on the previous investigation of the $\mu(n)$ and $\mu(T)$ data are summarized in Table 5.5. The range of the values for the trap density N_t and the lateral grain size L was obtained by adjusting these parameters for the different experimental mobility values in the carrier concentration range from $n \approx 5 \cdot 10^{19}$ cm^{-3} to $5 \cdot 10^{20}$ cm^{-3}.

Table 5.5: Parameters for the scattering mechanisms in ZnO:Al and $Zn_{1-x}Mg_xO$:Al determined from the $\mu(n)$ and $\mu(T)$ Hall data. The ranges for the values of the trap density N_t and the lateral grain size L have been obtained by adjusting these parameters for the different experimental mobility values for carrier concentrations between $n \approx 5 \cdot 10^{19}$ cm^{-3} and $5 \cdot 10^{20}$ cm^{-3}. The values in brackets stem from the fit of the $\mu(n)$ data with variable N_c.

Parameter	ZnO:Al	$Zn_{0.88}Mg_{0.12}O$:Al
E_{ac} [eV]	8.1 ± 0.8	(8.1 ± 0.8)
$\hbar\omega_0$ [meV]	125 ± 2	(125 ± 2)
ΔE [eV]		2.7
N_t [10^{13} cm^{-2}]	2...9 (6.9 ± 0.2)	2...9 (7.8 ± 0.6)
L [nm]	10...50 (17 ± 2)	10...50 (10 ± 2)

A variation of the lateral grain size between 10 nm and 50 nm is reasonable with respect to the results of the cross-sectional TEM measurements. Remarkably, the trap density N_t in the range of $2 \cdot 10^{13}$ cm^{-2} to $9 \cdot 10^{13}$ cm^{-2} corresponds to an electrically active defect concentration at the grain boundaries between 1 at.% and 5 at.% (assuming an areal atomic concentration of $(7 \cdot 10^{22})^{2/3}$ atoms/cm^2 = $1.7 \cdot 10^{15}$ atoms/cm^2 in ZnO). These values are considerably high.

Using the single values for N_t and L determined from the $\mu(n)$ data, the other parameters as given in Table 5.5, and the average m^* as used before, the relative contribution of the scattering mechanisms at room temperature for degenerate conditions can be calculated. The results are shown in Figure 5.13.

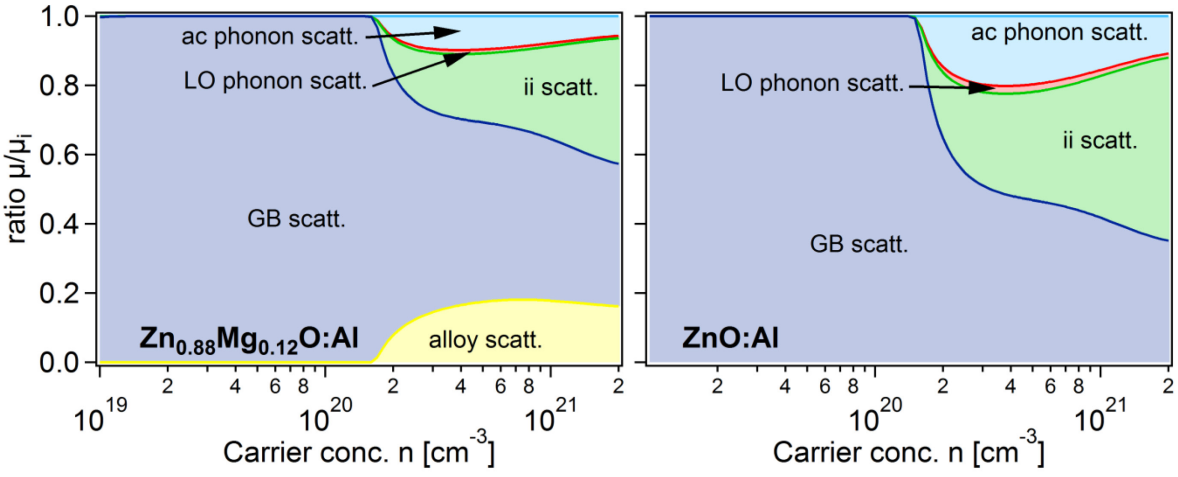

Figure 5.13: Relative contribution of the scattering mechanisms in the $Zn_{0.88}Mg_{0.12}O$:Al (*left*) and ZnO:Al (*right*) films (alloy scattering: yellow, acoustical mode phonon scattering: light blue, longitudinal-optical mode phonon scattering: red, ionized impurity scattering: green, grain boundary scattering: dark blue) as a function of the free carrier concentration for degenerate conditions.

The scattering in the films is dominated by grain boundary scattering and ionized impurity scattering. While the grain boundary scattering is absolutely dominant in the range below $n \approx 10^{20}$ cm^{-3}, it still prevails above these values. This is due to the inaccurate description of $\mu(n)$ when using a single trap state concentration and lateral grain size. A more accurate model for the grain boundary scattering as a function of the free carrier concentration would reduce this dominance. The phonon scattering is not negligible in both materials. It accounts to at least more than 20 % of the scattering in ZnO:Al and 10 % in $Zn_{0.88}Mg_{0.12}O$:Al. The contribution of the longitudinal-optical phonon scattering is far less in comparison to the acoustical phonon scattering, which is in contrast to the findings of Rode[71]. But Rode referred to non-degenerate ZnO, which means the scattering mechanisms may well be different in his case. The portion of ionized impurity scattering is, as expected, increasing with increasing free carrier concentration.

These results show that it is possible to model the scattering mechanisms in degenerately doped ZnO, but they also show the necessity to verify that the fit parameters are not correlated to each other. Furthermore, it became clear that a model, for example the classical Seto model, may explain one dependence ($\mu(n)$) very well, whereas it may be completely unable to model related data from the same samples ($\mu(T)$). Therefore, one has to be very cautious when interpreting the results presented in the literature for investigations of scattering mechanisms, especially in degenerate semiconductors. On this account, the Seebeck coefficient of the samples has been determined to obtain additional information that can be used to consolidate the previous results.

5.2.3 Seebeck Coefficient as a Function of the Carrier Concentration

The Seebeck effect is the generation of a majority carrier current in a material by a temperature gradient. Therefore, it can also be used to extract information about the transport properties of the free carriers in a semiconductor. Figure 5.14 shows the Seebeck coefficients of the ZnO:Al and $Zn_{1-x}Mg_xO$:Al films deposited at different substrate temperatures in the range of ~30 °C to 500 °C using DC, 13.56 MHz RF, and 27.12 MHz RF plasma excitation.

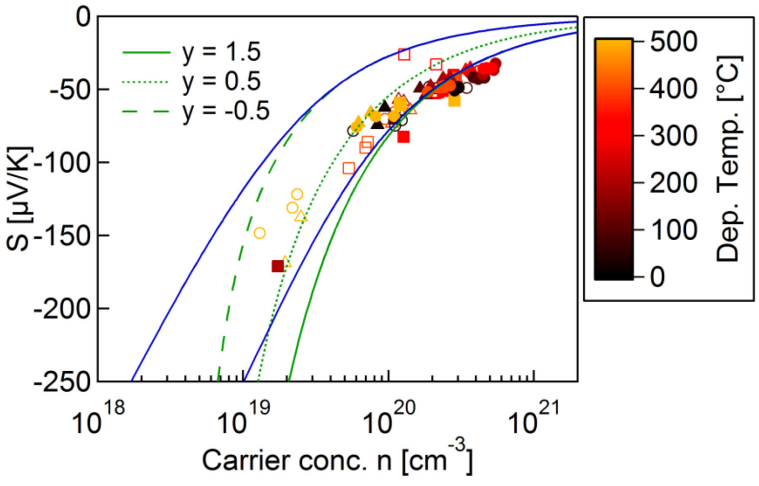

Figure 5.14: Seebeck coefficient *S* as a function of the free carrier concentration *n* of the ZnO:Al (filled symbols) and $Zn_{1-x}Mg_xO$:Al (open symbols) films deposited at temperatures between ~30 °C and 500 °C using DC (squares), 13.56 MHz (triangles), and 27.12 MHz (circles) plasma excitation frequency. The green lines represent theoretical values determined by Equation (5.11) using *y* = 1.5 (solid line), *y* = 0.5 (dotted line), and *y* = –0.5 (dashed line). The blue lines show the Seebeck coefficient for *y* = 1.5 and *y* = –0.5 using a more exact theoretical solution (Equation (5.12)).

The Seebeck coefficient is negative, which proves that electrons are the majority charge carriers. The absolute values are high for low free carrier concentrations and decreasing with increasing free carrier concentration in the range from approximately –200 µV/K to –50 µV/K. Values of this order have also been measured by Ellmer and Mientus[251] for their magnetron sputtered In_2O_3:Sn and ZnO:Al films. They are even comparable to the values reported by Kishimoto et al.[252] for RF sputtered degenerate n-type PbTe. The green curves in Figure 5.14 are calculated using the formula for the Seebeck coefficient in a degenerate parabolic semiconductor (see Reference 50 page 82),

$$S = -\frac{k}{e}\left(y+\frac{3}{2}\right)\frac{\pi^2}{3}\frac{1}{\eta}, \tag{5.11}$$

and $\eta kT = E_F - E_c$ according to Nilsson (Equation (2.26)). In this formula y, the scattering exponent, describes the dominant scattering mechanism: $y = 1.5$ for scattering at ionized impurities, $y = 0.5$ for piezoelectric scattering, $y = 0$ for scattering at neutral impurities, and $y = -0.5$ for scattering at acoustical phonons, dislocations, or grain boundaries.[251,253] For high carrier concentrations, the measured data are close to the curve for $y = 1.5$, which points to ionized impurity scattering as the dominant scattering mechanism. This is consistent with the results of the previous section and Ellmer and Mientus[251]. For lower free carrier concentrations, there are deviations from the curve for the ionized impurity scattering. These values are closer to the theoretical curves for the neutral impurity scattering ($y = 0$) or acoustical phonon, dislocation, or grain boundary scattering ($y = -0.5$). This is again in agreement with the results of the previous section, in which it was shown that below $n \approx 10^{20}\,\mathrm{cm}^{-3}$ the main scattering mechanism is grain boundary scattering.

An additional reason for the deviation of the curves from the experimental data for low free carrier concentrations is the fact that Equation (5.11) is only an approximation for high values of η, which means high values of the free carrier concentration. The (more) exact theoretical value for the Seebeck coefficient for parabolic materials is given by[253]

$$S_y = -\frac{k}{e}\left[\frac{\left(y+\frac{5}{2}\right)\Gamma(y+\frac{3}{2})\mathscr{F}_{y+3/2}(\eta)}{\left(y+\frac{3}{2}\right)\Gamma(y+\frac{1}{2})\mathscr{F}_{y+3/2}(\eta)}-\eta\right] = -\frac{k}{e}\left[\frac{\left(y+\frac{5}{2}\right)F_{y+3/2}(\eta)}{\left(y+\frac{3}{2}\right)F_{y+1/2}(\eta)}-\eta\right], \tag{5.12}$$

where $\mathscr{F}_j(\eta) = \frac{1}{\Gamma(j+1)}\int_0^\infty \frac{x^j}{e^{x-\eta}+1}\mathrm{d}x = \frac{1}{\Gamma(j+1)}F_j(\eta)$ is the Fermi-Dirac integral. For integer values of j, the integral can be extended into a polynomial depending on $F_j(-\eta)$. For negative arguments, the expansion is, independent of j, convergent and the Fermi-Dirac integral can be expressed as $F_j(-\eta) = \Gamma(j+1)\sum_{r=1}^{\infty}\frac{(-1)^{r+1}e^{-r\eta}}{r^{j+1}}$.[254] For the expansion of the Fermi-Dirac integrals with the negative argument, the first term is sufficient for the simulation of the Seebeck coefficient. The polynomial expression for the positive arguments has been tabulated by Blakemore (see Reference 255 page 361). With that, the more exact formula of the Seebeck coefficient is given by

$$S_{y=1.5} = -\frac{k}{e}\left[\frac{4\cdot 6\left(-e^{-\eta}+\frac{\eta^4}{24}+\frac{\pi^2\eta^2}{12}+\frac{7\pi^4}{360}\right)}{3\cdot 2\left(e^{-\eta}+\frac{\eta^3}{6}+\frac{\pi^2\eta}{6}\right)}-\eta\right] \tag{5.13}$$

for ionized impurity scattering and

$$S_{y=-0.5} = -\frac{k}{e}\left[\frac{2\left(-e^{-\eta}+\frac{\eta^2}{2}+\frac{\pi^2}{6}\right)}{\ln\left(1+e^{\eta}\right)}-\eta\right] \tag{5.14}$$

for scattering at acoustical phonons, dislocations, or grain boundaries. For large values of η, these equations reduce to the approximated result given by Equation (5.11) for the corresponding scattering exponent. Another way to calculate the Fermi-Dirac integrals $F_j(\eta)$ is to use Lerch's transcendental

function $\Phi(z,s,a)$ and the relation $F_j(\eta) = \Gamma(j+1)e^{\eta}\Phi(-e^{\eta},j+1,1)$ in Mathematica[256,253] The results of the simulations with the more precise solution are shown as solid blue lines in Figure 5.14 on page 96. Clearly, these solutions are more appropriate to describe the dependence of the Seebeck coefficient on the free carrier concentration.

The models previously discussed take into account the grain boundary scattering only by a specific scattering exponent. More elaborated models for the Seebeck coefficient in polycrystalline materials, however, are very scarce in literature. A formula derived by Jerhot and Vlček[257] correlates the Seebeck coefficient in polycrystalline materials, where thermionic carrier transport prevails, to the size of the region in the grain with a low resistivity d_{bulk} and the size of the intergrain region with a high resistivity d_{GB},

$$S_{poly} = \frac{S_{sc}}{1+\frac{d_{GB}}{d_{bulk}}}, \tag{5.15}$$

where S_{sc} is the Seebeck coefficient of the single crystalline material (valid for $d_{bulk} \gg d_{GB}$). Jerhot and Vlček pointed out that the size of the intergrain region is usually small in comparison to the grain size, and therefore the Seebeck coefficient is still approximately given by the prevailing scattering mechanism in the bulk of the grains. However, this model is not applicable to free carrier concentrations below $n \approx 10^{20}$ cm^{-3}, where the depletion region extends over the whole grain and the electronic transport is nearly completely suppressed.

Kajikawa[253] proposed a more appropriate solution to describe the Seebeck coefficient in degenerate polycrystalline materials. According to the energy filtering model, he assumed that the momentum relaxation time $\tau(E)$ is not influenced for $E > E_B$ (E_B: potential barrier height at the grain boundary), while $\tau = 0$ for $E < E_B$ and obtained (with $\varepsilon_B = E_B/(kT)$)

$$S_{poly} = -\frac{k}{e}\left[\frac{\left(\frac{1}{1+e^{\varepsilon_B-\eta}}\right)\varepsilon_B^{y+5/2} + (y+5/2)F_{y+3/2}(\varepsilon_B,\eta)}{\left(\frac{1}{1+e^{\varepsilon_B-\eta}}\right)\varepsilon_B^{y+3/2} + (y+3/2)F_{y+1/2}(\varepsilon_B,\eta)} - \eta\right], \tag{5.16}$$

where $F_j(\varepsilon_B,\eta)$ is defined as

$$\begin{aligned}
F_0(\varepsilon_B,\eta) &= F_0(\eta-\varepsilon_B),\\
F_1(\varepsilon_B,\eta) &= F_0(\eta-\varepsilon_B)\varepsilon_B + F_1(\eta-\varepsilon_B),\\
F_2(\varepsilon_B,\eta) &= F_0(\eta-\varepsilon_B)\varepsilon_B^2 + 2F_1(\eta-\varepsilon_B)\varepsilon_B + F_2(\eta-\varepsilon_B),\\
F_3(\varepsilon_B,\eta) &= F_0(\eta-\varepsilon_B)\varepsilon_B^3 + 3F_1(\eta-\varepsilon_B)\varepsilon_B^2 + 3F_2(\eta-\varepsilon_B)\varepsilon_B + F_3(\eta-\varepsilon_B).
\end{aligned} \tag{5.17}$$

Using the height of the potential barrier according to Seto's model as a function of the free carrier concentration for a trap density at the grain boundaries of $N_t = 5\cdot10^{12}$ cm^{-2} in Kajikawa's model, the values for the Seebeck coefficient shown as solid red lines in Figure 5.15 on page 99 are determined.

Apparently, the introduction of a potential barrier mostly increases the absolute value of the Seebeck coefficient. If, for a decreasing free carrier concentration from $1\cdot10^{20}$ cm^{-3} to $1\cdot10^{19}$ cm^{-3}, a transition from the region where the ionized impurity scattering is dominant ($y = 1.5$) to the region where the grain boundary scattering prevails ($y = -0.5$) is assumed, the general trend of the experimental data is at least not in disagreement with the model. Unfortunately, no formulae for a gradual transition are available. The improvement of the theoretical description using Kajikawa's model for the Seebeck coefficient as a function of the free carrier concentration in polycrystalline materials is not obvious in Figure 5.15, but it will be essential to explain the temperature dependence of the Seebeck coefficient.

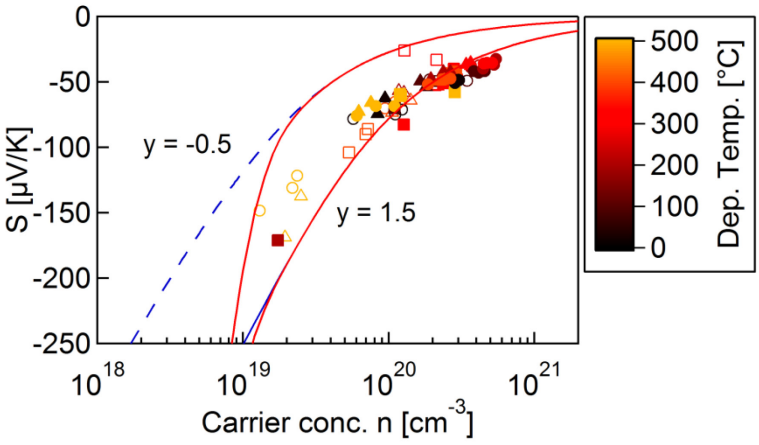

Figure 5.15: Seebeck coefficient as a function of the free carrier concentration using the model proposed by Kajikawa[253] (red lines) for the scattering in polycrystalline materials for the two situations where either ionized impurity scattering prevails (y = 1.5) or grain boundary scattering is dominant (y = –0.5). For comparison, S according to Equation (5.12) is also shown (blue lines).

5.2.4 Seebeck Coefficient as a Function of the Temperature

With the home-built setup, it was also possible to perform temperature dependent Seebeck measurements in a small temperature range between 40 °C and 80 °C. Figure 5.16 shows the results for the ZnO:Al films deposited at different substrate temperatures with 13.56 MHz plasma excitation frequency.

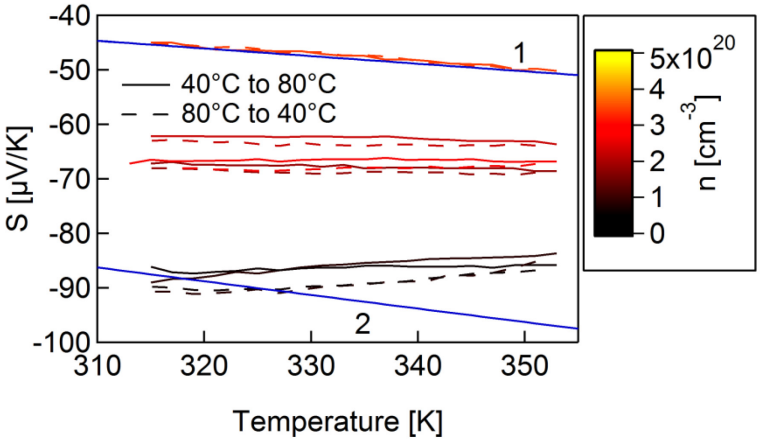

Figure 5.16: Seebeck coefficient S as a function of the temperature T for the ZnO:Al films grown with 13.56 MHz plasma excitation frequency and a substrate temperature in the range of ~30 °C to 500 °C. The solid lines show the results of the first measurement for increasing temperature, the dashed lines denote the second measurement for decreasing temperature. The solid blue lines show the theoretical curves according to Equation (5.13).

The Seebeck coefficients of the ZnO:Al films exhibit, similar to the Hall mobility, a very general qualitative trend: The values are decreasing with increasing temperature for high free carrier concentrations, they are temperature independent for average carrier concentrations, and the values are increasing with increasing temperature for low free carrier concentrations. The temperature dependence for small absolute values of the Seebeck coefficient and high free carrier concentrations can be explained by the temperature dependence of η. In this regime, η is proportional to 1/T, and therefore the Seebeck coefficient is proportional to T (see Equation (5.11)). In consequence, the absolute value of the Seebeck coefficient increases with rising temperature, and hence the value becomes more negative. The blue line '1' shows the theoretical curve using Equation (5.13) and a carrier concentration of $n = 2.4 \cdot 10^{20}$ cm^{-3}. This is very close to the value of $n = 3.4 \cdot 10^{20}$ cm^{-3} determined by the Hall measurement. The slope is in very good agreement with the experimental data as well, showing that the theory is able to accurately predict the temperature dependence of the Seebeck coefficient for large η. If, however, the carrier concentrations are lower, the theory according to Equation (5.13) will still predict a negative slope of the Seebeck coefficient (see the blue line '2' for large absolute values of the Seebeck coefficient). This is in contrast to the experimental data. The

experimentally observed temperature independence or even the positive slopes are reproducible, which means they are no measurement artefact.

This effect can be related to the increasing dominance of the potential barriers at the grain boundaries. The temperature dependence will be attenuated or reversed when the potential barrier height becomes significant in comparison to the energy difference $E_F - E_c$. Figure 5.17 shows the Seebeck coefficient as a function of the free carrier concentration and the corresponding temperature dependence.

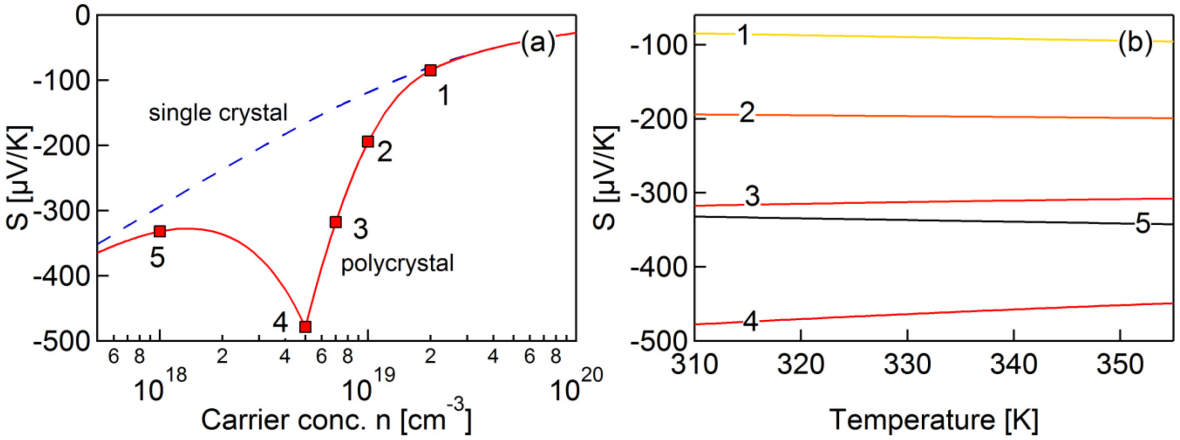

Figure 5.17: (a) Simulated Seebeck coefficient as a function of the free carrier concentration for the grain boundary scattering with potential barriers according to Kajikawa[253]. The potential barrier height has been calculated using the formula of Seto ($N_t = 5 \cdot 10^{12}$ cm^{-2}, L = 10 nm). (b) Seebeck coefficient as a function of the temperature using the free carrier concentrations of the marked points in (a).

Unfortunately, the model of Kajikawa is not able to correctly predict both, the absolute value of the Seebeck coefficient and the temperature dependence, for the region where the grain boundary scattering dominates ($n < 10^{20}$ cm^{-3}). The potential barrier has a much stronger effect on the Seebeck coefficient in this model than it is observed for the experimental values. Still, with the help of the theoretical model for the grain boundary scattering including the potential barriers, it is possible to qualitatively explain the temperature dependence of the Seebeck coefficient: When the potential barrier height is negligible in comparison to the value of $E_F - E_c = \eta kT$, a negative slope is observed for the temperature dependence of the Seebeck coefficient ('1'). As the potential barrier height increases, while at the same time η decreases due to the decreasing free carrier concentration, the temperature dependence weakens ('2') until finally, when the potential barrier maximum is in the same range as the Fermi energy or higher, the slope of the curve is positive (('3'),('4')). If the potential barrier height decreases again for even lower free carrier concentrations, the effect is reversed. The changing slope of $S(T)$ can therefore qualitatively be explained as a result of the potential barriers at the grain boundaries in the films. Hence, similar to the Hall effect measurements, the dominance of the ionized impurity scattering for high free carrier concentrations above $n \approx 5 \cdot 10^{20}$ cm^{-3} and the influence of the grain boundary scattering for lower carrier concentrations can be inferred from the data, although the theoretical models for the description of the Seebeck coefficient as a function of the free carrier concentration or the temperature are by far not as elaborated as the models for the description of the Hall mobility in semiconductors.

5.3 The Origin of the Trap States at the Grain Boundaries

The previous discussion showed that grain boundary scattering significantly limits the mobility of polycrystalline ZnO films. Since the trap states at the grain boundaries mainly determine this

scattering mechanism, their origin needs to be identified. Usually, crystallographic defects are assumed to cause the trap states at the grain boundaries.[83,94] However, Sato et al.[258] found that the disturbed atomic ordering does not lead to potential barriers at the grain boundary if the material is undoped. They performed a comprehensive experimental and theoretical study of the electrical transport over a single grain boundary in undoped and Pr- as well as Co-co-doped bicrystals in order to understand the electrical characteristics (I-V curves) of ZnO varistors, which also exhibit a polycrystalline morphology. If the material was undoped, they observed linear I-V curves. But if dopants (Pr, Co) were introduced, they segregated to the grain boundaries and promoted the formation of acceptor-like defects that led to non-linear I-V curves indicating potential barriers at the single grain boundary of their bicrystals. This is a first hint that not the altered atomic structure at the grain boundaries is the reason for the trap states, but the dopant material.

The relation between the trap state density and the crystalline quality in the ZnO:Al and $Zn_{1-x}Mg_xO$:Al films can be examined on the basis of the electronic transport in the polycrystalline and epitaxial films investigated in Chapter 4 (see Figure 5.18).

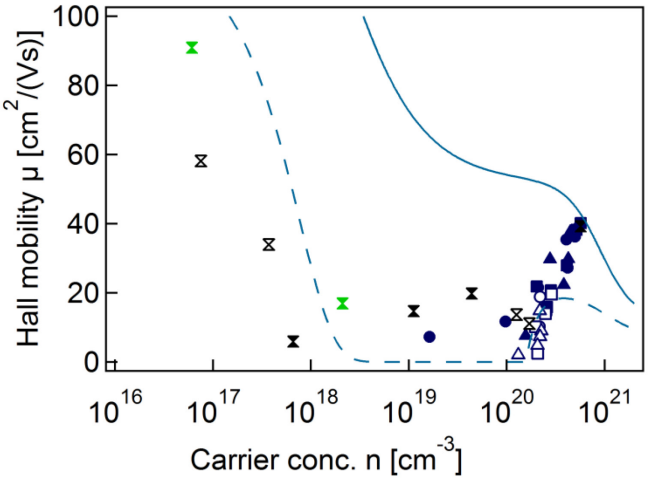

Figure 5.18: Hall mobility μ as a function of the carrier concentration *n* for the heteroepitaxial (blue) and homoepitaxial (black: ZnO:Al or $Zn_{1-x}Mg_xO$:Al, green: ZnO) films. The symbols denote the growth and the substrates the following way: a-sapphire: circles, c-sapphire: squares, r-sapphire: triangles, homoepitaxy: double triangles. The solid line is a fit to single crystalline ZnO data using the semi-empirical formula of Masetti. The dashed line is a fit to the transport data of the polycrystalline ZnO:Al and $Zn_{1-x}Mg_xO$:Al films taking into account ionized impurity scattering and grain-barrier limited transport for arbitrary degeneracy (N_t = $(7.0 \pm 0.3)\cdot10^{13}$ cm^{-2}, L = (14 ± 2) nm).

A comparison of the transport data of the hetero- and homoepitaxially grown films with the fit curve for μ(n) of the polycrystalline films (dashed line in Figure 5.18) shows that the epitaxial films are also strongly influenced by grain boundary scattering (see the low effective mobility in the carrier concentration range of $n \approx 10^{18}$ cm^{-3} to 10^{20} cm^{-3}). This may be surprising since especially the homoepitaxially grown films exhibit much less grain boundaries (see Section 4.2). However, according to theoretical and experimental work, even a single grain boundary can limit the electronic transport significantly.[242,258] The trap density $N_t = (8.5 \pm 0.2)\cdot10^{13}$ cm^{-2} (L = (55 ± 2) nm) obtained from a fit with the combined transport model to the data of the homo- and heteroepitaxially grown films is comparable to that of the polycrystalline films ($N_t = (7.0 \pm 0.3)\cdot10^{13}$ cm^{-2}). Taking into account, that the rocking curve widths are (much) smaller for the heteroepitaxial and homoepitaxial films compared to the polycrystalline films, one can expect the grain boundaries to have (much) less structural defects in the (homo-) epitaxial films. The comparable trap density for the polycrystalline and the epitaxial films then shows, that the structural defects at the grain boundaries cannot be the origin of the trap states. Considering the work of Sato on the electronic transport in bicrystals, the trap states at the grain boundaries are most likely caused by the dopant material, Al in this case.

This hypothesis is not only supported by the work of Sato[258], but also by the work of other authors.[223,225,231,259,260] Figure 5.19 on page 102 shows the Hall mobility as a function of the free carrier concentration of doped ZnO films prepared with different Al contents in the target by several groups.

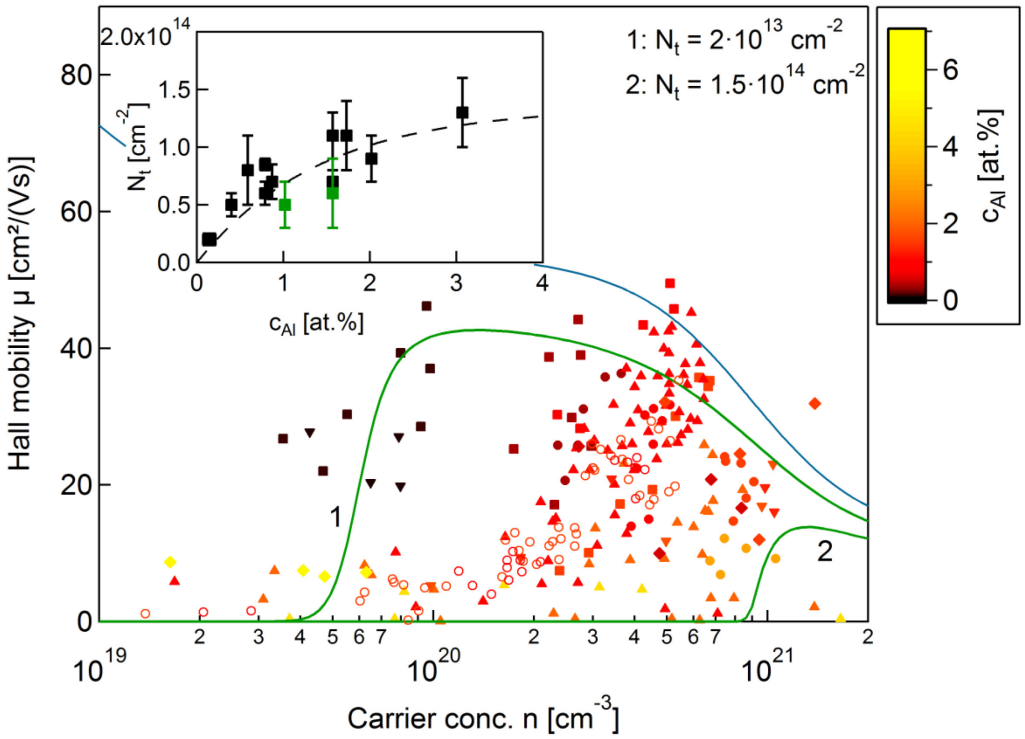

Figure 5.19: Hall mobility μ as a function of the free carrier concentration *n* for doped ZnO films prepared from targets with different dopant concentrations. The data were taken from Agashe et al.[259] (circles, ZnO:Al), Berginski et al.[223] (squares, ZnO:Al), Cornelius and coworkers[225] (triangles up, ZnO:Al), Suzuki et al.[231] (diamonds, ZnO:Al), Terasako et al.[260] (triangles down, ZnO:Ga), and this work (open circles). The solid blue line represents the data of the single crystalline ZnO and therefore mainly the ionized impurity scattering, while the solid green lines are simulations with the combined transport model for arbitrary degeneracy taking into account ionized impurity scattering and grain-barrier limited transport (using the theoretical value for N_c and the effective mass according to the data of Young et al.). The inset presents the trap densities at the grain boundaries N_t as a function of the dopant concentration in the films c_{Al} determined in this work (green squares) and from the literature data (black squares). The dashed line shows a fit with a function of the form $A(1 - \exp(-B \cdot c_{Al}))$.

If the Al concentration in the target is increased, the Al concentration in the films also rises.[261] Consequently, according to the hypothesis presented above, an increase of the trap state concentration at the grain boundaries for an increased Al concentration in the targets/films is expected. The results for the trap densities at the grain boundaries N_t determined using the combined transport model for the data published by the various groups are summarized in Table 5.6 on page 103 and shown in the inset of Figure 5.19.

Although different deposition techniques have been used, a general trend is observed: The trap density at the grain boundaries is increasing when the dopant concentration in the ZnO films is raised. For the lowest dopant concentrations (≈0.15 at.%), a trap density of $N_t = 2 \cdot 10^{13}$ cm^{-2} is determined, while for high dopant concentrations in the range of 3 at.%, a trap density of roughly $N_t = 1.5 \cdot 10^{14}$ cm^{-2} is calculated (see the green solid lines in Figure 5.19). The trap density is first increasing quickly with increasing dopant concentration and seems to saturate for dopant concentrations higher than approximately 3 at.%. This may be related to the formation of secondary phases. It could be possible that, when the dopant materials is bound in the form of Al_2O_3 or $ZnAl_2O_4$, it is no longer inducing acceptor like defects, which are assumed to be the cause of the trap state density according to the work of Sato.[258]

In consequence, the influence of the grain boundary scattering in ZnO can be reduced by either eliminating the grain boundaries completely, which is for a practical application and especially magnetron sputtered films unrealistic, or by reducing the concentration of trap states at the grain

Table 5.6: Trap state densities at the grain boundaries N_t for doped ZnO films deposited on glass substrates determined by modelling μ(n) reported by the various groups with the combined transport model. IP: ion plating, MS: magnetron sputtering, RMS: reactive magnetron sputtering, RF-MS: radio-frequency magnetron sputtering, PLD: pulsed laser deposition. The dopant concentration is referred to the whole compound.

Film	c_{dopant} [at.%]	Method	N_t [10^{13} cm^{-2}]	Reference
ZnO:Ga	0.13	IP	2.0 ± 0.5	260
ZnO:Al	0.16	RF-MS	2.0 ± 0.5	223
ZnO:Al	0.4	RF-MS	5.0 ± 1.0	223
ZnO:Al	0.4	RF-MS	5.0 ± 1.0	259
ZnO:Al	0.59	PLD	8 ± 3	231
ZnO:Al	0.79	RF-MS	6.0 ± 1.0	223
ZnO:Al	0.79	RF-MS	8.5 ± 0.5	259
ZnO:Al	0.87	DC-RMS	7 ± 1.5	225
ZnO:Al	1.02	RF-MS	5 ± 2	this work
ZnO:Al	1.57	RF-MS	7.0 ± 1.0	223
ZnO:Al	1.57	RF-MS	11 ± 2	259
ZnO:Al	1.57	DC-,RF-MS	6 ± 3	this work
ZnO:Ga	1.73	IP	11 ± 3	260
ZnO:Al	2.02	DC-RMS	9 ± 2	225
ZnO:Al	3.07	RF-MS	13 ± 3	259

boundaries. This would be possible by reducing the concentration of the dopant. However, the free carrier concentration is required to be very high. Since the activation of the dopant Al in ZnO is only in the range of 30 % (see Section 7.1.2), it would be of great interest to find ways to increase the activation of the Al to be able to reduce the amount of Al in the films while keeping the free carrier concentration constant. Another possible solution would be the use of a different dopant material with a higher dopant activation.

5.4 Chapter Conclusions

The charge carrier scattering mechanisms in doped ZnO and $Zn_{1-x}Mg_xO$ films have been investigated in detail. First, a description of the single crystalline material was established. Using literature data, it was found that the scattering in single crystalline ZnO can be explained by phonon scattering, which is dominant for low free carrier concentrations ($n < 10^{17}$ cm^{-3}), and ionized impurity scattering, prevailing above free carrier concentrations of $n \approx 10^{17}$ cm^{-3}. Based on the theory for ionized impurity scattering, a semi-empirical description of the ionized impurity scattering in the films investigated was deduced from these data. Subsequently, polycrystalline films were studied by means of Hall-effect and Seebeck-coefficient measurements as a function of the free carrier concentration and the temperature. The dominant scattering mechanisms in the degenerately doped polycrystalline films are ionized impurity scattering for free carrier concentration above $n \approx 5 \cdot 10^{20}$ cm^{-3} and grain boundary scattering for lower values. Furthermore, it was found that the charge carrier transport is basically limited by the same scattering mechanisms in the ZnO:Al and $Zn_{1-x}Mg_xO$:Al films. Only for $Zn_{1-x}Mg_xO$:Al an additional scattering mechanism, most likely alloy scattering, was identified.

The simple fit model, developed for the description of the Hall mobility as a function of the free carrier concentration as well as the temperature for arbitrary degeneracy of the semiconductor, was applied to the experimental data. While this model cannot improve the description of the experimental data for μ(n), the mobility as a function of the temperature is much more accurately modelled than it

would be possible using the classical theory of Seto for non-degenerate semiconductors. From the fit to the data, trap densities at the grain boundaries in the range of $N_t = 2 \cdot 10^{13}$ cm^{-2} to $9 \cdot 10^{13}$ cm^{-2} have been determined. These principal results obtained from the Hall measurements have been confirmed by Seebeck measurements. Finally, by comparison of the electronic transport in polycrystalline and epitaxial films, it was shown that the trap density at the grain boundaries is not owing to the altered atomic structure in the grain boundary region, but caused by the segregation of the dopant material to the grain boundaries, where it presumably forms acceptor-like defects.

For technical applications, the results imply that the influence of the grain boundaries can only be diminished when the grain boundaries are eliminated completely, which is practically impossible for magnetron sputtered films. Another solution would be a reduction of the dopant concentration to decrease the trap density at the grain boundaries and therefore the grain boundary scattering. Hence, it must be the aim to find dopant materials with a higher dopant activation in comparison to Al, which allow for a reduction of the dopant concentration while maintaining the free carrier concentration. In a similar manner, the degradation of the electronic properties of the $Zn_{1-x}Mg_xO$:Al films in comparison to the films prepared without Mg could be minimized when using a low amount of alloy material. If the desired increase of the band gap can only be achieved with a high amount of MgO, it might therefore be more favourable to use other elements, for example BeO, that could induce the same change with a lower concentration of the alloy material in the films (see Section 2.1.4).

6. The Role of High-Energetic O^- Ions and Phase Segregation

The deposition parameters influence the properties of the grown films significantly. The influence, for instance, can be due to an alteration of the composition of the films, the structural properties, or the electronic properties. As mentioned earlier, for a sputtering process the important parameters are, among others, the pressure of the working gas,[171] the type of the working gas (see Section 7.2), the arrangement of the substrate and the target,[262] the plasma excitation frequency (see Section 6.1.2), and the substrate temperature during the deposition. Often, also a radial distribution of the structural and electronic properties in the films with respect to the position of the substrate relative to the target axis is observed (see Section 6.2).[114,166,263,264] The origin of the correlation between the deposition parameters and the film properties, however, is not yet fully understood. In the following, the relation between several deposition parameters and their influence on the film properties will be elucidated and traced back to the role of high-energetic ion bombardment and phase segregation in magnetron sputtered ZnO films.

Results, presented in this chapter, have partly been published already in References [A], [C], and [E] from the list in the appendix.

6.1 A Qualitative Model

Compositional, electronic, and structural properties of doped ZnO films prepared at substrate temperatures between ~30 °C and 500 °C have been analysed in this work to formulate a qualitative model to explain the effect of the process parameters on the film properties. These investigations included resistivity and Hall measurements, X-ray diffraction measurements, Rutherford backscattering spectrometry, and comparisons with theoretical calculations in literature. The qualitative model will first be presented and then verified for depositions with varying discharge frequencies in the next two subsections.

6.1.1 Deduction of the Qualitative Model

It is known already for a long time, that the growing films are exposed to a bombardment by high-energetic particles during sputtering.[120] Because of their high energies, these particles can have a strong impact on the structural properties of the films. Mattox[265] reviewed the effects of the bombardment of thin films with energetic species. He distinguished surface and subsurface effects of the bombardment. In the surface region, the energetic particles can, for example, lead to the desorption of weakly bonded species, to the sputtering of surface atoms, to an enhanced mobility of atoms on the surface, and to enhanced chemical reactions. In the subsurface region, the particles may be implanted, lead to displacements of lattice atoms, or lead to trapping of mobile species at lattice defects.

In a magnetron discharge, particles with the highest energies are reflected atoms (neutralized ions) and negative ions.[120] Reflected atoms originate from a near central collision of a high-energetic ion (mostly Ar) with a target atom, which leads to a backscattering towards the substrate.[120] The maximum energy of the reflected atoms can be calculated by[120]

$$E_p = \left(\frac{m_t / m_p - 1}{m_t / m_p + 1}\right)^2 \cdot E_{p_0} = \left(\frac{m_t / m_p - 1}{m_t / m_p + 1}\right)^2 \cdot e\left(V_{pl} - V_t\right), \tag{6.1}$$

where m_t/m_p is the mass ratio between the target atom and the projectile, E_{p0} is the original energy of the projectile, e is the elementary charge, V_{pl} is the plasma potential, and V_t is the target voltage. According to this relation, for scattering at Zn, a reflected Ar atom retains 6 % of its original energy ($E_p \approx 0.06E_{p0}$), and for scattering at O, it conserves 18 % ($E_p \approx 0.18E_{p0}$). These energies are much smaller in comparison to the energies gained by negative ions, which are formed at the target surface. These ions are accelerated across the target sheath to energies corresponding to the full cathode sheath potential $E_{ion-} = e(V_{pl} - V_t)$, which means several hundred eV in the case of DC sputtering. A thermalization of these high-energetic negative ions is unlikely due to the small scattering cross section with the sputtering gas for such high energies.[120]

Especially for sputtering of ZnO from ceramic targets or with an oxygen-containing sputtering atmosphere, a high amount of high-energetic negative oxygen ions is present (see Section 6.2). Since the defect formation energies in ZnO are in the range of some ten eV only,[266,267] it can hence be expected, that the bombardment of the films with the high-energetic particles (O^- ions) will lead to severe structural damage in the ZnO films prepared by magnetron sputtering.

Structural Properties

The crystallite sizes and the c-axis lattice parameters of ZnO:Al films prepared using 13.56 MHz plasma excitation frequency at different substrate temperatures during the deposition ranging from ~30 °C to 500 °C are shown in Figure 6.1.

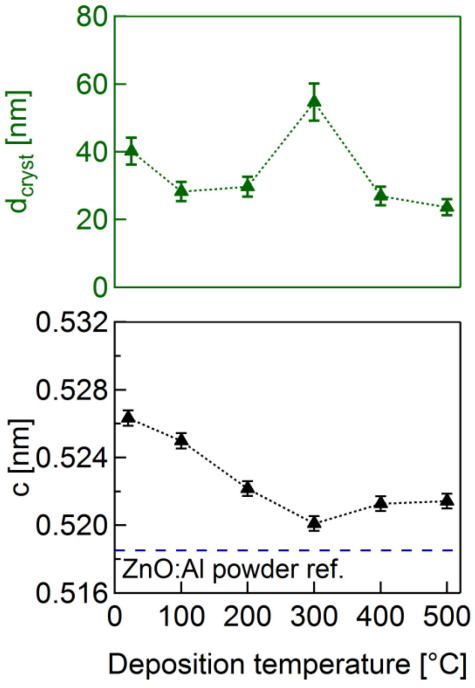

Figure 6.1: Crystallite size d_{cryst} and c-axis lattice parameter c of ZnO:Al films prepared using 13.56 MHz plasma excitation frequency at substrate temperatures between ~30 °C and 500 °C. The powder reference value for the c-axis of ZnO:Al is taken from JCPDS 36-1451 and literature data[201].

The crystallite sizes exhibit a maximum value of 55 nm at T_{sub} = 300 °C. In general, they are increasing for deposition temperatures from ~30 °C to 300 °C and decreasing for T_{sub} > 300 °C. The c-axis lattice parameter is strongly elongated with respect to the ZnO:Al powder value (c_{ref} = 0.51853(2) nm, taken from JCPDS 36-1451 and Reference 201) for the deposition without intentional heating ($\Delta c/c_{ref}$ = (1.50 ± 0.09) %). This elongation decreases with increasing deposition temperature. Above T_{sub} = 300 °C, the c-axis lattice parameter is nearly constant.

The elongation of the c-axis lattice parameter can be explained by the formation of interstitial defects due to the implantation of high-energetic oxygen into the lattice. Together with other structural defects caused by the collision cascades, this leads to a small crystallite size due to the reduction of the size of the coherently scattering domains in comparison to a perfect material. If the deposition temperature is increased from room temperature to 300 °C, more and more of these interstitial defects can be annealed out during the growth of the film.[17] This reduces the elongation of the c-axis lattice parameter and increases the crystallite size. For deposition temperatures above 300 °C, most of these defects are already annealed out during the growth of the film and the lattice parameter is close to the powder reference values. The decrease of the crystallite size for T_{sub} > 300 °C can be attributed to the formation of segregated phases, which will be discussed in the following.

Compositional Properties

The chemical composition of the ZnO:Al and $Zn_{1-x}Mg_xO$:Al films as a function of the deposition temperature is shown in Figure 6.2.

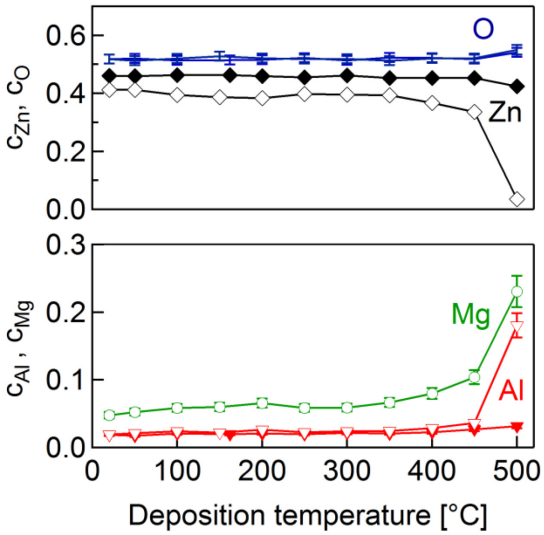

Figure 6.2: Chemical composition as a function of the deposition temperature for ZnO:Al and $Zn_{1-x}Mg_xO$:Al films deposited on glassy carbon, determined by Rutherford backscattering spectrometry. Filled symbols denote the ZnO:Al films and open symbols represent the $Zn_{1-x}Mg_xO$:Al films. Measured elements: O (without symbols), Zn (diamonds), Al (triangles down), Mg (circles).

The Al-dopant concentration is nearly constant for both materials up to temperatures of approximately 350 °C at (2.1 ± 0.3) at.% in the ZnO:Al films and (2.3 ± 0.2) at.% in the $Zn_{1-x}Mg_xO$:Al films. For T_{sub} > 350 °C a slight increase of the Al and O content, accompanied by a decrease of the Zn content, is observed for the ZnO:Al films. A similar behaviour is found for the $Zn_{1-x}Mg_xO$:Al films, but there it is much more pronounced. The above mentioned Al concentrations are far above the solubility limit of approximately 0.3 at.% under thermodynamic equilibrium conditions.[268] However, for non-equilibrium conditions, which exist especially for magnetron sputtering, the solubility limit can be increased to values of approximately 2...3 at.%.[95,225] For even higher concentrations of Al, the formation of secondary phases such as Al_2O_3 or $ZnAl_2O_4$ is expected.[95] In the $Zn_{1-x}Mg_xO$:Al films, the additional formation of $MgAl_2O_4$ might occur. The increase of the Al (and Mg) content and the simultaneous decrease of the Zn content can then be explained by the different vapour pressures of the metals and the enthalpies of formation of the oxides of the metals: Zinc has the highest vapour pressure[269] and the lowest affinity to oxygen[27] (see Table 6.1).

Table 6.1: Standard enthalpy of formation Δ_fH^0 of the oxides of the metals present during the deposition,[27] related to one metal atom.

Compound	Δ_fH^0 [kJ/mol]
ZnO	–347.9
MgO	–601.7
$(Al_2O_3)_{0.5}$	–834.8

This means that it has the highest tendency to re-evaporate from the substrate, because it is only likely to remain on the substrate in the form of ZnO. At the same time, Al and Mg are increasingly competing with Zn in the formation of oxides for increasing deposition temperatures. Hence, the deposition of Al and Mg compounds is increasingly preferred over the deposition of Zn. This effect is less pronounced for the ZnO:Al, because there only the Al is competing with the Zn in the formation of an oxide.

Although the Al content for deposition temperatures above 300 °C is even exceeding the values of the non-equilibrium solubility limit, it was not possible to detect the segregated phases by X-ray diffraction measurements. According to Sieber et al.[95] as well as Han and coworkers[270], the segregation of Al_2O_3 or $ZnAl_2O_4$ occurs mainly at the grain boundaries with small domain sizes, making the secondary phases undetectable by conventional X-ray diffraction. Furthermore, it obstructs the grains from growing larger, which explains the decreasing crystallite size with increasing deposition temperatures above 300 °C.

Electronic Properties

Due to the close relation between the structural and the electronic properties of the films, the bombardment with high-energetic negative oxygen ions and the phase segregation has an influence on the electronic properties of the films as well. Figure 6.3 shows the resistivity ρ, the free carrier concentration *n*, and the Hall mobility of the carriers μ of the ZnO:Al films prepared with 13.56 MHz plasma excitation frequency as a function of the deposition temperature.

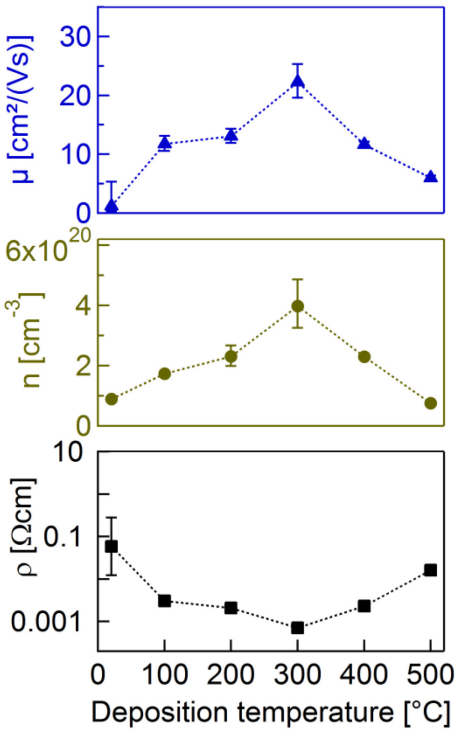

Figure 6.3: Resistivity ρ, free carrier concentration *n*, and Hall mobility μ of ZnO:Al films prepared using 13.56 MHz plasma excitation frequency at substrate temperatures between ~30 °C and 500 °C.

The resistivity and the carrier concentration exhibit a bowl- and a hill-shaped behaviour, respectively. For deposition temperatures between ~30 °C and 300 °C, the resistivity is decreasing from approximately $6 \cdot 10^{-2}$ Ωcm to $(7.0 \pm 0.5) \cdot 10^{-4}$ Ωcm. For higher deposition temperatures, the resistivity is again increasing to $\rho = (1.6 \pm 0.5) \cdot 10^{-2}$ Ωcm at $T_{sub} = 500$ °C. The carrier concentration and the Hall mobility of the carriers show the opposite trend: For deposition at room temperature, the free carrier concentration is $n = (8.9 \pm 0.5) \cdot 10^{19}$ cm^{-3}, while it increases to a maximum value of $(4.0 \pm 0.9) \cdot 10^{20}$ cm^{-3} for deposition at 300 °C. For substrate temperatures $T_{sub} > 300$ °C, the free carrier concentration decreases until it reaches $(7.59 \pm 0.07) \cdot 10^{19}$ cm^{-3} at 500 °C. The Hall mobility of the

carriers increases from approximately 1 cm²/(Vs) to (22 ± 3) cm²/(Vs) for deposition temperatures of ~30 °C and 300 °C, respectively, and declines to (6.0 ± 0.4) cm²/(Vs) for an increase of T_{sub} from 300 °C to 500 °C. The trend of the Hall mobility is a direct consequence of the variation of the free carrier concentration and can be explained by the combined transport model taking into account ionized impurity scattering and grain barrier limited transport as discussed in the previous chapter.

Knowing from the RBS analysis that the Al-dopant concentration is mainly constant for deposition temperatures between ~30 °C and 300 °C and that a significant phase segregation is not expected in this temperature region, the temperature dependence of the carrier concentration below T_{sub} = 300 °C can only be explained by the formation of compensating defects. Compensating defects in ZnO are zinc vacancies (V_{Zn}) or oxygen interstitials (O_i).[17,271,272] Since the structural analysis strongly indicates that interstitial defects are formed, oxygen interstitial defects (O_i) are most likely responsible for the variations of the structural and electronic properties below T_{sub} = 300 °C. Usually, these O_i defects are not considered to be significant for the electronic properties of ZnO due to their high enthalpy of formation compared to donor-like defects. However, the formation enthalpy of the compensating defects depends on the chemical conditions during the deposition and decreases with increasing Fermi energy of the growing ZnO film. In fact, it gets close to or even becomes smaller than the formation enthalpy of donor-like defects for high Fermi levels.[15,272] Since the films investigated here are degenerately doped, it can be assumed that the formation enthalpy of the compensating oxygen interstitial defects is at least in the same range as that of the donor-like intrinsic defects, and therefore it is plausible that oxygen interstitial defects are forming due to the bombardment of the growing films with high-energetic negative oxygen ions.

On the other hand, it could be objected that also Zn vacancies are acceptor-like defects and that they have a lower enthalpy of formation in comparison to the O_i defects over the whole range of Fermi energies.[15,272] In addition to that, it is not directly clear whether a vacancy in an ionic material will lead to an increase or a decrease of the lattice parameters. Usually, a missing atom leads to a relaxation of the lattice resulting in a compression. In ionic materials, however, the missing ion may lead to a repulsion of the charged neighbouring atoms and therefore to an increase of the lattice constants. As a matter of fact, in ZnO, a Zn vacancy will lead to an outward relaxation of the surrounding O atoms of 10 % with respect to the equilibrium Zn-O bond length.[17] On the other hand, these calculations for the defect chemistry as well as the formation energies of the different defects are performed for thermodynamic equilibrium conditions. Since magnetron sputtering is a deposition process far away from the thermodynamic equilibrium, the formation of a higher amount of oxygen interstitial defects can certainly not be excluded, even though the equilibrium formation energy of the Zn vacancy is lower. Actually, experimental studies on the radiation damage in ZnO, performed by Wendler et al.[267], have shown that point defects in the Ar implanted films can be fitted using displacement energies of E_d(Zn) = 65 eV and E_d(O) = 50 eV. Audren et al.[273] also observed more displaced atoms in the oxygen sublattice in comparison to the Zn sublattice for their Co implanted ZnO films. Noh and coworkers[274] measured the photoluminescence of their pulsed laser deposited epitaxial ZnO:Al films and related the changes of the electrical properties caused by thermal treatments to the formation of oxygen interstitial defects as well.

Therefore, the relation between the electronic and structural properties of the films can be explained by the following model:

Interstitial defects are formed due to the bombardment of the growing films with high-energetic negative oxygen ions. These defects are responsible for the c-axis lattice expansion, and the electrically active oxygen interstitials compensate a part of the free carriers. When the deposition temperature is increased from ~30 °C to 300 °C, more and more of these defects can already be annealed out during the growth of the film. This reduces the compensation and leads to higher free

carrier concentrations. Above temperatures of 300 °C, an increased phase segregation of Al_2O_3, $ZnAl_2O_4$, and/or $MgAl_2O_4$ leads to an increasing number of inactive dopant atoms and thus to a decreasing free carrier concentration. Additionally, defect complexes of O_i and Al, leading to an inactivation of the dopant, may also be formed, which will be discussed more detailed in Chapter 7.[275]

6.1.2 A First Test of the Qualitative Model

Direct experimental evidence for the formation of interstitial oxygen defects is difficult to obtain, especially in polycrystalline materials and for the low expected amount of less than 1 at.%. A first test of the qualitative model can be performed by modifying the plasma excitation frequency for the deposition of the ZnO films. This influences the dynamic equilibrium between the formation of acceptor-like interstitial oxygen defects (O_i) compensating the extrinsic electron donors (Zn_{Al}) at lower substrate temperatures and the self-annealing of the interstitial defects at higher deposition temperatures due to a decrease of the mean energy of the O^- ions with increasing plasma excitation frequency.[192] A decreasing energy should then, according to the model, improve the electronic and structural properties of the films for lower deposition temperatures.

Plasma Parameters

Figure 6.4 shows ion energy spectra, which were measured for the different plasma excitation frequencies under conditions comparable to those for the film deposition, which means the same working pressure (0.3 Pa), the same working gas (argon), a similar target-to-(detector entrance)substrate distance (60 mm), and the same stoichiometry of the target (1.6 at.% Al). These measurements were performed in a different system with a quadrupole mass spectrometer as described in Section 3.5.3.

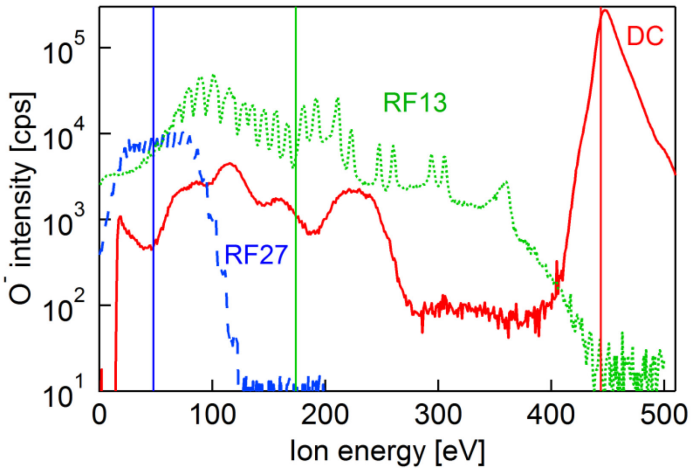

Figure 6.4: Ion energy spectra of negative oxygen ions (O^-) for a 27.12 MHz RF (blue, dashed line, RF27), a 13.56 MHz RF (green, dotted line, RF13), and a DC (red, solid line) discharge maintained at 50 W. The vertical solid lines at $-eV_t$ represent the target potentials V_t (*e*: elementary charge).

The energy spectrum of the O^- ions in the DC plasma discharge exhibits a high and sharp peak around the energy corresponding to the target potential (vertical solid red line, 444 eV). Although the thermalization in the sputtering gas is rather ineffective for such high energies and the ions travel through the plasma mostly undisturbed, there are interactions with the plasma that become obvious from the weak and broad features at lower ion energies. These ions are fragments of heavier oxygen-containing ions, for instance AlO^-, ZnO^-, O_2^-.[276] The fragments of the parent-molecule ion share the original energy $E_p \approx -eV_t$ according to their masses $E_f = m_f/m_p \cdot E_p$.[160] For example, for the process $O_2^- \rightarrow O^- + O$, the fragment will be detected with an energy $E_f \approx -0.5eV_t$.

The ion energy spectrum of the O^- ions for the 13.56 MHz RF plasma discharge differs significantly from the DC discharge case. The distribution is much broader, which is caused by the periodic

modulation of the target potential V_t around the self-bias potential $V_{DC,self\text{-}bias}$.[276] Additionally, there are many small and sharp peaks in the ion energy spectra. These features are no measurement artefact, but can be attributed to run time effects due to the oscillating sheaths at the target and at the PPM, respectively.[276] Further, the absolute value of the target potential (–174 V) is much lower in comparison to that of the DC discharge. This is due to the more effective ionization in the plasma caused by the oscillatory motion of the electrons, which leads to a lower target voltage if the power is kept constant.[277] The flux of the O^- ions to the substrate/PPM orifice is lower compared to the DC case as well. For 27.12 MHz RF plasma excitation frequency, the trend is continued. The distribution is, similar to the 13.56 MHz discharge, very broad and the target potential (–48 V) is again decreased.

The measurements performed in collaboration with Dr. Thomas Welzel showed an increase of the floating potential V_{fl} with increasing discharge frequency. This reduces (DC) or increases (RF) the average energy of the high-energetic negative oxygen ions reaching the substrate surface. This energy can be approximated by $\langle E \rangle = e(V_{fl} - V_t)$ – the difference between the value of the floating potential and the average target voltage multiplied by the elementary charge. Table 6.2 summarizes the potentials and the energies for the different discharge frequencies.

Table 6.2: Average target potentials $V_{DC,self\text{-}bias}^{Gen}$ taken from the display of the generator, average floating potential V_{fl} measured with a digital multimeter at the orifice of the plasma process monitor, average negative oxygen (O^-) ion energy $\langle E \rangle_{O^-}$ determined from the ion energy spectra, and average O^- ion energy corrected for the floating potential $\langle E \rangle_{O^-,substrate}$, which is the average energy expected at the substrate surface.

Discharge	$V_{DC,self\text{-}bias}^{Gen}$ [V]	V_{fl} [V]	$\langle E \rangle_{O^-}$ [eV]	$\langle E \rangle_{O^-,\,substrate}$ [eV]
DC	–444 ± 5	–17.1 ± 1.0	443	426
13.56 MHz RF	–174 ± 1	10.0 ± 1.0	156	166
27.12 MHz RF	–48 ± 1	30.2 ± 0.5	58	88

Taking into account the floating potential, the energies are shifted slightly, but the general trend remains the same. Therefore, it can be concluded that the average energy of the high-energetic O^- ions is reduced when increasing the plasma excitation frequency. The flux of the high-energetic negative ions is also decreasing with increasing plasma excitation frequency, which means that the energy input into the films in general is decreasing with increasing plasma excitation frequency.

Since the PPM measurements were performed in a different system, the target potentials are marginally different for the film deposition. The average energy of the high-energetic negative oxygen ions can therefore only be estimated from the target voltages, because the floating potentials are not known. Yet, the target voltages showed the same trend, and hence a decreasing average energy of the O^- ions can also be assumed for the system used for the film deposition.

Structural Properties

Figure 6.5 on page 112 shows the crystallite size d_{cryst} and the c-axis lattice parameter c of ZnO:Al and $Zn_{1-x}Mg_xO$:Al films deposited using DC, 13.56 MHz (for ZnO:Al already shown in the previous section), and 27.12 MHz plasma excitation frequency.

The measured X-ray diffraction patterns reveal again a strong (0001) texture of the deposited films, and for all plasma excitation modes, the films show a significant c-axis lattice expansion for deposition temperatures below approximately 300 °C. For a change from 27.12 MHz to 13.56 MHz plasma excitation frequency, the maximum expansion of the c-axis at a deposition temperature of $T_{sub} \sim 30$ °C is increasing from (1.2 ± 0.3) % to (2.4 ± 0.3) % for the $Zn_{1-x}Mg_xO$:Al films and from (0.7 ± 0.1) % to (1.5 ± 0.1) % for the ZnO:Al films with respect to a c-axis lattice constant of

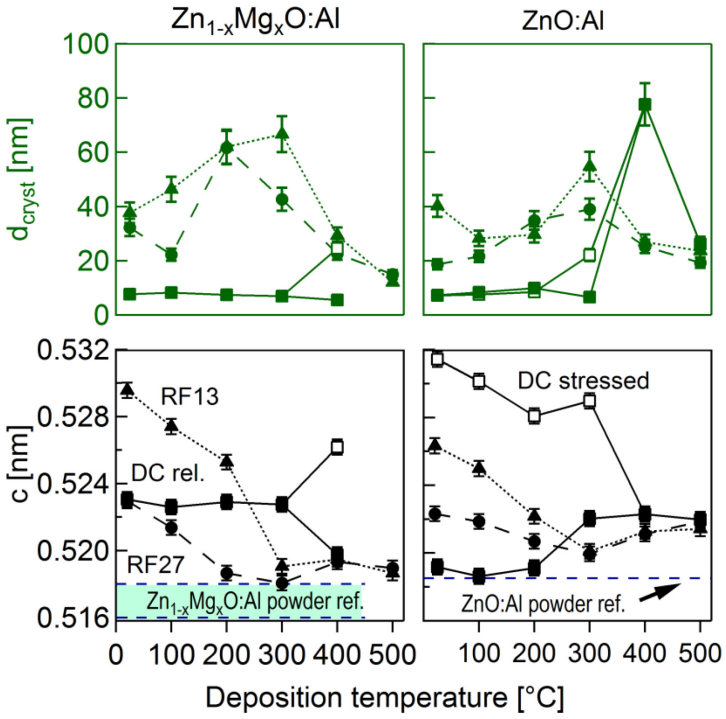

Figure 6.5: Crystallite size d_{cryst} and c-axis lattice parameter c for $Zn_{1-x}Mg_xO$:Al (*left*) and ZnO:Al (*right*) films deposited at different plasma excitation frequencies as a function of the substrate temperature. Solid lines: DC (stressed phase: open symbols, relaxed phase: filled symbols), dotted lines: 13.56 MHz RF, dashed lines: 27.12 MHz RF. The powder reference values for the unstrained c-axis lattice parameters were taken from JCPDS 36-1451 and References 39, 200, and 201.

0.517(1) nm for the relaxed $Zn_{1-x}Mg_xO$:Al and 0.51853(2) nm for the relaxed ZnO:Al (taken from JCPDS 36-1451 and References 39, 200, and 201).

While the RF sputtered films exhibit only one strong and narrow (0002) diffraction peak (see Figure 6.6 (a)), some DC sputtered films have contributions from (0001) oriented crystals with different states of stress, leading to broadened (0002) diffraction peaks with a shoulder (see Figure 6.6 (b)).

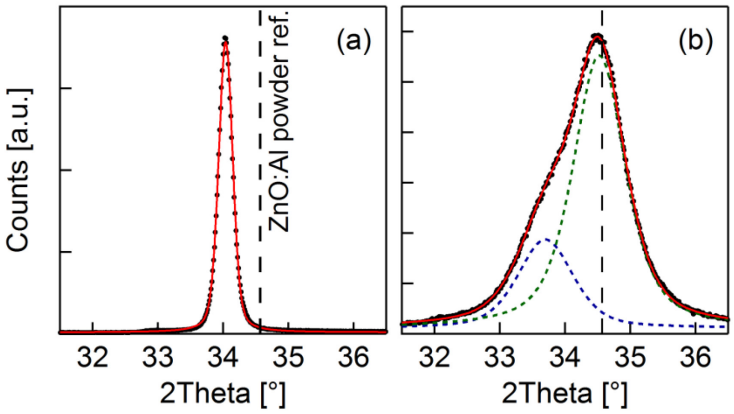

Figure 6.6: Representative X-ray diffraction patterns of the (0002) peaks of ZnO:Al films deposited at ~30 °C by 13.56 MHz plasma excitation frequency (a) or DC excitation (b) (differently scaled for better comparison). The raw data (black dots) have been fitted by the sum (solid red line) of one or two pseudo-Voigt shaped peaks (dashed blue and green line). The dashed vertical lines show the powder reference value for ZnO:Al.

Therefore, two values for the c-axis lattice parameter and crystallite size, respectively, are given in Figure 6.5. Taking this into account, it is found that the c-axis parameters corresponding to the partially relaxed phases are nearly equal for DC as well as RF excitation for deposition temperatures above T_{sub} = 300 °C.

The crystallite sizes vary between 10 nm and 70 nm for the RF sputtered $Zn_{1-x}Mg_xO$:Al films and 20 nm and 55 nm for the RF sputtered ZnO:Al films. For DC plasma excitation, the crystallite sizes are generally much smaller – in the range of 6 nm to 25 nm and 7 nm to 26 nm in the $Zn_{1-x}Mg_xO$:Al and ZnO:Al films, respectively. An exception is the average crystallite size of nearly 80 nm in the DC sputtered ZnO:Al film deposited at 400 °C. The largest crystallite sizes are mainly obtained for the films deposited at the substrate temperature leading to the lowest resistivities for the different

excitation modes ($T_{sub}(\rho_{min})$). For the $Zn_{1-x}Mg_xO$:Al films deposited in the DC mode at 500 °C no data is presented, because it was not possible to fit the diffraction peak due to the low signal intensity.

These results can be explained by the qualitative model: The average energy of the high-energetic negative oxygen ions is approximately corresponding to the target voltage during the deposition, which means ~500 eV for DC sputtering and ~170 eV as well as ~90 eV for 13.56 MHz and 27.12 MHz RF sputtering, respectively. The decrease of the energy of the bombarding O^- ions leads to fewer interstitial defects, which can be attributed to the shallower implantation of the oxygen into the growing ZnO film allowing for a higher rate of annealing out of the created defects during the growth of the film (for a quantitative discussion see Section 6.1.3).[278] This annealing out then reduces the c-axis lattice expansion of the films deposited at higher plasma excitation frequencies, which fits to the observations for the 13.56 MHz and 27.12 MHz RF plasma excitation. The peaks corresponding to a c-axis lattice parameter of approximately 0.519 nm for the ZnO:Al films prepared by pulsed DC sputtering below 400 °C, which do not fit the trend at first glance, can be explained by the formation of a partially relaxed ZnO phase, in which crystallographic defects are formed to relieve the stress.[279] The stressed phase for DC sputtering, on the other hand, shows the strongest lattice expansion compared to the other excitation frequencies. This corresponds to the highest energy the negative oxygen ions have in the case of DC sputtering. For $T_{sub} \geq 400$ °C, the coexistence of the stressed and the partially relaxed phase vanishes, which can be attributed to the annealing out of the defects during the growth of the film, decreasing the lattice expansion. For the $Zn_{1-x}Mg_xO$:Al films, a coexistence of a stressed and a relaxed phase is not observed below $T_{sub} = 400$ °C. Based on the data for the RF sputtered ZnO:Al and $Zn_{1-x}Mg_xO$:Al films, it can be expected that the c-axis lattice expansion in the $Zn_{1-x}Mg_xO$:Al films would even be stronger than that in the ZnO:Al films. However, below $T_{sub} = 400$ °C a fully stressed phase with c-axis lattice parameters above 0.53 nm seems to be unstable and appears to relax to a partially stressed phase. For 400 °C, where the induced stress should be lower, because most of the lattice expanding defects should already be annealed during growth, a part of the fully stressed phase may still be stable. This can explain the c-axis lattice parameter at $T_{sub} = 400$ °C that is higher than those for $T_{sub} < 400$ °C. The rest of the phase relaxes to a stress level lower than that for $T_{sub} < 400$ °C. The stronger lattice expansion, which is generally observed in the $Zn_{1-x}Mg_xO$:Al films, can be attributed within the qualitative model to a higher amount of interstitial defects caused by a stronger bombardment of these films induced by the MgO in the target, which will be discussed more detailed in Section 6.2.2.

That the smallest crystallite sizes were measured for the films DC sputtered below $T_{sub} \approx 300$ °C, can be explained by a high amount of defects created due to the relaxation of the stressed phase. That the crystallite sizes of the RF sputtered films are generally larger but do not differ significantly from each other for the 13.56 MHz and the 27.12 MHz deposition, although the beneficial effect of the reduced particle energy is clearly visible in the c-axis lattice expansion and the electrical properties, however, is not as clear. Probably, the crystallite size determined by X-ray diffraction is mostly limited by defects other than point defects. Grain boundaries or segregated phases, for example, can lead to a significant broadening of the peaks. The strong variations of d_{cryst} for the DC sputtered ZnO:Al films in the deposition temperature range from 300 °C to 500 °C can be explained by the vanishing of the defect rich stressed phase from 300 °C to 400 °C and a strong increase of the amount of segregated phases from 400 °C to 500 °C.

Electronic Properties

The beneficial effect of an increased plasma excitation frequency on the structural properties becomes apparent in the reduced c-axis lattice expansion. This is, according to the qualitative model with regard to the O_i defects, closely related to the electronic properties. The resistivity ρ, the free carrier

concentration n, and the Hall mobility of the carriers μ of the ZnO:Al and $Zn_{1-x}Mg_xO$:Al films deposited by DC and RF sputtering are shown in Figure 6.7.

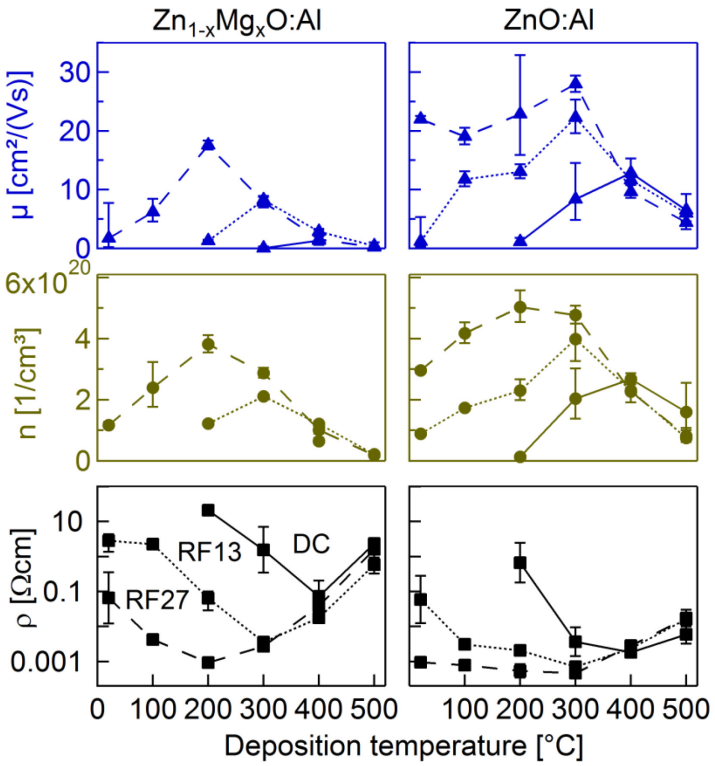

Figure 6.7: Resistivity ρ, free carrier concentration n, and Hall mobility μ for DC (solid lines), 13.56 MHz RF (dotted lines) and 27.12 MHz RF (dashed lines) sputtered $Zn_{1-x}Mg_xO$:Al (*left*) and ZnO:Al (*right*) films as a function of the deposition temperature.

The general trend of the resistivities is similar for the three discharge frequencies and for both types of oxides: with increasing T_{sub} the resistivities decrease and reach a minimum at temperatures in the range of 200 °C (27.12 MHz) to 400 °C (pulsed DC). For further increased deposition temperatures, ρ increases significantly for all plasma excitation modes. The achieved minimal resistivities (see Table 6.3) and the deposition temperature for the minimal resistivity $T_{sub}(\rho_{min})$ are decreasing with increasing plasma excitation frequency. Though similar trends are observed for the $Zn_{1-x}Mg_xO$:Al and the ZnO:Al films, the minimal ρ of the $Zn_{1-x}Mg_xO$:Al films is always higher – by a factor of about 40, 5, and 2 for DC, 13.56 MHz, and 27.12 MHz plasma excitation, respectively. Remarkably, the resistivities for deposition temperatures below $T_{sub}(\rho_{min})$ are significantly different, while they are nearly the same for higher deposition temperatures, which means independent on the excitation mode. The minimal resistivity values and the maximal free carrier concentrations and effective Hall mobilities are summarized in Table 6.3.

The highest values determined for the Hall mobility and the free carrier concentration were $\mu_{max} = (28.0 \pm 1.4)$ cm²/(Vs) and $n_{max} = (4.8 \pm 0.3) \cdot 10^{20}$ cm^{-3}, respectively, for ZnO:Al films grown by 27.12 MHz RF sputtering at a deposition temperature of 200 °C. This maximal free carrier concentration is still well below the reported maximum of $n \approx 1.5 \cdot 10^{21}$ cm^{-3} (see Reference 20) and corresponds to an electrical activation of the dopant Al of only (33 ± 6) %. For the ZnO:Al films prepared at 27.12 MHz plasma excitation frequency, the resistivities are in the same range as the lowest values reported from other groups (approximately $2 \cdot 10^{-4}$ Ωcm)[163,236]. These groups, however, used arc evaporation, characterized by low particle energies, or prolonged annealing with capping layers at $T > 500$ °C after the film deposition.

The decrease of the resistivity with increasing plasma excitation frequency, which is observed for deposition temperatures below $T_{sub}(\rho_{min})$ can be attributed to the increase of the free carrier concentration n and the Hall mobility of the carriers μ. As already pointed out, the decrease of the

Table 6.3: Minimal resistivity values ρ_{min} as well as maximal free carrier concentrations n_{max} and Hall mobility values μ_{max} for ZnO:Al and $Zn_{1-x}Mg_xO$:Al films sputtered at different plasma excitation frequencies.

Excitation mode	Parameter	$Zn_{1-x}Mg_xO$:Al	ZnO:Al
DC	ρ_{min} [Ωcm]	$(7 \pm 4)\cdot10^{-2}$	$(1.8 \pm 0.4)\cdot10^{-3}$
	n_{max} [cm^{-3}]	$(6 \pm 1)\cdot10^{19}$	$(2.7 \pm 0.2)\cdot10^{20}$
	μ_{max} [$cm^2/(Vs)$]	0.05 ± 0.04	13 ± 2
13.56 MHz RF	ρ_{min} [Ωcm]	$(3.6 \pm 0.2)\cdot10^{-3}$	$(7{,}0 \pm 0{,}5)\cdot10^{-4}$
	n_{max} [cm^{-3}]	$(2.11 \pm 0.05)\cdot10^{20}$	$(4.0 \pm 0.7)\cdot10^{20}$
	μ_{max} [$cm^2/(Vs)$]	8.3 ± 0.5	22 ± 3
27.12 MHz RF	ρ_{min} [Ωcm]	$(9.3 \pm 0.1)\cdot10^{-4}$	$(4.7 \pm 0.1)\cdot10^{-4}$
	n_{max} [cm^{-3}]	$(3.8 \pm 0.3)\cdot10^{20}$	$(4.8 \pm 0.3)\cdot10^{20}$
	μ_{max} [$cm^2/(Vs)$]	18 ± 1	28 ± 1

energy of the bombarding O^- ions leads to fewer interstitial defects due to the shallower implantation of the oxygen into the growing ZnO film. Since the oxygen interstitial defects form, based on density-functional calculations, acceptor levels, thus compensating the free carrier concentration, the increasing carrier concentration with increasing discharge frequency is in very good agreement with the qualitative model.

The lower carrier concentrations in the $Zn_{1-x}Mg_xO$:Al films could also be explained by a stronger bombardment with high-energetic negative oxygen ions leading to more interstitial defects and therefore a stronger compensation of the free carriers. On the other hand, reduced free carrier concentrations have also been reported for $Zn_{1-x}Mg_xO$:Al films deposited by pulsed laser deposition,[37,45] where the growing films are less exposed to high-energetic ion bombardment. This points to the fact, that the segregation of additional phases, which can only be present in the $Zn_{1-x}Mg_xO$:Al films, such as $MgAl_2O_4$, is dominant and likely to reduce the free carrier concentration over a wide range of deposition temperatures. Additionally, an increase in the free-electron effective mass for the films containing Mg in comparison to pure ZnO:Al was proposed by Cohen et al.[41] as a possible reason for the reduction of the free carrier concentration. They assumed a hydrogenic donor dopant model, according to which the donor activation energy increases with increasing effective mass, which would decrease the doping efficiency. However, the films investigated here are degenerately doped. In this case, the ionization energy of the dopants is negligible, and hence the applicability of the hydrogenic donor dopant model is questionable. Most likely both effects, an increased negative oxygen ion bombardment and the possible formation of additional secondary phases, are the reason for the lower free carrier concentrations in the $Zn_{1-x}Mg_xO$:Al films in comparison to the ZnO:Al films investigated here. The changes in the Hall mobility are then just a consequence of the variations of the carrier concentration and can be explained by the combined transport model as it has been discussed earlier.

As already pointed out, for the deposition temperatures above the optimum value, no significant changes with varying plasma excitation frequency are observed. Apparently, the ion energy has no strong influence on the phase segregation, which is assumed to govern the film properties above $T_{sub}(\rho_{min})$. This is in agreement with the expectations and the observations for the resistivity, the free carrier concentration, the Hall mobility, the c-axis lattice expansion, and the crystallite size. The decrease of $T_{sub}(\rho_{min})$ with increasing plasma excitation frequency is attributed to a change in the balance of the creation of defects due to the bombardment and the annealing out of the defects: if the plasma excitation frequency f_{plasma} is increasing, the average energy of the high-energetic negative

oxygen ions is decreasing, which leads to less damage that can be annealed out more easily. Therefore, the optimum temperature is decreasing with increasing f_{plasma}.

These results are supported by experiments of Wang et al.[261] and Minami and coworkers[20]. Wang placed the substrates off-axis and perpendicular to the target in the RF sputtering system to deposit doped ZnO thin films of high optical and electronic quality, and Minami deposited ZnO:Al films with extremely high free carrier concentrations (n = 1.5·10^{21} cm^{-3}) using a similar setup. Most likely, the reduced high-energetic negative oxygen ion bombardment introduced less compensating interstitial oxygen defects, and therefore higher free carrier concentrations and a better electronic quality could be achieved. Generally, it seems, by the use of plasma-assisted deposition techniques, which do not exhibit high-energetic particles, high free carrier concentrations and low resistivities can be attained more easily. Suzuki et al.[231], for example, prepared ZnO:Al films by pulsed laser deposition and obtained ρ = 1.43·10^{-4} Ωcm and n = 1.4·10^{21} cm^{-3} using the normal configuration with the substrate placed parallel in front of the target.

Annealing Experiments

To further test the role of the high-energetic negative oxygen ion bombardment and the phase segregation on the electronic and structural properties of the films, an annealing experiment was performed. The films were annealed in vacuum with a total pressure of p < 5·10^{-5} Pa for 1 h at 300 °C and subsequently for 1 h at 400 °C. Figure 6.8 shows the electronic properties of the films after the annealing (red lines).

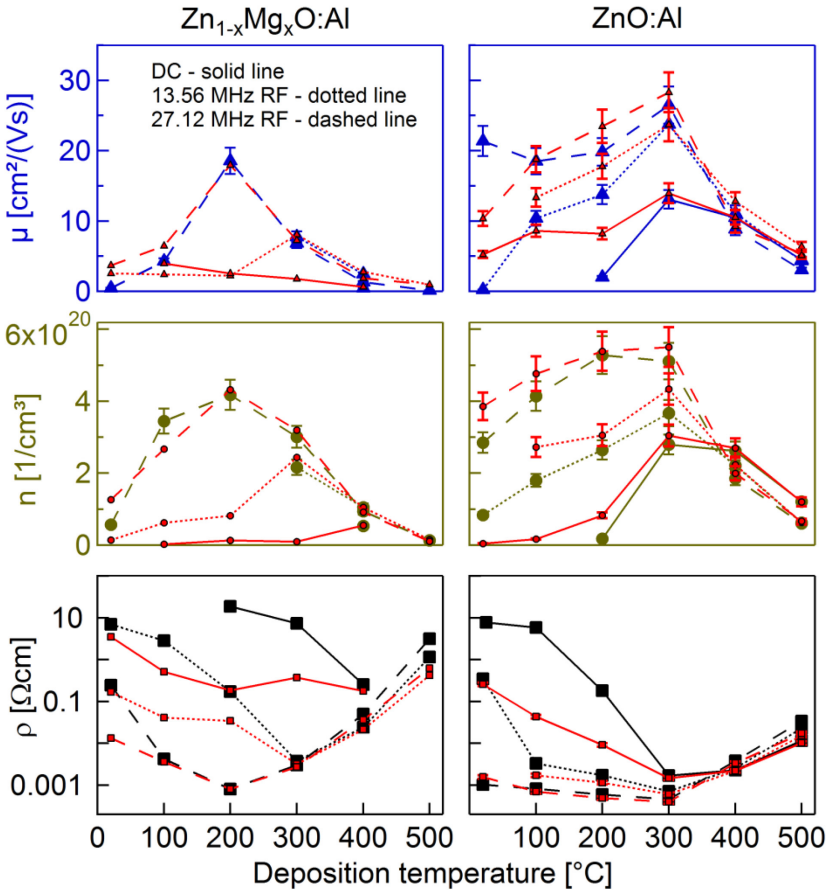

Figure 6.8: Resistivity ρ, free carrier concentration n, and Hall mobility of the charge carriers μ for the $Zn_{1-x}Mg_xO$:Al (*left*) and ZnO:Al (*right*) films deposited between ~30 °C and 500 °C using DC (solid line), 13.56 MHz RF (dotted line), and 27.12 MHz (dashed line) plasma excitation frequency after an annealing treatment (red lines and symbols). For comparison, the data of the as-deposited films are also shown.

The resistivity of the samples is decreased for deposition temperatures below $T_{sub}(\rho_{min})$. The strongest improvement is observed for the DC sputtered films, while almost no decrease of ρ is found for the films, where ρ was very low from the beginning, which means the films deposited using 27.12 MHz plasma excitation frequency. Hence, it is not possible to significantly reduce the resistivity of the best

films by annealing in vacuum. According to the qualitative model, the annealing in vacuum allows for an annealing of the interstitial oxygen defects. This increases the free carrier concentration and the Hall mobility and reduces the resistivity, which is consistent with the observations. For temperatures above $T_{sub}(\rho_{min})$, where the segregation of other phases is believed to be dominant, no changes occur. This is reasonable, because the deposition temperature was higher than the annealing temperature, which means for that temperature some kind of equilibrium was already reached. Furthermore, the influence of an elevated temperature is stronger during the deposition in comparison to a subsequent annealing, where the diffusion can only take place by thermal activation.

Although the free carrier concentration and the Hall mobility were changed due to the annealing, the Hall mobility as a function of the free carrier concentration does not show a different trend (see Figure 6.9).

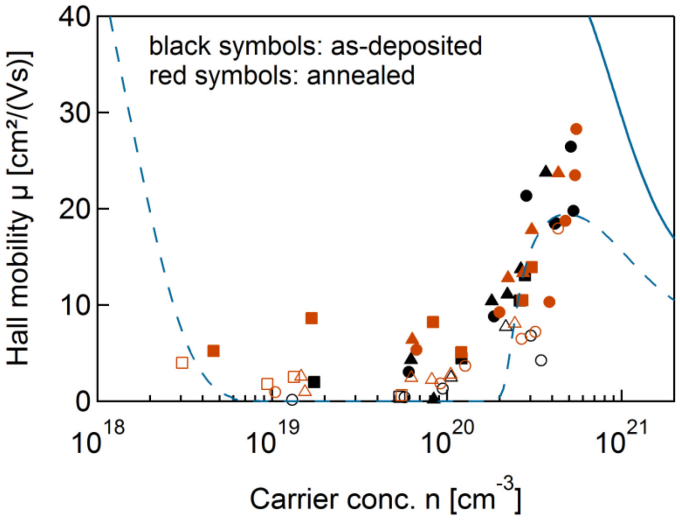

Figure 6.9: Hall mobility μ as a function of the free carrier concentration *n* for the as-deposited and annealed samples. The black symbols denote the as-deposited films, while the red markers show the data for the annealed samples (full symbols: ZnO:Al, open symbols: $Zn_{1-x}Mg_xO$:Al). The dashed line shows a fit with the combined transport model for arbitrary degeneracy (N_c according to the theory). The solid line shows the Masetti curve for single crystalline ZnO.

Only for free carrier concentration below 10^{20} cm^{-3}, the mobility of the charge carriers is slightly higher. The average trap density at the grain boundary of the annealed samples $N_t = (5.5 \pm 0.3)\cdot 10^{13}$ cm^{-2} is also similar to that of the as-deposited films ($N_t = (4.3 \pm 0.3)\cdot 10^{13}$ cm^{-2}). Hence, the charge carrier scattering in these films is still dominated by grain boundary scattering and ionized impurity scattering, which points to fact that the annealing has no influence on the potential barriers at the grain boundaries.

Interestingly, the c-axis lattice parameter and the crystallite size do not change in consequence of the annealing (see Figure 6.10 on page 118). Only for the ZnO:Al films prepared by DC sputtering, the strongly stressed phase vanished almost completely. The unchanged crystallite sizes point to the absence of recrystallization effects. Further, the constancy of the c-axis lattice parameters can only be explained as a result of a relatively small change of the interstitial defect concentration in the films. If only electrically active O_i defects would be causing the lattice expansion, this should be visible, because the relative change of the number of these defects (as can be inferred from the free carrier concentration) is large. Hence, it was deduced that not only electrically active defects are formed, but also electrically inactive interstitial defects are contributing to the lattice expansion. The O_i split configuration, for example, is an electrically inactive interstitial defect that could contribute to the lattice expansion.[17] In conclusion, this annealing experiment mainly supports the qualitative model. Additionally, in Section 7.1.2 a long time annealing experiment for 18 h at 600 °C used to force the phase segregation will be presented.

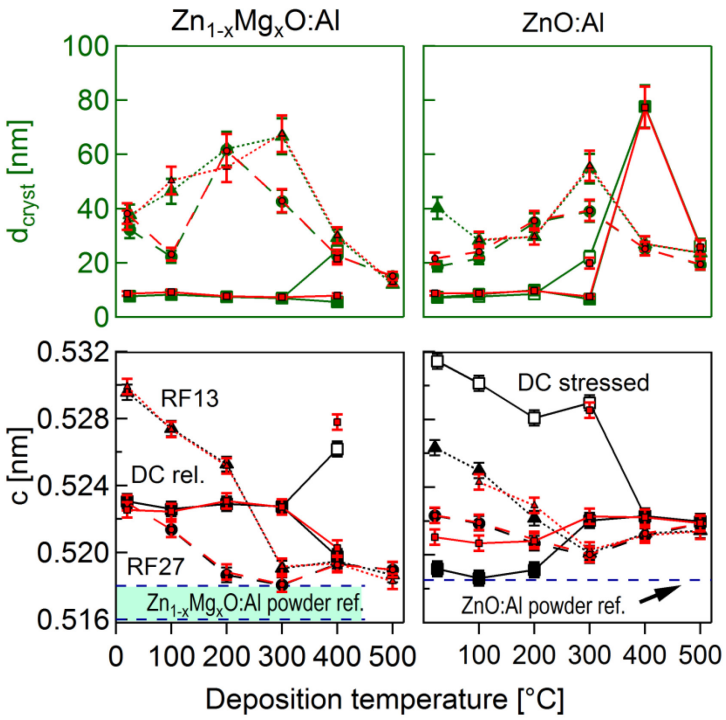

Figure 6.10: Comparison of the c-axis lattice parameters *c* and crystallite sizes d_{cryst} for the as-deposited (black and green markers) and annealed films (red markers). Solid lines: DC, dotted lines: 13.56 MHz RF, dashed lines: 27.12 MHz RF.

6.1.3 Quantification of the Model

In the following, the effects discussed for the qualitative model will be quantified. First, the formation of segregated phases will be modelled. After that, the defects introduced by the ion bombardment will be described by equations, and eventually the results will be combined to model the experimental data.

Quantification of the Phase Segregation

In the qualitative model it is assumed that defect complexes or segregated phases are responsible for the deactivation of the dopant at high deposition temperatures. In both cases, the Al dopant has to diffuse to form these phases or defect complexes. Investigations of the distribution of the dopant in the film (see Section 7.4) show that the dopant is not homogeneously distributed, but that regions with a strong enhancement of the concentration are present. Unfortunately, these regions cannot yet be correlated to grain boundaries within this work. However, since the phase segregation is believed to occur preferentially at grain boundaries, this will be assumed to be able to quantify the model. To describe the phase segregation in a confined volume in the sample, the formula for the kinetics of grain boundary segregation first described my McLean[280] will be used. He applied Fick's law for the diffusion from two semi-infinite half crystals taking into account a constant enrichment factor $\alpha = c_{Al,GB}(\infty)/c_{Al,b}$, where $c_{Al,b}$ is the bulk solute concentration and $c_{Al,GB}(\infty)$ is the concentration at the grain boundary at infinite times.[281] With $c_{Al,b}(0,T)$ at $t = 0$, the time dependence of $c_{Al,GB}(t,T)$ is given by[281]

$$\frac{c_{Al,GB}(t,T) - c_{Al,GB}(0,T)}{c_{Al,GB}(\infty) - c_{Al,GB}(0,T)} = 1 - e^{\frac{4D(T)t}{\alpha^2 d^2}} \left(1 - \mathrm{erf}\sqrt{\frac{4D(T)t}{\alpha^2 d^2}}\right), \tag{6.2}$$

where d is the boundary layer thickness and $D(T) = D_{0,Al} e^{-\frac{E_{Al}}{kT}}$ is the bulk diffusion coefficient with the activation energy for the diffusion of the Al atoms E_{Al}. To simplify the model and to take into account only the enrichment of the Al at the grain boundary or in a certain region in the film, the value $c_{Al,GB}(0,T)$ is set to zero. Furthermore, it is assumed that all of the Al present in the bulk of the

crystallite will eventually diffuse to the grain boundary. For simplicity, the grain and the grain boundary are assumed to be of cubic shape with edge lengths L, b, and c as well as d, b, and c, respectively. A schematic illustration of the geometry is shown in Figure 6.11.

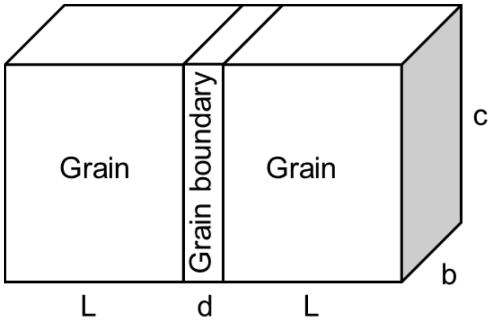

Figure 6.11: Schematic representation of the geometry used for the calculation of the segregation of phases to the grain boundaries in the ZnO:Al and $Zn_{1-x}Mg_xO$:Al films.

Using this notation, the bulk concentration of the Al is given by $c_{\mathrm{Al,b}} = N_{\mathrm{Al}}/(Lbc)$, where N_{Al} is the number of Al atoms present in the grains at a certain time $t = 0$. This leads to

$$\alpha = \frac{c_{Al,GB}(\infty)}{c_{Al,b}} = \frac{N_{\mathrm{Al}}/dbc}{N_{\mathrm{Al}}/Lbc} = \frac{L}{d}. \tag{6.3}$$

The quantitative model will eventually be compared to the results of the electrical measurements, which average over the bulk of the grain and the grain boundary region. To take this into account, the concentration of the enriched (segregated) Al at the grain boundary will be averaged over the whole volume of the bulk of the grain and the boundary region by multiplying the concentration at the grain boundary by d/L. Using Equations (6.2) and (6.3), the concentration of Al segregated to other phases, $c_{\mathrm{Al,segr}}(t,T) \coloneqq c_{\mathrm{Al,GB}}(t,T)$, and hence not contributing to the free carrier concentration, is given by

$$c_{\mathrm{Al,segr}}(t,T) \coloneqq c_{\mathrm{Al,GB}}(t,T) = c_{\mathrm{Al,b}}\left(1 - e^{\frac{4D_{0,\mathrm{Al}}e^{-\frac{E_{\mathrm{Al}}}{kT}}t}{L^2}}\left[1 - \operatorname{erf}\sqrt{\frac{4D_{0,\mathrm{Al}}e^{-\frac{E_{\mathrm{Al}}}{kT}}t}{L^2}}\right]\right). \tag{6.4}$$

Due to numerical issues in the evaluation of this term, Equation (6.4) has to be simplified. For a sufficiently large range of parameters D_0, t, L, and E_{Al}, the exponential term can be approximated by 1 for low temperatures. For high temperatures, this approximation is in coincidence with the exact values of Equation (6.4). The simplified formula for the concentration of segregated Al is

$$c_{\mathrm{Al,\,segr}}(t,T) = c_{\mathrm{Al,b}} \cdot \operatorname{erf}\sqrt{\frac{4D_{0,\mathrm{Al}}t}{L^2}e^{-\frac{E_{\mathrm{Al}}}{kT}}}. \tag{6.5}$$

A comparison between the exact and the approximated formula is shown in Figure 6.12 on page 120. A change of the model parameters D_0, L, E_{Al}, and t shifts or stretches and compresses the temperature dependence of the $c_{\mathrm{Al,segr}}/c_{\mathrm{Al,b}}$ values, while the general trend remains the same. With respect to the simplification of the formula, which would otherwise not be applicable to a fit procedure, the deviations of the approximation from the exact solution are reasonably small.

Annealing of the Oxygen Interstitial Defects

For the annealing of the oxygen interstitial defects, a model based on the work of Morehead and Crowder[282] will be used. Morehead and Crowder described the ion induced damage in crystalline Si by assuming an ion-bombardment induced damage in a cylindrical volume. A portion of that volume representing an outer shell of this cylinder is subsequently annealed out due to the out diffusion of defects from the damaged region. Here, the same idea but a different geometry will be applied.

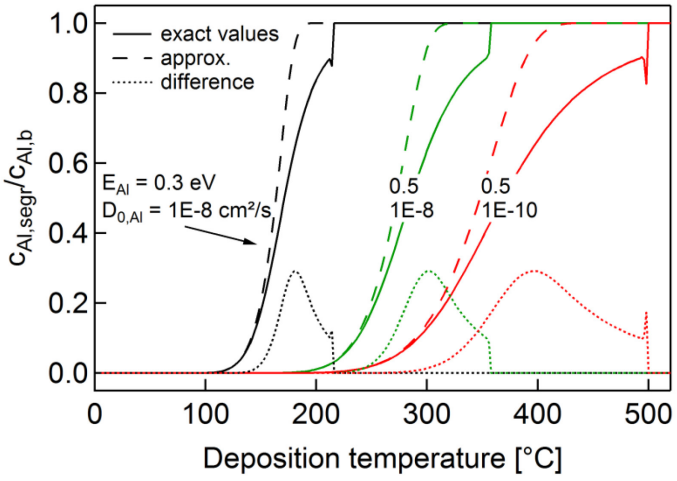

Figure 6.12: Comparison between the values for $c_{Al,segr}/c_{Al,b}$ calculated according to Equation (6.4) (exact solution, solid lines) and Equation (6.5) (approximation, dashed lines) as a function of the temperature. Also shown is the difference between these two solutions (dotted lines). L = 10 nm and t = 1 s were kept constant, while E_{Al} and $D_{0,Al}$ were varied.

Assuming a damaged cuboid-shaped volume of the film with the edge lengths z, l, and m, where z denotes the direction perpendicular to the film surface (l and m are the in-plane dimensions of the film), and neglecting the film growth, the number of defects $N_{Oi}(0)$ at a certain starting point of time $t = 0$ is given by

$$N_{O_i}(0) = c_{O_i}(0) \cdot zml, \tag{6.6}$$

where c_{Oi} is the concentration of the interstitial defects. The implantation depth of the ions z can be estimated with the help of SRIM[283] simulations to be in the range of 0.9 nm, 0.5 nm, and 0.4 nm, for 500 eV, 200 eV, and 100 eV oxygen ion energy, respectively. Furthermore, a homogeneous distribution of the defects in the considered volume is supposed. That is not correct, because (i) the implantation profiles usually exhibit a Gaussian distribution of the implanted atoms around the depth z, and (ii) the bombardment is present constantly while the film is growing, which will most likely lead to a complicated depth profile of the defects created by the bombardment with O⁻ ions. On the other hand, the implanted atoms will leave a tail of defects. Hence, to assume a damage of the whole volume is at least reasonable. The remaining number of defects after a certain time t is

$$N_{O_i}(t,T) = c_{O_i}(0) \cdot ml(z - \delta z(t,T)), \tag{6.7}$$

where $\delta z(t,T)$ is the portion of the cuboid that has been healed due to the diffusion of defects to the surface of the film. This region will be identified with the diffusion length $L_d = \sqrt{(4Dt)}$. Consequently, the concentration of the remaining defects is given by

$$c_{O_i}(t,T) = \frac{N_{O_i}(t,T)}{zml} = c_{O_i}(0)\left(1 - \sqrt{\frac{4tD_{0,O_i}}{z^2}e^{-\frac{E_{O_i}}{kT}}}\right). \tag{6.8}$$

Comparison with Experimental Data

The number of compensating oxygen interstitial defects and the amount of Al bound in electrically inactive phases is directly reflected in the free carrier concentration. The free carrier concentration n can be expressed in terms of the absolute concentration of Al decreased by the number of compensating oxygen interstitial defects and the amount of electrically inactive Al by

$$n(t,T) = c_{Al,b} - c_{Al,b} \cdot \mathrm{erf}\sqrt{\frac{4D_{0,Al}t}{L^2}e^{-\frac{E_{Al}}{kT}}} - 2c_{O_i}(0,T)\left(1 - \sqrt{\frac{4tD_{0,O_i}}{z^2}e^{-\frac{E_{O_i}}{kT}}}\right). \tag{6.9}$$

The factor 2 in the third term in Equation (6.9) is due to the charge state of the compensating oxygen interstitial of '–2', which has been selected, because it is the energetically most favourable configuration for high Fermi energies.[272]

Data for diffusion constants D of O and Al in ZnO are rare in literature and scatter over a wide range. Tomlins et al.[284], for example, found values for the prefactor D_0 for diffusion of oxygen in ZnO between ~10^{-6} cm²/s and ~10 cm²/s in the temperature range from 850 °C to 1200 °C for two ZnO single crystals prepared by different groups (but measured with the same setup!). Furthermore, the value for the activation energy depends on the diffusion mechanism. For intrinsic diffusion, which occurs in a lattice of high quality, a large activation energy E_O in the range of 3.6 eV to 4.2 eV is necessary for the diffusion of O in ZnO.[284] However, if defects are already present, this activation energy is strongly reduced. Tomlins and coworkers[284] refer to values of approximately 1.3 eV for the extrinsic diffusion of oxygen in ZnO. For diffusion of Al in ZnO, Freer[285] reported $D = 5.3 \cdot 10^{-3} e^{-2.74[eV]/(kT)}$ cm²/s in the temperature range between 1050 °C and 1160 °C. This value is in accordance with the results of Vines and coworkers[286] for epitaxial magnetron sputtered ZnO:Al films. Using L = 10 nm, t = 1 s, and z = 0.5 nm, the temperature dependence of the segregated phases and the remaining concentration of the compensating oxygen interstitials for different values of the activation energies and diffusion prefactors D_0 can be calculated (see Figure 6.13).

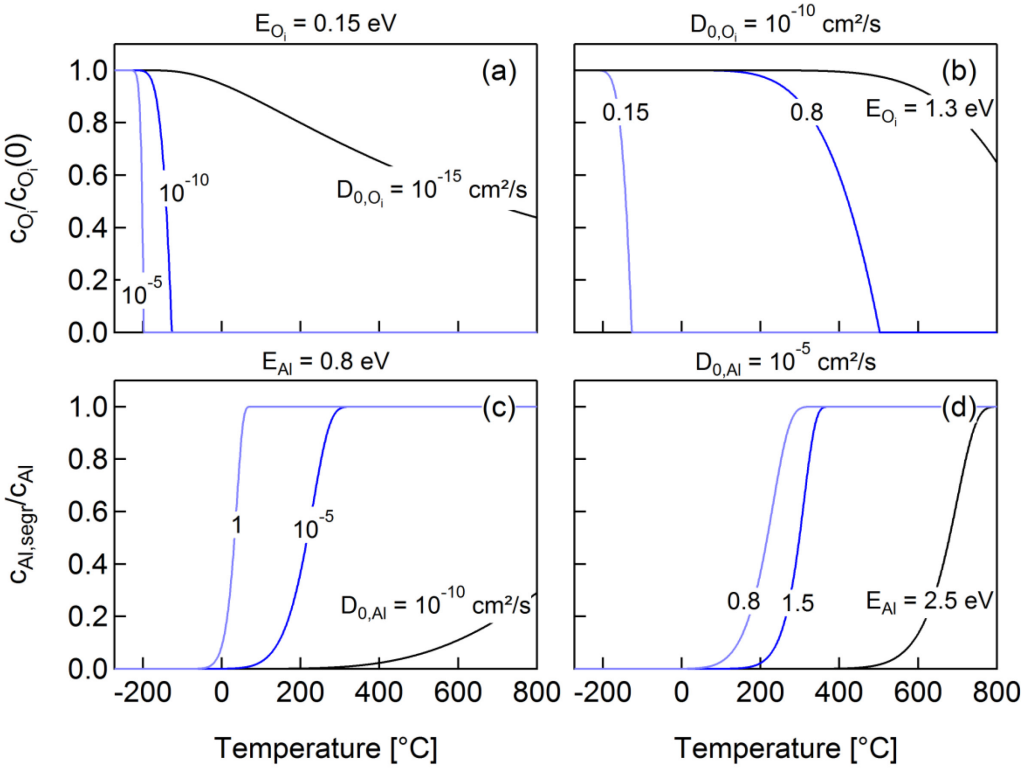

Figure 6.13: Relative concentration of the compensating oxygen interstitial defects (O_i) for different diffusion prefactors D_0 (a) and different activation energies E_{Oi} (b) as a function of the (deposition-) temperature. (c) and (d) show the relative amount of segregated Al, $c_{Al,segr}/c_{Al}$, for different diffusion prefactors D_0 and activation energies E_{Al}, respectively.

The diffusion parameters have a strong influence on the amount of oxygen interstitial defects and the segregated Al as a function of the (deposition-) temperature. Generally, the diffusion prefactor D_0 and the activation energy E have a similar influence. If these parameters are changed to increased diffusivities, the number of oxygen interstitials is decreased and the phase segregation is increased already at lower deposition temperatures. The opposite effect occurs for a lower diffusivity. The slope of the curves can mostly be changed by the prefactor D_0. For a low value of D_0, the change of the

amount of oxygen interstitials or segregated phases is spread over a wide range of temperatures. The actual temperature for the onset of the effects is then mostly correlated to the activation energy. To account for the experimentally observed trend of the free carrier concentration as a function of the deposition temperature, the amount of phase segregation and compensating oxygen interstitials must change slowly in the temperature range between ~30 °C and 500 °C. With respect to the simulation, this can only be achieved for low values of the diffusion prefactor D_0 to simulate the small variations with temperature and low activation energies E_{Oi} and E_{Al} to simulate the onset of the thermal effects at those relatively low temperatures. The other parameters, L, z, and t have a minor influence on the simulation and will be kept constant in the following.

Figure 6.14 shows the carrier concentration as a function of the deposition temperature for DC, 13.56 MHz RF, and 27.12 MHz RF sputtered $Zn_{1-x}Mg_xO$:Al and ZnO:Al films fitted by Equation (6.9). For the fitting procedure, it has been taken into account that the number of oxygen interstitials and the free carrier concentration cannot become negative.

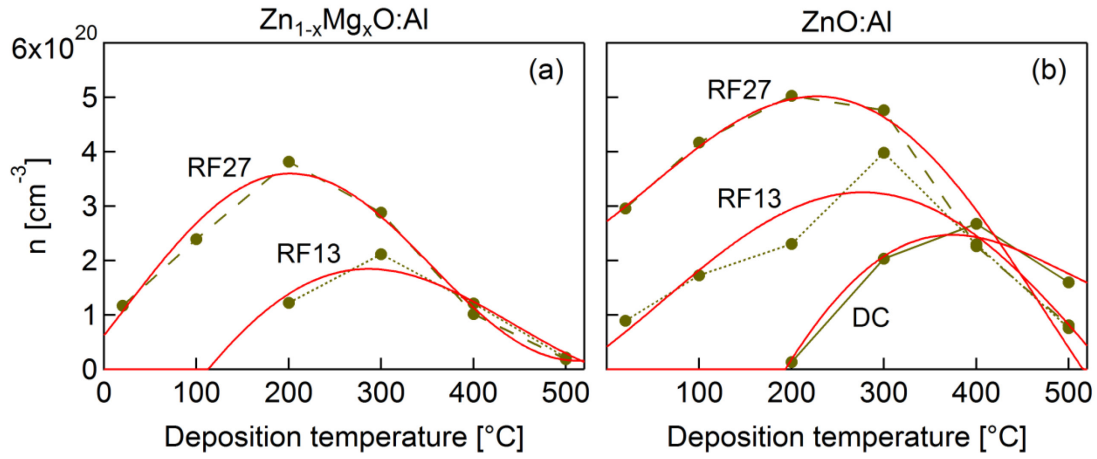

Figure 6.14: Fit of Equation (6.9) to the experimental data of the free carrier concentration n determined by Hall measurements for the $Zn_{1-x}Mg_xO$:Al (a) and ZnO:Al (b) films. The lines with markers show the experimental data for 27.12 MHz (RF27), 13.56 MHz (RF13), and DC plasma excitation and the red lines without markers show the fit curves. L = 10 nm, z = 0.5 nm, $c_{Al,b} = 1.7 \cdot 10^{21}$ cm^{-3}, and t = 1 s have been kept constant. E_{Al} and E_{Oi} were changed until the deviation of the simulated data from the experimental data was sufficiently small and then also kept constant. c_{Oi}, $D_{0,Oi}$, $D_{0,Al}$ were variable.

The shape of the experimental data can only be reproduced when assuming low activation energies of E_{Al} = 0.4 eV and E_{Oi} = 0.15 eV as well as E_{Al} = 0.5 eV and E_{Oi} = 0.15 eV for the $Zn_{1-x}Mg_xO$:Al and the ZnO:Al films, respectively. For higher activation energies, the slope becomes steeper and the slow increase and decrease of the free carrier concentration with increasing temperature cannot be simulated properly. The fit parameters are summarized in Table 6.4.

Table 6.4: Parameters for the fit of Equation (6.9) to the experimental data for the free carrier concentration n as a function of the deposition temperature T_{sub} for films deposited at different plasma excitation frequencies. E_{Al}, E_{Oi} = 0.15 eV, L = 10 nm, z = 0.5 nm, and t = 1 s have been kept constant.

Material	Parameter	DC	13.56 MHz RF	27.12 MHz RF
$Zn_{1-x}Mg_xO$:Al	$c_{Oi}(0)$ [cm^{-3}]		$(1.08 \pm 0.17) \cdot 10^{21}$	$(0.918 \pm 0.012) \cdot 10^{21}$
E_{Oi} = 0.15 eV	$D_{0,Oi}$ [cm²/s]		$(3 \pm 3) \cdot 10^{-15}$	$(4.6 \pm 0.5) \cdot 10^{-15}$
E_{Al} = 0.4 eV	$D_{0,Al}$ [cm²/s]		$(0.5 \pm 0.7) \cdot 10^{-10}$	$(1.1 \pm 0.2) \cdot 10^{-10}$
ZnO:Al	$c_{Oi}(0)$ [cm^{-3}]	$(1.3 \pm 0.2) \cdot 10^{21}$	$(0.89 \pm 0.04) \cdot 10^{21}$	$(0.77 \pm 0.04) \cdot 10^{21}$
E_{Oi} = 0.15 eV	$D_{0,Oi}$ [cm²/s]	$(4 \pm 2) \cdot 10^{-15}$	$(1.5 \pm 0.7) \cdot 10^{-15}$	$(2.1 \pm 0.9) \cdot 10^{-15}$
E_{Al} = 0.5 eV	$D_{0,Al}$ [cm²/s]	$(2 \pm 2) \cdot 10^{-10}$	$(0.8 \pm 0.5) \cdot 10^{-10}$	$(1.6 \pm 0.7) \cdot 10^{-10}$

The values for the concentration $c_{Oi}(0)$ are decreasing with increasing plasma excitation frequency for both materials. This is consistent with the expectations based on the qualitative model since the number of interstitial oxygen defects should be reduced by a lower flux and energy of the high-energetic negative oxygen ions as it is observed for an increased plasma excitation frequency. The concentration is slightly higher in the $Zn_{1-x}Mg_xO$:Al films in comparison to the ZnO:Al films, which is in accordance with the qualitative model as well. The diffusion prefactors $D_{0,Oi}$ and $D_{0,Al}$ are smaller in comparison to the values determined for the ZnO single crystals which are above 10^{-6} cm²/s. Furthermore, as already pointed out, the shape of the curves can only be reproduced for activation energies much lower than the literature values ($E_{O,lit}$ = 1.3 eV, $E_{Al,lit}$ = 2.74 eV). Using the values $D_{0,Oi} \approx 2 \cdot 10^{-15}$ cm²/s and $D_{0,Al} \approx 10^{-10}$ cm²/s and the activation energies determined by the fit, the diffusion constants at 300 °C are roughly in the range of $D_{Oi} \sim 10^{-16}$ cm²/s and $D_{Al} \sim 10^{-15}$ cm²/s. Hence, the oxygen diffusion constant is comparable to the values determined by Tomlins et al.[284] for 1000 °C.

For extrinsic diffusion, it is assumed that the activation energies remain at a minimum value while the prefactor D_0 increases with increasing defectiveness of the material.[284] This cannot explain the low activation energies accompanied by the low diffusion prefactors D_0 determined for the samples investigated here. The model has certainly strong deficiencies. Yet, the temperature dependence is always exponential even if the equations would be changed slightly, and hence for higher activation energies, the annealing out or phase segregation always starts at higher temperatures and the changes appear more quickly, which would not fit to the experimental data. Therefore, the activation energies are indeed likely to be smaller than the values for the extrinsic diffusion of the elements in ZnO.

There are certain effects that can enhance the diffusivity of the elements in ZnO. It has, for example, been observed, that the diffusion in polycrystalline samples is enhanced in comparison to single crystalline materials by the propagation of the elements along the grain boundaries.[287] More precisely, a reduced activation energy for the diffusion in polycrystalline ZnO (see Fig. 2 in Reference 287) can tentatively be inferred from a comparison of data for single crystalline and polycrystalline ZnO by Haneda et al.[287]. Furthermore, it has been observed that the diffusion parameters depend on whether a dopant and what kind of a dopant is present in the host material. For ZnO doped with Al, for instance, an increase of the diffusivity of oxygen was determined by Sabioni et al.[288]. Another mechanism, which could be responsible for the decreased activation energy, is radiation-enhanced diffusion. Marton et al.[289] studied the diffusion of Ag in sputtered Ni films under 1 keV and 4 keV Ar ion irradiation and found activation energies in the range of some 10 meV for the diffusion under irradiation, while the activation energies for thermal diffusion are in the range of 1 eV to 2 eV for Ag in Ni. Similar differences in the activation energies have also been observed by Pappas and coworkers[290] for radiation-enhanced diffusion of La in CeO_2. This is in very good agreement with the values of a few 10 meV determined for the diffusion of Al and O in ZnO for the films deposited here. Hence, radiation-enhanced diffusion is a reasonable explanation for the low activation energies, because the films deposited by magnetron sputtering are exposed to a bombardment (irradiation) with high-energetic negative oxygen ions. It can therefore be concluded, that the diffusion in these films is not only thermally activated, but increased due to the presence of grain boundaries as well as the dopant Al and radiation-enhanced.

6.2 Radial Distribution of Electronic and Structural Properties

The previous sections showed that the relation between the most important deposition parameters and the structural and electronic properties of the films can be explained by a bombardment of the growing layers with high-energetic negative oxygen ions and the formation of secondary phases or defect

complexes. Another important effect, which reveals the relation between the deposition process and the film properties, is that ZnO films sputtered onto stationary substrates usually exhibit a radial distribution of the electronic and structural properties.[166] The homogeneity of the sputtered films depends on the specific deposition conditions such as the type and the size of the target (circular, cylindrical), its erosion state,[114] the target-to-substrate distance,[263] the plasma-excitation frequency, the plasma excitation power,[263] the arrangement of the magnetic fields and the substrates,[262] static or non-static deposition conditions,[168] and the deposition temperature and pressure[166]. The origin of this radial distribution, however, is still under discussion. Mostly there exist two explanations:

(i) The inhomogeneities are caused by the spatial distribution of the amount and the activity of oxygen reaching the film surface[263] or

(ii) the property distribution is caused by a radially inhomogeneous bombardment of the growing film by high-energetic oxygen ions or atoms[166].

While in model (i) the local deterioration of the structural and electronic properties is explained as a result of excess oxygen reaching the substrate surface, in model (ii) it is argued that the ion bombardment decreases the crystalline quality locally, leading to deteriorated electric properties.

In the following, it will be shown that only model (ii) can describe the origin of the radial distribution of the film properties correctly. To this end, the same deposition system with a moveable magnetron was used to compare radial distributions of fluxes and energies of different negative and positive ions for DC and RF discharges with the electrical and structural properties of deposited films. First, the film deposition was performed, and afterwards the magnetron was rotated by 180° so that it was faced by the plasma process monitor. The characterization of the plasma has kindly been carried out by Dr. Thomas Welzel. Unfortunately, the only targets available for this investigation had a high Al content (4.6 at.%), which led to high resistivities. In consequence, it was not possible to measure the Hall effect in these samples. The discussion of the electric film properties is therefore restricted to the resistivity. Nevertheless, the results of this investigation are generally valid.

6.2.1 Influence of the Target Erosion State and Plasma Excitation Mode

Negative Ions

The radially resolved ion energy spectra were measured for the most prominent negative ions, O^-, AlO^-, and ZnO^-.[160,276] The intensities have been summed over the whole energy region of 0 eV to 500 eV, and it was found that the summed intensities vary strongly for the different ions. The O^- ions have by far the highest intensity, followed by the AlO^- ions and the ZnO^- with at least one order of magnitude lower intensity.

These measurements were performed for the DC sputtering not only on a planar target, but also on the same target in an eroded state. The deliberate erosion was carried out in the DC sputtering mode for approximately 16 h using 50 W generator power, which yielded an erosion groove with a depth of nearly 1.2 mm. The cross-sectional profile of the intentionally eroded target is shown in Figure 6.15 on page 125. The profile can be described reasonably well by two Gaussian functions. The fit parameters $\sigma_z = (3.05 \pm 0.07)$ mm, $r_0 = (13.37 \pm 0.06)$ mm, and $z_{max} = (1.15 \pm 0.02)$ mm will be used later for the numerical simulation of the radial distribution of the high-energetic negative ions (see Section 6.2.3).

Most important for the film properties, however, is the energy distribution of the different ions. Figure 6.16 on page 125 representatively shows the radially resolved ion energy distribution functions (IEDFs) of the O^- ions for DC and RF sputtering from the planar ZnO/Al_2O_3 target and the same target in the eroded state.

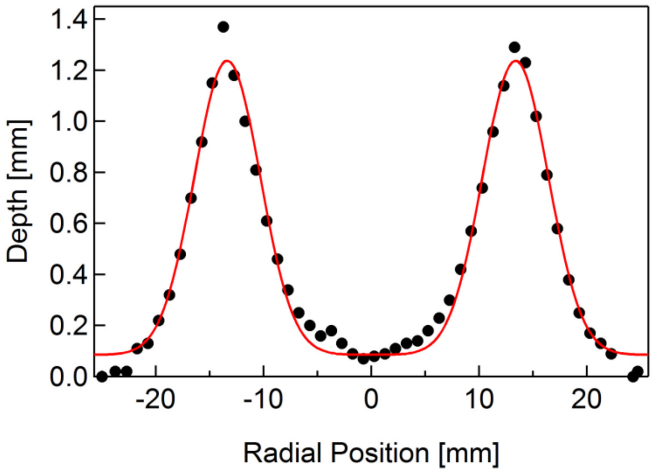

Figure 6.15: Cross-sectional profile of the ZnO/Al_2O_3 target after the deliberate erosion for 16 h by DC sputtering with a power of 50 W. The profile was measured mechanically with a radial resolution of roughly 1.2 mm. The red line shows a fit with two Gaussian functions according to Equation (6.10) in Section 6.2.3. The fit parameters are $\sigma_z = (3.05 \pm 0.07)$ mm, $r_0 = (13.37 \pm 0.06)$ mm, and $z_{max} = (1.15 \pm 0.02)$ mm.

The DC IEDFs show a sharp maximum at energies of approximately 465 eV, which corresponds to the ions formed at the target surface and accelerated across the cathode sheath potential. The measured radial distribution of the negative ions is characterized by an intensity maximum opposite the race track of the target, a lower intensity opposite the centre of the target, and the lowest intensities at large radial positions. This can be explained by the torus-like magnetic electron confinement leading to the highest plasma density in front of the race track of the target. Therefore, the sputtering is strongest in that region, which accounts for the maxima in the radial distribution of the negative ions travelling through the plasma mostly undisturbed and mainly perpendicular to the target surface.[291]

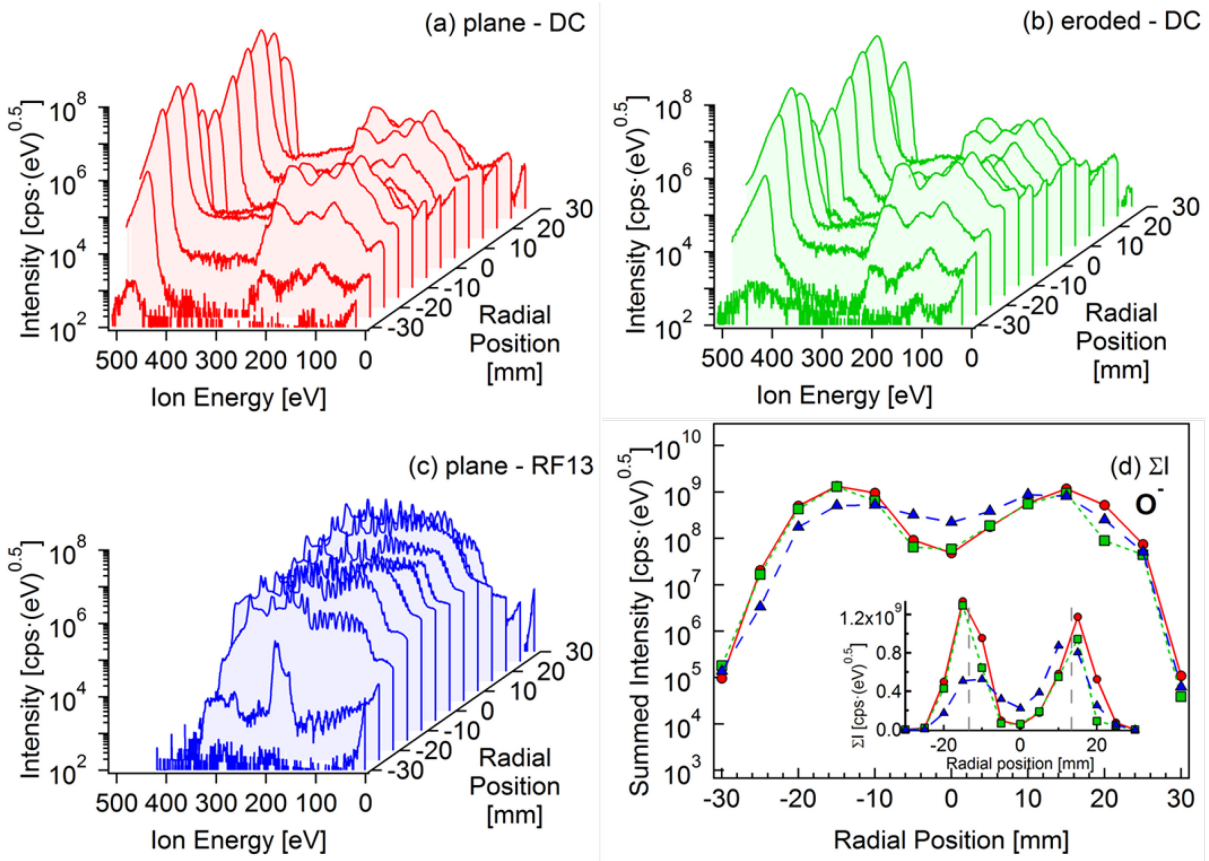

Figure 6.16: Radially resolved ion energy distribution functions (IEDFs) of the most abundant negative ion (O^-) for DC (a),(b) and 13.56 MHz RF (c) sputtering from the planar target (a),(c) and the target in the eroded state (b). (d) shows the radially resolved summed intensity $\Sigma(O^-)$ (0...500 eV) (DC, planar: solid line and circles, red; DC, eroded: dotted line and squares, green; RF, planar: dashed line and triangles, blue). The inset shows the summed intensity on a linear scale. The vertical lines indicate the position of the race track.

The measured IEDFs of O^- for DC sputtering from the target in the eroded state (see Figure 6.16 (b)) do not differ significantly from that of the uneroded target. Only the high-energetic part is shifted to slightly lower values (448 eV) in comparison to the uneroded target (464 eV). This can be explained by the reduction of the target potential caused by an enhanced ionization of the process gas. In the regions where the target becomes thinner, the target surface moves nearer to the magnets, and hence the magnetic field strength and the ionization increase. The summed intensities of the negative oxygen ions for DC sputtering of the planar (red) and the eroded target (green) are compared in Figure 6.16 (d). No significant differences in the radial distributions are observed, which is in contrast to investigations of Ellmer and Welzel[291] who measured a lower intensity of the negative ions for the eroded target. This can be attributed to the stronger erosion of the target used by Welzel and Ellmer (~2.5 mm) in comparison to the one investigated here (~1.2 mm). Additionally, an uncompensated small drift of the detector may obscure the small intensity reduction.

The IEDFs for the 13.56 MHz RF sputtering (see Figure 6.16 (c)) differ, as it has already been shown in the preceding section, significantly from the DC case. The energy distributions are much broader and there is no sharp peak at high energies. The maximum energy of the ions (~360 eV) and their intensities are lower. The radial distribution of the summed intensity of the O^- ions in the case of 13.56 MHz RF sputtering is qualitatively similar to that of the DC case (see Figure 6.16 (d)). There are intensity maxima opposite the race track positions as well. However, the distribution is broader, and therefore the disparity of the ion intensity between the race track and centre position is less pronounced.

The energetic bombardment of the films during the deposition can be described by the energy flux or the momentum flux.[276] The energy flux is defined as the total flux of the ions multiplied by their energy, and the momentum flux is the total flux of the ions multiplied by their momentum.[276,292] In the case of DC sputtering, the average energy $\langle E \rangle$ is nearly the same for the different ions measured for sputtering from the planar target ($\langle E \rangle$ = (463.3 ± 0.6) eV) as well as for sputtering from the target in the eroded state ($\langle E \rangle$ = (446 ± 2) eV). Therefore, the energy flux scales mainly with the intensity of the different ions. The average momentum $\langle p \rangle$ expressed in terms of the average energy $\langle E \rangle$ is $\langle p \rangle = \sqrt{2m\langle E \rangle}$, which means that the momentum flux mainly scales with the flux of the ions and the square root of their mass. The intensity of the O^- ions is at least 14 and 78 times higher in comparison to the summed intensity of the AlO^- ions and the ZnO^- ions, respectively, for the DC excitation. Taking into account the different masses of the ions ($m_{AlO^-} \approx 43$ u, $m_{ZnO^-} \approx 81$ u, $m_{O^-} \approx 16$ u, u: atomic mass unit), the momentum flux is at least 9 and 35 times higher for the O^- ion in comparison to the AlO^- and ZnO^- ions, respectively. This means both, the momentum flux and the energy flux, are highest for the O^- ions, and therefore the O^- ions will have the strongest impact with respect to the structural damage and the deterioration of the electronic properties of the films in the case of DC sputtering. For the 13.56 MHz RF sputtering, the average energies of the different ions are also nearly the same ($\langle E \rangle$ = (149 ± 6) eV). Taking into account their intensities, which are again more than one order of magnitude higher for the O^- ions in comparison to the other ions, also in the case of RF sputtering the O^- ions will have the strongest effect.

Positive Ions

The IEDFs were also measured for the most prominent positive ions for the planar target in DC and RF sputtering mode and for the eroded state of the target in DC sputtering mode. The most prominent positive ion is Ar^+ with approximately two orders of magnitude higher intensity in comparison to the other ions. The second highest intensity is observed for the Zn^+ ion, followed by Al^+ and O^+. The radially resolved IEDFs of the positive ions are shown exemplarily for Ar^+ in Figure 6.17 on page 127.

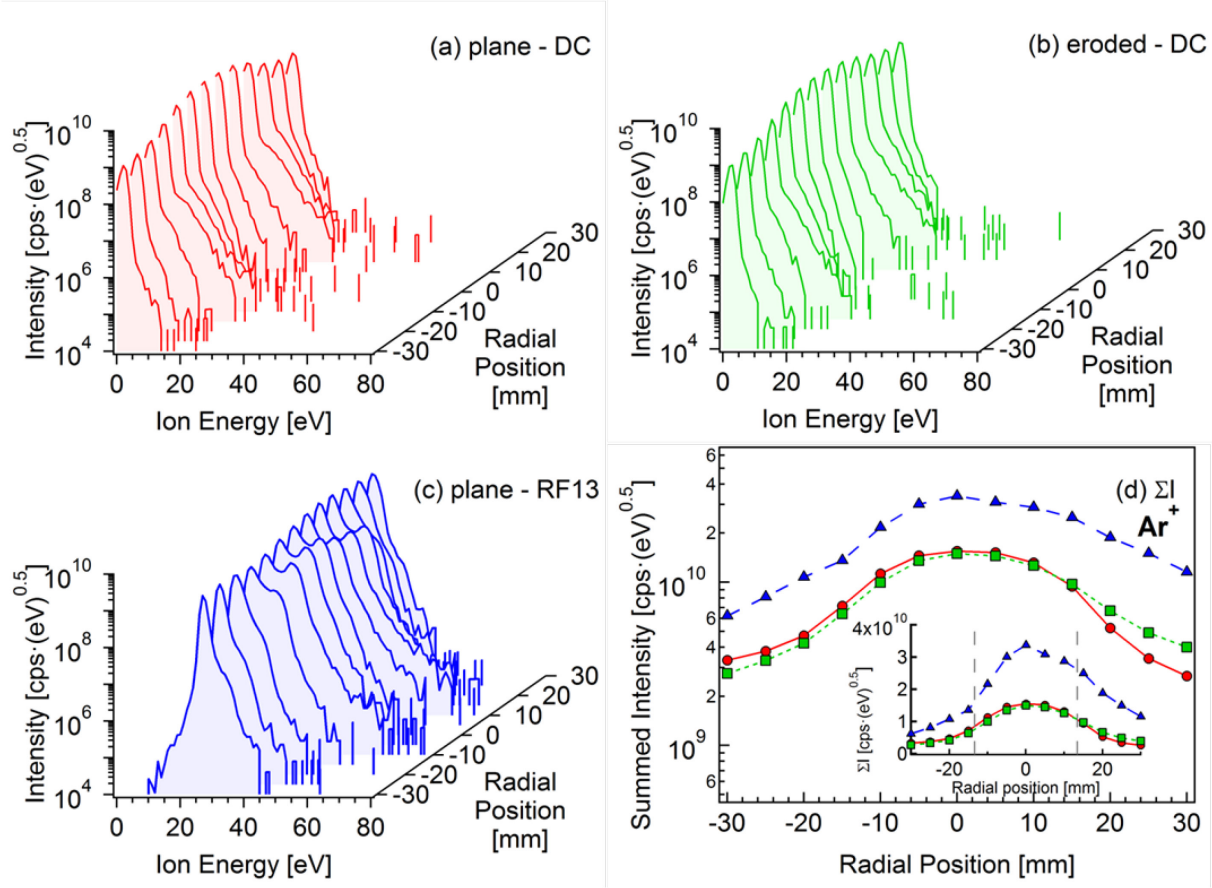

Figure 6.17: Radially resolved ion energy distribution functions of the most abundant positive ion (Ar^+) for DC (a),(b) and RF (c) sputtering of the planar target (a),(c) and the target in the eroded state (b). (d) shows the radially resolved summed intensity Σ(Ar^+) (0...500 eV) (DC, planar: solid line, circles, red; DC, eroded: dotted line, squares, green; RF, planar: dashed line, triangles, blue). The inset shows the summed intensity on a linear scale. The vertical lines indicate the position of the race track.

The energies of the positive ions are mainly between 0 eV and 40 eV with respect to a grounded surface, which is much lower compared to those of the negative ions. Hence, they would reach a grounded substrate with an average energy in the range of 0 eV to 1 eV in the case of DC sputtering from a planar or eroded target, and an average energy of 30 eV for RF sputtering from the planar target. These energies correspond to the plasma potential, because the ions originate from the bulk of the plasma near to the substrate/PPM orifice. However, when the substrate potential is floating, the energies are higher in the case of DC sputtering and lower for the RF plasma excitation.

The radial distribution of the positive ions is similar for DC and RF excitation as well as the planar and the eroded target (see Figure 6.17 (d)). However, they exhibit a radial distribution quite different to that of the negative ions, because they have a maximum in the intensity opposite the centre of the target. This distribution coincides with the thickness distribution of the films, which also exhibits a maximum opposite the centre of the target (see Figure 6.18 on page 128) and corresponds to the distribution of the neutral atoms, which mostly contribute to the film growth.[293]

Electrical Film Properties

After the plasma characterization and the film deposition had been performed quasi-simultaneously, the films were removed from the chamber and investigated with respect to their structural and electronic properties. The radially resolved film thickness d_{film}, resistivity ρ, c-axis lattice parameter c, and crystallite size d_{cryst} of the samples prepared by DC and 13.56 MHz RF sputtering from the target in the two erosion states are shown in Figure 6.18 on page 128.

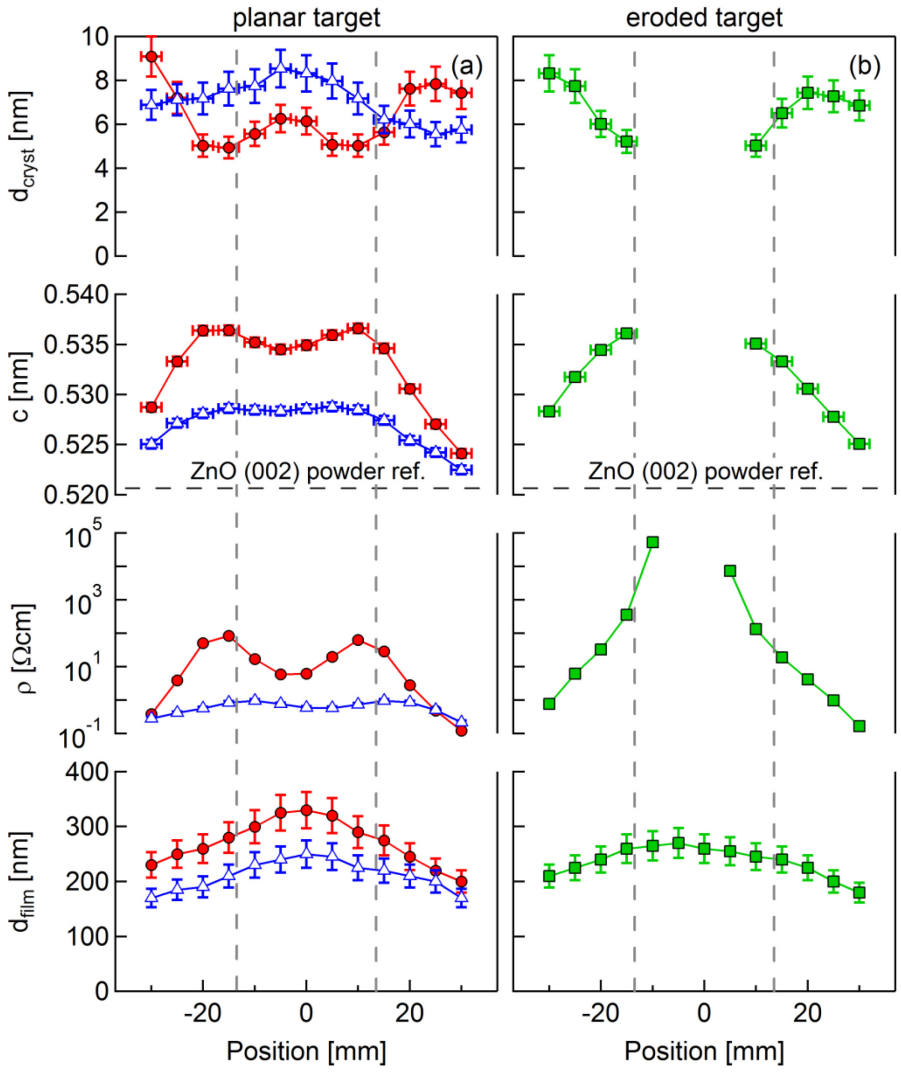

Figure 6.18: Radially resolved film thickness d_{cryst}, resistivity ρ, c-axis lattice parameter c, and crystallite size d_{cryst} determined by resistivity, Hall, and XRD measurements for DC (filled symbols) and 13.56 MHz RF (open symbols) sputtered films from the planar (a) and the eroded (b) target.

The resistivity of the film DC sputtered from the planar target (filled symbols) exhibits two maxima ((74 ± 11) Ωcm) approximately opposite the racetrack of the target, which is denoted with vertical lines in the graph. In the centre of the substrate, the resistivity is lower ((6 ± 0.6) Ωcm), while it is lowest at large radial values ((0.121 ± 0.014) Ωcm). This distribution is qualitatively very similar to the radial distribution of the negative (oxygen) ions. Even the slight differences of the radial distribution of the negative ions between DC and RF sputtering are reproduced in the radial distribution of the resistivity of the films: for the RF sputtered layer, there is still a radial variation with two maxima, but the peaks are much broader leading to a stronger overlap and a smaller variation of the resistivity. The non-uniformity of the resistivity, defined as the ratio between the resistivity opposite the race track ρ_{rt} and the resistivity opposite the centre of the target ρ_c, $r = \rho_{rt}/\rho_c$, is $r = 12 \pm 2$ and $r = 1.633 \pm 0.014$ for the DC sputtered and RF sputtered film, respectively. The difference is due to a strongly decreased resistivity in the region opposite the race track from $\rho_{DC,rt} = (74 \pm 11)$ Ωcm to $\rho_{RF,rt} = (0.95 \pm 0.09)$ Ωcm for the RF sputtered film. For large radial values, on the other hand, the resistivities are very similar ($\rho_{RF,\pm 30\ mm} = (0.270 \pm 0.010)$ Ωcm, $\rho_{DC,\pm 30\ mm} = (0.25 \pm 0.13)$ Ωcm).

The electronic and structural properties of the film prepared from the eroded target by DC sputtering are presented in Figure 6.18 (b). The radial distribution of the resistivity is completely different. While the films sputtered from the planar target exhibit two maxima opposite the race track, the film sputtered from the eroded target has only one maximum opposite the centre of the target with a much higher value of ρ. The values in the centre of the sample were too high to be measured with the 4-point

probe, and therefore the non-uniformity of the resistivity could not be determined. The difference between the resistivity in the centre of the target and for larger radial values is at least more than 5 orders of magnitude. This trend is in contrast with the measured radial distribution of the O^- ions. For these, no significant differences between the planar and the eroded state of the target can be observed (see Figure 6.16 (d) on page 125). For large radial values, however, the resistivity of the film prepared from the target in the eroded state ($\rho_{DC,\pm 30\ mm} = (0.5 \pm 0.3)\ \Omega cm$) is again very similar to that of the planar target ($\rho_{DC,\pm 30\ mm} = (0.25 \pm 0.13)\ \Omega cm$) in the case of DC sputtering.

Structural Film Properties

The c-axis lattice parameters of the film prepared from the uneroded target by DC sputtering (see Figure 6.18 (a)) show a strong lattice expansion in comparison to the powder reference value of $c_{ref} = 0.52066$ nm (JCPDS 36-1451) for all radial positions. This can be explained by compressive in-plane stress,[294,295] caused by the interstitial defects. Again, the radial variation is comparable to that of the high-energetic negative ions, which means two maxima are observed. A maximum expansion of the c-axis lattice parameter of $\Delta c/c_{ref} = (3.05 \pm 0.10)\,\%$ is found opposite the race track of the target. The crystallite sizes show the reverse trend of the resistivities and the c-axis lattice parameters. They vary between 5 nm and 9 nm with highest values at the largest radial positions (9 nm), lower values in the centre of the target (6 nm), and lowest values opposite the race track of the target (5 nm).

In the film RF sputtered from the planar target, the c-axis lattice parameters are less expanded but show the same trend. The radial distribution of the lattice parameter is once more characterized by two peaks opposite the race track of the target. However, the distribution is much broader in comparison to that of the DC sputtered films. The maximal c-axis expansion is $\Delta c/c_{ref} = (1.54 \pm 0.10)\,\%$. The crystallites are generally larger for the RF sputtered film (d_{cryst} between 6 and 9 nm). Although they also exhibit a maximum in the centre of the film and lower values opposite the race track, d_{cryst} is not increasing for large radial values. Up to now, this deviation from the expected behaviour cannot be explained.

A much stronger radial variation of the c-axis lattice parameter and the crystallite size is observed for the sample DC sputtered from the eroded target. This correlates with the much higher resistivity variation. For the centre position of the substrate, it was not even possible to determine the lattice parameter, because the sample was X-ray amorphous in that region. For large radial values, the c-axis lattice parameter is comparable to that of the film DC sputtered from the planar target ($c_{eroded,\pm 30\ mm} = (0.5267 \pm 0.0016)$ nm, $c_{plane,\pm 30\ mm} = (0.5264 \pm 0.0023)$ nm). The crystallite sizes decrease from the outer radial positions to the centre of the sample. For larger radii, the values are in the range of 7 nm to 8 nm and therefore comparable to d_{cryst} of the film DC sputtered from the uneroded target.

6.2.2 Influence of MgO in the Target

Similar measurements have also been performed on a planar sintered 2-inch diameter ceramic $ZnO/MgO/Al_2O_3$ (85/10/5 mol.% (≈ 4.6 at.% Mg, ≈ 4.6 at.% Al)) target using DC and RF excitation. Because of the high amount of Al and Mg in the target and the films, the structural and electronic properties of the films were poor. Their resistivities were outside the measuring range of the 4-point-probe system and the films were almost X-ray amorphous, which means it was not possible to reliably determine c-axis lattice parameters and crystallite sizes. Still, the PPM measurements will be discussed, because they give insight into the effects of the MgO in the target on the flux and the energy of the ions.

Negative Ions

For sputtering from the $ZnO/MgO/Al_2O_3$ target, the IEDFs of O^-, AlO^-, ZnO^-, and MgO^- were measured. Similar to the sputtering from the target without Mg, the highest intensity is measured for the O^- ions, followed by the AlO^- and the ZnO^- ions with at least one order of magnitude lower intensity. The lowest intensity, 3 orders of magnitude below the intensity of the O^- ions, is observed for the MgO^- ions. Generally, also for sputtering from the $Zn_{1-x}Mg_xOAl$ target, the intensities measured for the negative ions in the case of RF sputtering are reduced in comparison to the DC excitation.

The average energies of the negative ions for DC sputtering are in the range of $\langle E \rangle = (406 \pm 2)$ eV, which is slightly lower in comparison to those determined for the ZnO/Al_2O_3 target ($\langle E \rangle = (463.3 \pm 0.6)$ eV). This difference can be explained by a higher ion induced secondary electron emission coefficient γ of MgO in comparison to that of ZnO.[296] An increased γ for the target containing MgO increases the number of secondary electrons formed due to the ion bombardment of the target. Hence, the conditions for sustaining the plasma are improved, and therefore the target voltage and the ion energy are reduced when using a constant power.[297]

For RF sputtering, the average energies of the negative ions are much lower in comparison to the DC case, but have a larger spread ($\langle E \rangle = (153 \pm 10)$ eV), which is consistent with the observations for the ZnO/Al_2O_3 target. Since the average energies of the different negative ions are again similar to each other, the same relationship between the ion intensity and the energy flux as well as the momentum flux as determined for the ZnO/Al_2O_3 target exists. Therefore, the strongest impact on the electronic and structural properties of the growing films is also expected for the high-energetic O^- ions when using the $ZnO/MgO/Al_2O_3$ target.

A comparison of the radial distribution of the fluxes of the O^- ions for DC and RF sputtering from the ZnO/Al_2O_3 (thin lines) and $ZnO/MgO/Al_2O_3$ (thick lines) target is shown in Figure 6.19.

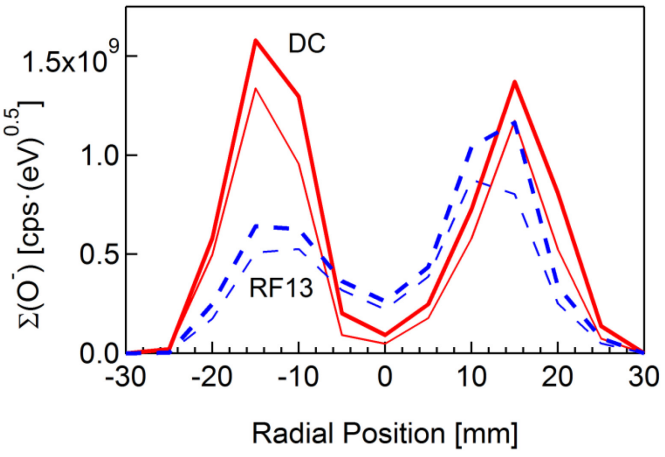

Figure 6.19: Radially resolved summed intensities $\Sigma(O^-)$ (0...500 eV) measured with the PPM for radial steps of 5 mm for O^-. The solid lines show the summed intensities for the planar targets in the DC sputtering mode and the dashed lines show the summed intensities for the planar targets using 13.56 MHz plasma excitation frequency. Thick lines represent the $ZnO/MgO/Al_2O_3$ target and thin lines denote the measurement using the ZnO/Al_2O_3 target.

The radial distribution of the negative O^- ions is, as expected, similar for both targets, which means the radial distribution of the ion intensity exhibits two pronounced maxima for DC sputtering and two broader and weaker intensity maxima for RF plasma excitation. In general, the summed intensities for sputtering from the target containing MgO are slightly higher. This is in accordance with the higher ion induced secondary electron emission coefficient γ for the target which contains MgO. This does not only lead to a slightly reduced target potential but also to a higher amount of O^- ions formed, because the enlarged number of electrons close to the target surface increases the probability of the formation of negative ions. This is some experimental evidence for the fact that the MgO in the target leads to a higher amount of O^- ions and supports the hypothesis about the differences between the electronic and structural properties of the ZnO:Al and $Zn_{1-x}Mg_xO$:Al films.

Positive Ions

IEDFs of the positive ions were measured for Ar^+, Zn^+, Al^+, Mg^+, and O^+. Also for the positive ions, the same trend as for the ZnO/Al_2O_3 target is observed: The intensities of the positive ions of the sputtering gas (Ar^+) are the most prominent, while a decreasing intensity is measured for Zn^+, Al^+, and O^+, respectively. The flux of Mg^+ is ranging between that of Al^+ and O^+. The average energies of the positive ions are 0 eV to 1 eV for the DC sputtering and ~30 eV for the RF excitation with respect to a grounded surface, similar to the values determined for the ZnO/Al_2O_3 target. Hence, the effect of the MgO in the target is not noticeable for the positive ions, which is due to the fact that these ions originate from the plasma body directly in front of the target. The fluxes and the radial distribution of the positive ions of the $ZnO/MgO/Al_2O_3$ are similar to those of the ZnO/Al_2O_3 target as well.

6.2.3 Numerical Simulation and Discussion

For the uneroded ZnO/Al_2O_3 target, a direct correlation between the structural as well as the electronic properties and the radial distribution of the negative ions can be observed. At those positions where the radial distribution of the negative ions exhibits the two maximal intensities, the resistivity of the films is high and the lattice expansion is strong. In these regions also a small crystallite size is observed. The positive ions, on the other hand, have a different radial distribution. They exhibit their maximum intensity opposite the centre of the target. This does not coincide with the radial distribution of the electrical or structural properties of the films and excludes them as an origin of the radial distribution of the film properties. Furthermore, the positive ions have much smaller energies in comparison to the negative ions and therefore their energy or momentum flux is not significant. The radial distribution of the majority of neutral atoms, which also exhibit significantly lower energies compared to the negative ions, is reflected in the thickness distribution of the films and is comparable to that of the positive ions and hence not correlated to the radial distribution of the electronic and structural properties of the films as well. Neutralized ions reflected from the target surface could, in principle, exhibit similar radial distributions with a double peak structure. However, their distribution should be significantly broadened due to the roughness of the target surface giving rise to a more diffuse backscattering, and they also have rather low energies in comparison to the high-energetic negative ions.[120] Actually, all other species exhibit radial distributions not corresponding to the observed film properties. Therefore, it can be concluded that the bombardment of the films with high-energetic negative oxygen ions is responsible for the characteristic radial dependence of the film properties. Hence, if the supply of excess oxygen mentioned in the model of Minami et al.[263] is referring to non-high energetic oxygen, it cannot explain the radial distribution of the film properties, and consequently it must be concluded that the model introduced by Tominaga et al.[166] is more appropriate.

If the sputtering mode is changed from DC to RF excitation, still a similar radial distribution with two maxima of the resistivity and the c-axis lattice expansion and two minima of the crystallite size can be observed and correlated to the two maxima of the intensity of the negative ions, but the radial distribution of the ions and the structural as well as electronic properties becomes broader. This effect can be related to the larger plasma-torus, which is usually observed in the case of RF sputtering and can be explained as follows: For DC sputtering, the electrons that leave their cycloidal path in the confinement regions of the magnetic field will readily move to the anode. Due to the oscillating potentials this is not as easy for the electrons in the RF case, which results in the formation of a larger plasma torus. This is connected to a broader radial distribution of accelerated Ar^+ ions towards the target and therefore to a broader distribution of secondary electrons created. This, in turn, results in a broader radial distribution of the negative ions. Beyond that, the RF sputtering leads to a lower

average energy of the negative ions, which reduces the impact of the O^- ions on the structural and electronic properties. The reduced bombardment of the growing film is reflected in the lower lattice expansion and the lowered resistivity in comparison to the DC sputtering, which is due to the decreased number of compensating interstitial oxygen defects. The larger crystallite sizes can be explained by the reduced number of extended defects, such as stacking faults, created by the bombardment of the growing film by high-energetic O^- ions.

For the eroded target, the situation is quite different. While the radial distribution of the negative ions as measured with the PPM is similar to that of the uneroded target, the structural as well as electronic properties of the films show a completely different trend. The maximal lattice expansion and resistivity and the lowest crystallite size are observed opposite the centre of the target. This discrepancy can be explained by the limited acceptance angle of the mass spectrometer the following way: The high-energetic ions are assumed to be accelerated in the cathode sheath on trajectories perpendicular to the target surface. Since scattering in the plasma for such high energies is not very likely, the negative ions will traverse the plasma mostly undisturbed and not change their direction.[298] That means, only those ions which originate from target areas that are not too much tilted with respect to the normal direction (the direction normal to the planar target surface) can be detected by the PPM. In the case of the planar target, all trajectories are parallel to the normal direction and therefore all ions will be detected if the PPM is placed opposite their formation region. For the eroded target, however, an erosion groove and therefore a curved target surface exists. A large part of the trajectories of the high-energetic negative ions will be tilted with respect to the normal direction, and hence the ions will not be detected by the PPM, which will lead to a discrepancy between the true and the measured radial distribution of the negative ions.

To substantiate this hypothesis, a simple simulation of the radial distribution of the high-energetic negative ions at the substrate surface/PPM orifice was performed. The target erosion profile *z(r)* has been measured and fitted by two Gaussian functions (see Figure 6.15 on page 125). Restricting the problem to two dimensions, the erosion profile can be described by

$$z(r) = z_{\max} \cdot e^{-\frac{1}{2}\left(\frac{r-r_0}{\sigma_z}\right)^2} + z_{\max} \cdot e^{-\frac{1}{2}\left(\frac{r+r_0}{\sigma_z}\right)^2}, \tag{6.10}$$

where r is the radial position on the target ($-r_{\max} \le r \le r_{\max}$), r_0 is the position of the erosion groove, $z_{\max}$ is the depth of the erosion groove, and σ_z is a parameter describing the width of the erosion groove. It should be noted that r does not represent a cylindrical coordinate. The geometry and the notation used is schematically illustrated in Figure 6.20 on page 133.

When the ions are accelerated in the direction perpendicular to the target surface, they will reach the substrate surface at a radial position

$$r'(r) = r + \left(d + z(r)\right)\frac{\mathrm{d}z(r)}{\mathrm{d}r}, \tag{6.11}$$

where d is the distance between the target and the substrate. Additionally, the intensity of the sputtered atoms and therefore also the accelerated negative ions is assumed to have the same radial distribution as that of the erosion groove. This is reasonable, because the erosion groove is a fingerprint of the flux of the sputtered atoms. Since for a point r' on the substrate, several starting points r exist, the number of ions reaching the substrate surface at a certain position r' cannot be determined analytically. To solve this problem, the target and substrate region have been dissected into intervals of equal size ($\Delta r = \Delta r_i = r_i - r_{i-1} = 0.08$ mm, $\Delta r' = \Delta r'_j = r'_j - r'_{j-1} = 0.3$ mm) and a numerical solution has been determined. Taking this into account, an ion originating from a certain position r_i on the target will reach the substrate at a position

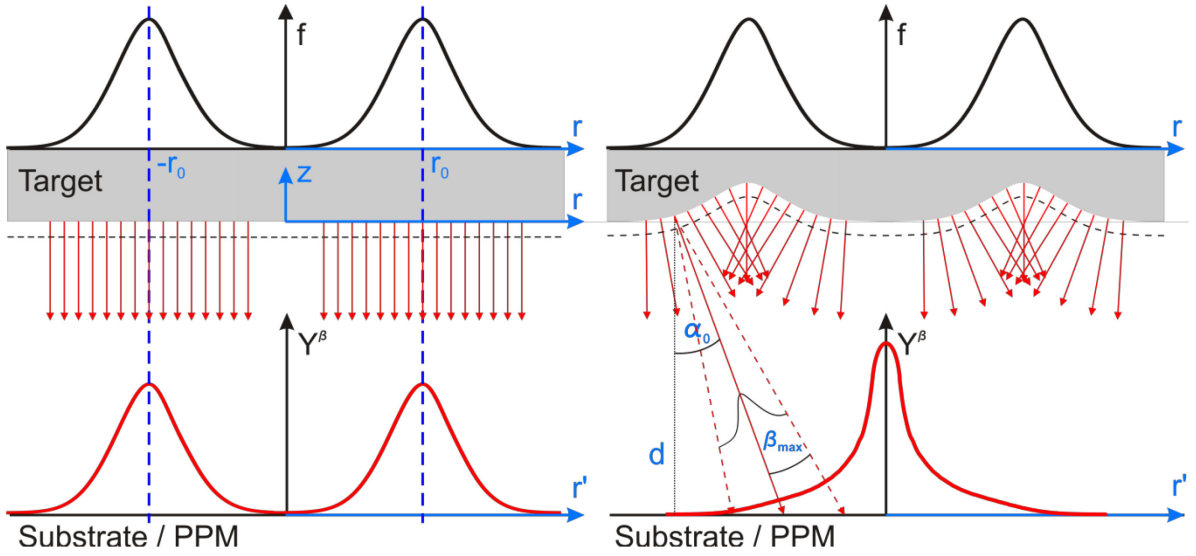

Figure 6.20: Schematic illustration of the geometry for the planar (*left*) and the eroded (*right*) target and the notation for the simulation. f and Y^{β} denote the ion flux at the target and the substrate surface, respectively, α_0 is the tilt of a selected trajectory of an ion with respect to the z-axis, d is the target-to-substrate distance, and β_{max} is the maximum angular deflection of the ions passing the plasma.

$$r'_{\mathrm{j}}(r_{\mathrm{i}}) = r_{\mathrm{i}} + \left(d + z(r_{\mathrm{i}})\right)\left.\frac{\mathrm{d}z(r)}{\mathrm{d}r}\right|_{r_{\mathrm{i}}}. \tag{6.12}$$

The resulting intensity Y_{k} in a certain interval $(r'_{\mathrm{k-1}}, r'_{\mathrm{k}})$ in the substrate region, scaled by $f_{\max}$, is given by

$$Y_{\mathrm{k}} = \sum_{\mathrm{i}} \frac{|r_{\mathrm{i}}|\Delta r}{|r'_{\mathrm{j}}|\Delta r'} \frac{1}{\cos\left(\arctan\left(\left.\frac{\mathrm{d}z(r)}{\mathrm{d}r}\right|_{r_{\mathrm{i}}}\right)\right)} \left(f_{\max} \cdot e^{-\frac{1}{2}\left(\frac{r_{\mathrm{i}}-r_0}{\sigma_z}\right)^2} + f_{\max} \cdot e^{-\frac{1}{2}\left(\frac{r_{\mathrm{i}}+r_0}{\sigma_z}\right)^2} \right), \quad \mathrm{i}: r'_{\mathrm{j}}(r_{\mathrm{i}}) \in (r'_{\mathrm{k-1}}, r'_{\mathrm{k}}) \tag{6.13}$$

as a function of the origin of the ion r_{i}. Only those ions originating from the target surface position r_{i} were counted which reach the substrate in the interval $(r'_{\mathrm{k-1}}, r'_{\mathrm{k}})$. The fluence rate at a certain radial position r_{i} is supposed to be homogeneous around the target. Therefore, the angular size of the interval Δr_{i} and $\Delta r'_{\mathrm{j}}$ was also taken into account in Equation (6.13) to consider the 3-dimensionality of the underlying problem. Considering the curvature of the target, the size of the emitting area on the target is

$$|r_{\mathrm{i}}|\Delta r \cdot \frac{\Delta\varphi}{\cos\left(\arctan\left(\left.\frac{\mathrm{d}z(r)}{\mathrm{d}r}\right|_{r_{\mathrm{i}}}\right)\right)}, \tag{6.14}$$

where $\Delta\varphi$ denotes the polar angle covered by the area. The receiving area on the substrate is $|r'_{\mathrm{j}}|\Delta r' \cdot \Delta\varphi$. To correct the intensity for the different sizes of the emitting and receiving area, the areas were then set into relation. This leads to divergent intensities for very small absolute values of r'_{j} (see simulation in Figure 6.21 on page 135), which was disregarded and considered as an inaccuracy of the model.

Due to interactions with the plasma, a slight deflection of the high-energetic ions is expected. Therefore, an angular distribution of the trajectories of the ions around the direction normal to the substrate surface has been included in the model as well. The intensity of the ions around the angle

perpendicular to the target surface was again assumed to be Gaussian (with a width σ_β). To implement this, a discrete angular variable K_m ranging from $-\beta_{max}$ to β_{max} with $K_0 = 0°$, describing the deflection of the ions from the trajectory perpendicular to the target surface, was introduced together with the Gaussian intensity distribution. With this, the position on the substrate r'^{β}_j and the intensity Y^{β}_k in a certain interval $\Delta r'_k$ is given by (note: the superscript β is only used to denote the introduction of the angular variable K_m. It is no number index.)

$$r'^{\beta}_j(r_i, K_m) = r_i + \left(d + z(r_i)\right)\tan\left(K_m + \arctan\left(\left.\frac{\mathrm{d}z(r)}{\mathrm{d}r}\right|_{r_i}\right)\right),$$

$$Y^{\beta}_k = \sum_{i,m} \frac{|r_i|\Delta r}{\left|r'^{\beta}_j\right|\Delta r'} \frac{1}{\cos\left(\arctan\left(\left.\frac{\mathrm{d}z(r)}{\mathrm{d}r}\right|_{r_i}\right)\right)} \frac{1}{\sigma_\beta\sqrt{2\pi}} e^{-\frac{1}{2}\left(\frac{K_m}{\sigma_\beta}\right)^2} \left(f_{max}\cdot e^{-\frac{1}{2}\left(\frac{r_i - r_0}{\sigma_z}\right)^2} + f_{max}\cdot e^{-\frac{1}{2}\left(\frac{r_i + r_0}{\sigma_z}\right)^2}\right), \quad \text{i,m: } r'^{\beta}_j(r_i, K_m) \in (r'_{k-1}, r'_k)$$

(6.15)

As a last step, a maximum absolute value for the angle $\alpha_m = K_m + \arctan\left(\left.\frac{\mathrm{d}z(r)}{\mathrm{d}r}\right|_{r_i}\right)$, which describes the tilt of the trajectories of the ions with respect to the z-axis, was introduced to take into account the limited acceptance angle of the PPM of approximately ±3° (see Reference 160). Summarizing the previous derivation, the main components of the model are the erosion state of the target, the radial distribution of the intensity of the ions at the target, the angular distribution around the trajectory perpendicular to the target, the ratio between emitting and receiving area, and the acceptance angle of the mass spectrometer.

Figure 6.21 on page 135 shows the results of a simulation of the radial distribution of the negative ions for different target erosion states (left), different values of the erosion groove width/ion distribution width σ_z (middle) and different values of the angular distribution of the trajectories σ_β (right). All simulations have been performed using a maximum flux of $f_{max} = 1.25\cdot10^9$ a.u., a target-to-substrate distance d = 60 mm, and a radial position of the erosion groove at r_0 = 15 mm. The upper row of Figure 6.21 presents the intensity of the high-energetic negative ions on the substrate surface (acceptance angle ±90°) and the lower row displays the intensity, which would be measured with the PPM (acceptance angle ±3°).

For the planar target (z_{max} = 0 mm), the intensity distribution of the ions in front of the target is simply transferred to the substrate surface (see Figure 6.21 (a)), which means two maxima are observed opposite the race track position of the target. This is also true for the simulation of the ion distribution for the measurement with the PPM (see Figure 6.21 (d)). The intensity simulated for the PPM is slightly lower due to the angular distribution of the trajectories, which will inhibit some of the ions from being measured. Significant are the changes when the target becomes more eroded. In this case, the radial distribution of the negative ions on the substrate surface does not show two maxima anymore, but one maximum opposite the centre of the target. This is caused by the curvature of the target, because a substantial amount of ions then has a large angle with respect to the normal direction and will either be transported to larger or to smaller radial positions. When moving to larger radial positions, the intensity is decreasing due to the relation between the receiving and the emitting area. The ions moving closer to the centre of the substrate, on the other hand, will impinge on a smaller area, and therefore the intensity is increased in those regions (ignoring the singularity in the centre of the substrate). For the radial distribution measured with the PPM, however, no significant differences can be observed. The two peaks in the intensity remain visible, only the absolute value of the intensity is decreasing. This is due to the fact, that the ions with a large tilt with respect to the z-axis cannot be

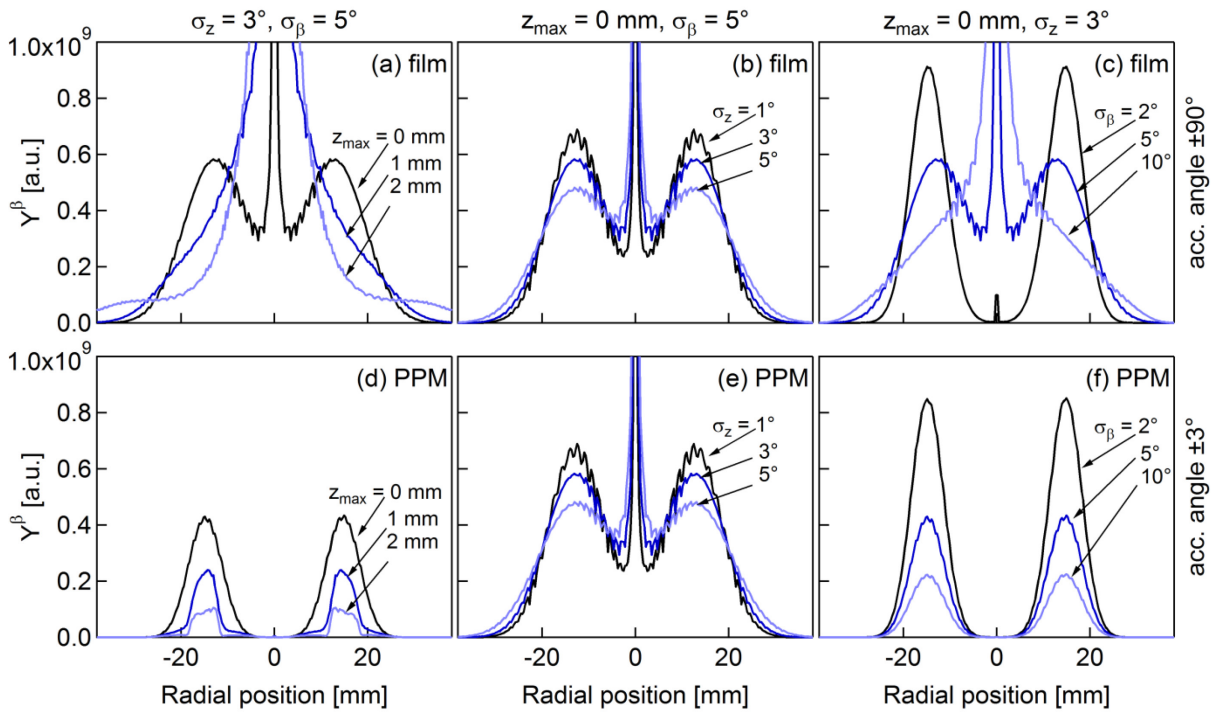

Figure 6.21: Simulations of the distribution of the negative ions on the film surface (acceptance angle ±90°) and for the measurement with the PPM (acceptance angle ±3°). The simulations were performed for different σ_z, σ_β, and z_{max}. In the left, centre, and right row, two values out of z_{max}, σ_β, and σ_z have been kept constant, while one was varied, respectively. The constant parameters are each given as a header of the row. f_{max} = 1.25·10^9 a.u., r_0 = 15 mm, and d = 60 mm were kept constant for all simulations.

detected by the PPM. Therefore, PPM measurements using an eroded target will not show the true radial distribution of the high-energetic negative ions.

The changes of the radial distribution of the negative ions due an alteration of the other parameters can, in principle, be explained by the same effects. A broader erosion groove and intensity distribution width σ_z (see Figure 6.21 (b) and (e)) of the negative ions in front of the target leads to a broader distribution in front of the substrate and, depending on whether the acceptance angle of the PPM is high enough to detect this effect, also a broader distribution measured with the PPM (with a decreasing intensity due to the increasing amount of ions reaching the PPM orifice with angles larger than the acceptance angle). The same effect would occur for an eroded target. A comparable general trend is observed for a change of the width of the angular distribution σ_β around the trajectory perpendicular to the target surface (see Figure 6.21 (c) and (f)). For small angles on a planar target, the radial distribution at the substrate surface is similar to that of the negative ions at the target surface. When the angular distribution is broadened, a situation comparable to that of the eroded target occurs, where the highest intensity of the negative ions on the substrate surface is exhibited opposite the centre of the target. This is again only due to the relation between the receiving and the emitting areas for the ions with large angles of the trajectories with respect to the z-axis. The PPM is once more not able to resolve this effect due to the limited acceptance angle.

In Figure 6.22 on page 136, the results of the simulation of the radial distribution of the intensity of the high-energetic negative ions Y^β are compared to the experimental values. The relevant simulation parameters are summarized in Table 6.5 on the same page.

In the case of DC sputtering from the planar target, the simulation is able to reproduce the radial distribution of the high-energetic negative oxygen ions as measured with the PPM quite accurately (see Figure 6.22 (d)). The radial distribution of the resistivity, on the other hand, differs slightly from the simulated distribution of the negative ions at the substrate surface (see Figure 6.22 (a)). Besides the

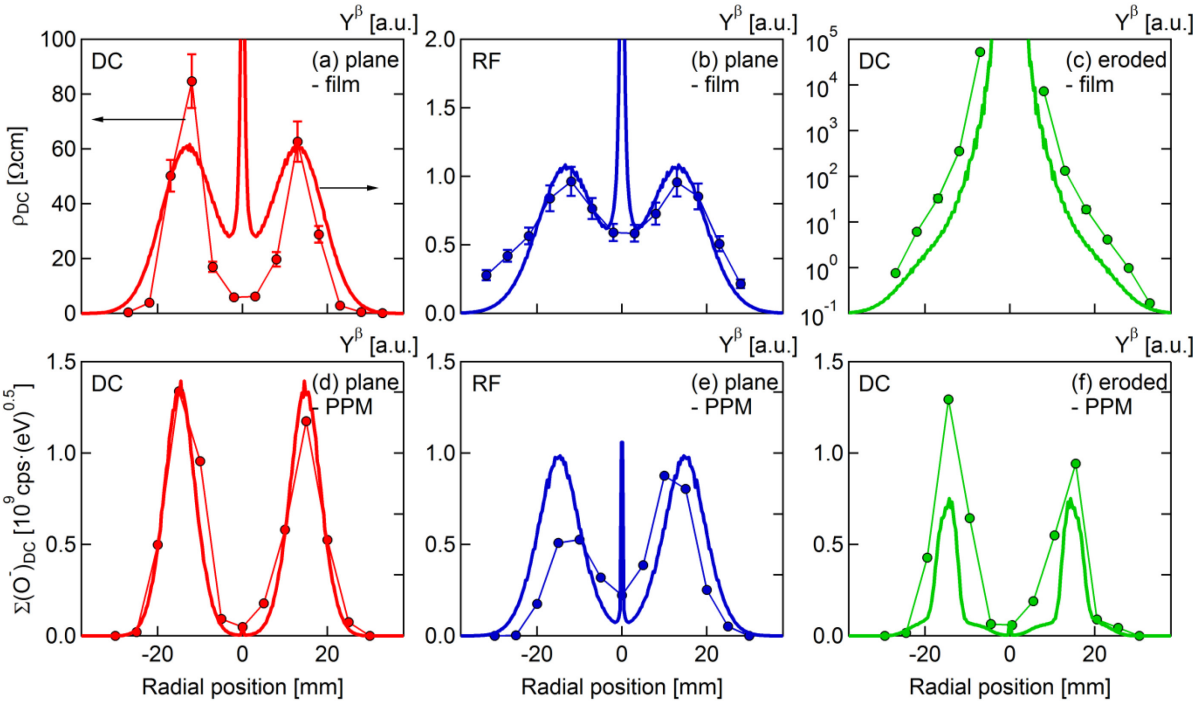

Figure 6.22: Comparison of measured (lines with markers) resistivities ρ and summed negative oxygen ion intensities Σ(O⁻) (0-500 eV) with simulations for the radial distribution of the intensity of the high-energetic negative oxygen ions Y^{β} (thick solid lines) for DC sputtering of the planar target (red, *left*) and the eroded target (green, *middle*) as well as 13.56 MHz RF sputtering of the planar target (blue, *right*). For the simulation of the PPM measurements (*bottom*) an acceptance angle of ±3° has been used, while the simulations of the intensity distribution at the substrate surface (*top*) have been performed with an acceptance angle of ±90°.

simplicity of the model, this can be explained by the oxygen bombardment that introduces acceptor-like interstitial defects in the material, which lead to a compensation of the extrinsic dopant Al and reduce the free carrier concentration. If the free carrier concentration is changed, the mobility will also be affected and therefore, according to $\rho = (en\mu)^{-1}$, the resistivity is not likely to be directly proportional to the flux of the high-energetic ions. For the RF sputtering (see Figure 6.22 (b) and (e)), the broader distribution of the negative ions can be taken into account by introducing a broader width σ_z of the distribution of the negative ions at the target surface. This leads to a slight broadening of the simulated distribution for the PPM measurements and a stronger broadening of the simulation for the radial distribution of the ions at the substrate surface. This is directly reflected in the experimental values.

The most important point of the simulation, however, becomes apparent for the DC sputtering of the eroded target (see Figure 6.22 (c) and (f)), because it can explain that there is no difference in the radial distribution of the ions measured with the PPM for the planar and eroded target, although the resistivity distribution is completely altered. Using the same parameters for the simulation, but only

Table 6.5: Parameters for the simulation of the radial distribution of the high-energetic negative ions in the substrate region (acceptance angle ±90°) or at the PPM orifice (acceptance angle ±3°) for the planar ZnO:Al target in DC and RF sputtering mode as well as the eroded target in DC mode.

Parameter	Plane, DC	Plane, 13.56 MHz RF	Eroded, DC
r_0 [mm]	15	15	15
σ_z [mm]	3.4	5	3.4
z_{max} [mm]	0.15	0.22	1.2
σ_β [°]	5	5	5
acc. angle [°]	3/90	3/90	3/90

changing the acceptance angle from ±3° (PPM) to ±90° (substrate surface), the distribution is changed from a profile with two maxima of the flux opposite the race track positions to a profile, where a maximum of the flux is observed opposite the centre of the target. Only then, a qualitative agreement with the radial distribution of the resistivity of the ZnO:Al film deposited by DC sputtering from the eroded target is reached. Again, the exact shapes cannot be reproduced, but the general trend can be explained as a result of the different acceptance angles of the substrate surface and the mass spectrometer.

These results are in agreement with investigations by Menner and Powalla[114] who studied resistivity variations of a new (planar) and an old (eroded) target as well. They also found two maxima of the resistivity opposite the race track position for ZnO:Al films DC sputtered from a planar ceramic target and one maximum of the resistivity opposite the centre when using an eroded target. A comparison of the structural properties of ZnO films reactively DC sputtered from a plane and an eroded Zn target was performed by Severin and coworkers.[264] Their films exhibited two peaks in the lattice expansion of the films for the new target opposite the race track positions and a strong decrease in the crystalline quality opposite the centre of the eroded target as well. Maximum lattice expansions of $\Delta c/c_{ref} = (3.22 \pm 0.06)\,\%$ for the new target and $\Delta c/c_{ref} = (3.02 \pm 0.06)\,\%$ for the eroded target can be calculated from their 2θ values for the (0002) peak, which is comparable to the values determined here for the films sputtered using the planar target. Tominaga et al.[166] investigated the working gas pressure dependence of the resistivity maxima opposite the erosion groove for DC sputtering from a ceramic ZnO target and found a decreasing non-uniformity of the radial distribution of the resistivity with increasing pressure from approximately 1.3 Pa to 13 Pa. They attributed this to the bombardment of the films by high-energetic oxygen atoms. However, the explanation is basically the same compared to this work, because the effect is related to an increasing thermalization and scattering of the high-energetic oxygen and an angular broadening of the trajectories with respect to the direction perpendicular to the target surface with increasing pressure.

Since the films in this work were prepared using a ZnO/Al_2O_3 and a $ZnO/MgO/Al_2O_3$ target with a high amount of Al (4.7 at.%), they exhibited resistivities too high to be suitable as TCO. Therefore, the results of this section have been verified by DC sputtering of a ZnO:Al film using an already eroded target with a more appropriate composition to prepare films with low resistivities (ZnO/Al_2O_3 98.4/1.6 mol.% (1.6 at.% Al)). Its erosion state was comparable to the eroded ZnO/Al_2O_3 target mainly used for this investigation. The resistivity of this film also showed a maximum opposite the centre of the target ($\rho_{DC,0\ mm} = (3.5 \pm 0.4)\cdot 10^{-2}\ \Omega cm$, $\rho_{DC,\pm 30\ mm} = (1.9 \pm 0.2)\cdot 10^{-3}\ \Omega cm$), while the measured flux of the ions is maximal opposite the race track positions, which means the same fundamental tendencies are observed. Measurements of the Hall effect on this sample showed a decrease of the Hall mobility as well as the free carrier concentration with increasing resistivity from large radial positions to the centre of the substrate, which supports the assumption about the decrease of the free carrier concentration due to the high-energetic negative oxygen ion bombardment. In general, such lateral variations have not only been reported for ZnO films but also for other TCO materials (for example In_2O_3:Sn).[120] Since these materials contain oxygen as well, it is to be expected that high-energetic negative oxygen ions will form during the sputtering.

6.3 Chapter Conclusions

It has been shown, that the high-energetic O^- ion bombardment and the formation of secondary phases or defect clusters are crucial with respect to the compositional, electronic, and structural properties of magnetron sputtered ZnO:Al and $Zn_{1-x}Mg_xO$:Al films. To explain these effects, a qualitative model has

been established, which relates the deposition temperature to the resulting film properties. According to this model, the properties of the films can be explained by the dynamic equilibrium between the formation of acceptor-like interstitial oxygen defects (O_i) compensating the extrinsic electron donors (Zn_{Al}) at lower substrate temperatures, the self-annealing of the interstitial defects at higher deposition temperatures up to $T_{sub}(\rho_{min})$, and phase segregation leading to an inactivation of the Al-dopant at temperatures above $T_{sub}(\rho_{min})$. This hypothesis has been tested by increasing the plasma discharge frequency from DC to 27.12 MHz, which reduces the average energy of the bombarding ions. The beneficial effect of the reduced energy became apparent in increased free carrier concentrations, which were accompanied by decreased resistivities and an improved structural quality of the films. Further, on the basis of the model, the generally lower free carrier concentration in the $Zn_{1-x}Mg_xO$:Al films could be attributed to a stronger bombardment during the growth of these films caused by the MgO in the target. Additionally, a first attempt to quantify the results of the qualitative model has been made. This quantification revealed that the diffusion of O and Al in the films, which is a prerequisite for the annealing out of the interstitial defects and the formation of segregated phases, is significantly enhanced in comparison to thermally activated diffusion by the bombardment of the growing films by high-energetic negative ions.

Furthermore, the qualitative model has been used to explain the radial distribution of the structural and electronic properties with respect to the position of the substrate relative to the target axis. On the basis of experimental data in combination with a simulation of the radial distribution of the high-energetic negative ions, it has clearly been pointed out that the bombardment with these ions is the reason for the radial inhomogeneity of the resistivity as well as the crystallite size and the lattice expansion. These results further substantiate the hypothesis of the model about the role of high-energetic O^- ions. They have to be taken into account not only for ZnO, but also for other semiconducting films, where negative ions are formed at the target surface, which means for other oxides (ITO, FTO) as well as for sulfides and selenides, which are of interest especially for the preparation of the absorber layers in the chalcopyrite thin film solar cells. Since the formation of these high-energetic ions is an inherent property of the magnetron sputter process for these materials, it can only be the aim to reduce the impact of the bombardment of the growing films. This can for example be achieved by increasing the plasma discharge frequency, choosing targets with a lower electron emission coefficient, or the thermalization of the high-energetic ions by higher process pressures.

In the next chapter, the qualitative model will be employed for the interpretation of the experimental data as well. In addition to explaining the observations, this will contribute to review the assumptions about the relation between the deposition parameters and the electronic as well as structural properties of the doped ZnO:Al and $Zn_{1-x}Mg_xO$:Al films made in the model.

7. Doping of Zinc Oxide Films

The doping of ZnO is known and used for many decades now to achieve low electrical resistivities of the material.[22] In course of time, a great variety of dopant elements have been used to create free carriers in ZnO. The highest free carrier concentrations that can be achieved are in the range of $1.5 \cdot 10^{21}$ cm^{-3} for ZnO:Al films deposited by magnetron sputtering or pulsed laser deposition, a limit which also holds for In_2O_3:Sn, the TCO material with the lowest resistivity today. Since the results of the previous chapters have shown that a reduction of the dopant element concentration decreases the density of trap states at the grain boundaries and therefore the influence of the grain boundary scattering, it is of interest to study different dopant materials with respect to their activation, the activation mechanisms, and their influence on the structural properties. In this chapter, the electronic, structural, and optical properties of differently doped ZnO films, all deposited under the same conditions, will be discussed in detail and compared to literature data to determine the influence of the different dopant materials. Additionally, the spatial distribution of the dopant element Al in the films is investigated.

Results, presented in this chapter, have partly been published already in References [A], [B], and [C] from the list in the appendix.

7.1 Doping with Al, Ga, or In

The most common dopant materials for ZnO are Al and Ga. They have already been used for doping of ZnO in the 1950s.[22] While maximal free carrier concentrations of $n \approx 1.5 \cdot 10^{21}$ cm^{-3} have been achieved by doping with Al, Ga doping led to maximal free carrier concentrations of $n \approx 1.2 \cdot 10^{21}$ cm^{-3} for films deposited by ion plating. [299] For magnetron sputtered Ga-doped films, it seems the highest carrier concentration reported is only $9.6 \cdot 10^{20}$ cm^{-3}.[300] The electrically active form of these group III elements is assumed to be the position on the Zn lattice site, where they contribute one electron to the conduction band.[17] From that point of view, Ga is reported to be the most promising dopant element, because the ionic radius[38] of Ga^{3+} (47 pm) is smaller compared to Zn^{2+} (60 pm) but larger than that of Al^{3+} (39 pm), thus leading to less deformation of the ZnO lattice if substituted on the Zn lattice sites.[301] Doping of ZnO films with In is less often reported in literature. However, In-doped ZnO films are found to have a high conductivity and transmittance as well as an excellent surface roughness.[302-304] Czternastek and coworkers[305], for instance, reported free carrier concentrations of $4 \cdot 10^{20}$ cm^{-3} for DC magnetron sputtered films from a Zn-In alloy target with 3 at.% In, and Huang et al.[306] reported approximately $5.4 \cdot 10^{20}$ cm^{-3} for films prepared by RF co-sputtering of ZnO and In leading to resistivities in the order of 10^{-3} Ωcm. It seems, higher free carrier concentrations in the range of $n \approx 10^{21}$ cm^{-3} have not been reported yet. Interestingly, the ionic radius of In^{3+} for 4-fold coordination is 62 pm,[38] which is only 3.3% larger compared to the Zn^{2+} ion. Therefore, it could be expected that the doping should be effective and the structural quality high.

7.1.1 Structural Properties of the Films

Figure 7.1 shows the crystallite size d_{cryst} and the c-axis lattice parameter c of the ZnO:M (M = Al, Ga, In) films deposited at temperatures between ~30 °C and 500 °C using 13.56 MHz plasma excitation frequency.

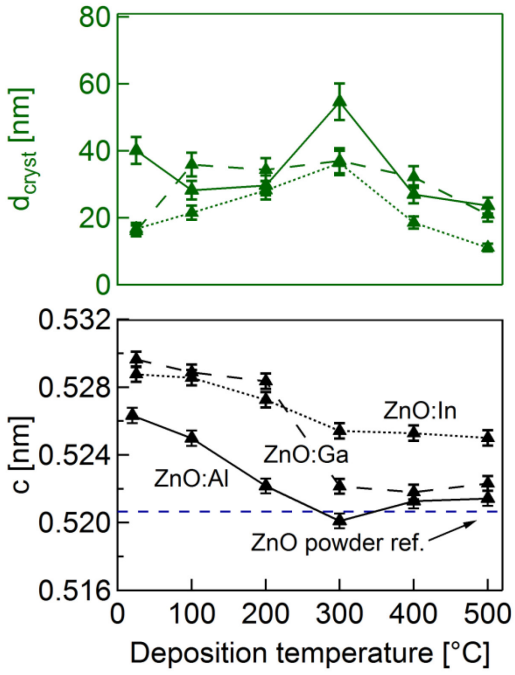

Figure 7.1: Crystallite size d_{cryst} and c-axis lattice parameter c for ZnO:Ga films (dashed lines) and ZnO:In films (dotted lines) as a function of the substrate temperature. The powder reference value for the unstrained c-axis lattice parameter was taken from JCPDS 36-1451. For comparison, the data of the ZnO:Al (solid line) films are also shown.

Generally, the trend of the c-axis lattice parameter expansion is similar for all doped ZnO films. In particular, the ZnO:Ga films exhibit a decreasing c-axis lattice expansion from $\Delta c/c_{ref}$ = (1.72 ± 0.09) % with respect to the ZnO powder value for the film deposited at room temperature to (0.28 ± 0.09) % for the film deposited at 300 °C. Above T_{sub} = 300 °C, the lattice parameter is nearly temperature independent. The elongation of the c-axis for lower deposition temperatures is stronger compared to that of the ZnO:Al films prepared under similar conditions. Since this elongation can mainly be attributed to the bombardment with high-energetic negative oxygen ions, it is not primarily correlated to the incorporation of the Ga on the Zn lattice sites, which is thought to disturb the ZnO lattice less compared to the incorporation of Al. The bombardment by O^- ions, however, is strongly dependent on the shape and the depth of the erosion groove of the target (see Section 6.2). These parameters were different for the ZnO:Al and the ZnO:Ga target, and therefore the absolute values of the c-axis elongation cannot be compared directly. Still, in the region, where most of the interstitial defects are assumed to be annealed out ($T_{sub} \geq$ 300 °C), a comparison of the c-axis length is possible: The smallest lattice parameters obtainable for the ZnO:Al and ZnO:Ga films are (0.5201 ± 0.0004) nm and (0.5218 ± 0.0004) nm, respectively. Assuming that these values are close to the relaxed state, the higher value for the ZnO:Ga films can be explained by the larger ionic radius of the Ga atoms. The crystallite sizes, which are in the range of 15 to 35 nm, are similar to those obtained in the ZnO:Al films. Hence, no general difference in the structural properties of the Al and Ga doped samples can be found here.

The lattice expansion of the ZnO:In films is on a high level, but does not change very much with increasing deposition temperature. With respect to the powder reference value of undoped ZnO, the lattice expansion decreases from (1.56 ± 0.09) % for the film deposited at room temperature to (0.84 ± 0.09) % for T_{sub} = 500 °C. The values for deposition temperatures above 300 °C are much higher compared to those of the ZnO:Al or ZnO:Ga films. This can again be explained by an even

larger ionic radius of the In^{3+} ions in comparison to the Al^{3+} and Ga^{3+} ions. The crystallite sizes in the range of 10 nm to 35 nm are comparable to the ZnO films doped with Ga or Al. It is therefore not possible to conclude about a beneficial effect of the small difference of the size of the In^{3+} and the Zn^{2+} ion of only 3.3 % on the structural properties.

7.1.2 Electronic Properties of the Films

Resistivity, Free Carrier Concentration, and Hall Mobility

Figure 7.2 shows the resistivity ρ, the free carrier concentration *n*, and the Hall mobility μ of the doped ZnO films prepared at 13.56 MHz plasma excitation frequency.

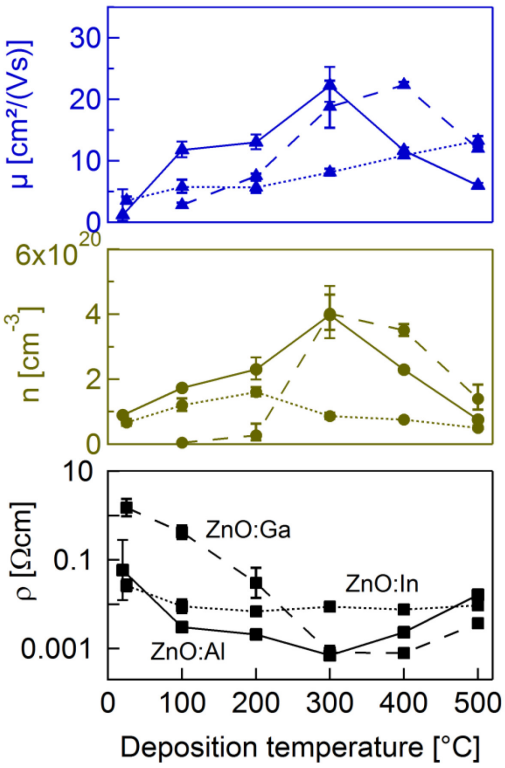

Figure 7.2: Resistivity ρ, carrier concentration *n*, and Hall mobility of the carriers μ for the ZnO:Ga (dashed lines) and ZnO:In (dotted lines) films deposited at substrate temperatures in the range from ~30 °C to 500 °C with 13.56 MHz plasma excitation frequency. For comparison, the data of the ZnO:Al (solid lines) films are also shown.

The trends observed for the structural parameters correspond to those of the electrical properties. The ZnO:Ga films also exhibit the typical bowl-shaped curve for the resistivity as a function of the deposition temperature and the hill-shaped curve for the Hall mobility and the free carrier concentration. The lowest resistivity of the ZnO:Ga films ($\rho = (8.0 \pm 0.8) \cdot 10^{-4}$ Ωcm) is only slightly higher compared to that of the ZnO:Al films prepared under similar conditions ($\rho = (7.0 \pm 0.7) \cdot 10^{-4}$ Ωcm). Also the Hall mobilities and carrier concentrations for these samples are almost equal. The highest carrier concentration in the ZnO:Ga films is $n = (4.0 \pm 0.6) \cdot 10^{20}$ cm^{-3}, while the value for ZnO:Al is $n = (4.0 \pm 0.9) \cdot 10^{20}$ cm^{-3}. The highest Hall mobilities are $\mu_{ZnO:Ga} = (22.3 \pm 0.5)$ $cm^2/(Vs)$ and $\mu_{ZnO:Al} = (22.2 \pm 3)$ $cm^2/(Vs)$.

The variation of the resistivity with changing deposition temperature for the ZnO:In films is also much less pronounced in comparison to the ZnO films prepared with other dopants. The highest value, obtained for deposition at ~30 °C, is $\rho = (0.027 \pm 0.009)$ Ωcm, whereas the lowest value is $\rho = (0.007 \pm 0.002)$ Ωcm. This is a change by a factor of roughly 4. In contrast to this value, the ratio between the lowest and the highest resistivity is about 100 for the ZnO:Al films and 2000 for the ZnO:Ga films. The carrier concentration in the ZnO:In films is between $n = 5 \cdot 10^{19}$ cm^{-3} and $1.6 \cdot 10^{20}$ cm^{-3} with a maximum at 200 °C deposition temperature. This low carrier concentration

corresponds to the values reported in literature, which are mainly below $6 \cdot 10^{20}$ cm^{-3} (see Table 7.4 on page 167). In contrast to the situation for the ZnO:Al and ZnO:Ga films, the Hall mobility of the carriers in the ZnO:In films is increasing over the whole temperature range from (3.5 ± 0.6) cm²/(Vs) to (13 ± 0.7) cm²/(Vs). This is a completely different trend, which can be examined in more detail by analysing the Hall mobility of the free carriers as a function of their concentration.

Figure 7.3 shows the Hall mobility data of the Zn(Mg)O:Al films together with the data of the ZnO:Ga and ZnO:In films.

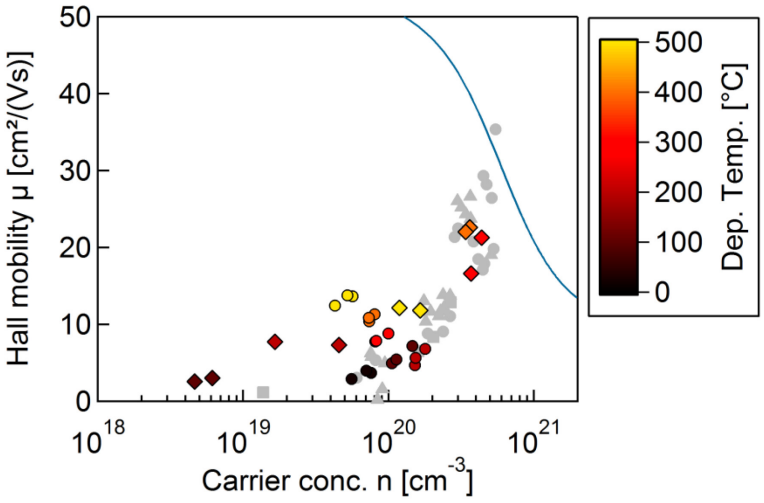

Figure 7.3: Hall mobility μ as a function of the free carrier concentration *n* for the ZnO:Ga (diamonds) and ZnO:In (circles) films prepared at 13.56 MHz in the temperature range between ~30 °C and 500 °C. For comparison, the data of the Zn(Mg)O:Al films (grey) prepared by DC (squares), 13.56 MHz RF (triangles), and 27.12 MHz RF (circles) sputtering are also shown.

The data points of the ZnO:Ga films follow the trend of the Zn(Mg)O:Al films. Their transport is also dominated by scattering at grain boundaries. The comparable crystallite sizes determined by X-ray diffraction point to a similar crystalline quality, and therefore it is reasonable to assume that the lateral grain sizes are also comparable. Together with the comparable dopant contents in the target/films (target: 1.6 at.% Al and 1.3 at.% Ga), which lead, according to the discussion about the origin of the trap states, to a comparable amount of trap states at the grain boundaries, this explains the similarity of the grain boundary scattering for both materials. Only the trap densities at the grain boundaries for lower free carrier concentrations seem to be slightly reduced in comparison to the ZnO:Al films, because the Hall mobilities are higher in the free carrier concentration range between $n \approx 10^{19}$ cm^{-3} and 10^{20} cm^{-3}.

The data points of the ZnO:In films are close to those determined for the ZnO:Ga and ZnO:Al. However, the trend is unusual, because the mobility is highest for the films deposited at the highest temperatures, even though the grain size for these samples is reduced. In consequence, the increasing mobility can only be explained by a dominant influence of a decreasing trap state density. Interestingly, the ZnO:In films show a decrease of the preferred orientation for high deposition temperatures. For these samples, the ZnO $(10\bar{1}0)$ and ZnO $(10\bar{1}1)$ peaks were clearly visible. This has not been observed for any other of the films deposited in this investigation. A possible explanation for the unexpected μ(*n*) dependence could therefore be that the grain boundaries in these samples with low preferred orientation have different properties with respect to the segregation of the dopant, which may lead to a lower value of the trap density at the grain boundaries and hence to the observed behaviour. Actually, decreasing the preferred orientation has been proposed by Ellmer and Mientus[235] to further reduce the resistivity of the TCOs.

Dopant Activation

The dopant activation was calculated based on the dopant content in the films determined by Rutherford backscattering spectrometry. The dopant content can be converted into an absolute

concentration if the density of the films is known. The density was measured by X-ray reflectometry and is ρ = (4.7 ± 0.2) g/cm^3. Using the molar mass M_i and the concentration c_i of the elements in the Zn(Mg)O:M (Me = Al, Ga, In) films, the dopant concentration was calculated by

$$n_{\text{dopant}} = \frac{\rho}{c_{\text{Zn}} M_{\text{Zn}} + c_{\text{Mg}} M_{\text{Mg}} + c_{\text{O}} M_{\text{O}} + c_{\text{dopant}} M_{\text{dopant}}} c_{\text{dopant}} N_{\text{A}}, \tag{7.1}$$

where N_A is Avogadro's constant. The ratio n/n_{dopant} between the free carrier concentration n and the dopant concentration in the films n_{dopant} defines the dopant activation. The RBS measurements were performed for $Zn_{1-x}Mg_xO$:Al films prepared using 13.56 MHz and 27.12 MHz RF sputtering, and no significant difference in the composition of the films has been found. It will be assumed, that the composition is also the same for the DC sputtered films and that from the composition of the ZnO:Al films deposited at 13.56 MHz the compositions of the DC and 27.12 MHz RF sputtered films can be inferred as well. Figure 7.4 shows the activation of the dopants in the ZnO:Al and $Zn_{1-x}Mg_xO$:Al films deposited at DC, 13.56 MHz, and 27.12 MHz plasma excitation frequency and in the ZnO:Ga and ZnO:In films sputtered with 13.56 MHz as a function of the substrate temperature during the deposition.

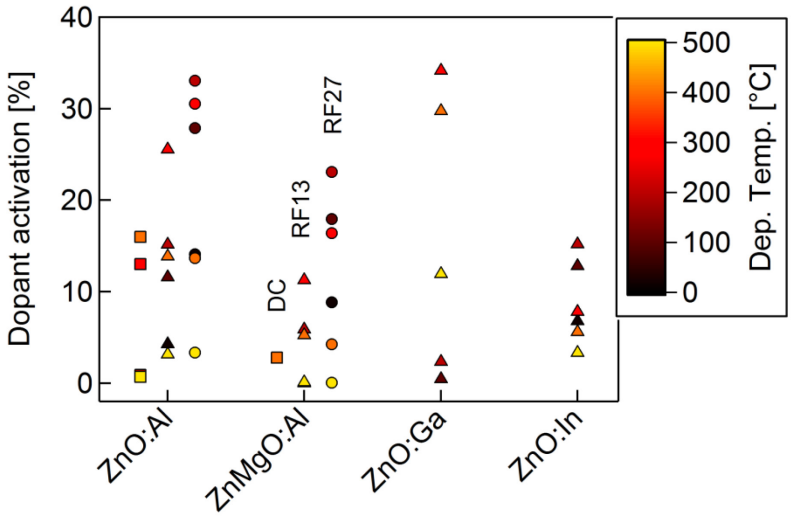

Figure 7.4: Activation of the dopants in ZnO:Al and $Zn_{1-x}Mg_xO$:Al films deposited at DC (squares), 13.56 MHz (triangles), and 27.12 MHz (circles) plasma excitation frequency as well as ZnO:Ga and ZnO:In films deposited at 13.56 MHz. The substrate temperatures were varied between ~30 °C and 500 °C.

The highest dopant activations for the different plasma excitation modes are summarized in Table 7.1.

Table 7.1: Maximal dopant activation for ZnO:Al, ZnO:Ga, ZnO:In, and $Zn_{1-x}Mg_xO$:Al films deposited by DC, 13.56 MHz RF, and 27.12 MHz RF sputtering at substrate temperatures between ~30 °C and 500 °C.

Discharge	Max. dopant activation [%]			
	ZnO:Al	$Zn_{1-x}Mg_xO$:Al	ZnO:Ga	ZnO:In
DC	16 ± 3	2.8 ± 0.7		
13.56 MHz RF	26 ± 5	11 ± 2	34 ± 6	15 ± 3
27.12 MHz RF	33 ± 6	23 ± 4		

Since the Al concentration is almost constant at c_{Al} = (2.1 ± 0.3) at.% for deposition temperatures up to 350 °C, the dopant activation is directly corresponding to the free carrier concentration n in that temperature range. According to the qualitative model, the number of free electrons, and therefore the apparent dopant activation, is reduced by the oxygen interstitial defects for lower deposition temperatures. For deposition temperatures above $T_{\text{sub}}(\rho_{\text{min}})$, the phase segregation leads to an inactivation of the dopant Al and hence to a decrease of the dopant activation. However, even the highest dopant activation, obtained for ZnO:Al films deposited using 27.12 MHz discharge frequency

at 200 °C is only (33 ± 6) %. Although the dominance of the mechanisms for the inactivation of the dopant, the formation of O_i defects and segregated phases or defect complexes, changes with increasing deposition temperature, it must therefore be concluded that both effects seem to significantly contribute to the inactivation of the dopant even for $T_{sub}(\rho_{min})$.

The dopant activation for Ga was more difficult to determine, because RBS measurements cannot resolve the Ga and the Zn signals. Both elements are very close in the RBS spectra, which leads to overlapping peaks due to the finite thickness of the film. Hence, the Ga content in the films cannot be specified. However, a rough estimation of the Ga content in the films was derived from the data of Wang et al.[261]. They published a comprehensive study on dopants in magnetron sputtered ZnO including data about the dopant contents in the targets and in the films. These data are presented in Figure 7.5 together with data of Park et al.[301] and the films investigated here.

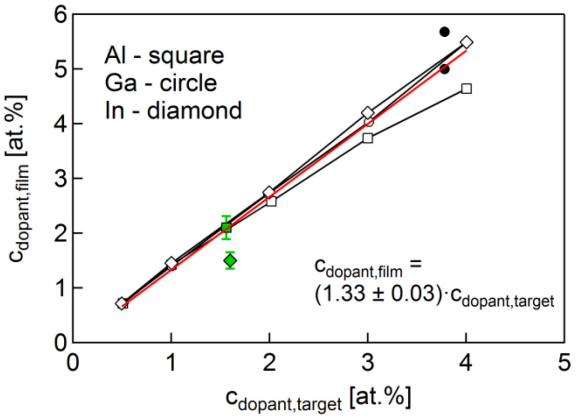

Figure 7.5: Dopant concentrations in the films as a function of the dopant concentrations in the targets for ZnO films deposited by magnetron sputtering with different dopants. The data were taken from Reference 261 (open symbols) and 301 (filled circle). Included are also data measured for the films investigated here (filled diamond and square). The solid red line represents a fit to the data of all dopant materials, excluding the value for In in the films investigated here (filled diamond), which results in $c_{dopant,film} = (1.33 \pm 0.03) \cdot c_{dopant,target}$.

The relation between the concentration of the dopant material in the target and in the film is for low dopant concentrations almost linear. A line fit (red solid line) reveals a ratio $c_{dopant,film}/c_{dopant,target} = (1.33 \pm 0.03)$ for the goup III elements Al, Ga, and In in ZnO films magnetron sputtered at moderate temperatures below approximately 300 °C, process pressures between 0.3 Pa and 1.3 Pa, and sputtering powers ranging from 50 W to 100 W. Only the data for In of the films investigated here is deviating from the other data. Taking this relation into account and assuming a density of the films comparable to that of the ZnO:Al films (4.7 ± 0.2 g/cm^3), the maximum dopant activation in the ZnO:Ga films deposited at 13.56 MHz from the target with a Ga content of 1.3 at.% ($c_{Ga,film} \approx (1.69 \pm 0.07)$ at.%) is (34 ± 6) % (see also Figure 7.4 on page 143). This is a first indication for a higher activation rate of the dopants in ZnO:Ga films. Similar results were obtained by Cornelius[307] who reported a maximum dopant activation of approximately 50 % for doping with Ga and 35 % when using Al. Wang and coworkers[261] also observed higher carrier concentrations for magnetron sputtered ZnO:Ga films in comparison to ZnO:Al films with the same amount of dopant material.

The dopant activation in the ZnO:In films is between (6.8 ± 1.2) % for $T_{sub} \sim 30$ °C and a maximum of (15 ± 3) % for deposition at 200 °C, and hence nearly the same in comparison with the ZnO:Al films for deposition temperatures up to 200 °C. For higher temperatures, the dopant activation is lower but less strong decreasing, so that it is again comparable to that of the ZnO:Al films at deposition temperatures of 500 °C. The similarity of the dopant activation in the low temperature regime points to the fact, that the negative oxygen ion bombardment is not the reason for the small changes of the resistivity with increasing deposition temperatures. The difference is exhibited in the temperature regime, where the phase segregation or formation of defect clusters is dominating the electronic properties. Comparing the enthalpy of formation of In_2O_3 with that of Ga_2O_3 and Al_2O_3, less phase segregation is expected in the ZnO:In films (see Table 7.2 on page 145) since the formation of In_2O_3 is energetically less favourable.

Table 7.2: Standard enthalpy of formation[27] $\Delta_f H^0$ of the most stable oxides for the metals present during the deposition, related to one metal atom, and ionic radii[308] for the ions acting as a dopant, which are expected to substitute the Zn in tetrahedral configuration. CN: coordination number.

Compound	$\Delta_f H^0$ [kJ/mol]	Ion	Ionic radius (CN = 4) [pm]
ZnO	–347.9	Zn^{2+}	60
$(B_2O_3)_{0.5}$	–631.6	B^{3+}	11
$(Al_2O_3)_{0.5}$	–834.8	Al^{3+}	39
$(Ga_2O_3)_{0.5}$	–539.6	Ga^{3+}	47
$(In_2O_3)_{0.5}$	–465.4	In^{3+}	62

Less strong phase segregation, however, is in contrast with the lower dopant activation for 300 °C and 400 °C. Actually, the tendency of the system to form other phases is higher at moderate deposition temperatures (300 °C) compared to the ZnO:Al films, but the temperature dependence is less strong, which means that the amount of segregated phases does not increase as strong with increasing temperature as it is the case for ZnO:Al or ZnO:Ga. If the dopant activation is indeed dominated by the diffusion of In and the segregation of other phases, the difference between ZnO:In on the one hand and ZnO:Al and ZnO:Ga on the other hand could be related to the change of the preferred orientation and therefore to the change of the crystalline structure of the ZnO:In with increasing deposition temperature, which may have an impact on the diffusion behaviour of the In.

Dopant Incorporation

To gain insight into the chemical environment of the dopant elements, X-ray absorption spectroscopy measurements have been performed. Figure 7.6 (a) to (c) on page 146 show the X-ray absorption spectra of the Al-K edge for the ZnO:Al and $Zn_{1-x}Mg_xO$:Al films and the Ga-K edge for the ZnO:Ga films prepared at deposition temperatures between ~30 °C and 500 °C using 13.56 MHz plasma excitation frequency in comparison with reference spectra from the literature.

The Al-K edge spectra of the ZnO:Al (Figure 7.6 (a)) show almost no variations for the complete range of deposition temperatures. This is also true for the $Zn_{1-x}Mg_xO$:Al films up to a deposition temperature of 400 °C. For both materials, the spectra show similar features at similar energies: A first peak at (1560 ± 0.2) eV and (1561 ± 0.5) eV, the second and highest peak at (1565.2 ± 0.2) eV and (1566.2 ± 0.5) eV, and a broad and weak peak at (1575 ± 1) eV and (1577 ± 0.5) eV for the ZnO:Al and $Zn_{1-x}Mg_xO$:Al films, respectively. For comparison, in Figure 7.6 (a), the X-ray absorption spectra of the Al-K edge of AlN are shown as well. AlN is isostructural to ZnO (both materials have the hexagonal wurtzite structure and belong to the space group $P6_3mc$), where the Al atoms in AlN occupy positions equal to those of the Zn atoms in ZnO. The similarity of the Al-K edge absorption spectra of AlN and ZnO is therefore an indication that most of the Al atoms are placed on Zn lattice sites. This is a clear experimental evidence for the doping model, where the Al atoms are localized on Zn lattice sites to donate one electron to the conduction band. Generally, the appearance of the absorption of the Al-K edge of the films investigated here is very similar to that reported by other authors for magnetron sputtered and pulsed laser deposited Al-doped ZnO with an Al concentration in the range of 2 at.% to 3 at.%.[309,310]

Figure 7.6 (b) and (d) show the Al-K edge and Mg-K edge absorption, respectively, of $Zn_{1-x}Mg_xO$:Al films deposited at 300 °C and 500 °C together with the reference spectra of the phases which are most likely to form at high deposition temperatures, α-Al_2O_3, $ZnAl_2O_4$, and $MgAl_2O_4$. The Al-K edge X-ray absorption spectrum of the $Zn_{1-x}Mg_xO$:Al film prepared at 500 °C clearly differs from the spectra for

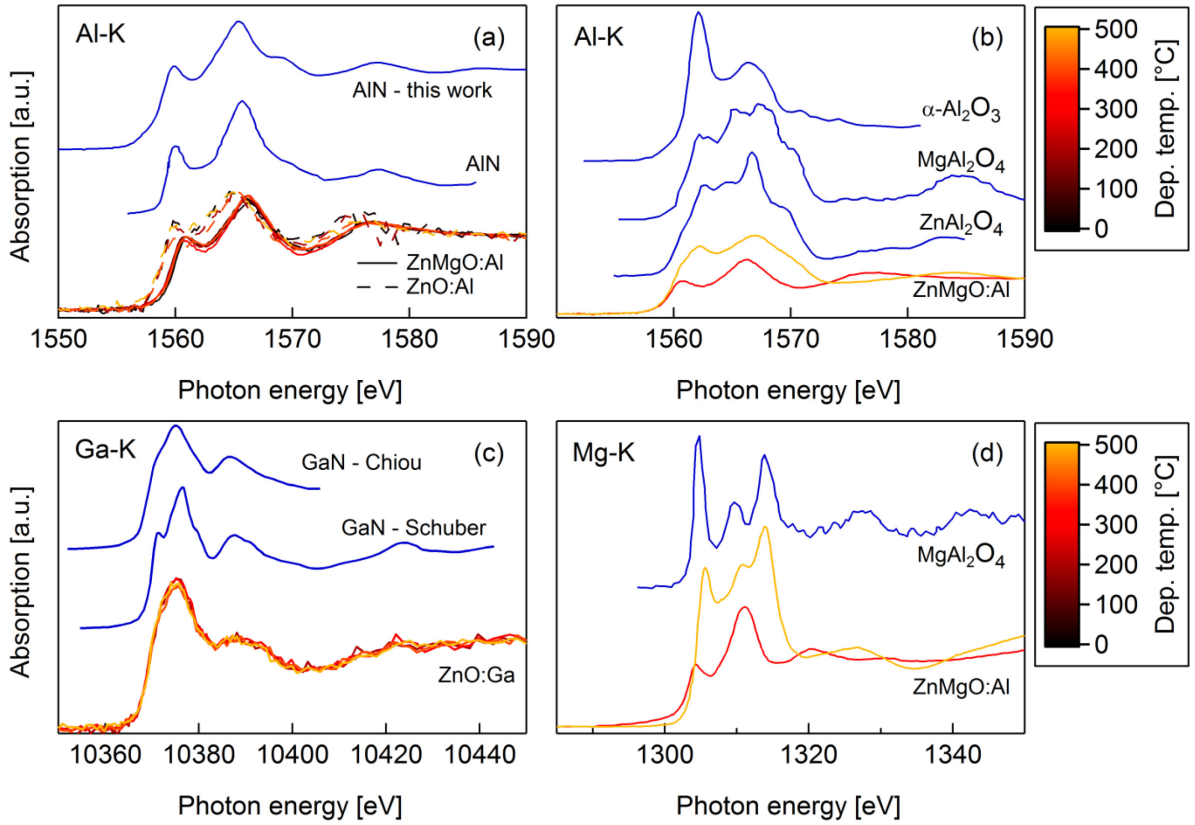

Figure 7.6: (a) X-ray absorption spectra of the Al-K edge of ZnO:Al (dashed lines) and $Zn_{1-x}Mg_xO$:Al (solid lines) films prepared at substrate temperatures between ~30 °C and 500 °C (400°C for $Zn_{1-x}Mg_xO$:Al) together with reference spectra (blue lines) from AlN films deposited in this work and literature values (see Reference 311). (b) X-ray absorption spectra for $Zn_{1-x}Mg_xO$:Al films deposited at 300 °C and 500 °C together with reference spectra[309,310,312] for $ZnAl_2O_4$, $MgAl_2O_4$, and α-Al_2O_3. The reference spectra have been shifted on the energy axis for better comparison: AlN: –4 eV, $ZnAl_2O_4$: +5 eV, $MgAl_2O_4$: –5 eV, and α-Al_2O_3: –5.75 eV. Experimental values for AlN from Reference 311 were taken for polarization perpendicular to the c-axis of the AlN, which is a situation comparable to the experiments performed in this investigation. (c) X-ray absorption spectra of the Ga-K edge for the ZnO:Ga films prepared at substrate temperatures between 200 °C and 500 °C together with reference spectra for GaN by Schuber et al.[313] and Chiou and coworkers[314]. The reference spectra have been shifted as well: GaN - Schuber: –7 eV, GaN - Chiou: –3 eV. (d) X-ray absorption spectra of the Mg-K edge of $Zn_{1-x}Mg_xO$:Al films deposited at 300 °C and 500 °C together with the reference spectrum[312] for $MgAl_2O_4$ (shifted by –4 eV). The data presented were measured in the total electron yield mode.

lower deposition temperatures or ZnO:Al. It has some similarities with the reference spectra, because the features between 1560 eV and 1570 eV are high in intensity compared to the absorption for higher energies, the highest peak is much broader, and the difference in the intensity between the first peak at (1562.2 ± 0.2) eV and the second peak at (1567 ± 0.2) eV is smaller compared to the spectra for lower deposition temperatures. A mixture of Al on Zn lattice sites, α-Al_2O_3, $ZnAl_2O_4$, and $MgAl_2O_4$, measured with a lower energy resolution compared to the reference spectra, may lead to the observed absorption spectrum for the $Zn_{1-x}Mg_xO$:Al film prepared at 500 °C. The features of the Mg-K edge for the sample prepared at 500 °C also clearly differ from those of the $Zn_{1-x}Mg_xO$:Al films deposited at lower T_{sub}. They strongly resemble the Mg-K edge absorption spectrum of the $MgAl_2O_4$. These changes would then be a result of the high amount of segregated phases expected for this sample as it can also be inferred from the RBS data (see Section 6.1.1). Furthermore, since this effect does not occur for the ZnO:Al films and especially the Mg-K edge is modified, which would not be the case if only $ZnAl_2O_4$ was formed, it can be concluded that a significant amount of $MgAl_2O_4$ must be present in that film. Hence, the stronger tendency to form segregated phases in $Zn_{1-x}Mg_xO$:Al can be attributed to the additional formation of $MgAl_2O_4$. The amount of segregated phases cannot reliably be quantified, but qualitative differences to the lower deposition temperatures can clearly be identified.

Similar to the comparison of the ZnO:Al film data with the AlN data, the GaN literature data can be compared to the ZnO:Ga films to determine the position of the Ga atoms in the lattice, because GaN is isostructural to ZnO as well. In this case, the Ga atoms in the GaN occupy the respective places of the Zn atoms in ZnO. Also the X-ray absorption at the Ga-K edge of the ZnO:Ga films shows the same basic features as that of the GaN literature data: A high first peak at (10375 ± 1) eV, which is broadened for the films investigated here and for the data of Chiou et al.[314] in comparison to the data of Schuber and coworkers[313], a second peak in the region of (10388 ± 2) eV, and a slow increase of the intensity for energies higher than 10400 eV. The broadening may partly be explained by a different energetic resolution during the measurements. Furthermore, Schuber investigated samples deposited by molecular beam epitaxy. This resulted most likely in films of much higher structural quality compared to the films investigated here, which may also have an influence on the appearance of the features. From this comparison, it can be concluded that the Ga is preferentially positioned on Zn lattice sites as well, which supports the doping model for the group III elements in ZnO. Furthermore, no significant difference among the spectra of the films deposited at different temperatures can be detected.

Although phase segregation is assumed to dominate the electronic properties for deposition temperatures above 300 °C, no significant phase segregation is visible for the ZnO:Al films even up to deposition temperatures of 500 °C. Yet, one has to keep in mind that the concentration of the Al in the films is low, which leads to noisy spectra and complicates the detection of the secondary phases. Furthermore, relating the change of the free carrier concentration of the ZnO:Al films from 300 °C to 500 °C, $\Delta n = 3 \cdot 10^{20}$ cm^{-3}, to the absolute concentration of Al atoms in the films, $c_{Al} \approx 1.7 \cdot 10^{21}$ cm^{-3}, an increase of the Al bound in secondary phases of only 20% of the Al present in the films is expected. On the other hand, the formation of phases like Al_2O_3 or $ZnAl_2O_4$ has been detected by Yoshioka et al.[310] for his as-deposited PLD samples (T_{sub} = 600 °C) only for concentrations of Al well above 19 at.%. They discussed this, based on experimental data and theoretical calculations, with the formation of a metastable homologous $(ZnO)_3Al_2O_3$ phase as it has been observed for In-Zn-O compounds. This phase has the same basic structure as the wurtzite ZnO except that certain sheets of Zn are replaced by Al, either completely (CN = 6, CN: coordination number) or partially (CN = 4,5).[309] Although the formation of such highly ordered structures is energetically much less favourable in comparison to the formation of Al_2O_3 or $ZnAl_2O_4$, it could explain the experimental observations. This hypothesis is supported by an investigation of Vinnichenko et al.[309] who also did not observe the segregation of Al_2O_3 or $ZnAl_2O_4$ in their as-deposited DC magnetron sputtered films even for dopant concentrations up to 19 at.%, but found the segregated phases after an annealing treatment of these films. They concluded that the Al is incorporated in a metastable phase. In this homologous structure, Al atoms with different coordination numbers are present. Therefore not all of the Al can be electrically active, which would be an explanation for the increasing deactivation of the dopant for higher deposition temperatures if the homologous structure would be formed as secondary phase.

To review these assumptions, annealing experiments were performed in this investigation as well. A film deposited at a substrate temperature of 300 °C on Si was subsequently annealed for 18 h at 600 °C in vacuum ($p < 10^{-5}$ mbar). The results of the X-ray absorption spectroscopy measurements are shown in Figure 7.7 on page 148.

While the Zn-K edge and O-K edge show no significant modification after the annealing process (not shown here), the Al-K edge is changed to a shape similar to that of $ZnAl_2O_4$. However, X-ray diffraction measurements did not show the segregation of any phases, which means that the $ZnAl_2O_4$ must be nanocrystalline (with grain sizes smaller than ~2 nm). The resistivity of the samples was strongly increased (ρ_{ann} = (0.24 ± 0.02) Ωcm, $\rho_{as\text{-}dep}$ = (4.5 ± 0.5)·10^{-4} Ωcm) due to a decrease of both,

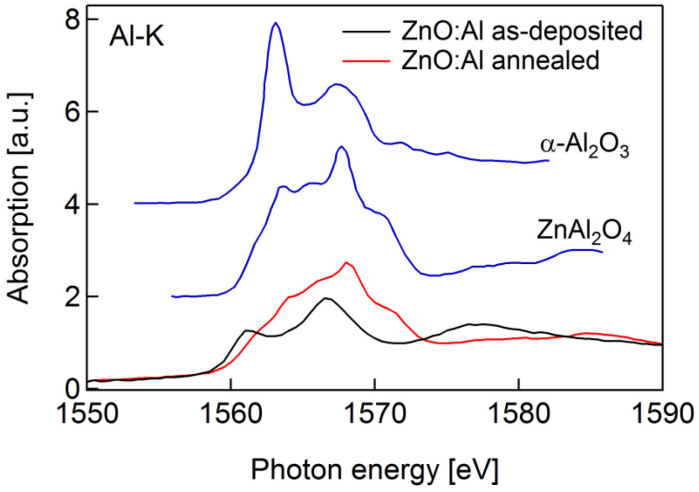

Figure 7.7: X-ray absorption spectra of the Al-K edge for a ZnO:Al film prepared at a substrate temperature of 300 °C with subsequent annealing in vacuum for 18 h at 600 °C together with reference spectra[309,310] for $ZnAl_2O_4$ and α-Al_2O_3. The reference spectra have been shifted to fit to the energy calibration: $ZnAl_2O_4$: +6 eV and α-Al_2O_3: –4.75 eV. The data presented were measured in the total electron yield mode.

the free carrier concentration (n_{ann} = (1.4 ± 0.2)·10^{19} cm^{-3}, $n_{as\text{-}dep}$ = (5.3 ± 0.5)·10^{20} cm^{-3}) and the Hall mobility (μ_{ann} = (2 ± 3) $cm^2/(Vs)$, $\mu_{as\text{-}dep}$ = (26 ± 4) $cm^2/(Vs)$). Relating the decrease of the free carrier concentration to the formation of $ZnAl_2O_4$, a value of roughly 30 % can be calculated for the amount of Al bound in the form of secondary phases after the annealing process. Since this is in the same range as the value determined for the ZnO:Al films deposited using 300 °C and 500 °C, where no other phase was detected, it would support the hypothesis of Yoshioka[310] and Vinnichenko[309].

Unfortunately, no theoretical calculations exist for the Al-K edge absorption of defect complexes like they were proposed by Roberts et al.[275] or Frank and Köstlin[315]. They suggested that electrically inactive complexes of the dopant metal and interstitial or regular oxygen atoms may be formed. If the amount of such defect complexes increases, the dopant activation decreases. It could be possible that a significant amount of these defect complexes forms without changing the signature of the absorption edge of the dopant metal. Furthermore, as will be shown later in Section 7.4, the main part of the Al-dopant in the as-deposited films is segregated at the interface region between the substrate and the film. However, the total electron yield signal of the X-ray absorption spectroscopy is very surface sensitive, which means it stems from a surface region of the film of some nm thickness only. It is therefore plausible that the segregated phases in the as-deposited films cannot be detected by the total electron yield measurement. The fluorescence yield signal, whose information depth is the whole film thickness, on the other hand, was of such a bad quality that an interpretation with respect to the formation of other phases was not possible. Taking this into account and the fact that the formation of the highly ordered homologous phase is energetically very unlikely, the most probable cause for the decrease of the free carrier concentration for deposition temperatures above 300 °C in the as-deposited films is still the formation of defect complexes and/or the segregation of Al_2O_3 or $ZnAl_2O_4$ or other Al-containing compounds.

7.1.3 Optical Properties of the Films

Transmittance, Reflectance, and Absorption Coefficient

As shown in the previous sections, Al, Ga, and In are suitable to prepare films with a low resistivity and a high structural quality. The TCOs, however, are also supposed to have a high transparency in the visible region (roughly 400 nm to 800 nm). Figure 7.8 on page 149 shows the transmittance and $(\alpha h\nu)^2$ of an undoped ZnO and an undoped $Zn_{1-x}Mg_xO$ (similar target content of MgO in comparison to the target used for the deposition of the $Zn_{1-x}Mg_xO$:Al films) film as well as an Al-doped ZnO film, all prepared at 300 °C.

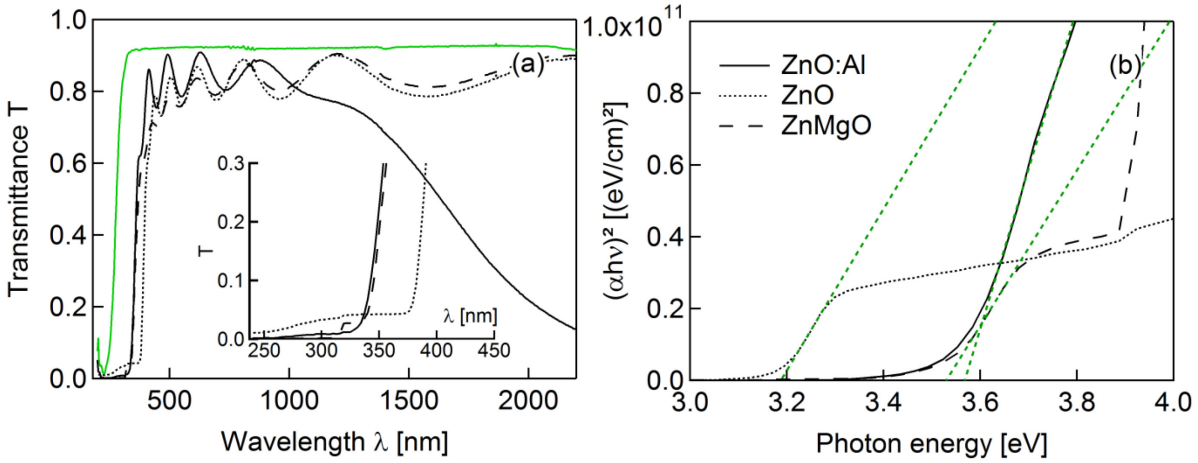

Figure 7.8: Transmittance as a function of the wavelength (a) and $(\alpha h\nu)^2$ as a function of the photon energy (b) for an undoped ZnO (dotted line) and $Zn_{1-x}Mg_xO$ (dashed line) film and a ZnO:Al film (solid line), all prepared at 300 °C. Also shown is the transmittance of the uncoated borosilicate glass substrate (solid green line, (a)) and line fits to $(\alpha h\nu)^2$ (dashed green lines, (b)).

Both, the stack of the ZnO film together with the borosilicate glass substrate (dotted line) as well as the $Zn_{1-x}Mg_xO$ film and the glass substrate (dashed line), have a high optical transmittance. This can be inferred from the small reduction of the average transmittance of the layer stack (T_{avg} = 80 %) in comparison to the uncoated substrate, which has an average transmittance of 92 %. Although the ZnO:Al film has a resistivity orders of magnitudes lower in comparison to the ZnO film (ρ_{ZnO} = (470 ± 50) Ωcm, $\rho_{ZnO:Al}$ = (7.2 ± 0.7)·10^{-4} Ωcm), its average transmittance in the spectral region from approximately 400 nm to 800 nm wavelength is comparable with T_{avg} = 84 %. For higher wavelengths, the absorption due to plasmons is decreasing the transmittance.

A shift of the onset of the transparency in the low wavelength (high energy) region is observed from the undoped ZnO to the doped ZnO:Al film. While the ZnO film begins to absorb the light at energies higher than approximately 3.2 eV, the ZnO:Al film only starts to absorb the light for energies higher than roughly 3.6 eV. This is caused by the increased Fermi energy for higher free carrier concentrations and can be explained by the Burstein-Moss effect (see Section 2.1.3). The optical band gap of the undoped $Zn_{1-x}Mg_xO$ film, on the other hand, is comparable to that of the Al-doped ZnO film. This is due to the incorporation of the Mg, which is known to increase the band gap of the ZnO as has been shown in Section 2.1.4.

When the deposition conditions are changed, not only the electrical but also the optical properties are affected. To explore this effect, Figure 7.9 on page 150 shows the transmittances and the Tauc plots for the determination of the optical band gaps for the ZnO:Al and $Zn_{1-x}Mg_xO$:Al films for different deposition temperatures ranging from ~30 °C to 500 °C.

All samples exhibit a high average transmission in the spectral region between 400 nm and 800 nm. For the ZnO:Al films, the average transmittance of the layer stack prepared at ~30 °C is T_{avg} = 79 %. The average transmittance slightly increases up to 84 % for T_{sub} = 300 °C and is then constant for $T_{sub} \geq$ 300 °C. A similar behaviour is observed for the $Zn_{1-x}Mg_xO$:Al films. For these layers, the average transmittance T_{avg} is lower at deposition temperatures below 300 °C (T_{avg} = 81 %) and constant at 85 % for $T_{sub} \geq$ 300 °C, which is slightly higher in comparison to the ZnO:Al films and likely caused by the higher average transmittance of T_{avg} = 93 % of the quartz substrate. Values higher than T_{avg} = 80 % or T_{avg} = 85% have also been reported by Clatot et al.[23] for their pulsed laser deposited and by Minami et al.[20] for their RF sputtered highly doped ZnO films, respectively.

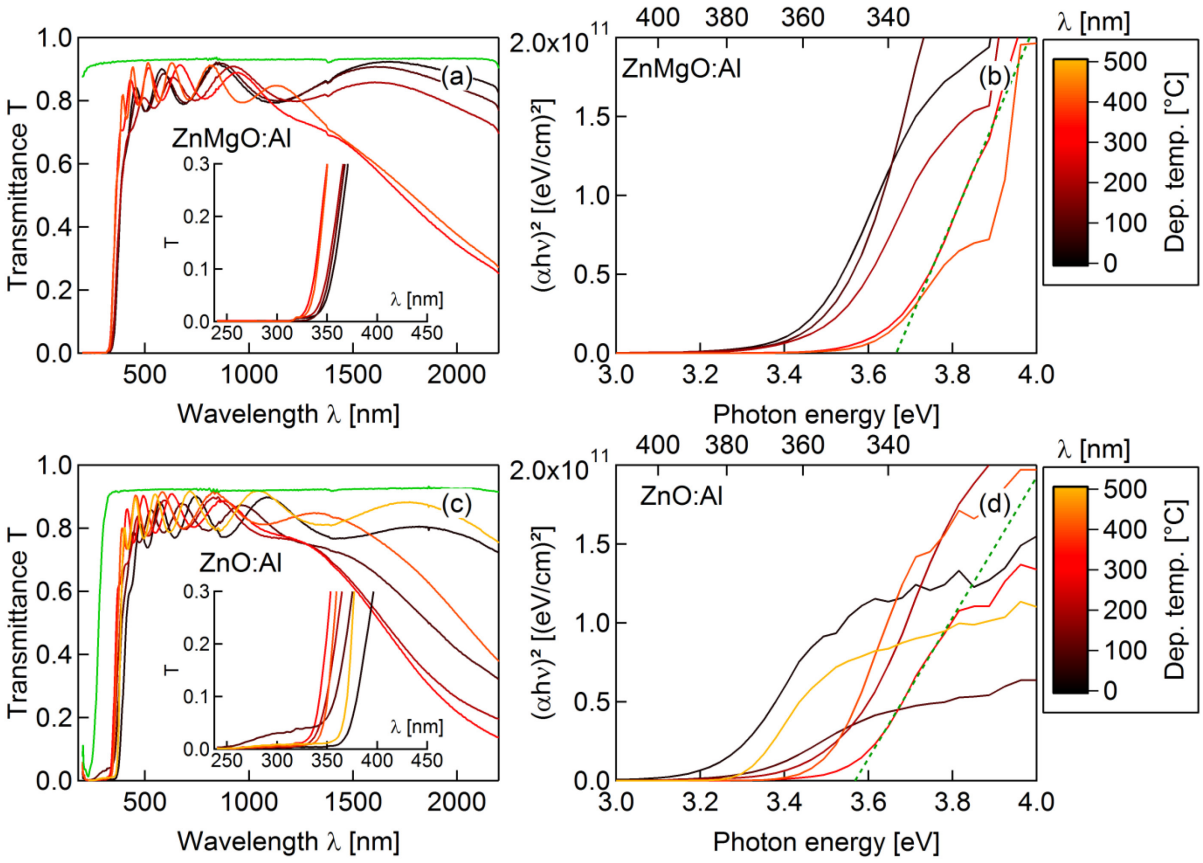

Figure 7.9: Transmittance as a function of the wavelength (*left*) and $(\alpha h\nu)^2$ as a function of the photon energy (*right*) for $Zn_{1-x}Mg_xO$:Al (*top*) and ZnO:Al (*bottom*) films prepared at substrate temperatures between ~30 °C and 500 °C. Also shown is the transmittance of the pure substrate (solid green line, borosilicate glass for the ZnO:Al films and quartz glass for the $Zn_{1-x}Mg_xO$:Al films). (b) and (d) additionally show a line fit to the films deposited at 300 °C. The intersection of this line with the x-axis for $(\alpha h\nu)^2 = 0$ is the optical band gap determined from the Tauc plot.

For higher wavelengths, the absorption of both materials is quite different for the different deposition temperatures. While for the room temperature deposited films and the films deposited at 500 °C the transmittance is on a high level even for longer wavelengths in the region of 1000 nm to 2200 nm, it is strongly reduced for the samples prepared at deposition temperatures in between these two values. This reduction is due to the high free carrier concentration in these samples, which leads to a strong absorption in the near infrared region. This is consistent with the hill-shaped dependence of the carrier concentration determined by the Hall measurements.

The transmittance and the Tauc plot of the ZnO:Ga and ZnO:In films deposited between ~30 °C and 500 °C are shown in Figure 7.10 on page 151.

The spectra are quite similar to those of the ZnO:Al films. The ZnO:Ga films (together with the glass substrate) have a rather high average transmittance in the region between 400 nm and 800 nm, which increases from T_{avg} = 82 % for the film deposited at room temperature to 87 % for the film deposited at 300 °C and then reduces to 85 % for deposition at T_{sub} = 500 °C. Furthermore, the interference pattern is less pronounced. This can be attributed to the low film thickness of only 100 nm to 150 nm for the ZnO:Ga films in comparison to 400 nm to 550 nm for the ZnO:Al films. The onset of the absorption in the films for low wavelengths is at even higher energies compared to those of the ZnO:Al films. It is therefore closer to the absorption edge of the substrate. Nevertheless, the highest energy used for the interpretation of the data is approximately 3.9 eV, which equals 320 nm. For this value, the transmittance of the substrate is only decreased by about 4 % with respect to the value for longer wavelengths. The higher optical band gap is therefore not influencing the data analysis significantly. In

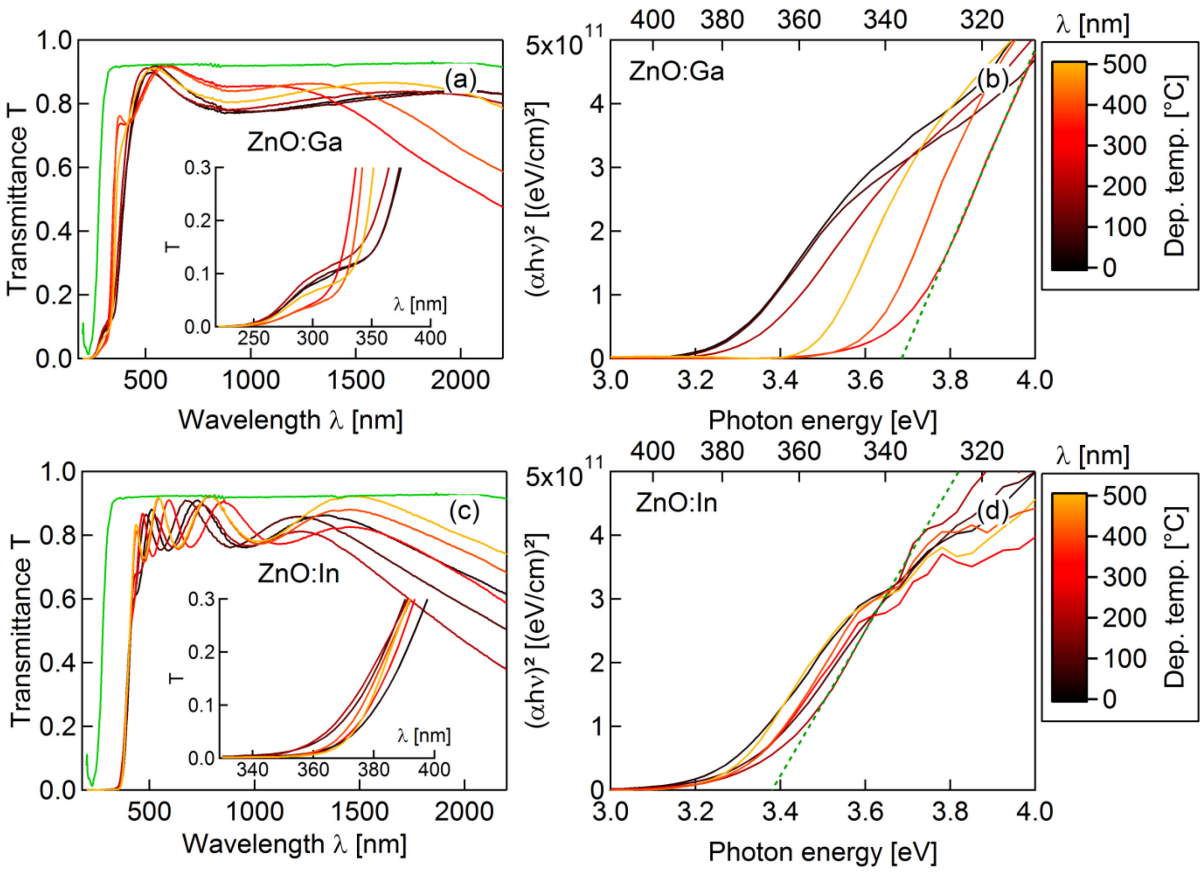

Figure 7.10: Transmittance as a function of the wavelength (*left*) and $(\alpha h\nu)^2$ as a function of the photon energy (*right*) for the ZnO:Ga (*top*) and ZnO:In (*bottom*) films prepared at substrate temperatures between ~30 °C and 500 °C. Also shown is the transmittance of the pure borosilicate glass substrate (green, solid). (b) and (d) additionally show line fits to the data of a ZnO:Ga film deposited at 300 °C and a ZnO:In film deposited at 200 °C, respectively.

general, the curves for the ZnO:Ga in the Tauc plot are covering a wider range of energies in comparison to the ZnO:Al films. This is reflected in a wider spread of the values for the optical band gap (see Figure 7.11 on page 152).

The ZnO:In layers show again stronger interference patterns in the transmission, which is due to their higher film thickness (280 nm to 360 nm) in comparison to the ZnO:Ga films. These values are comparable with the film thicknesses of the ZnO:Al films. The average transmittance (including the substrate) in the spectral region between 400 nm and 800 nm is above 79 % for all films, but the values are generally lower compared to those of the ZnO:Al and ZnO:Ga films. Actually, for deposition at $T_{sub} \leq 300$ °C, the average transmittance T_{avg} is between 80 % and 79 %, and for higher temperatures it is slightly increasing to 82 %. Minami et al.[20] reported values above 85 % for their RF sputtered ZnO:In films, which are higher than those reported here. This can be attributed to their optimized deposition conditions. For DC sputtered films, Czternastek and coworkers[305] obtained optical transmittances between 70 % and 80 %. The ZnO:In films investigated here show a strong absorption in the near infrared region over the whole range of deposition temperatures of the films. This is due to the rather temperature independent carrier concentration.

Band Gap Energies

As discussed in Section 3.3, the most common way of determining the optical band gap using transmittance and reflectance data is the Tauc plot. The results for the optical band gaps inferred from the Tauc plot as a function of the deposition temperature for the doped Zn(Mg)O films are shown in Figure 7.11 on page 152.

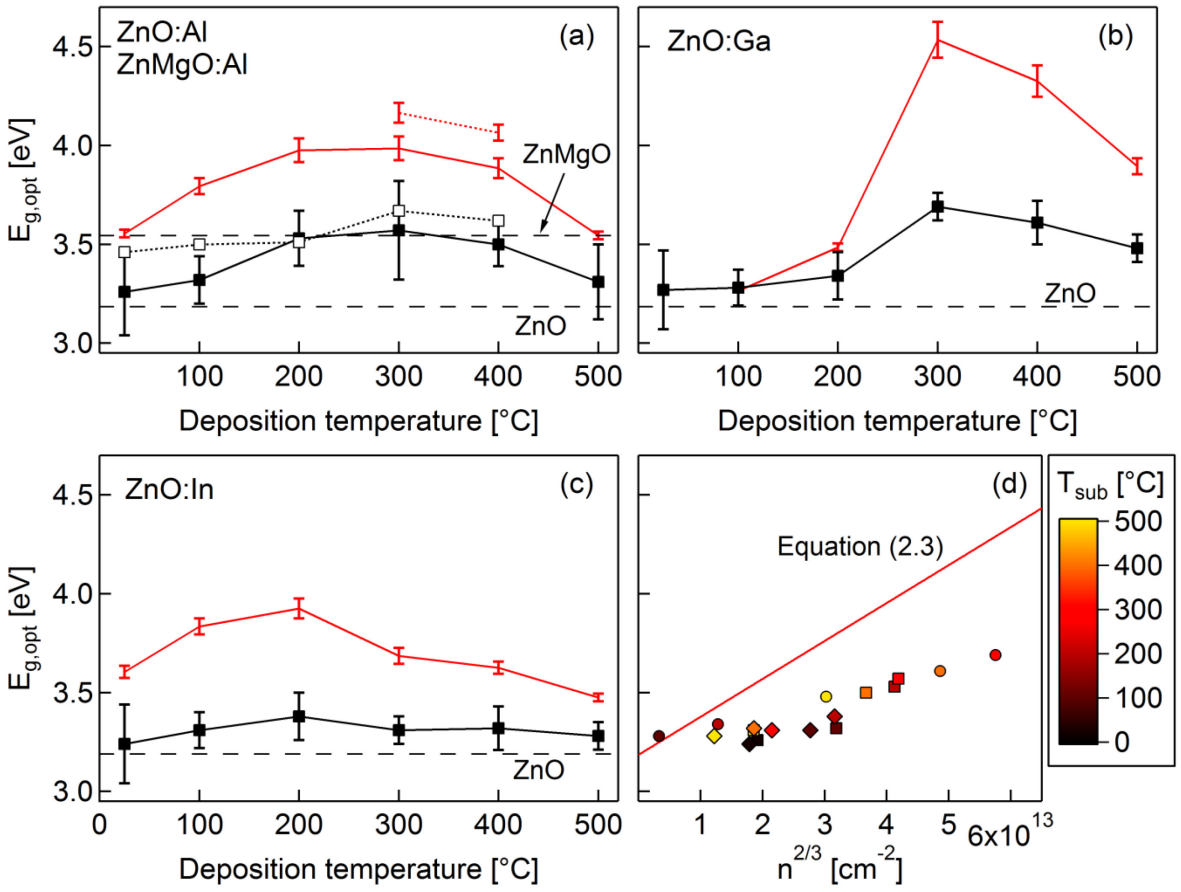

Figure 7.11: Optical band gap energy $E_{g,opt}$ for the ZnO:Al ((a), solid lines), $Zn_{1-x}Mg_xO$:Al ((a), dotted lines), ZnO:Ga (b), and ZnO:In (c) films deposited at 13.56 MHz, determined by linear regression in the Tauc plot. As a reference, the optical band gap values $E_{g,opt}$ for the undoped ZnO and $Zn_{1-x}Mg_xO$ films deposited at 300 °C are given as horizontal lines. Values for the expected optical band gap shift according to the Burstein-Moss effect (Equation (2.3), $m_n^* = 0.28m_e$, $m_p^* = 0.59m_e$) are shown as solid red lines and referred to the band gap values of the undoped films. (d) shows the optical band gaps of the doped ZnO films (Al: squares, Ga: circles, In: diamonds) as a function of $n^{2/3}$ together with the theoretical curve for the Burstein-Moss shift.

According to the expectation, the optical band gaps also follow the hill-shaped trend of the free carrier concentrations. Furthermore, the values for the band gaps are mostly increased with respect to the values of the undoped ZnO or $Zn_{1-x}Mg_xO$. For the ZnO:Al, the lowest values are determined for the films prepared at room temperature ($E_{g,opt}$ = (3.3 ± 0.2) eV). Due to the shift of the Fermi level, the optical band gap energy then increases to a maximum value of $E_{g,opt}$ = (3.6 ± 0.3) eV for deposition at 300 °C. Clatot et al.[316] determined optical band gaps of 3.8 eV and 4.0 eV with the help of the Tauc plot for their ZnO:Al films deposited by PLD at room temperature and at 100 °C, respectively. In this small parameter window, they observed the same trend, but the absolute values were higher. The carrier concentration in their films was around $6 \cdot 10^{20}$ cm^{-3}, which is comparable to the films investigated here and can therefore be no reason for this discrepancy. The difference may be a result of uncertainties in the interpretation of the onset of the absorption due to the polycrystallinity of the films. Dimova-Malinovska et al.[184], on the other hand, obtained values between 3.36 eV and 3.41 eV for their RF magnetron sputtered ZnO:Al films, which are in better agreement to the results obtained here. They also observed the same temperature behaviour: $E_{g,opt}$ = 3.36 eV for films prepared at 150 °C, $E_{g,opt}$ = 3.41 eV for films deposited at 275 °C, and $E_{g,opt}$ = 3.33 eV for films grown at 500 °C.

As already pointed out, the optical band gap energy of the undoped $Zn_{1-x}Mg_xO$ film is higher in comparison to that of the ZnO film. Taking into account that the MgO content in the ZnO/MgO target is the same in comparison to the ZnO/MgO/Al_2O_3 target, a Mg content in the range of 6 at.% in the

$Zn_{1-x}Mg_xO$ film can be expected. An overview of literature data for the band gap energies of $Zn_{1-x}Mg_xO$ films has been given in Section 2.1.4. According to that, the relation between the band gap energy and the Mg content is $E_g = (3.33 \pm 0.02) + (1.98 \pm 0.11) \cdot x$ [eV]. A Mg content of 6 at.% corresponds to $x \approx 0.12$. For this value, a band gap energy of (3.57 ± 0.03) eV is expected from the literature data, which is in very good agreement with the value determined for the undoped $Zn_{1-x}Mg_xO$ film in this work shown as filled green circle in Figure 2.5 on page 11 ($E_{g,opt} = (3.56 \pm 0.01)$ eV). Generally, the values of the doped $Zn_{1-x}Mg_xO$:Al films are closer to the values of the undoped film in comparison to the ZnO:Al films. They vary between (3.46 ± 0.09) eV for the room temperature deposited film, which is actually 0.1 eV smaller than the band gap of the undoped reference film, and (3.67 ± 0.17) eV for the film deposited at 300 °C, but it has to be taken into account that these values have large errors.

The optical band gap values of the ZnO:Ga films are ranging between $E_{g,opt} = (3.27 \pm 0.07)$ eV and $E_{g,opt} = (3.69 \pm 0.12)$ eV. Park and coworkers[301] determined optical band gaps for their room temperature DC and RF sputtered ZnO:Ga of $E_{g,opt} = 3.06$ eV and $E_{g,opt} = 3.2$ eV, respectively. Makino et al.[317] reported values of nearly $E_{g,opt} = 4$ eV for their ion plated ZnO:Ga films, which is due to the high free carrier concentration of $n \approx 1.1 \cdot 10^{21}$ cm^{-3}. This is in good agreement with the values determined for the films investigated here. These band gap values of the ZnO:Ga films are comparable to those of the ZnO:Al for deposition temperatures below 300 °C and slightly higher by 0.1 eV to 0.2 eV for the films deposited at $T_{sub} \geq 300$ °C. This is caused by the higher carrier concentration in the ZnO:Ga films for deposition temperatures above 300 °C and a difference in the local disorder, which will be discussed later.

The optical band gap values of the ZnO:In films cover the range between 3.24 eV and 3.38 eV. Ilican et al.[318] reported comparable values of $E_{g,opt} = 3.3$ eV for their ZnO:In films deposited by spray pyrolysis. The values for ZnO:In are similar to those determined for the ZnO:Al films and ZnO:Ga films at very low or high temperatures. For intermediate deposition temperatures $E_{g,opt}$ of the ZnO:In films is lower. This trend corresponds again to the small changes of the free carrier concentration.

The values for the Burstein-Moss shift calculated according to Equation (2.3) using $m_n^* = 0.28m_e$ and $m_p^* = 0.59m_e$ are represented as solid red lines in Figure 7.11 on page 152. The offset for ΔE_g^{BM} is set to the values of the undoped reference films, hence the red lines show $E_{g,opt} = E_{g,ref} + \Delta E_g^{BM}$. Especially for the ZnO:Al and ZnO:In films, the qualitative agreement is very good and the calculated values are able to reproduce the temperature dependence of the optical band gap properly. This clearly shows, that the shift of the optical band gap energy can be related to the increase of the Fermi energy and therefore to the Burstein-Moss shift. However, the calculated values for the optical band gap energy are too high (see Figure 7.11 (d)), which is a known effect.[30-32] There are several possible explanations for this discrepancy. For example, errors in the interpretation of the optical measurements could be caused by a difference in the structural quality of the films. In fact, a difference in the Urbach tails can influence the onset of the absorption and hence the value for the band gap determined by the Tauc plot. This is especially reasonable since the differences in first stages of the increasing absorbance for the undoped and the Al-doped sample are quite large (see Figure 7.8 on page 149). For the undoped ZnO (0001) single crystal, for instance, a band gap energy of $E_{g,opt} = (3.14 \pm 0.03)$ eV is determined, which is lower in comparison to $E_{g,opt} = (3.19 \pm 0.03)$ eV of the undoped ZnO film and shows the influence of the crystallinity on the value of the band gap energy determined by the Tauc plot. Another reason for the discrepancy between the calculated and the measured optical band gaps is an overestimation of the increase of the Fermi energy with increasing free carrier concentration, because Equation (2.3) does not take into account the non-parabolicity of the energy bands. However, it is known that ZnO exhibits a non-parabolicity of the conduction band, for which the effective mass is increasing with increasing free carrier concentration.[16] This is caused by a higher density of states in the non-parabolic band in

comparison to the parabolic band and leads, with increasing free carrier concentration, to a slower increase of the Fermi energy/optical band gap in the samples than predicted with the equations for the parabolic band. Additionally, there is a band gap narrowing in highly doped semiconductors caused by the interactions of the electrons and the charged dopant atoms.[30,32] It is likely, that all these effects are contributing to the discrepancy between the measured optical band gaps and the calculated values.

Local Disorder

In Chapter 4, it has been shown that the disruption of the symmetry of the crystals leads to the formation of states in the band gap, which are detectable in the optical absorption and emission spectra as Urbach tails. This disruption is not only caused by intrinsic defects but it can also be induced by dopants. To explore this effect, Figure 7.12 shows the Urbach plots of the doped ZnO films deposited at different substrate temperatures in the range between ~30 °C and 500 °C. Table 7.3 on page 155 summarizes the Urbach energies, which were determined by fitting Equation (4.4) to the absorption data shown in Figure 7.12.

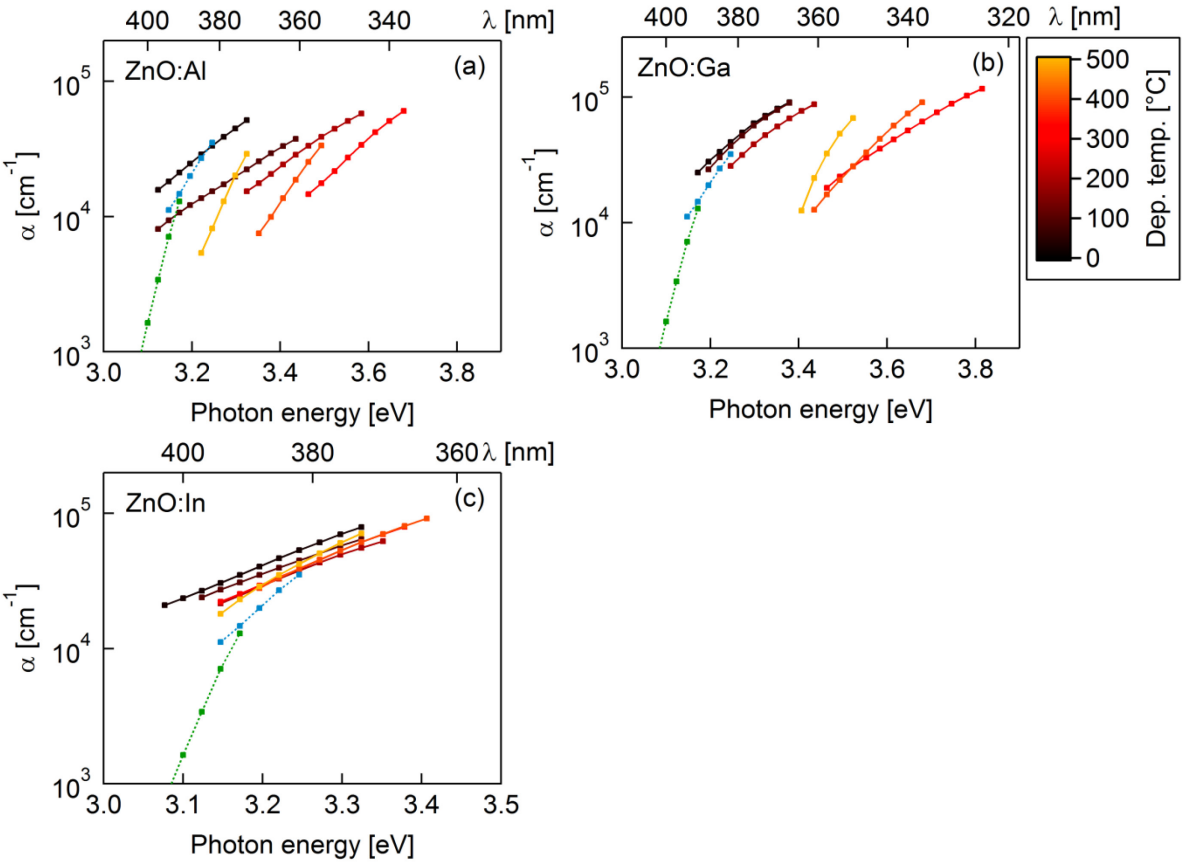

Figure 7.12: Urbach plots of ZnO:Al (a), ZnO:Ga (b), and ZnO:In (c) films deposited at substrate temperatures between ~30 °C and 500 °C as a function of the photon energy and the wavelength of the light. The dotted lines show the absorption of the ZnO single crystal (green line) and the ZnO film (blue line), both undoped. The data for the $Zn_{1-x}Mg_xO$:Al films has already been shown in Figure 4.6 on page 66 and will be omitted here.

The slopes of the curves, which correspond to the Urbach energies, are quite different for the different films. The absorption as a function of the photon energy for the ZnO single crystal (dotted green lines in Figure 7.12) exhibits the steepest slope, which corresponds to the smallest Urbach energy of E_U = (30 ± 3) meV and therefore, consistently, to a low disorder. The undoped ZnO film (dotted blue lines) has a higher Urbach energy ((86 ± 3) meV), pointing to a stronger disorder in the film. This is expected since it is a polycrystalline film. The doped ZnO:Al film (also deposited at 300 °C) has again a higher Urbach energy (E_U = 154 ± 4) meV). Obviously, the introduction of dopants introduces

Table 7.3: Urbach energies for polycrystalline ZnO:Al, ZnO:Ga, and ZnO:In films determined by fitting Equation (4.4) to the absorption data. For the Ga- and In-doped ZnO films prepared at 200 °C, 400 °C, and 500 °C, the values are calculated by fitting the equation to the higher and lower end of the curves in Figure 7.12 to consider the nonlinear slope. The errors are then one standard deviation of the average of the two values obtained by the fit. Reference values for an undoped ZnO single crystal and an undoped ZnO film are also given.

	E_U [meV]			
Sample	**Undoped**	**Al-doped**	**Ga-doped**	**In-doped**
ZnO single crystal	30 ± 3			
ZnO film (300 °C)	86 ± 3			
ZnO:M (RT)		171 ± 2	170 ± 40	186 ± 2
ZnO:M (100 °C)		208 ± 2	160 ± 30	206 ± 2
ZnO:M (200 °C)		201 ± 5	170 ± 30	190 ± 10
ZnO:M (300 °C)		154 ± 4	190 ± 30	182 ± 3
ZnO:M (400 °C)		94 ± 5	130 ± 20	180 ± 10
ZnO:M (500 °C)		61 ± 5	80 ± 30	140 ± 20

disorder in the material. This has also been observed by Caglar et al.[319], who determined Urbach energies roughly in the range of 150 meV to 250 meV for their doped ZnO, which increased for increasing dopant concentration in the films. As already pointed out, for the different deposition temperatures, basically a decreasing Urbach energy is observed for the ZnO:Al films. The film deposited at room temperature has a slightly lower Urbach energy. Interestingly, this corresponds to the slightly higher crystallite size determined by XRD measurements for this sample and also to the results of Dimova-Malinovska et al.[184].

The general trend of the Urbach energies of the ZnO:In and ZnO:Ga films is similar to that of the ZnO:Al films. For low deposition temperatures, the films exhibit high Urbach energies pointing to strong structural disorder, which decreases with increasing deposition temperature. The Urbach energies of the ZnO:Ga films investigated here are comparable to those reported by Wei et al.[202] for epitaxial Ga-doped $Zn_{1-x}Mg_xO$ (5 at.% Mg, $x \approx 0.1$) grown by pulsed laser deposition at 650 °C. They determined values between approximately 100 meV and 130 meV for Ga contents in the range of 1 at.% to 3 at.% (the Ga content of the films investigated here is calculated to be (1.69 ± 0.07) at.%). Aghamalyan et al.[320] reported E_U = 467 meV for their as-deposited e-beam evaporated ZnO:Ga films on c-sapphire (0001) substrates. Their undoped ZnO reference exhibited an Urbach energy of approximately 90 meV. Obviously, the influence of the dopant on the structural disorder in the films is also related to the preparation conditions, since the difference between the undoped and the doped sample is much higher for the films of Aghamalyan and coworkers in comparison to the results of this study.

While the ZnO:Al films exhibited values as low as 61 meV and the ZnO:Ga films only 80 meV, the ZnO:In films still have an Urbach energy of 140 meV at T_{sub} = 500 °C. This points to a stronger local structural disorder in comparison to the other films for high deposition temperatures. In general, the range covered by the Urbach energies of the ZnO:In films is smaller compared to that of the other dopants. This is consistent with the other observations regarding structural, electronic, and optical properties. The values for the ZnO:In films are comparable to the values of Caglar et al.[319] for their In-doped ZnO films prepared by the sol-gel method. They reported Urbach energies in the range of 150 meV to 250 meV for dopant concentrations between 0.7 at.% and 2.3 at.%. Ilican and coworkers[318] determined Urbach energies ranging from 85 meV to 105 meV for ZnO:In films prepared by spray pyrolysis, which is even lower. These results point to a very high structural quality of their films.

Although the crystallite size according to the XRD measurements is decreasing for temperatures above 300 °C the order in all the samples, according to the Urbach energy, is still increasing. Based on the qualitative model, this can be explained by the annealing out of the interstitial defects due to the higher mobility of the atoms during the formation of the film for higher substrate temperatures. These point defects do not cause a significant broadening of the XRD peaks and hence do not influence the crystallite size, while extended defects, which reduce the crystallite size determined by the XRD, on the other hand, may not affect the Urbach tail strongly. Therefore, the results obtained from the optical measurements for the local disorder support the qualitative model.

7.2 Hydrogen Co-Doping

A doping effect in ZnO is not only induced by group III elements but also by other elements, one of which is hydrogen. In fact, the doping action of hydrogen in ZnO is known already since the 1950s.[321,322] Yet, the role of hydrogen in ZnO was investigated in detail only in the last 10 years, initiated by a seminal theoretical paper of van de Walle[323].[22] Van de Walle showed in his density-functional theory study that hydrogen incorporated on interstitial lattice sites acts as a shallow donor. At the same time, experimental evidence for the doping action of hydrogen was found by Kang et al.[324], who prepared ZnO:H films with resistivities as low as $1 \cdot 10^{-3}$ Ωcm from a metallic Zn target by reactive magnetron sputtering in an Ar + H_2 atmosphere. Additionally, McKluskey and Jokela[325] proved the doping action of hydrogen in ZnO single crystals at comparatively low electron concentrations in the order of $5 \cdot 10^{17}$ cm^{-3}. Therefore, in this work, the co-doping of ZnO:Al and $Zn_{1-x}Mg_xO$:Al with hydrogen has been investigated in order to explore the possibilities to deploy the doping effect of the hydrogen on the Al-doped TCO films as a simpler route to further increase the carrier concentration of the layers in contrast to extensive parameter optimization.

The films were deposited by 13.56 MHz RF magnetron sputtering in an atmosphere of either pure Ar or Ar + H_2 with a total pressure of 0.3 Pa. The mass flow ratio $F_{H2}/(F_{H2} + F_{Ar})$ was varied from 0 % to 10 % and the films were deposited at room temperature or at T_{sub} = 300 °C, the temperature that yields the lowest resistivities for sputtering in pure argon. The chemical analysis was performed by Rutherford backscattering spectrometry (RBS) for O, Zn, Al, and Mg and by secondary ion mass spectrometry (SIMS) for hydrogen. The samples for the SIMS measurements were prepared in an Ar + D_2 (deuterium) instead of an Ar + H_2 atmosphere to avoid the high H_2 background from the vacuum system of the SIMS apparatus. This is reasonable, because the deuterium is likely to behave chemically in the same way as the hydrogen. The absolute deuterium concentration was calibrated with ZnO:Al and $Zn_{1-x}Mg_xO$:Al films, implanted by deuterium with a dose of $1 \cdot 10^{15}$ cm^{-2}.

7.2.1 Chemical Composition of the Films

Figure 7.13 on page 121 shows the concentrations of D(H), O, Zn, Al, and Mg in the ZnO:Al,H and $Zn_{1-x}Mg_xO$:Al,H films as a function of the hydrogen portion $F_{H2}/(F_{H2} + F_{Ar})$ in the sputtering gas.

The dependence of the concentration of the metallic elements on the hydrogen portion in the sputtering atmosphere is significantly different for both types of films. While the Zn content in the ZnO:Al films is decreasing only slightly, accompanied by a corresponding increase of the Al content, this effect is much stronger in the $Zn_{1-x}Mg_xO$:Al films. Furthermore, the influence of the hydrogen is more pronounced at 300 °C substrate temperature (solid lines). Apparently, the film composition is significantly (ZnO:Al) and strongly ($Zn_{1-x}Mg_xO$:Al) influenced by the hydrogen in the sputtering atmosphere. The absolute deuterium (hydrogen) concentration in the films prepared at room

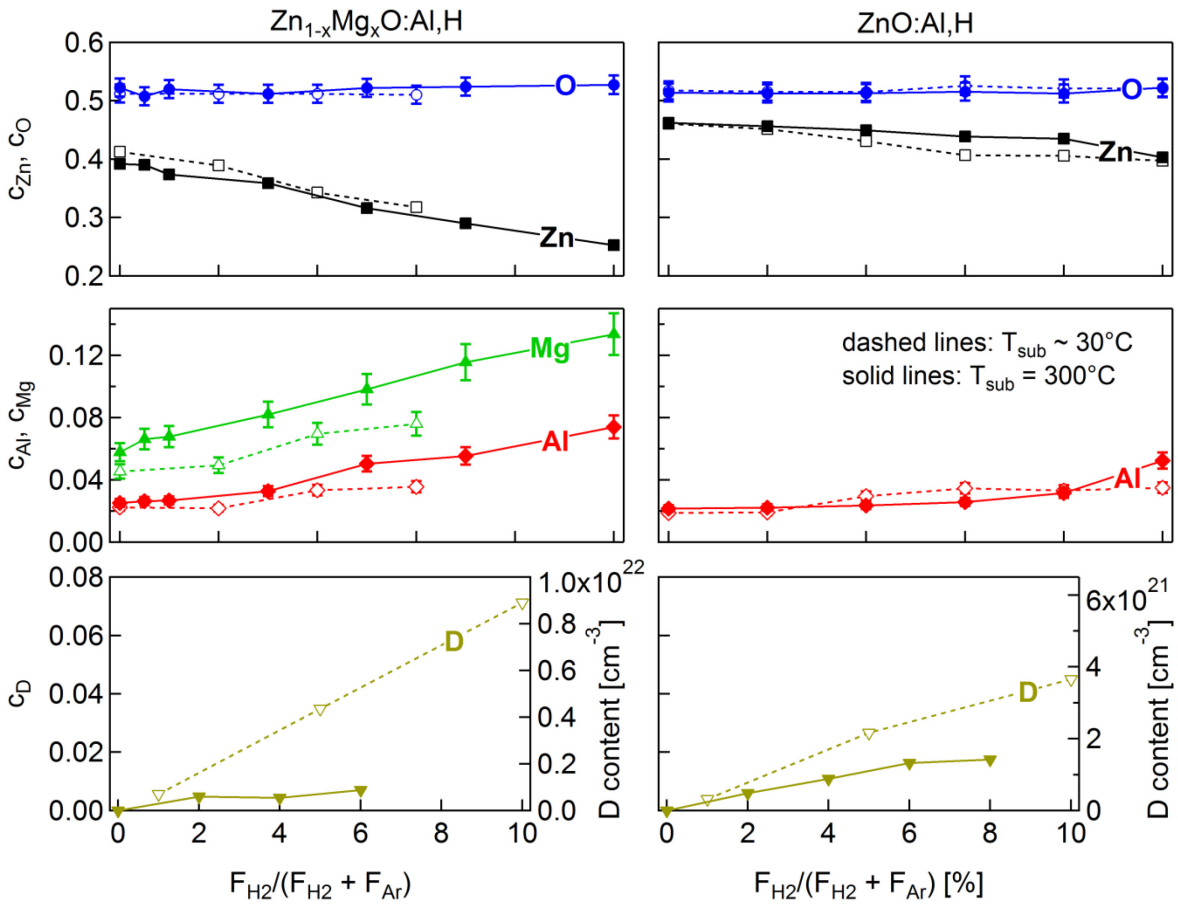

Figure 7.13: Chemical composition of $Zn_{1-x}Mg_xO$:Al,H and ZnO:Al,H films as a function of the hydrogen portion $F_{H2}/(F_{H2} + F_{Ar})$ in the sputtering gas for the deposition. The atomic concentration of O (blue, circles), Zn (black, squares), Al (red, diamonds), and Mg (green, triangle up) was determined by RBS, while the deuterium (hydrogen) content was measured by SIMS. The deuterium (hydrogen) content of the films c_D was estimated assuming a density of 4.7 g/cm³ of the films. Dashed lines and open symbols denote depositions at ~30 °C. Solid lines and filled symbols denote film growth at T_{sub} = 300 °C.

temperature was $(3.66 \pm 0.02)\cdot10^{21}$ cm^{-3} (< 4 at.%) for ZnO:Al and $(8.91 \pm 0.02)\cdot10^{21}$ cm^{-3} (< 8 at.%) for the $Zn_{1-x}Mg_xO$:Al films at a relative deuterium portion of 10 % in the sputtering gas.

The influence of the hydrogen on the composition of the films may be related to the formation of hydrides. Al and Mg are forming hydrides, AlH_3 and MgH_2, whereas no stable hydride of Zn exists. The stronger effect of the hydrogen on the composition of the $Zn_{1-x}Mg_xO$:Al films could then be explained by the preferred formation of the more stable MgH_2 (enthalpy of formation $\Delta_fH^0_{(298K)} = -74.5$ kJ/mol)[326] compared to AlH_3 ($\Delta_fH^0_{(298K)} = -11.4$ kJ/mol)[327]. However, the AlH_3 and MgH_2 were not detectable in the XRD, which could be due to a small domain size of these phases. To further investigate a possible formation of AlH_3 or MgH_2 in the films, X-ray absorption spectroscopy measurements were performed on the samples co-doped with hydrogen. Figure 7.14 on page 158 shows the results for the Mg-K and Al-K edge of the ZnO:Al,H and $Zn_{1-x}Mg_xO$:Al,H samples prepared with different portions of hydrogen in the sputtering atmosphere.

The general features of the Mg-K edge are very similar to those of the Al-K edge. There is a first peak at approximately 1305 eV, the highest peak at 1311 eV, and a very broad feature at 1320 eV (see Figure 7.14 (a) and (c)). For comparison, the first peak of the Al-K edge appears at 1562 eV, the highest peak at 1567 eV, and the broad feature at approximately 1578 eV (see Figure 7.14 (b) and (d)). The difference between the first and the second peak of the Al-K edge is 5 eV, while it is 6 eV for the Mg-K edge, and the difference from the highest peak to the broad feature is 11 eV in the case of the Al-K edge and 9 eV for the Mg-K edge. This similarity can be explained by the same 4-fold

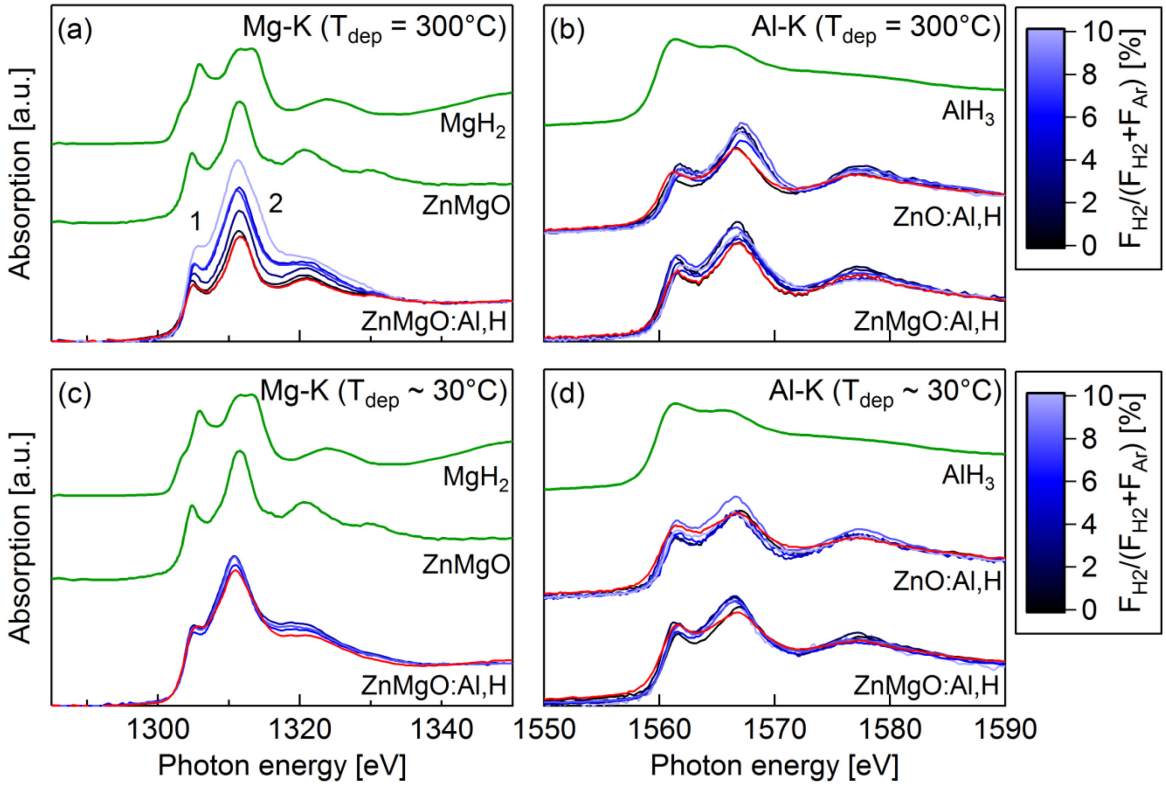

Figure 7.14: X-ray absorption spectra of the Mg-K edge (*left*) and the Al-K edge (*right*) for the ZnO:Al and $Zn_{1-x}Mg_xO$:Al films prepared either at 300 °C substrate temperature (*top*) or without intentional heating (*bottom*). Also shown are reference spectra of MgH_2 and AlH_3 powders and of an undoped $Zn_{0.88}Mg_{0.12}O$ film (solid green lines). The red lines represent a combination of the reference spectra and the spectra of the films deposited without hydrogen according to ratios determined from a worst case approximation.

coordination and the same electronic configuration, the Al^{3+} and the Mg^{2+} have when they occupy Zn lattice sites (according to Park and coworkers, the Mg is assumed to substitute Zn atoms on their lattice sites)[39]. The variations of the absorption of the Mg in the $Zn_{1-x}Mg_xO$:Al,H samples prepared at 300 °C (see Figure 7.14 (a)) is mostly due to uncertainties in the normalization of the data. A part of it could also be caused by the increasing amount of Mg built into the films for increasing hydrogen portion in the sputtering gas. The variations in the absorption of the films prepared at ~30 °C, on the other hand, are smaller, but this dataset only covers the range of 4 % to 8 % relative hydrogen flow during the deposition (see Figure 7.14 (c)). In comparison with the undoped $Zn_{1-x}Mg_xO$ film, these $Zn_{1-x}Mg_xO$:Al,H absorption spectra are smeared out. Since the data has been measured in the same system under similar conditions, the difference is likely to be caused by the Al dopant.

The formation of MgH_2 cannot clearly be inferred from the X-ray absorption data, because the MgH_2 powder shows in principle similar features: a first peak at 1306 eV, a second and highest peak, which actually consists of at least two separate peaks at 1311 eV and 1313 eV, and a broad feature at 1324 eV. At least for the films deposited at room temperature, it seems as if no significant amount of MgH_2 is formed, because the spectra do not differ from each other. For T_{sub} = 300 °C, peak shoulders become visible for depositions with high hydrogen flows (see Figure 7.14 (a) marks '1' and '2'), which might be related to the formation of MgH_2. However, the changes are too vague to be reliable evidence.

For the Al-K edges, shown in Figure 7.14 (b) and (d), no significant changes with increasing hydrogen portion $F_{H2}/(F_{Ar} + F_{H2})$ in the sputtering gas can be observed as well. The minor variations can mostly be attributed to the normalization, which is quite difficult for these datasets due to the bad signal quality, caused by the low amount of Al in the samples and the fact that the monochromator of the beamline transfers only low intensities for such high energies. Further, there is no substantial

difference of the Al-K edges between the $Zn_{1-x}Mg_xO$:Al,H and the ZnO:Al,H films deposited at the two different substrate temperatures.

The Al-K edge absorption of the AlH_3 reference powder also differs only slightly from the spectra observed for the films. Despite the fact that the peaks are very broad and the first peak has a higher intensity in comparison to the second peak, it resembles the three main peaks of the Al in ZnO: the first peak at 1561 eV, a second peak at 1566 eV, and a feature between 1570 eV and 1580 eV. Hence, the formation of AlH_3 can also not clearly be inferred from the X-ray absorption data.

If only the formation of AlH_3 would be responsible for the deactivation of the Al dopant at T_{sub} = 300 °C, an amount between 20 % (ZnO:Al,H) and 60 % ($Zn_{1-x}Mg_xO$:Al,H) (see Figure 7.15 on page 160 in the next section) of the hydrogen could be bound in AlH_3. This accounts to less than 5 % of the Al in the films, which could be in the form of AlH_3. When performing a worst case approximation and assuming that all the hydrogen in the films is either present in the form of AlH_3 or MgH_2, the following percentages for the Al and Mg bound in the hydride phases are obtained: For the ZnO:Al films, 40 % (T_{sub} ~ 30 °C) or 20 % (300 °C) of the Al may be bound in AlH_3, and in the $Zn_{1-x}Mg_xO$:Al films, 27 % (~ 30 °C) or 10 % (300 °C) of the Mg could have formed MgH_2, while 40 % (~30 °C) and 6 % (300 °C) of the Al may be present in the form of AlH3. This has been simulated by combining the reference spectra with the spectra for depositions without hydrogen according to the ratios mentioned before (see red lines in Figure 7.14). Although some of these percentages are very high, the changes in the spectra are marginal. This is also quantitative evidence that the reference spectra do not differ enough from the initial film spectra to yield reliable experimental evidence for the formation of hydrides from the X-ray absorption spectroscopy measurements. Therefore, further investigations with other methods are necessary.

An alternative explanation for the influence of the hydrogen on the chemical composition of the films is the increasingly reducing sputtering atmosphere for higher hydrogen portions. Comparing again the metals present during the deposition, Zn has the highest vapour pressure[269] and the lowest affinity to oxygen (see Table 6.1). As mentioned earlier, this means that Zn has the highest tendency to re-evaporate from the substrate. A lower tendency to re-evaporate from the substrate is present for the Mg and the lowest tendency for the Al. An increasing amount of hydrogen present during the sputtering reduces the amount of oxygen in the sputtering atmosphere available to form ZnO. But only if ZnO is formed, Zn is likely to remain on the substrate/film surface. This leads to a preference of Mg and Al in comparison to the Zn in the films. Therefore, the Al and Mg content are increasing while the Zn content is decreasing with increasing hydrogen flow. This effect is stronger for higher temperatures, because the vapour pressure for the Zn is higher in relation to that of the Al and Mg, and hence the tendency of the Zn to re-evaporate is even higher at elevated temperatures. For the ZnO:Al films, where no Mg is present, the effect is less pronounced, because these films contain only one competing element, Al, in a relatively low amount.

7.2.2 Electronic Properties of the Films

Relating the hydrogen content to the free carrier concentration and correcting the results for the carriers created by the Al as determined from the samples deposited without hydrogen, the electrical activation of the hydrogen can be calculated. To estimate the hydrogen content in the films for which the Hall effect was measured (prepared with a different hydrogen (deuterium) flow compared to the films measured with the SIMS probe), a simple linear interpolation between the measured concentrations was applied. The results are shown in Figure 7.15 on page 160.

An electrical activation of the hydrogen is only achieved for the deposition without intentional heating. In this case, the highest electrical activation of the hydrogen is roughly (14 ± 3) % for the

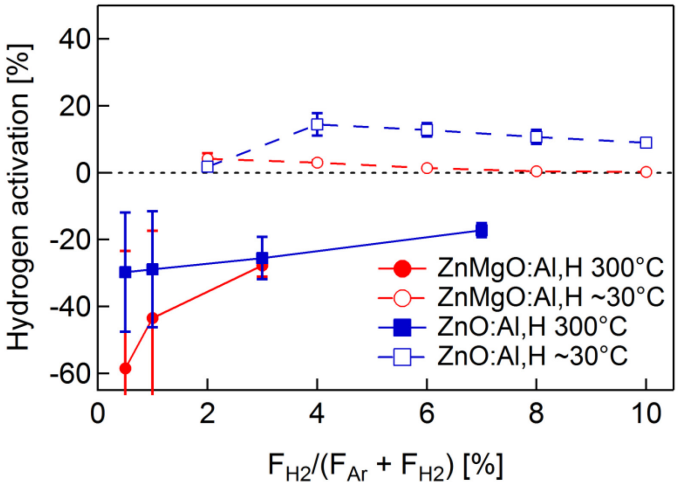

Figure 7.15: Activation of the hydrogen dopant as a function of the hydrogen portion in the sputtering gas determined for the ZnO:Al (blue lines, squares) and $Zn_{1-x}Mg_xO$:Al (red lines, circles) films deposited either at ~30 °C (dashed lines) or 300 °C (full lines). A negative activation refers to a reduction of the free carrier concentration due to the hydrogen.

ZnO:Al and (4 ± 2) % for the $Zn_{1-x}Mg_xO$:Al films. This means, only a small amount of the hydrogen in the samples is electrically active and acts as a donor. For the samples prepared at T_{sub} = 300 °C, the situation is completely different. There, the incorporation of hydrogen into the films leads to a strong reduction of the free carrier concentration and therefore to a deactivation of the Al dopant.

To examine the influence of the hydrogen on the electrical properties more closely, not only the free carrier concentration n but also the resistivity ρ and the Hall mobility μ of the samples prepared with different hydrogen portions $F_{H2}/(F_{Ar} + F_{H2})$ in the sputtering atmosphere deposited at either ~30 °C or 300 °C have been measured (see Figure 7.16).

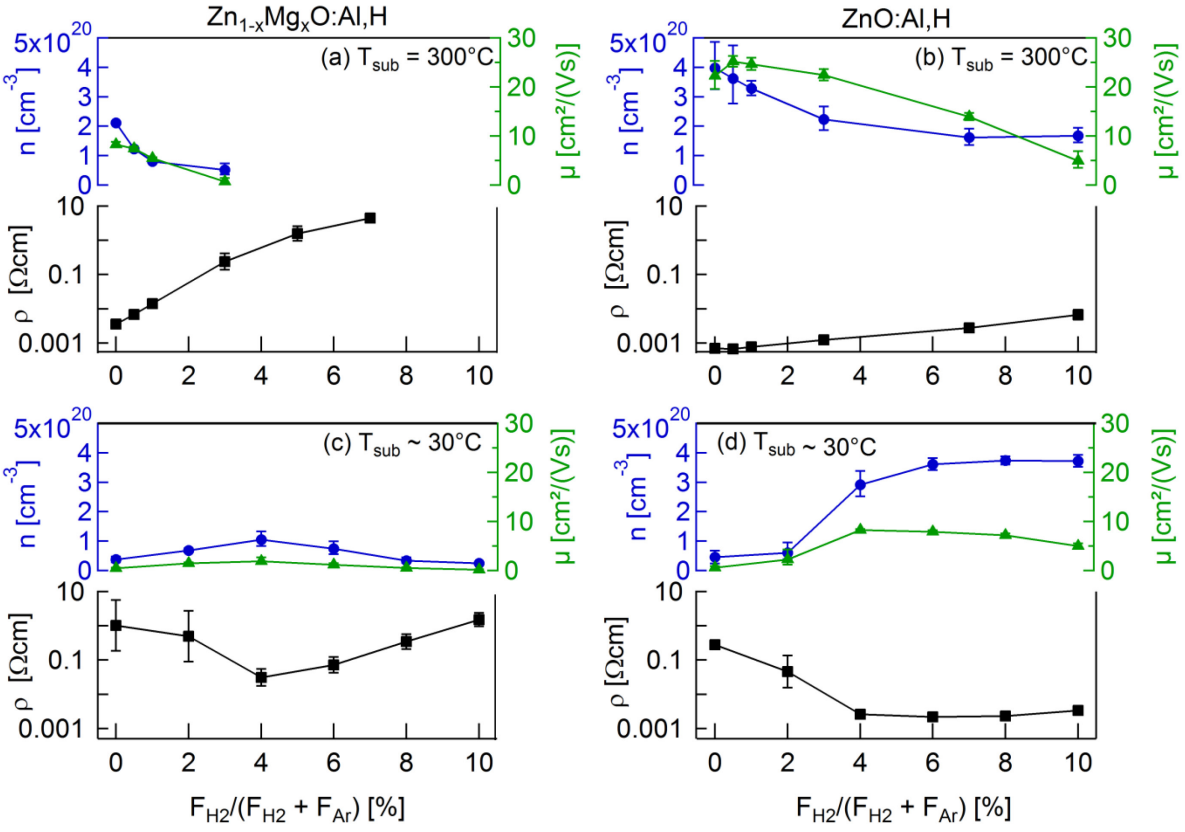

Figure 7.16: Resistivity ρ (squares), Hall mobility μ (triangles), and free carrier concentration n (circles) determined by Hall measurements for the samples deposited with a relative hydrogen portion $F_{H2}/(F_{Ar} + F_{H2})$ of up to 10 % in the sputtering gas. The $Zn_{1-x}Mg_xO$:Al,H (*left*) and ZnO:Al,H (*right*) films have been prepared either at ~30 °C (*bottom*) or 300 °C (*top*).

For the room temperature deposition, the resistivity decreases by two orders of magnitude for both types of films with increasing hydrogen portion. As already pointed out, in this case, the hydrogen introduces additional free carriers. Interestingly, there is a minimum in the resistivity for the $Zn_{1-x}Mg_xO$:Al films deposited at room temperature with 4 % relative hydrogen flow, while the resistivity above $F_{H2}/(F_{Ar} + F_{H2}) = 4$ % remains constant in the ZnO:Al films. For $T_{sub} = 300$ °C, on the other hand, the resistivity increases, contrary to the expected doping effect of the hydrogen. While the resistivity increase is about 1 order of magnitude for the ZnO:Al films, it is more than 3 orders of magnitude for the $Zn_{1-x}Mg_xO$:Al films. The ρ decrease (increase) is caused by a parallel increase (decrease) of the free carrier concentration n and the Hall mobility μ. Similar to the films prepared without hydrogen, the higher resistivities of the $Zn_{1-x}Mg_xO$:Al films are caused by lower free carrier concentrations as well as lower Hall mobilities compared to the ZnO:Al films.

These results show that the doping action of the hydrogen, which has been confirmed by experiment and DFT calculations,[323,328] depends on the deposition temperature. In literature, however, the reports are mostly limited to the case of successful doping. Ruske et al.[328], for instance, mentioned a reduction of the resistivity of about 35 % (from $7 \cdot 10^{-4}$ Ωcm to $4.5 \cdot 10^{-4}$ Ωcm) for their ZnO:Al and ZnO:Al,Y films prepared in an Ar + H_2 atmosphere at 200 °C due to an increase of the free carrier concentration and a slight decrease of the mobility. Incidentally, they detected a constant Al concentration and a hydrogen concentration up to 2 at.% in their films. Kim et al.[329] also reported a decrease of the resistivity in their H-Ga-doped ZnO films prepared at 80 °C and 160 °C deposition temperature, caused by an increase of the electron concentration accompanied by a slight decrease of the carrier mobility. The decrease of the resistivity can be explained by the donor-like character of the hydrogen when it is bound to oxygen or oxygen vacancies or when it is in interstitial lattice positions.[323,330-332] H_2 molecules, on the other hand, do not create energy levels in the band gap of ZnO.[330] On the contrary, first principles calculations of Kim et al.[330], one of the few works considering not only the doping action of hydrogen but also the compensating effect, show that the hydrogen molecules create states in the valence band of ZnO (see Figure 7.17).

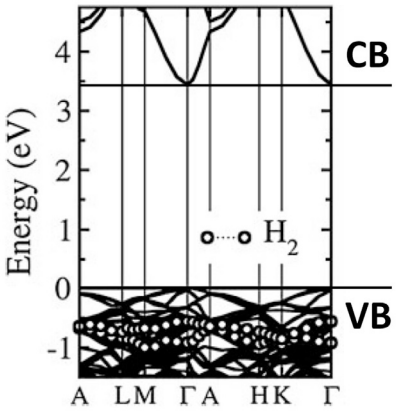

Figure 7.17: Band dispersion of ZnO with an H_2 molecule after Reference 330. The bands marked with a circle correspond to H_2.

They are therefore able to reduce the free carrier concentration in the ZnO films. Taking that into account, it is reasonable to assume for the ZnO:Al,H and $Zn_{1-x}Mg_xO$:Al,H films that the hydrogen is incorporated on interstitial (H_i) or in oxygen bond-center (H_O) lattice positions acting as a shallow donor when the films were deposited at ~30 °C. At 300 °C deposition temperature, on the other hand, H_2 molecules are formed, which do not donate free electrons but instead create states in the valence band and reduce the free carrier concentration. The formation of H_2 at $T_{sub} > 200$ °C is consistent with the results of Lavrov et al.[331] who reported the vanishing of the Raman line of H(D) in ZnO at 230 °C (180 °C) caused by the diffusion of H(D) and the formation of $H_2(D_2)$ molecules. This effect is even more likely for highly doped ZnO films, where the Fermi energy is already in the conduction band.[323,331]

The basic trend of the Hall mobility as a function of the free carrier concentration in the ZnO:Al,H and $Zn_{1-x}Mg_xO$:Al,H films can be explained by the combined transport model, which takes into account ionized impurity and grain boundary scattering. This is illustrated in Figure 7.18, which shows the Hall mobility μ as a function of the free carrier concentration *n* for these films.

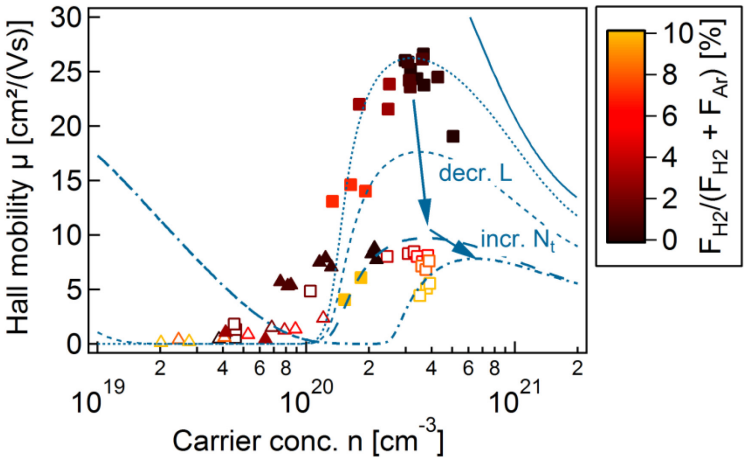

Figure 7.18: Hall mobility μ as a function of the free carrier concentration *n* for the ZnO:Al,H (squares) and the $Zn_{1-x}Mg_xO$:Al,H (triangles) films prepared at ~30 °C (open symbols), or 300 °C (filled symbols). The full line is the fit curve to the data of the single crystalline ZnO. The dashed and dotted lines are combined fit curves taking into account ionized impurity scattering and grain boundary scattering (N_c according to the theory) for different grain sizes *L* and trap densities at the grain boundary N_t (dotted line: N_t = $3.5 \cdot 10^{13}$ cm^{-2}, *L* = 15 nm; line with small dashes: $N_t = 3.5 \cdot 10^{13}$ cm^{-2}, *L* = 7 nm; line with large dashes: $N_t = 3.5 \cdot 10^{13}$ cm^{-2}, *L* = 3 nm; dash-dotted line: $N_t = 6 \cdot 10^{13}$ cm^{-2}, *L* = 3 nm).

A grain boundary trap density of $N_t \approx 3.5 \cdot 10^{13}$ cm^{-2} (dotted line) explains the main trend of the Hall mobilities for both materials, but especially for the ZnO:Al,H films prepared at ~30 °C (open squares), the deviations from the theoretical curve with increasing amount of hydrogen become obvious. This trend has also been observed by Kim et al.[330] for their films deposited without intentional heating. However, they did not interpret this behaviour. With respect to the theoretical curve, the Hall mobility for these films is increasing slower than expected, until it finally decreases for very high carrier concentrations without a significant change of the free carrier concentration. This trend can be explained by an increase of the trap density at the grain boundaries N_t and a decrease of the lateral grain size *L*. Taking into account the strong degradation of the structural quality (which will be discussed in the following), leading to decreased grain sizes on the one hand, and the increasing amount of the dopant Al, leading to a higher concentration of trap states on the other hand, both is reasonable. The trend of an increasing trap density and a reduced grain size is denoted in Figure 7.18 (dotted line: $N_t = 3.5 \cdot 10^{13}$ cm^{-2}, *L* = 15 nm; dashed lines: $N_t = 3.5 \cdot 10^{13}$ cm^{-2}, *L* = 7 nm, *L* = 3 nm; dash-dotted line: $N_t = 6 \cdot 10^{13}$ cm^{-2}, *L* = 3 nm).

The stability of the hydrogen doping was tested by remeasuring the electrical properties of the samples after approximately 240 days as it was done by McCluskey and Jokela[325] for lower-doped ZnO. For the samples prepared at 300 °C, no significant change in the electrical properties have been observed (the changes in the carrier concentration *n* and the Hall mobility μ were mostly smaller than the measuring error of about 5 %). This is consistent with the formation of H_2 molecules in these films, which is the energetically favourable configuration and thus not expected to change.[331] When the samples were prepared at room temperature with less than 4 % relative hydrogen flow, they exhibited a slight decrease of the resistivity accompanied by an increase of the free carrier concentration as well as the Hall mobility. For the films prepared with more than 4 % relative hydrogen flow, the opposite was observed. The increase of the resistivity for the samples prepared with more than 4 % relative hydrogen flow can be explained by the fact, that the H donor is not completely stable over time periods of several weeks.[325] Nevertheless, the electrical properties of those samples were still much better than for the samples prepared without hydrogen. Apparently, the main part of the H donors must have still been existent. The decrease of the resistivity of the samples prepared with less than 4 %

relative hydrogen flow might be caused by a low amount of hydrogen in the samples that remains in the atomic form and diffuses to form electrically active bond configurations, eventually.

7.2.3 Structural Properties of the Films

Another remarkable effect of the hydrogen co-doping is the drastic reduction of the crystalline quality of the deposited films. Figure 7.19 provides an overview of the crystalline quality of the ZnO:Al,H and $Zn_{1-x}Mg_xO$:Al,H films deposited with different hydrogen portions in the sputtering gas.

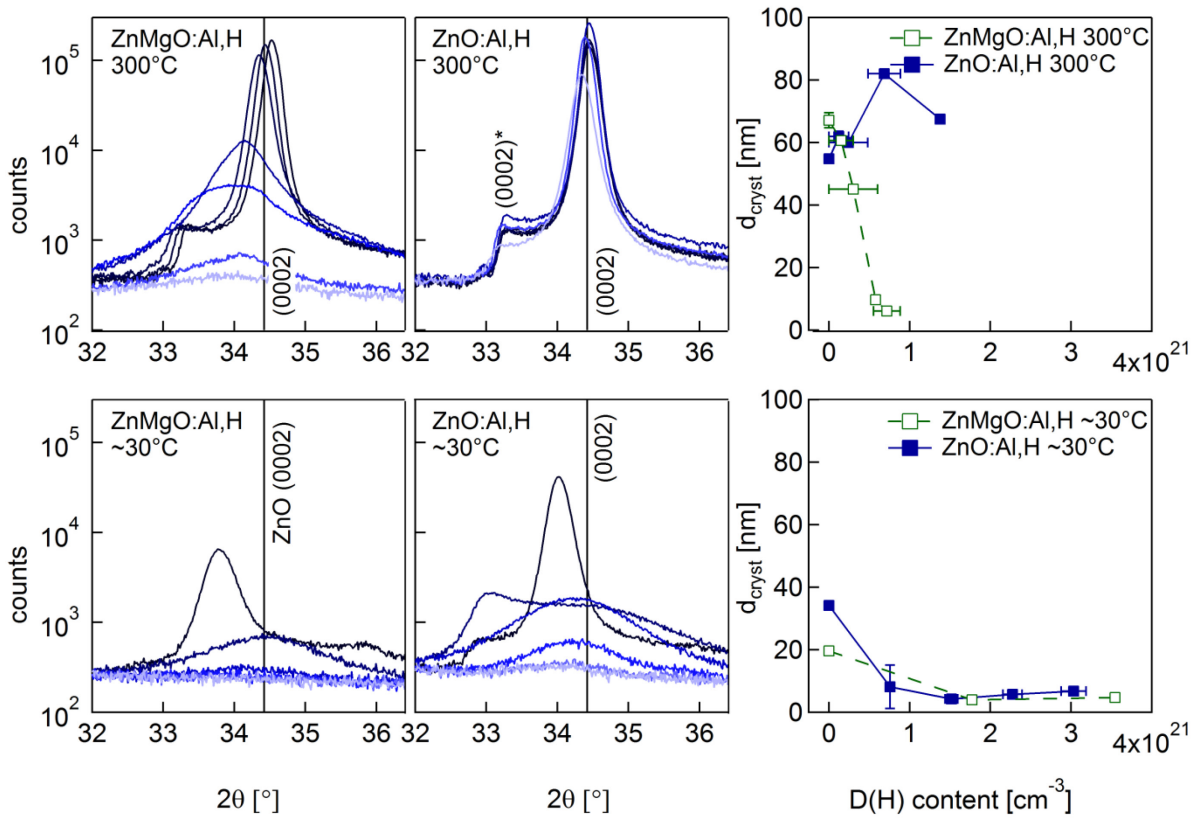

Figure 7.19: X-ray diffraction patterns of $Zn_{1-x}Mg_xO$:Al,H (*left*) and ZnO:Al,H (*middle*) films deposited at 300°C (*top*) or ~30 °C (*bottom*) for different hydrogen portions $F_{H2}/(F_{Ar} + F_{H2})$ in the sputtering gas (color changing from dark to bright with increasing hydrogen flow). Indicated by vertical solid lines are the powder reference values for the ZnO (0002) peak (JCPDS 36-1451). Because of the degradation of the X-ray source also peaks from the W-L_α lines are visible [(0002)*]. The graphs on the right side show the grain size as a function of the deuterium (hydrogen) content in the films.

The films show again the (0001) preferred orientation. For most of them, the 2θ position of the (0002) peak is strongly shifted with respect to the ZnO powder value (JCPDS 36-1451: c_{ref} = 0.52066 nm) showing a maximum measured relative deviation of up to (1.76 ± 0.09) % for the $Zn_{1-x}Mg_xO$:Al,H and (3.26 ± 0.09) % for the ZnO:Al,H films. For the deposition at room temperature, the peaks become very broad and change their position back to the powder values with increasing hydrogen portion. Plausibly, the high bond length flexibility of the amorphous film structure leads to a relaxation of the film stress. An increase of the c-axis lattice parameter has also been observed by Kim et al.[330] for their RF sputtered ZnO:H films. The strong increase of the full width at half maximum and the decrease of the diffraction peak intensity can be interpreted first as a decrease in crystallite size and then as a more or less X-ray amorphous film growth with increasing H_2 portions in the sputtering gas. The crystallite sizes are in the range of 60 nm to 80 nm only for the films prepared at 300 °C with low H_2 contents. For the ZnO:Al,H films the crystallite size does then not decrease significantly, while the crystallite

size of the $Zn_{1-x}Mg_xO$:Al,H films quickly decreases to values below 4 nm with increasing H_2 content, which again points to a strong influence of the Mg. At room temperature deposition, the films become nearly X-ray amorphous above H contents of approximately $1.5 \cdot 10^{21}$ cm^{-3} ($\lesssim$ 2 at.%) in the layers. According to Lee and coworkers[333] this may be caused by the inhibition of the crystalline growth due to the passivation of the growing film surface.

Since the amorphization is very interesting for applications of the films for example as active channel layers in transparent thin-film transistors with a high carrier mobility, where currently amorphous TCOs from the In-Ga-Zn-O system developed by the Hosono group[238] are under investigation, the effect of the amorphization of the layers prepared at room temperature was explored more detailed. To this end, transmission electron microscopy and atomic force microscopy measurements have been carried out on selected samples. The results of the atomic force microscopy measurements, kindly performed by Man Nie, are shown in Figure 7.20.

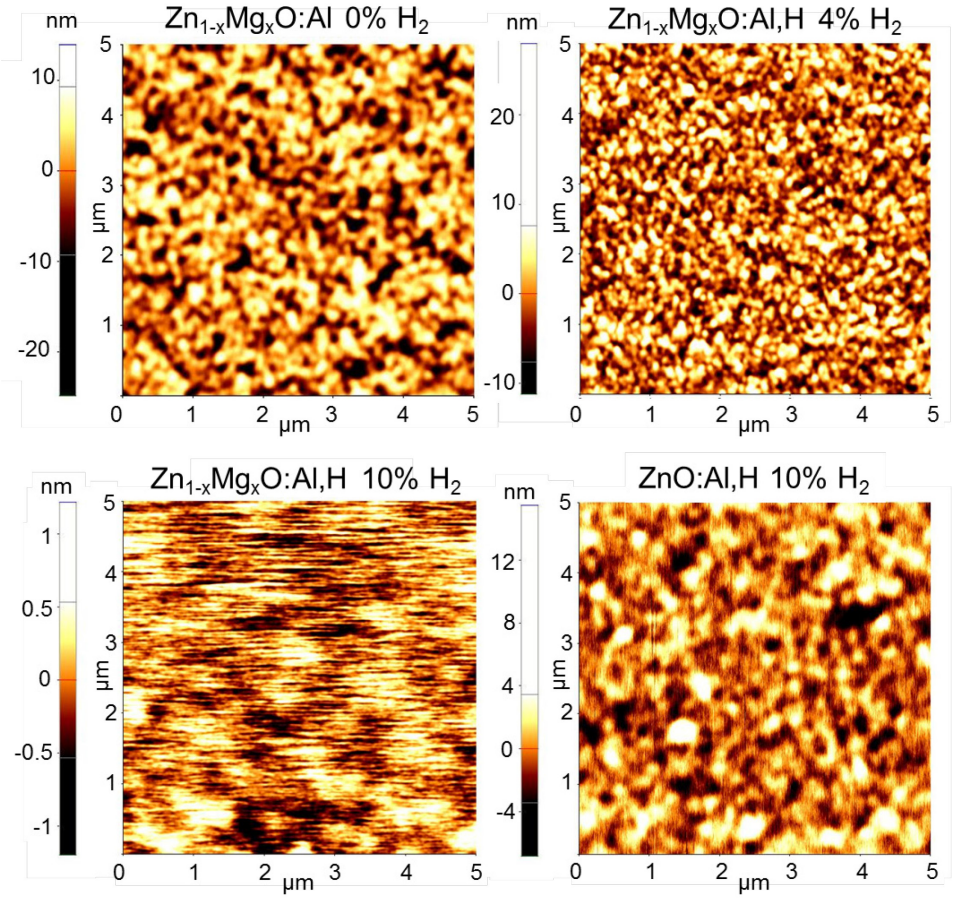

Figure 7.20: Atomic force microscopy images of the surface of selected $Zn_{1-x}Mg_xO$:Al,H and ZnO:Al,H films prepared with different hydrogen portions $F_{H2}/(F_{Ar} + F_{H2})$ in the sputtering gas at ~30 °C. The measurements have kindly been performed by Man Nie.

For increasing hydrogen portion during the deposition of the $Zn_{1-x}Mg_xO$:Al,H films, first the grains become smaller (4 % H_2) and then the surface roughness vanishes almost completely (10 % H_2). In particular, the root mean square surface roughness decreases from 4.7 nm for the film deposited without hydrogen via 3.9 nm (4 % H_2) to 0.3 nm for the film deposited with 10 % H_2 flow. This is a strong indication that the films have a much finer crystalline structure in comparison to the films prepared without hydrogen, because an amorphization of the films is usually related to a very smooth surface.[334] As a comparison, also the surface of the ZnO:Al,H film prepared with 10 % relative hydrogen flow during the deposition is shown. The root mean square roughness is 1.8 nm for this film and is therefore slightly higher in comparison to the $Zn_{1-x}Mg_xO$:Al,H film prepared with

$F_{H2}/(F_{H2} + F_{Ar})$ = 10 %. This is consistent with the XRD measurements, where still a very broad (0002) peak is detectable for the ZnO:Al,H film.

To examine the crystalline structure throughout the bulk of the film, cross-sectional transmission electron microscopy measurements have been performed. Figure 7.21 shows the TEM images for selected samples.

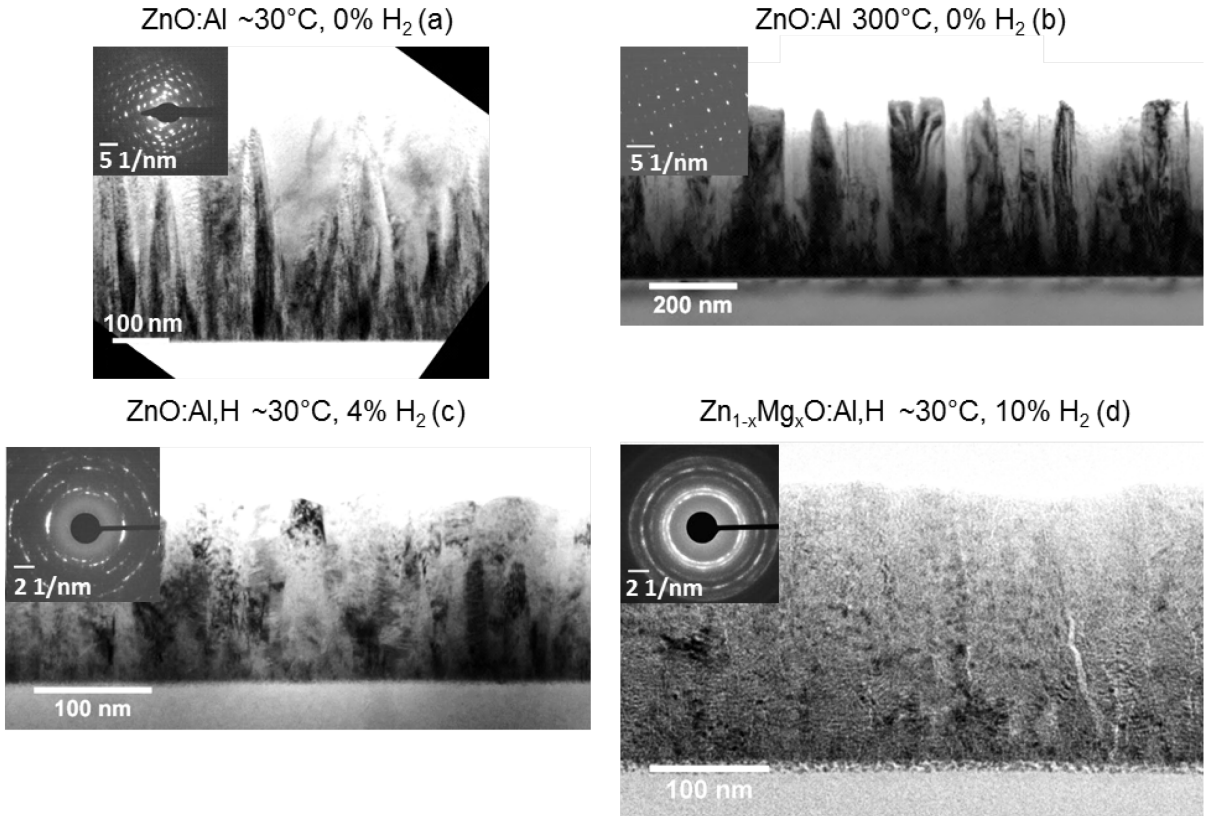

Figure 7.21: Cross-sectional transmission electron micrographs of selected ZnO:Al,H and $Zn_{1-x}Mg_xO$:Al,H films prepared with or without hydrogen in the sputtering atmosphere. The upper row shows a comparison of ZnO:Al films prepared without hydrogen either at ~30 °C or at 300 °C. The lower row shows the cross sections of ZnO:Al and $Zn_{1-x}Mg_xO$:Al films prepared at ~30 °C with different flows of hydrogen. (c) Cross section of the room temperature deposited film with the best electronic properties. (d) Cross section of the film with the strongest amorphization. The insets show the electron diffraction patterns taken from the regions shown in the main images.

In Figure 7.21 (a) and (b), the crystalline structure of the ZnO:Al films prepared without hydrogen at ~30 °C and at 300 °C is compared. Both films show the typical columnar growth. The columns extend mostly from the interface between the film and the substrate to the film surface. The lateral extension of the columns is in the range of 40 to 115 nm for the film prepared at ~30 °C and, as already mentioned in Chapter 4, 50 to 150 nm for the film prepared at 300 °C. For the ZnO:Al,H film grown at ~30 °C, on the other hand, the columnar growth is barely visible (see Figure 7.21 (c)). Although this film deposited with 4 % relative hydrogen flow exhibits the lowest resistivity, the bright and dark areas in the image are much smaller, which also points to a lower structural quality. This explains the low crystallite size of only 4 nm, which has been determined from the XRD pattern. For the $Zn_{1-x}Mg_xO$:Al,H film deposited at ~30 °C with $F_{H2}/(F_{Ar} + F_{H2})$ = 10 % – the film with the strongest amorphization as derived from the XRD analysis – the columnar growth and the preferred orientation of the crystallites indeed vanished (see Figure 7.21 (d)). The transmission electron microscopy investigation showed crystallite sizes in the range of 2 nm to 11 nm, which means the film is nanocrystalline. The amorphous TCOs mentioned earlier, however, are not only X-ray amorphous but also show no distinct peaks and features in transmission electron microscopy.[335] It might be possible to

produce amorphous $Zn_{1-x}Mg_xO$:Al films when using higher hydrogen portions in the sputtering atmosphere or a higher Mg content.

Obviously, the hydrogen has a strong effect on the structural properties of the ZnO:Al and $Zn_{1-x}Mg_xO$:Al films. This effect is more pronounced in the $Zn_{1-x}Mg_xO$:Al,H films, which cannot be explained in detail up to now. It could be related to the formation of MgH_2. This, however, is not ascertained yet. Despite the decrease of the crystalline quality, the electrical properties of the films deposited at ~30 °C are remarkably good. Similar electrical properties compared to the films deposited with 4 % hydrogen flow at ~30 °C are only reached without hydrogen at approximately 200 °C deposition temperature. Although the free carrier concentration n and the Hall mobility μ are similar in this case, the crystalline quality of the films prepared without hydrogen is significantly higher. Furthermore, the lowest resistivity of the films prepared with hydrogen is only one order of magnitude higher in comparison to the optimized deposition conditions without hydrogen, for which $T_{sub} = 300$ °C is used. The hydrogen therefore does not only create free carriers but also seems to reduce the influence of the grain barriers, possibly due to the passivation of the trap states at the grain boundary. This opens up the possibility to prepare reasonably well conductive films at low deposition temperatures, for instance on temperature sensitive substrates like plastic foils.

7.3 Comparison to Other Dopants

In the preceding sections it was shown that ZnO can successfully be doped with various elements. Table 7.4 on page 167 summarizes the most important structural, electronic, and optical properties of the films doped with the different elements from this investigation (prepared using 13.56 MHz plasma excitation frequency) and of films prepared by other groups.

In general, the effect of the dopant on the structural and electronic properties of the ZnO films is very similar for Al, Ga, and In. All the dopants decrease the crystalline quality when being introduced to the lattice, which can be seen from the crystallite size and the Urbach energies of the doped films in comparison to the undoped layer (see Table 7.4). This effect has also been observed by Clatot et al.[316] in their pulsed laser deposited ZnO:Si films and is to be expected, since the introduction of a dopant leads to disorder in the films. In their films, they observed crystallite sizes in the range of 5 to 20 nm,[23] which is comparable to the crystallite sizes determined for the films investigated here. An influence of the dopant on the structural properties has also been observed by Gao and coworkers[336] for RF magnetron sputtered B-doped ZnO films. Their films exhibited a change in the crystallographic orientation due to the incorporation of B in the room temperature deposited films. This is comparable to the loss of the preferred orientation for the ZnO:In films deposited at high temperatures.

All dopants increase the free carrier concentration and the conductivity by orders of magnitude. The highest free carrier concentrations are usually achieved for the ZnO:Al and ZnO:Ga films ($n_{Al} \leq 1.5 \cdot 10^{21}$ cm^{-3}, $n_{Ga} \leq 1.1 \cdot 10^{21}$ cm^{-3}) with a slightly higher dopant activation in the Ga-doped films in comparison to the ZnO:Al films. These films also exhibit the lowest resistivities in the range of $2 \cdot 10^{-4}$ Ωcm. Very high carrier concentrations and low resistivities of $1.2 \cdot 10^{21}$ cm^{-3} and $3.8 \cdot 10^{-4}$ Ωcm, respectively, have also been reported by the group of Minami[20] for their RF magnetron sputtered Si-doped ZnO films. Clatot et al.[316] achieved at least $\rho = 7.7 \cdot 10^{-4}$ Ωcm ($n = 6.8 \cdot 10^{20}$ cm^{-3}, $\mu = 12$ cm²/(Vs)) for their pulsed laser deposited Si-doped ZnO films. Both results are, however, worse in comparison to the best values in the range of $2 \cdot 10^{-4}$ Ωcm. For their RF sputtered B-doped ZnO films, Minami and coworkers[20] obtained a resistivity of $6.4 \cdot 10^{-4}$ Ωcm, but a higher amount of approximately 5 at.% of the dopant material was needed to achieve this value in comparison to the other dopants, for which the optimal resistivity is reached with 1...2 at.%. These B-doped films had

Table 7.4: Summary of the most important parameters of the ZnO films with the lowest resistivities, prepared with different dopants for the investigation here and by several other authors and techniques. The electrical parameters are determined from Hall measurements. As a comparison, the values for undoped ZnO films are given as well. c_{imp} is the impurity concentration in the films. If the information is only given for the target composition, it is denoted by (tar.). act_{imp} is the dopant activation. The deposition temperature is given in brackets after the dopant activation (RT: deposition without intentional heating). RF-MS: radio-frequency magnetron sputtering, DC-MS: DC magnetron sputtering, PLD: pulsed laser deposition, IP: ion-plating, SG: sol-gel processes.

Dopant	c_{imp} [at.%]	act_{imp} [%] (T_{dep})	ρ [10^{-4} Ωcm]	n [10^{20} cm^{-3}]	μ [cm²/(Vs)]	d_{cryst} [nm]	T_{avg} [%]	$E_{g,\,opt}$ [eV]	E_U [meV]	Method	Reference
None	0	n.a.	~5·10^6	n.a.	n.a.	62	80	3.19	86 ± 3	RF-MS	this work
	0	(RT)	32	0.51	38		>85				20
	0	(100 °C)					>80	3.3		PLD	316
Al	2.1	26 ± 5 (300 °C)	7.1	4.0	22	30	84	3.6	154	RF-MS	this work
	1.6 (tar.)	(RT)	1.9	15	22		>85			RF-MS	20
	1.5 (tar.)	(100 °C)	5.8	6.3	17		>80	4.0		PLD	316
	1 (tar.)	(275 °C)				13.4		3.41	120	RF-MS	184
	2.6	31 (RT)	6.25	3.4	22		>85			RF-MS	261
	1.6 (tar.)	(100 °C)	3.5	7.4	24		>80	3.69		RF-MS	259
Ga		34 ± 6 (300 °C)	8.2	4.0	19	37	87	3.69	190	RF-MS	this work
	0.9 (tar.)	(RT)	8.1	4.4	28		>85				20
	2 (tar.)	58 (250 °C)	3.5	9.6	20.6	41	<90			RF-MS	300
	1.5 (tar.)	(100 °C)	4.9	8.0	16		>80	3.8		PLD	316
	5.68	(RT)	39.0	3.6	12.3	25	>80	3.46		RF-MS	301
	5	(RT)	141.0	4.1	4.0	23	>80	3.28		DC-MS	301
	4	33 (RT)	5.6	5.5	20		>85			RF-MS	261
	1.7 (tar.)	(120 °C)	2.5	11	23		>80	4.0		IP	317
	1.7 (tar.)	(200 °C)	1.8	11	31	44				IP	299
In	1.5	15 ± 3 (200 °C)	68	1.61	5.7	28	79	3.38	190	RF-MS	this work
	0.6 (tar.)	(RT)	8.1	4.0	20		>85				20
	4.2	33 (RT)	9.1	5.7	12		>85			RF-MS	261
	3 (tar.)	(RT)	55	3.1	3.8		70...80	3.42		DC-MS	305
	6.2	(RT)	13.9	5.4	10		>80	2.97		RF-MS	306
	3	(450 °C)	6000			36	>88	3.0	95	SP	318
B	4.3 (tar.)	(RT)	6.4	2.5	39		>85				20
	4.3 (tar.)	(RT)	93				>80				336
	1		25.4	0.9	25	~20				SP	337
Si	1.3 (tar.)	(<250 °C)	3.8	12	12		>85			RF-MS	338
	1.5 (tar.)	(450 °C)	7.7	6.8	12		>80	3.6		PLD	316
H,Al	2 (H_2),3 (Al)	14 ± 3 (RT, 4% H_2)	22	2.9	8.3	4.3				RF-MS	this work
	0.8 (Al,tar.)	(150 °C, 6% H_2)	4.14	5.4	28.1	23	86			RF-MS	333
	2 (H_2), 2 (Al)	(200 °C, 20% H_2)	4.5	6.9	20.6		>80			DC-MS	328
H,Ga	2.5 (Ga,tar.)	(160 °C, 10% H_2)	4.0	8.2	19		>85	4		DC-MS	329

only a carrier concentration of 2.5·10^{20} cm^{-3}. Pawar et al.[337] deposited ZnO:B films with a free carrier concentration and lowest resistivity of 9·10^{19} cm^{-3} and 2.54·10^{-3} Ωcm, respectively, by spray pyrolysis. This is a first indication that B is a rather unfavourable dopant for ZnO.

The dopant activation for the different dopants within one systematic investigation can be inferred from the data of Wang et al.[261] for their room temperature RF magnetron sputtered ZnO:M (M = Al,

Ga, In, Ge) films, because they actually measured the dopant content in the films, which is rarely done in literature dealing with different dopant materials. Unfortunately, they did not measure the density of the films, which is necessary to determine the dopant activation. For that reason, the density of the films is assumed to be similar to the films investigated here ((4.7 ± 0.2) g/cm^3). Assuming furthermore that the O concentration is always 50 % and that the dopant is incorporated to the expense of Zn, and assuming an error of 1 at.% for the O and Zn content and an error of 0.1 at.% for the dopant concentration as well as an error of $0.1 \cdot 10^{20}$ cm^{-3} for the free carrier concentration, the following dopant activations are determined: Al = (18 ± 3) %, Ga = (20 ± 3) %, In = (21 ± 3) %, Ge = (20 ± 3) %. In this case, the dopant activations are all quite low and comparable to each other in the range of 20 %. A higher dopant activation for the Ga-doped films can therefore not be assessed. Using ($c_{dopant,film} \approx 1.3 \cdot c_{dopant,target}$) for the conversion of the dopant content in the target to the dopant content in the film, the results for the room temperature RF sputtered ZnO films of Minami[20] can also be interpreted with respect to the dopant activation. Assuming the same composition and density, the following values are determined: Al = (104 ± 18) %, B = (5.9 ± 1.0) %, Ga = (56 ± 10) %, In = (76 ± 13) %. These dopant activations are significantly higher in comparison to the values determined from the data of Wang and coworkers, which is most likely due to their arrangement of the substrates. The substrates were placed perpendicular to the target, which reduces the bombardment of the growing films with high-energetic negative oxygen ions and decreases the amount of compensating defects, leading to a higher dopant activation. Interestingly, the activation of the Al is highest and reaches 100 %. This may be caused by an erroneous assumption about the density of the film for the calculation of the activation. If the density is higher, for example assumed to be the bulk value of ZnO, 5.68 g/cm^3,[339] an activation of the Al of (86 ± 14) % is calculated. This is still extraordinarily high. Then again, the corresponding carrier concentration of $1.5 \cdot 10^{21}$ cm^{-3} is one of the highest reported for ZnO. Boron, on the other hand, is clearly a dopant with a low efficiency as it can be inferred from the high B content needed to achieve reasonable free carrier concentrations. This is, according to the model for the origin of the trap states at the grain boundaries, not beneficial for the electronic transport. Therefore, B is not a favourable material to dope ZnO with, whereas Al, Ga, and In can be optimized to quite high activation rates. Nevertheless, the absolute activation of the dopants is still low, mostly below 50 % for magnetron sputtered films with only a few exceptions.

The highest carrier concentrations are mostly reached for PLD deposited films or for magnetron sputtered films taking special efforts, for example using a perpendicular arrangement of the substrates.[230,231,340] In these films with free carrier concentrations in the range of $1.5 \cdot 10^{21}$ cm^{-3} it can be expected that the dopant activation is very high. This shows, that the dopant activation strongly depends, among many other parameters, on the deposition method. Taking into account that the high-energetic particle bombardment is weak for the PLD depositions and that the samples with very high carrier concentrations of Minami et al.[230] have been deposited with magnetron sputtering orienting the substrates perpendicular to the target (which means that the high-energetic negative oxygen ion bombardment was reduced due to the glancing angle of the trajectory of the ions with respect to the substrate/film surface), the low dopant activations present for films sputtered without a special arrangement of the substrate can mainly be explained as a result of the bombardment of the growing films either causing compensating acceptor-like defects or radiation enhanced diffusion leading to an increased formation of secondary phases. Therefore, the low dopant activations are an inherent problem of the magnetron sputtering method that can be surmounted only by reducing the bombardment.

With respect to the preceding discussion, it can be summarized that the differences between the dopants Al, Ga, and Si are rather small. With In and B, the lowest resistivities which can be achieved are slightly higher. Only B seems to be an unsuitable dopant for ZnO since high dopant concentrations

are needed and only low dopant activations are achieved. According to the structural, optical, and electronic properties, Al and Ga seem to be the best dopant materials. However, this could also be due to the fact that these materials are now extensively investigated for over 60 years,[22] while only few groups investigated the doping of ZnO with B or Si. Another difficulty in comparing the dopants is due to the conditions under which the films were prepared. Even if the experiments are performed in the same system, different targets have to be used in the case of magnetron sputtering. However, it is known that the target properties strongly influence the film properties.[341] Therefore, the small differences in the film properties determined by single groups of researches are very hard to interpret in terms of the question what the most appropriate dopant material is. Eventually, the lowest resistivities and highest transparencies obtained using the different dopants after a long time of research by several groups will decide which dopant is most suitable, because this will average the best properties obtainable. For now, the abundance of Al and the high quality of the Al-doped TCOs, makes it the most favourable dopant.

7.4 Distribution of the Elements in the Films

The previous sections clarified that the formation of secondary phases in ZnO is one of the predominant effects to reduce the doping efficiency and hence the free carrier concentration. This segregation of phases is usually related to an inhomogeneous distribution of the dopant element in the films, which is known for a long time now.[281] Especially the changes of the mechanical behaviour of materials due to phase segregation at the grain boundaries has initially attracted much interest.[281] For materials such as ZnO, it has further been found that segregated phases at the grain boundary inhibit the grains from growing larger[270] and that they also have an impact on potential barriers at the grain boundaries. This segregation of the metal-oxide phases has for example been observed by high-resolution TEM measurements by Sieber and coworkers[95] in reactively co-sputtered ZnO:Al films, especially in the regions of high structural disorder. However, it seems no other group actually proved the existence of such phases in films sputtered at moderate temperatures yet.

To further examine the formation of secondary phases in as-deposited, magnetron sputtered films, the spatial distribution of the elements in the films measured by energy dispersive X-ray spectroscopy (EDX) implemented in the TEM instrument on cross sections of selected films and by atom probe tomography (APT) will be discussed in the following.

7.4.1 Results of EDX and TEM Measurements

Figure 7.22 on page 170 shows a mapping of the distribution of Zn, O, Mg, Al, and Si in a cross section of a $Zn_{1-x}Mg_xO$:Al film prepared at 300 °C on a Si substrate.

The substrate region and the film region can clearly be distinguished with the help of the Si, which is mainly detected in the substrate region. Still, there is also a weak Si signal in the film region and above the film surface. This can mostly be attributed to the sample preparation, but a certain diffusion of the Si into the film cannot completely be ruled out either. Generally, the strongest signal was obtained for the elements Zn and Si, a lower signal was detected from the O, and the lowest signals were observed for Al and Mg. This is consistent, since Al and Mg are present in the films only in a low amount, and the signal depends strongly on the fluorescence yield of the elements, which is higher for heavier elements.[342]

The distribution of the elements across the thickness of the film is inhomogeneous. For all elements, the signal decreases from the substrate interface to the film surface. This can be attributed to the

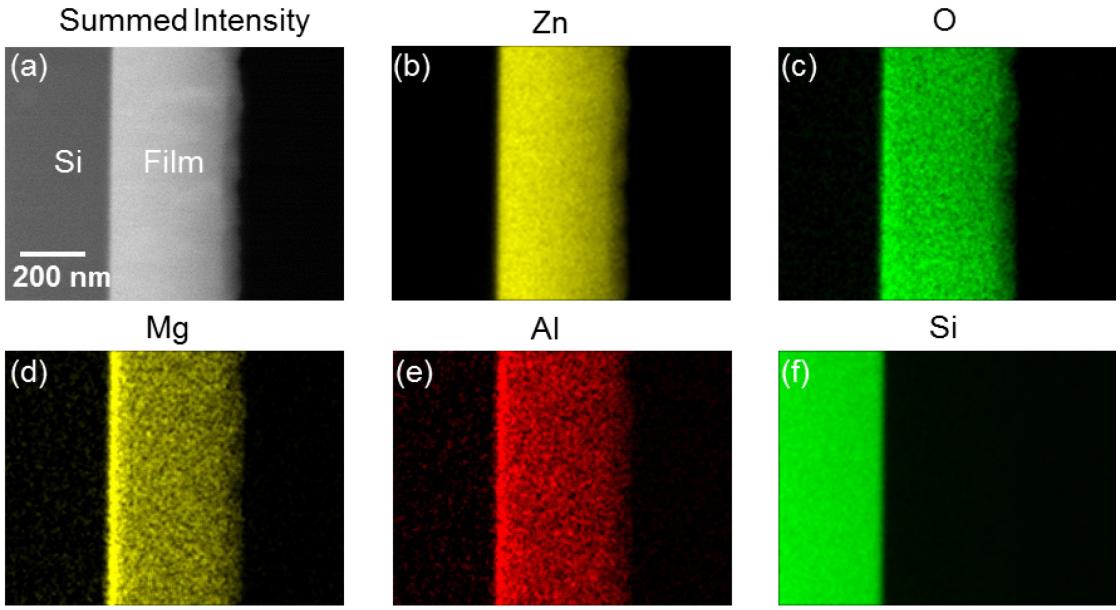

Figure 7.22: Maps of the spatial distribution of the elements Zn, O, Mg, Al, and Si in a cross section of a $Zn_{1-x}Mg_xO$:Al film deposited at 300 °C on a Si substrate. The elemental mapping was performed by energy dispersive X-ray spectroscopy at the Libra200 TEM. (a) shows the summed signal intensity, while the other images show the signal caused by the single elements. The color scale changes from dark to bright with increasing number of counts at a certain position on the map.

wedge-like thickness variation of the specimen due to the preparation, where the TEM sample is thicker in the substrate region and thinner in the surface region. This leads to a higher fluorescence signal originating from the thick regions of the sample. However, this is not the only inhomogeneity which can be observed. For some elements, an enrichment in the interface region between the substrate and the film is visible. This cannot only be a sample thickness effect, because at least one element, Zn, does not show an increase of the signal in the interface region to the substrate. To investigate this enrichment of the elements, the counts in the images have been summed up over the lateral direction in the films and plotted in Figure 7.23 as a depth profile. This procedure has also been performed for a ZnO:Al film prepared at 300 °C on a Si substrate.

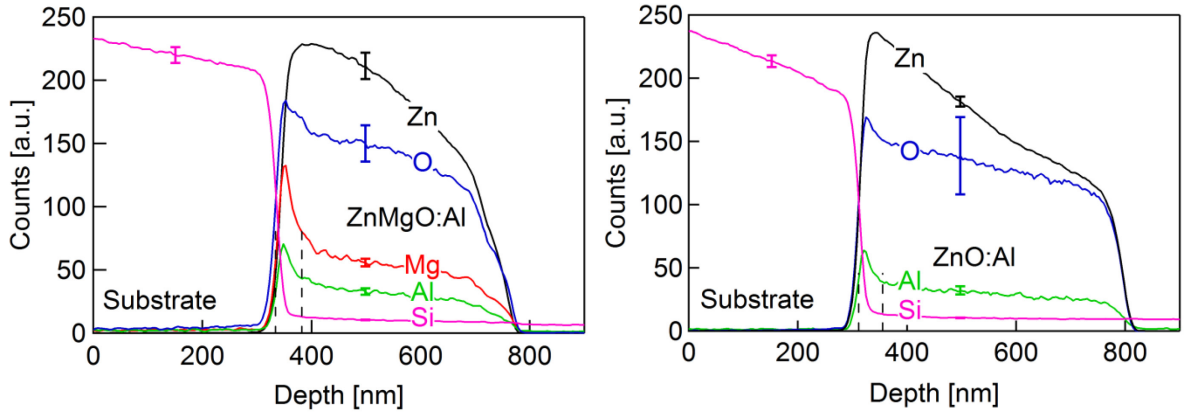

Figure 7.23: Depth profiles of the elements determined from the EDX maps on the cross sections of a ZnO:Al and $Zn_{1-x}Mg_xO$:Al film deposited at 300 °C on a Si substrate. The uncertainty of the data is indicated for selected data points. They have been determined from the variation of the signal in lateral direction.

The strong increase of the element concentration at the interface to the substrate is detected for Al and Mg in the ZnO:Al as well as the $Zn_{1-x}Mg_xO$:Al film. It may even carefully be deduced from the images that the O content is also increasing in that region. The effect is not related to the substrate, because similar elemental distributions have also been measured by EDX on films prepared on glass.

In outlines, the effect is also detected by RBS for the samples prepared on glassy carbon. There, it becomes more obvious for the samples prepared at substrate temperatures above 300 °C. Apparently, the effect is stronger for higher deposition temperatures. Because of the bad signal quality of Mg and Al, only for which this effect is detectable due to the large relative changes, no quantification of the increase of the element concentration as well as the thickness of this layer is possible from the RBS measurements. From the EDX profiles, on the other hand, the extension of this region can be estimated and is denoted with dashed vertical lines in Figure 7.23. For the ZnO:Al film, this region has a thickness of about 45 nm, and for the $Zn_{1-x}Mg_xO$:Al films, it is roughly 50 nm wide. For further investigation of this Al and Mg rich layer, dark field transmission electron microscopy has been performed on the cross sections of these films (see Figure 7.24).

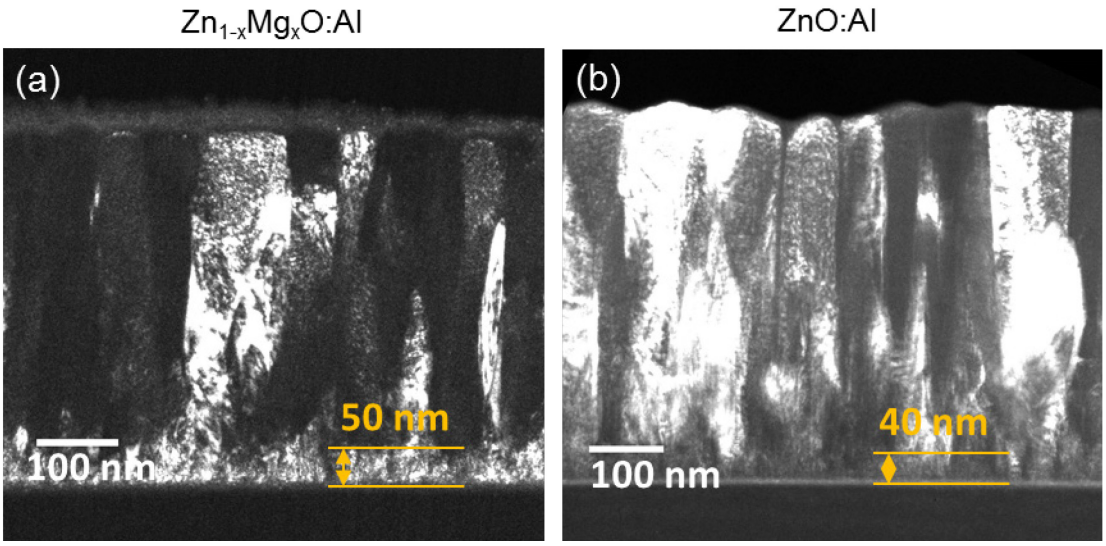

Figure 7.24: Transmission electron microscopy dark field images of regions close to the area, where the energy dispersive X-ray spectroscopy was performed. The defective regions close to the interface of the substrate are marked.

In the $Zn_{1-x}Mg_xO$:Al film, a distinct interface layer with a thickness of about (50 ± 5) nm is observed. It shows crystallites with an orientation different from that of most of the crystallites in the bulk of the film and with a much smaller grain size in the range mostly below 30 nm. In the ZnO:Al films, the interface layer is not as pronounced as in the $Zn_{1-x}Mg_xO$:Al films. It is only visible because the crystallites in the bulk do not extend to the interface. This layer has an approximate thickness of 40 nm as denoted in the figure. Vogel-Schäuble and coworkers[343] also found a highly defective nucleation zone at the interface to the substrate with a thickness of roughly 50 nm in their RF magnetron sputtered ZnO:Al films. These values are in very good agreement with the thickness of the layer with elevated concentrations of the Mg and Al. Therefore, a correlation between that defect-rich layer and the enrichment of the elements can be inferred. Additionally, such defective interface layers have also been observed for the samples prepared on glass. Besides, this depth dependence of the defect concentration has also been used to discuss the thickness dependence of the resistivity of ZnO films.[344-346] Actually, results from a series of ZnO:Al films deposited with increasing thickness from 30 nm to 515 nm showed that the resistivity is first strongly decreasing by about one order of magnitude with increasing film thickness from 30 nm to roughly 100 nm and then saturates for higher values.

The increased amount of Al and Mg may be related to the preferential evaporation of Zn from the substrate in the initial stages of the film growth, especially for higher substrate temperatures. Due to their lower vapour pressure, the Mg and Al atoms condense more easily on the substrate surface and form an Al-O and Mg-O rich nucleation layer for the condensation of the Zn. Such effects of nucleation layers on the condensation of Zn during deposition processes are known for a long time

now (see for example Reference 347 page 257 and following). The correlation of the enrichment of Al and Mg with the defect rich interface layer is in accordance with this hypothesis, because the nucleation layer is expected to be very defective. Additionally, Fourier transformed high-resolution transmission electron micrographs of this interface region, taken and analysed by Dr. Mythili Rengachari, showed the presence of α-Al_2O_3 and a spinel phase, which could be either $ZnAl_2O_4$ or $MgAl_2O_4$, in the defective interface layer. This is direct proof for the formation of secondary phases in the as-deposited films. The formation of these non-conductive secondary phases, which likely occurs in a larger amount in the interface layer in comparison to the bulk of the films due to the increased Al and Mg concentration, may also contribute to a reduced carrier concentration and mobility and hence to an increased resistivity in very thin films, where the thickness is not exceeding the thickness of the interface layer significantly.

7.4.2 Results of APT Measurements

To further investigate the distribution of the Al within the bulk of the films, atom probe tomography measurements have kindly been performed by Dr. Nelia Wanderka. These measurements were carried out on a ZnO:Al film grown on top of a Mo tip without intentional heating. Figure 7.25 shows the results for the elemental distribution of the Al in the film. While Figure 7.25 (a) presents the clusters whose concentration of Al exceeds 1.5 at.% in a region near the surface of the film, Figure 7.25 (b) and (c) display a region extending from the Mo tip to the surface of the film and a surface near region, respectively, where the volumes exceeding 0.75 at.% of Al concentration are marked.

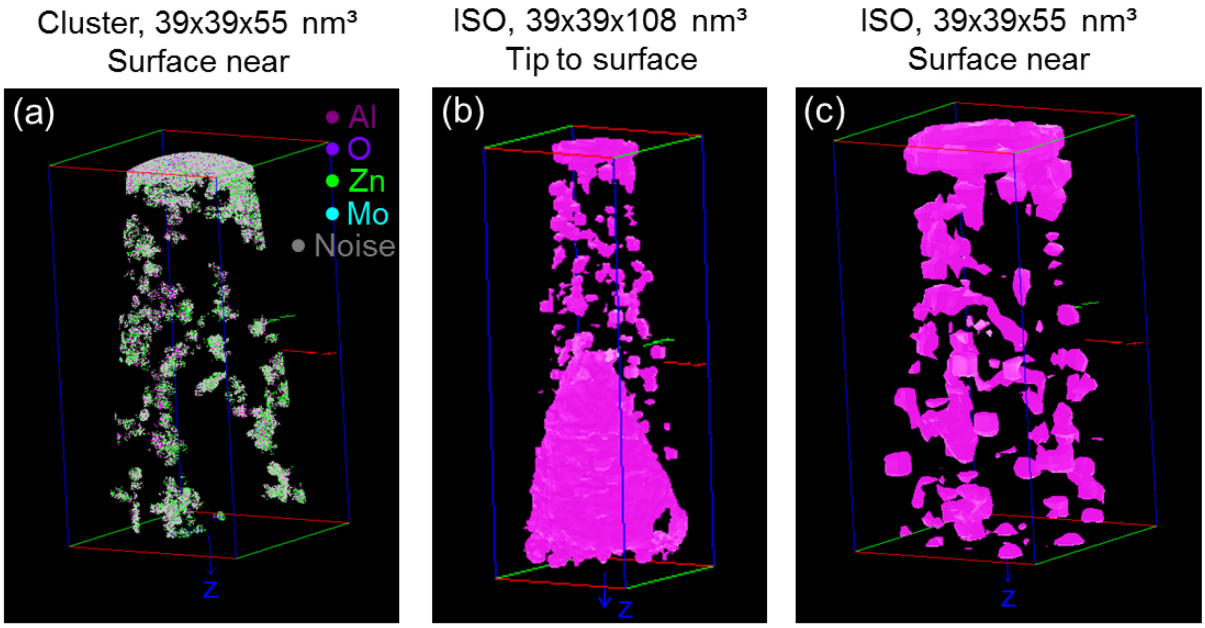

Figure 7.25: Distribution of the elements in a ZnO:Al film prepared on a Mo tip at room temperature for atom probe tomography measurements. The clusters with an Al concentration higher than 1.5 at.% in a surface near region of the film with a size of 39 x 39 x 55 nm³ are shown in (a), while the iso-concentration images for Al concentrations higher than 0.75 at.% in a region, which extends from the Mo tip to the surface of the film, and in the surface near region are presented in (b) and (c), respectively.

Also from the results of the atom probe tomography it is obvious that the Al is not distributed homogeneously in the films. For one thing, the film deposited on the Mo tip exhibits an enrichment of the Al in the interface region to the substrate as well (see Figure 7.25 (b)). This can be inferred from the shape of the Al enriched layer, which reflects the form of the Mo tip. The accumulation of the Al has hence not only been detected for samples prepared on Si, glass, or glassy carbon (not shown

before) but also on Mo. It is therefore not an effect depending on the substrate type, but an inherent property of the magnetron sputtered ZnO:Al and $Zn_{1-x}Mg_xO$:Al films. For another thing, the bulk of the film also exhibits an enrichment of the Al in certain regions. These regions are not homogeneously distributed throughout the bulk of the film, but they form clusters. Unfortunately, it was not possible to take a TEM image of the finally prepared tip. Therefore, the regions with a higher Al content cannot be related to grain boundaries or defect rich areas. However, these experiments are ongoing and TEM images will be prepared and correlated to the distribution of the dopant elements in the films.

Line (cylinder) profiles of the measured volume, similar to the depth profile of the EDX measurements, are shown in Figure 7.26. The inset of Figure 7.26 depicts the volume that has been used to determine the depth profile of the element concentration presented for Al and O.

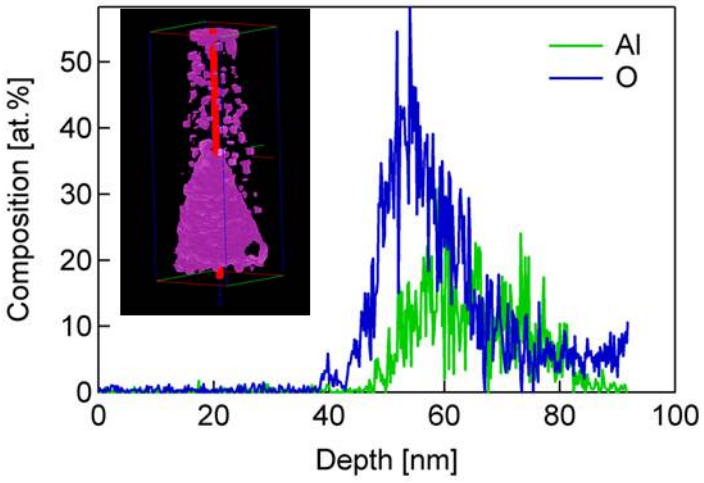

Figure 7.26: Depth profile of the concentration of Al and O in the ZnO:Al film. The depth profile has been extracted from the data of the APT measurements using a cylindrical volume (radius: 1.5 nm) as denoted in the inset by the red cylinder.

The Al enrichment on the Mo tip surface is considerable. According to the values determined from the line profile, a concentration in the range of 10 at.% to 15 at.% is present there. Outside this region, the measured concentrations are nearly 0 at.%. At least for the oxygen, this low value is a measurement error due to the evaporation of the O caused by the high laser power for the measurement. In fact, the O starts to evaporate untimely when the laser pulse is still building up. This conflicts with the triggering of the detector and the laser pulse, and therefore the O vanishes before the actual measurement after the laser pulse begins. In the Al-rich region, however, the measured O content increases to a value approximately 2 to 3 times higher than the Al content. This can be caused by a stronger bonding of the O in the material, which points to the formation of a more stable oxygen-containing phase or defect complex in that region.

Frank and Köstlin[315] proposed the following neutral defect complexes to be responsible for a deactivation of the dopant element in In_2O_3:Sn layers: translated from their analysis of the Sn dopant to the Al investigated here, an Al_2O complex, an Al_2O_4 complex, and a combination of the two before-mentioned with a stoichiometry of Al_4O_5. This means defects with a ratio of 2, 1/2, and 4/5 of the Al to the O concentration can be encountered. The ratio observed here is roughly 1/3, which does not fit to any of the defect complexes. Furthermore, the Al_2O complex is only loosely bound and can hence not explain the strongly bound O in the Al-rich region (assuming similar chemical properties of the Sn and Al in the defect complexes). The $(Al_2O)(Al_2O_4)$ complex contains loosely as well as strongly bound O and can therefore also be excluded. Only the Al_2O_4 complex contains solely strongly bound O and could be responsible for the O signal. This result is not very reliable, because there is no certainty about the accuracy of the O concentration in the Al rich interface region, but since the O is definitely bound stronger, this is an indication for the formation of a stable defect complex or a stable phase like Al_2O_3 or $ZnAl_2O_4$. The formation of a homologous phase as discussed by Yoshioka[310] and

Vinnichenko[309] with a stoichiometry of $(ZnO)_3Al_2O_3$ corresponds to an Al to O ratio of 1/3 as well. However, the homologous phase is not very stable, which makes it unlikely to be the explanation for the high Al signal in the interface region in comparison to the defect complexes or the segregated phases.

Summarizing, the enrichment of the dopant Al in the interface layer and probably also in certain regions in the bulk of the film, most likely the grain boundaries, is accompanied by the formation of stable secondary phases and presumably also Al_2O_4 defect complexes. Since the dopant is electrically inactive in these compounds, it must be the aim to reduce this phase segregation.

7.4.3 Possible Solutions to Reduce the Effects

A method to reduce the enrichment of Al (and Mg) in the interface layer to the substrate could be the use of a buffer layer. A very thin buffer layer which forms the necessary nuclei for the rapid condensation of the Zn may facilitate the growth of ZnO. Such a layer could be composed of pure metals with a low vapour pressure, for example silver, copper, or tin (see Reference 347 page 257 and following). Another possibility would be the use of low deposition temperatures in the early stages of the film growth to reduce the re-evaporation of the Zn from the substrate. With respect to the electric properties of the films, it would also be of interest to reduce the number of defects in the interface layer to facilitate the growth of ZnO with a higher structural quality. This might also have a positive effect on the amount of segregated phases since the segregation occurs preferentially at grain boundaries. A reduction of the number of defects could for example be achieved by reducing the plasma excitation frequency to reduce the bombardment of the film with high-energetic negative oxygen ions. Actually, Nomoto et al.[346] reported an improvement of the crystallinity of their DC sputtered films when they deposited a buffer layer by RF sputtering. Another possibility would be the reduction of the deposition rate for the early stages of the film growth to facilitate the formation of a ZnO phase of higher structural quality. Other parameters are the sputtering pressure or the oxygen partial pressure which could be adjusted differently at the beginning of the deposition. The works of Thornton for metals[119] and the transfer of his models to sputtering of ZnO by Ellmer[113] can be used as a guide to find the optimal deposition parameters for producing films/buffer layers of high crystalline quality. Since a high amount of Al, Mg, secondary phases, and defects introduces additional scattering of the free carriers, the inhibition of the formation of such an interface layer will not only increase the free carrier concentration in the films but also the charge carrier mobility.

7.5 Chapter Conclusions

The influence of Al, Ga, In, and Al + H on the electronic, optical, and structural properties of ZnO films has been investigated thoroughly, thus confirming Al and Ga as very suitable dopants for transparent conductive oxides to achieve a low conductivity and a high optical transmittance in the visible spectral region. Additionally, experimental evidence for the doping model, where the group III elements are localized on Zn lattice site in order to donate one electron to the conduction band, has been found by X-ray absorption spectroscopy measurements, and the qualitative model (see Section 6.1) was confirmed for dopants other than Al. The co-doping of ZnO:Al with hydrogen was found to be successful only for low deposition temperatures. Furthermore, it has a significant influence on the chemical composition and the structural properties of the films. These effects were strongly dependent on the material type and the deposition temperature. Most striking was the X-ray amorphization of the ZnO:Al,H and $Zn_{1-x}Mg_xO$:Al,H films for deposition at ~30 °C with a simultaneous decrease of the

resistivity by two orders of magnitude. This decreased resistivity is especially interesting for applications that require a low deposition temperature.

A comparison of the different dopant materials with literature data showed that the films prepared here are comparable to films of other groups. However, lowest resistivities of $2 \cdot 10^{-4}$ Ωcm and highest carrier concentrations of $1.5 \cdot 10^{21}$ cm^{-3} are not achieved, which can be attributed to the non-optimized deposition conditions. In principle, the differences between most of the dopant materials are very small and depend more on the preparation parameters of the films rather than the properties of the dopant material. Boron is the only dopant material, which exhibits a significantly lower doping efficiency, and is therefore unsuitable regarding the high amount of material needed to achieve high free carrier concentrations. Therefore, and because it is highly abundant, Al is the best dopant material to use in ZnO.

A detailed investigation of the spatial distribution of the Al in the ZnO:Al films, employing locally resolved EDX measurements and APT, revealed strong inhomogeneities of the Al concentration. Especially in the interface region to the substrate, a thick layer with a strong enrichment of the dopant material was found, which can be related to the formation of a Zn-depleted nucleation layer. The variations within the bulk of the film are most likely correlated to the segregation of the Al to grain boundaries. The Al is also present in the form of different phases in these areas, presumably segregated Al_2O_3 and/or $ZnAl_2O_4$. The stronger tendency to form segregated phases in the $Zn_{1-x}Mg_xO$:Al films in comparison to the ZnO:Al films was attributed to the possible formation of additional secondary phases such as $MgAl_2O_4$. A solution for the inhibition of the growth of such an interface layer would be the use of buffer layers or especially adapted process parameters in the initial stages of the film growth.

8. ZnO:Al and $Zn_{1-x}Mg_xO$:Al in $Cu(In,Ga)S_2$ Solar cells

In this work, the relation between the electronic transport and the structural properties of doped ZnO and $Zn_{1-x}Mg_xO$ films was investigated. Apart from the fundamental aspects, one aim of the investigation of the doped $Zn_{1-x}Mg_xO$ films was the preparation of films of sufficiently high quality for the use as front contact window layers with improved band alignment to the $Cu(In,Ga)S_2$ absorbers. Based on theoretical calculations, it is assumed that the position of the band edges has a significant effect on the open circuit voltage of the wide-gap chalcopyrite solar cells and therefore on the efficiency (see Section 2.5.2). In the following, the first results of the experiments using $Zn_{1-x}Mg_xO$:Al in wide-gap chalcopyrite thin films solar cells will be presented. The chapter is based on the work of Jonas Schulte, who was responsible for the preparation of the absorber layers and the completion of the solar cells and performed the characterization of the photovoltaic devices.

8.1 Preparation and Measurement Techniques

The $Cu(In,Ga)S_2$ absorber layers have been prepared either by reactive magnetron sputtering or by a sputtering process in combination with a rapid thermal annealing procedure. While the two step process including rapid thermal annealing for the preparation of $Cu(In,Ga)(S,Se)_2$ absorber layers is already used in industry and widely spread in research,[348] the sole sputtering of the absorber layer is a more uncommon approach. However, since most of the layers of the solar cell are sputtered and only the sulfurization is performed by a thermal annealing process, it is reasonable to establish a sputtering process which is able to readily produce $Cu(In,Ga)(S,Se)_2$. Especially today, where alternative buffer layers, that can be sputtered as well, are available, a direct one-step large area deposition process for the solar cells becomes feasible thereby.

For the two step process, which is a standard process performed at the Helmholtz-Zentrum Berlin (HZB), precursor layers of In and a Cu-Ga alloy were deposited by DC magnetron sputtering onto Mo-coated float glass substrates with the dimensions 12.5 x 50 mm².[349] The layer stack was then placed in a box together with elemental sulfur and transferred to a reaction chamber. By radiative heating with halogen lamps, the sulfurization was carried out at nominal temperatures of 450 °C to 600 °C for 3 min to 6 min. During this process, a CuS layer forms at the top of the $Cu(In,Ga)S_2$, which is removed afterwards by etching the sample in a potassium cyanide (KCN) solution. Usually, the solar cells are completed by chemical bath deposition of a CdS buffer layer, subsequent magnetron sputter deposition of a transparent window layer based on ZnO, and the evaporation of a Ni-Al grid. On these stripes with a size of 12.5 x 50 mm², 8 test cells were prepared, which were all evaluated to obtain average values for the solar cell parameters.

For the reactive DC co-sputtering of the $Cu(In,Ga)S_2$ absorber layers, performed by Jonas Schulte, two rectangular targets – a CuGa (85/15 wt.% ≈ 86.1/13.9 at.%) and an In target – and a mixture of Ar and H_2S (mass flow ratio 2/1) as process gas were used. The principal arrangement is depicted in Figure 8.1 on page 178.

Due to the high energies of the species in the plasma, the H_2S is dissociated and can react with the metals to form the chalcopyrite $Cu(In,Ga)S_2$ phase. The absorber layer is then also deposited on Mo

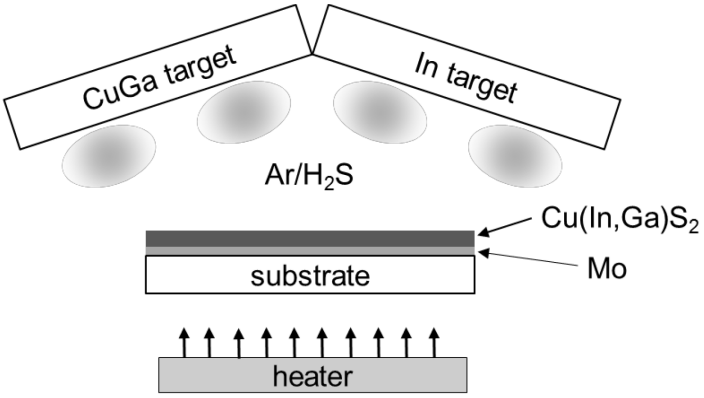

Figure 8.1: Scheme of the setup for the reactive magnetron sputtering of the $Cu(In,Ga)S_2$ absorber layers.

back contacts and, finally, the solar cells are, if not otherwise mentioned, finished the same way as the solar cells prepared using the rapid thermal annealing process.

The front contact layer consists of an intrinsic layer and a highly conductive layer. For the deposition of the intrinsic layer from the target that was also used for the deposition of the highly conductive layers, a relative flow of 10 % oxygen was added to the Ar-sputtering gas, which led to layers with a resistivity in the order of 2000 Ωcm. The targets had a composition of 98.4/1.6 mol.% (ZnO/Al_2O_3) and 88/10/2 mol.% ($ZnO/MgO/Al_2O_3$), respectively. Subsequently, without breaking the vacuum, the transparent contact window was deposited using a deposition temperature of 200 °C and 27.12 MHz plasma excitation frequency to ensure high electrical and structural film quality.

The characterization of the solar cells was carried out by I(V) measurements with 100 mW/cm² illumination at AM1.5 (AM: air mass) in a solar simulator.

8.2 Results Using ZnO:Al and $Zn_{1-x}Mg_xO$:Al as Window Layers

The first experiments were performed using the standard layer stack for the solar cells as described in Section 2.5.2, only replacing the intrinsic ZnO (i-ZnO) and the ZnO:Al layer by an i-$Zn_{1-x}Mg_xO$:Al and a $Zn_{1-x}Mg_xO$:Al layer, respectively, to determine the applicability of the $Zn_{1-x}Mg_xO$:Al films as front contact window layers. The absorber layers have been deposited by reactive co-sputtering. The results are always compared to a reference cell, which is finished with a window layer prepared according to the standard process available at the Helmholtz-Zentrum Berlin.

Figure 8.2 on page 179 shows a box plot of the efficiencies and the open circuit voltages of these solar cells. The boxes in the plot show the 75 % and 25 % percentiles, while the whiskers represent the 90 % and 10 % percentiles. The horizontal lines in the boxes mark the median and the markers denote the average values determined for the solar cells using the different window layers.

The results show, that the solar cells prepared with the ZnO:Al window layers deposited by the author of this work reach almost the same efficiencies in comparison to the reference cells. The reference cells were prepared from absorbers layers deposited in the same experiment series. However, the efficiencies are generally low as it is usually observed for wide-gap chalcopyrites. The cells finished with the ZnO:Al window layer reach an average efficiency of only 7.8 %, while the cells with the $Zn_{1-x}Mg_xO$:Al ($x \approx 0.12$) window layer exhibit 8.4 %, which is similar to the value of the reference cells. The generally low efficiencies are caused by the relatively low open circuit voltages, which are shown in Figure 8.2 (b). The reference cells exhibit an average open circuit voltage V_{oc} of 842 mV, while the cells with the ZnO:Al and $Zn_{1-x}Mg_xO$:Al window layers prepared in this work reach V_{oc} = 789 mV and V_{oc} = 798 mV, respectively. The solar cells with the $Zn_{1-x}Mg_xO$:Al window layers

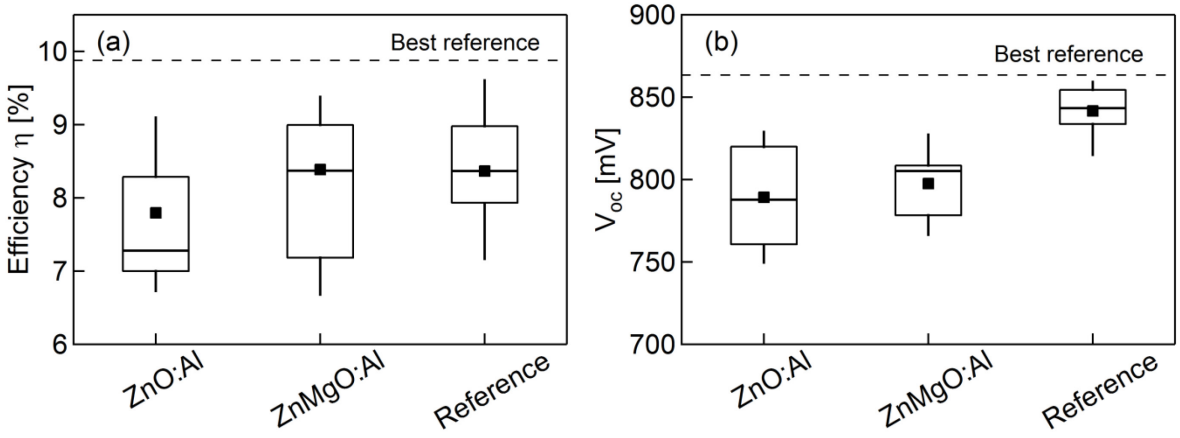

Figure 8.2: Box plot of the efficiency η (a) and the open circuit voltage V_{oc} (b) of the 3 best solar cells on each substrate using reactive co-sputtering for the deposition of the absorber. The reference data stem from the 3 best cells finished with the standard HZB ZnO:Al window and CdS buffer layer. All absorber layers have been prepared in one experiment series. The boxes show the 75 % and 25 % percentiles, while the whiskers represent the 90 % and 10 % percentiles. The horizontal lines in the boxes mark the median and the markers denote the average values.

exhibit slightly higher efficiencies and open circuit voltages in comparison to those prepared with the ZnO:Al window layers. However, this is not a significant difference, which is in contrast to the first expectations when using $Zn_{1-x}Mg_xO$:Al for an improved band alignment between the front contact and the absorber layer. On the other hand, the results show that the $Zn_{1-x}Mg_xO$:Al films are of similar quality with respect to the requirements of the solar cells and can be used as a front contact layer.

According to Yamada et al.[131], an increase of the open circuit voltage can only be achieved when the CdS layer is replaced. If the CdS buffer layer, which means the layer forming the interface to the absorber, is still present, the unfavourable negative band offset $\Delta E_c < 0$ between the absorber layer and the CdS layer is unmitigated even when followed by a positive ΔE_c between the $Zn_{1-x}Mg_xO$ layer and the CdS layer.

For this reason, experiments without a CdS buffer layer have been carried out. An alternative structure with a $Zn_{1-x}Mg_xO$ buffer layer has been suggested by Minemoto et al.[133] and successfully implemented in Cu(In,Ga)Se_2 and $CuInS_2$ solar cells.[133,350] In this investigation, the window layer was composed of i-$Zn_{1-x}Mg_xO$:Al and $Zn_{1-x}Mg_xO$:Al as described above. For comparison, solar cells with a ZnO:Al window layer and no CdS buffer were prepared as well. The absorber layers for these experiments were produced using the two step base-line process involving the rapid thermal annealing available at the HZB. The results for the efficiencies and the open circuit voltages are shown in Figure 8.3.

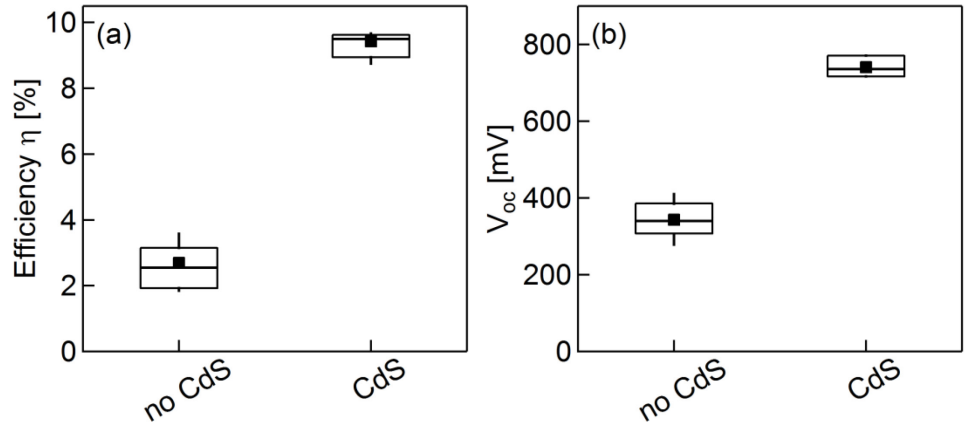

Figure 8.3: Boxplot of the efficiency η (a) and the open circuit voltage V_{oc} (b) of the 3 best cells with a CdS buffer layer or without a CdS buffer layer using $Zn_{1-x}Mg_xO$:Al (x ≈ 0.12) as a window layer.

While the solar cells prepared without a CdS buffer layer and using the ZnO:Al window layers showed an ohmic behaviour and no efficiency, the solar cells with the $Zn_{1-x}Mg_xO$:Al window layers are functioning. They exhibit diode characteristics and efficiencies in the range of 2.7 %. However, the efficiency is much lower in comparison to the solar cells prepared including the CdS buffer layer. This means the effect of an improved band alignment cannot be detected even when omitting the CdS buffer layer. Hence, the alternative cell design has to be further optimized to work with the $Zn_{1-x}Mg_xO$ layers investigated here.

Apparently, a buffer layer is required to achieve high efficiencies with the non-optimized cell design using the $Zn_{1-x}Mg_xO$:Al layers deposited here. As an alternative to CdS, Zn(O,S) buffer layers together with the $Zn_{1-x}Mg_xO$:Al windows were used in a next step. They were deposited in the group of Dr. Ahmed Ennaoui using chemical bath deposition and had a ZnS/(ZnS + ZnO) ratio between 0.5 and 1. According to Sáez Araoz (see Reference 351 page 98), a band gap energy and an electron affinity (defined as the energy difference between the conduction band minimum and the vacuum level) in the range of 3.6 eV and 4.4 eV, respectively, can be expected for the Zn(O,S) buffer layers. The electron affinity χ has been calculated using the value for stoichiometric or Cu-poor $CuInS_2$, $\chi = 4.9$ eV, determined by Hunger et al.[352], and the conduction band offset of 0.5 eV between $CuInS_2$ and Zn(O,S) reported by Sáez Araoz. These values are quite different from the CdS, which has a band gap energy of approximately 2.6 eV and an electron affinity of 4.5 eV, respectively.[131] This difference has an impact on the band alignment between the absorber and the buffer layer and may lead to the desired spike in the band diagram and hence, together with the $Zn_{1-x}Mg_xO$, to an increased open circuit voltage. The absorber layers for these experiments were again prepared using the two step base-line process involving the rapid thermal annealing available at the HZB. All ZnO:Al window layers stem from the standard process at the HZB. The results of the 3 best solar cells with Zn(O,S) buffer layers and ZnO:Al as well as $Zn_{1-x}Mg_xO$:Al window layers are shown and compared to cells with a CdS buffer layer in Figure 8.4.

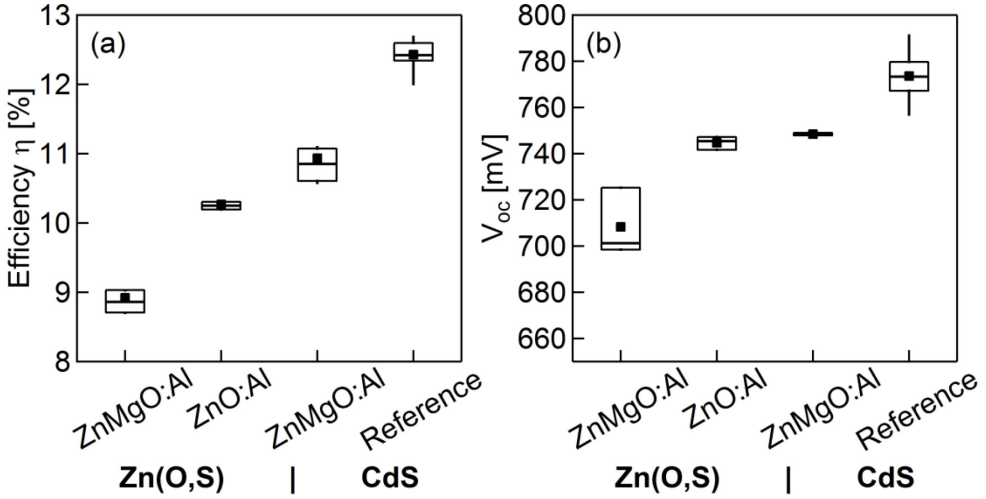

Figure 8.4: Boxplot of the efficiency η (a) and the open circuit voltage V_{oc} (b) of the 3 best cells with CdS and Zn(O,S) buffer layers using $Zn_{1-x}Mg_xO$:Al or ZnO:Al window layers. The reference cells have a CdS buffer layer and a ZnO:Al window layer.

The efficiencies of the solar cells prepared using $Zn_{1-x}Mg_xO$:Al as a window layer and the Zn(O,S) buffer layer ($\eta = 8.9$ %) are higher in comparison to those of the cells prepared without a buffer layer ($\eta = 2.7$ %). Hence, it can be concluded that the Zn(O,S) is acting as a buffer layer. The results were, however, slightly worse in comparison to the cells prepared with the CdS buffer, which exhibited efficiencies in the range of $\eta = 10.9$ %. This means that the different values of the band offsets have no positive effect on the band alignment and the performance of the solar cells when using $Zn_{1-x}Mg_xO$ as

a window layer. Furthermore, the solar cells with a CdS buffer and a $Zn_{1-x}Mg_xO$:Al window layer ($\eta = 10.9\,\%$) have a lower efficiency than those prepared with a ZnO:Al window layer ($\eta = 12.4\,\%$). This is significantly different to the results of the first experiments shown in Figure 8.2 on page 179 and illustrates the strong dependence of the results on the exact sample preparation conditions, where several process steps are included, all of which are not exactly reproducible. Therefore, the results have to be interpreted carefully when an improvement due to a difference in the layout of the solar cell shall be inferred. A comparison between the CdS and the Zn(O,S) buffer of the cells prepared with the standard HZB process window layers (ZnO:Al) shows a lower efficiency for the Zn(O,S) buffer layer as well, which means that the Zn(O,S) buffer is not as effective as the CdS.

The three experiment series have shown that it is not possible to improve the solar cells with the $Zn_{1-x}Mg_xO$:Al window layers without further investigations. This could be related to the Mg content in the $Zn_{1-x}Mg_xO$:Al ($x \approx 0.12$) films, which may be too low for improved band alignment to wide-gap chalcopyrite $Cu(In,Ga)S_2$ absorber layers. Actually, Yamada et al.[131] proposed a value of $x \approx 0.25$ for an absorber with a band gap of roughly 1.5 eV. To investigate the influence of the Mg content on the band alignment, systematic investigations of the band alignment in the wide-gap chalcopyrite solar cells are necessary. This involves extensive UV- and X-ray photoelectron spectroscopy measurements to determine the energy of the valence band edge, the work function, and the electron affinity of the window layer as well as the buffer and the absorber layer. These parameters can then be used to model the band alignment and make reliable predictions about the exact stoichiometry and doping needed for the window layers to achieve higher open circuit voltages and hence higher efficiencies.

8.3 Chapter Conclusions

Intrinsic and highly conductive ZnO:Al and $Zn_{1-x}Mg_xO$:Al layers have been deposited as front contact window layers in wide-gap $Cu(In,Ga)S_2$ chalcopyrite thin film solar cells. The results are based on the work of Jonas Schulte, whose responsibility was the preparation and detailed investigation of the reactively co-sputtered absorber layers. The study showed, that the electronic, structural, and optical quality of the $Zn_{1-x}Mg_xO$:Al layers was high enough for the use as front contacts in thin film solar cells. However, three different experimental series revealed the necessity of further investigations for the successful implementation of the $Zn_{1-x}Mg_xO$:Al window layers in the solar cells. In fact, cells with CdS, Zn(O,S), and without buffer layers have been prepared and characterized, and none of the experiments showed a significant increase of the efficiency when using the $Zn_{1-x}Mg_xO$:Al instead of the ZnO:Al as a front contact window layer. To clarify the reasons for the observed behaviour, more experiments with a wider range of parameters, for example other composition of the $Zn_{1-x}Mg_xO$:Al, are necessary. Additionally, the exact band parameters should be determined for the prepared films and theoretical calculations of the band alignment performed, to rule out any mitigating effects of the buffer layer or the combination of the layer stack in general. If this approach is not successful, other possible mechanisms for the reduced open circuit voltages have to be considered.

9. Conclusions and Outlook

9.1 Main Conclusions of This Thesis

The objective of this thesis was the systematic investigation of the relation between the structural properties, the electronic properties, and the electronic transport of doped ZnO and $Zn_{1-x}Mg_xO$ films. The influence of the deposition process and the deposition parameters on the structural properties and the resulting electronic properties of the films has been explored in detail and different models for the description of the effects have been proposed, which provide the basis for a deliberate improvement of the TCO film properties. The main results will be summarized in this section.

The films for this analysis were deposited by magnetron sputtering from ceramic targets at different substrate temperatures, one of the most important process parameters, ranging from ~30 °C to 500 °C. A variation of the plasma discharge frequency from DC via 13.56 MHz to 27.12 MHz was then used to further investigate the influence of the high-energetic ion bombardment on the growing films. Generally, the layers were deposited either on glass substrates yielding polycrystalline ZnO or single crystalline substrates for epitaxial growth, which allowed to examine the electronic transport in films with a strongly reduced number of grain boundaries. The depositions were usually performed in a pure argon atmosphere. Only for the co-doping of ZnO:Al and $Zn_{1-x}Mg_xO$:Al with hydrogen, the sputtering atmosphere was modified by the addition of H_2.

The characterization of the film properties was mainly performed by electrical measurements and structural measurements such as resistivity, Hall-effect, Seebeck-coefficient, and X-ray diffraction measurements. Additionally, the optical properties were determined by transmittance and reflectance measurements. However, several other techniques have also been employed to obtain complementary information on the electronic and structural properties as well as additional information on the chemical composition of the films and the parameters of the sputtering process.

Analysis of the Charge Carrier Scattering

Based on a survey of literature data, it was found that the charge carrier scattering in single crystals is dominated by phonon scattering for low free carrier concentrations ($n < 10^{17}$ cm^{-3}) and ionized impurity scattering for free carrier concentrations above $n \approx 10^{17}$ cm^{-3}. The transport in the polycrystalline films investigated here, on the other hand, is limited by ionized impurity scattering for carrier concentrations above $5 \cdot 10^{20}$ cm^{-3} and by grain boundary scattering for lower values, which has been shown consistently by both, Hall-effect and Seebeck-coefficient measurements. To describe the Hall mobility as a function of the free carrier concentration and the temperature over the whole range of free carrier concentrations investigated, a simple fit model for arbitrary degeneracy of the semiconductors, based on the formulae given by Garcia-Cuenca et al.[94, 95] and Seto[83], has been derived. In comparison to the classical model by Seto, this model can explain the temperature independence of the Hall mobility for degenerate conditions. Furthermore, it can be applied in a simple fit procedure while the other models proposed for degenerate semiconductors in the literature are analytically too complex for that.

Comparing the electronic transport between ZnO:Al and $Zn_{1-x}Mg_xO$:Al films, it was found that the transport is basically limited by the same mechanisms. Only in the $Zn_{1-x}Mg_xO$:Al films, an additional

scattering mechanism is observed, most likely alloy scattering. Hence, it must be the aim to keep the amount of the alloy material as low as possible to maintain a low resistivity. This means, if the necessary change of the band gap for the improved band alignment can only be obtained with a high amount of MgO, it is favourable to search for other alloy elements that can induce the same change with a lower amount of alloy material. This could for example be BeO.

Comparison of Epitaxial and Polycrystalline Films

The analysis of the electronic transport properties of epitaxially grown films showed that the lowest resistivity obtainable is only marginally influenced by the crystallinity of the sample. In fact, homoepitaxial films with a structural quality orders of magnitude higher in comparison to polycrystalline films exhibited similar resistivities. This is caused by the trap states at the grain boundaries that dominate the electronic transport for lower free carrier concentrations even if the number of grain boundaries is drastically reduced. The density of trap states at the grain boundary was nearly independent from the crystalline quality at a value of $N_t \approx 7...8 \cdot 10^{13}$ cm^{-2}. It was concluded that the trap density is not caused by the altered atomic structure in the grain boundary region but by the segregation of the dopant material to the grain boundary. Consequently, for practical applications, the grain boundary scattering can only be reduced when the amount of dopant material present in the films is decreased.

The crystalline quality of the $Zn_{1-x}Mg_xO$:Al films is slightly lower in comparison to that of the ZnO:Al films. This can be related to the disorder induced by the Mg in the ZnO lattice on the one hand and a stronger bombardment of the growing films with high-energetic negative oxygen ions on the other hand. Both effects have an impact on the electronic properties of the $Zn_{1-x}Mg_xO$:Al films and contribute to their higher resistivities.

The Role of High-Energetic Particle Bombardment and Phase Segregation

The investigation of films prepared at different substrate temperatures and plasma excitation frequencies revealed that a high-energetic O^- ion bombardment and the formation of other phases and/or defect complexes are crucial for the compositional, electronic, and structural properties of magnetron sputtered ZnO:Al and $Zn_{1-x}Mg_xO$:Al films. The influence of the deposition parameters on the film properties can be described by a qualitative model derived in this work. According to this model, the electronic properties are mainly determined by the interplay between acceptor-like defect (oxygen interstitials - O_i) generation by negative oxygen ion bombardment during the deposition at low substrate temperatures, the self-annealing of these defects during the film growth at moderate deposition temperatures, and the segregation of additional phases (Al_2O_3, $ZnAl_2O_4$, $MgAl_2O_4$) and presumably also Al_2O_4 defect complexes, in which the dopant is electrically inactive, at higher T_{sub}. Based on the model, the generally lower free carrier concentrations in the $Zn_{1-x}Mg_xO$:Al films in comparison to the ZnO:Al films can be explained by a stronger bombardment of the $Zn_{1-x}Mg_xO$:Al films due to the MgO in the target.

These results explain the effects of other deposition parameters on the film properties as well. The radial distribution of the electronic and structural properties for magnetron sputtered films, for example, can be interpreted as a consequence of the high-energetic particle bombardment. The high free carrier concentrations obtained by Minami[20] for the films deposited with the substrate perpendicular to the target surface can also be explained by a decreased bombardment. Further, the influence of the pressure during the sputtering process can be interpreted as a result of a thermalization of the high-energetic negative ions. The model even explains that the electric properties of films deposited by pulsed laser deposition are usually better, because the films are exposed to much less high-energetic particle bombardment during this deposition process. Hence, the applicability of the qualitative model is not limited to this investigation.

For the magnetron sputtering of materials with components inclined to form negative ions, this bombardment can only be reduced, not eliminated. Possible routes to decrease the impact of the ion bombardment are increased plasma excitation frequencies, the use of targets with a reduced secondary electron emission coefficient, and higher process pressures.

Analysis of the Doping of ZnO

The systematic study of the influence of the dopants Al, Ga, and In on the structural, electronic, and optical properties of ZnO confirmed that Al and Ga are efficient dopants in ZnO and $Zn_{1-x}Mg_xO$. Using the same deposition conditions, Ga seems to exhibit slightly higher dopant activations, which is interesting for the reduction of the dopant material while maintaining the free carrier concentration and can help to reduce the grain boundary scattering. Beyond that, the investigations using X-ray absorption spectroscopy revealed experimental evidence for the doping model of the group III elements, which are assumed to occupy Zn lattice sites. The co-doping of ZnO:Al and $Zn_{1-x}Mg_xO$:Al films with hydrogen showed a drastic influence of the hydrogen on the structural and electronic properties of the films. The films prepared without intentional heating exhibited a reduction of the resistivity by two orders of magnitude in comparison to the preparation without hydrogen despite a drastic decrease of the crystalline quality. This is especially interesting for the application of ZnO on temperature sensitive substrates.

Energy dispersive X-ray spectroscopy and atom probe tomography measurements revealed an inhomogeneous distribution of the dopant elements in the bulk of the films and at the interface to the substrate. The variations in the bulk of the films could be an indication that segregation of the metal-oxide phases at grain boundaries occurs, which leads to an inactivation of the extrinsic dopant and hence to an unwanted increase of the resistivity. The strong accumulation of the dopant material at the interface to the substrate with a thickness in the range of several ten nm is attributed to the formation of a Zn-depleted nucleation layer. In this layer, a TEM investigation showed the presence of secondary phases. Experimental evidence for a stronger phase segregation in the $Zn_{1-x}Mg_xO$ films was explained by the additional formation of $MgAl_2O_4$. Possible routes to reduce the formation of grain boundaries in the bulk of the film and inhibit the growth of an interface layer may be the use of seed layers or different deposition parameters in the first stages of the film formation.

Preparation of Solar Cells

First experiments using the optimized $Zn_{1-x}Mg_xO$:Al films investigated in this work as front contact windows in wide-gap chalcopyrite $Cu(In,Ga)S_2$ solar cells verified that the electronic and optical quality of the $Zn_{1-x}Mg_xO$:Al layers is sufficiently high for the application as transparent conductive oxides in thin film solar cells. However, despite the use of different approaches, which means omitting the CdS buffer layer or employing a Zn(O,S) buffer layer, a significant increase of the efficiency of the solar cells by utilizing $Zn_{1-x}Mg_xO$ for improved band alignment was not possible. This can most likely be attributed to the narrow parameter window for the improved band alignment and the lack of data available for the energetic positions of the band edges in the solar cell layer stack. Further investigations are necessary to successfully implement the band gap engineered TCO in the wide-gap chalcopyrite solar cell layer stack.

9.2 Outlook

Although new fundamental insights into the relation between the structural, the electronic, and the transport properties of ZnO, which can partly be transferred to other TCOs as well, were acquired

throughout this work, further research on a fundamental level as well as for the applications is necessary.

Competitiveness to ITO

Within the framework of this thesis, no tin-doped indium oxide films have been prepared. The proposed routes for a decrease of the resistivity of the doped ZnO films can be expected to have an impact on the ZnO:Al as well as the In_2O_3:Sn in a similar manner. Hence, most likely the ZnO:Al will remain to have higher resistivities in comparison to the ITO. However, it is not clear what the reason for this difference is. Hosono et al.[353] argued that the isotropy of the s-like wave function of the conduction band states in ITO guarantees an overlap of these states even if the crystal lattice is disturbed, which ensures a high mobility of the charge carriers. But the conduction band of ZnO is composed mainly of s-like metal wave functions as well, which means the same reasoning should also apply for ZnO.[7]

Obviously, further research is necessary and a more detailed investigation of the electronic, structural, and transport properties of the ITO is required. Especially a comparison of the properties of the In_2O_3:Sn with that of the ZnO:Al is needed to reveal the reason(s) for the lower resistivities obtainable in ITO. First works, attempting to compare the electric properties and the electronic transport of In_2O_3:Sn and ZnO:Al, mainly by Ellmer and Mientus,[235,251] showed that the trap density at the grain boundaries seems to be generally lower in the In_2O_3:Sn (see the high Hall mobilities for carrier concentrations below $n = 10^{19}$ cm^{-3} in Figure 9.1).

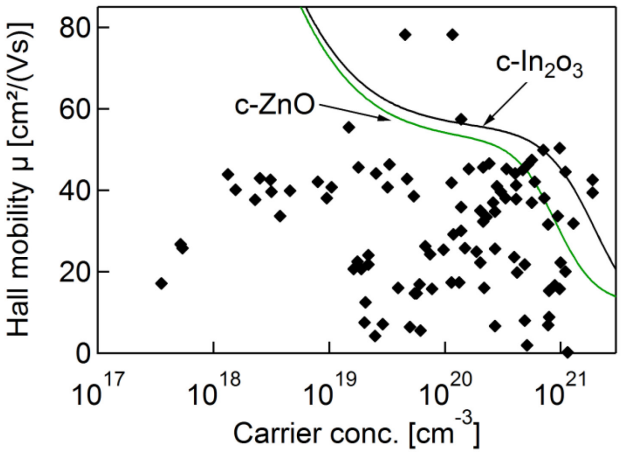

Figure 9.1: Hall mobility μ as a function of the free carrier concentration *n* for doped In_2O_3. The data were taken from References 235 and 251. The green solid line shows the Masetti curve for the doped ZnO single crystals using the values determined in this work and the black solid line shows the Masetti curve for the single crystalline doped In_2O_3 with parameters taken from Reference 235.

This leads to a higher charge carrier mobility and hence lower resistivities. Additionally, in the range of high free carrier concentrations ($n \geq 5 \cdot 10^{20}$ cm^{-3}), the mobility values for the single crystalline material are slightly higher, which means the ionized impurity scattering is lower. It can be speculated that the tendency for ionized impurity clustering is lower in tin-doped indium oxide. Still, a more detailed investigation is necessary to reveal the origin of the difference between In_2O_3:Sn and ZnO:Al.

Verification of the Qualitative Model

For further verification of the qualitative model, the existence of electrically active oxygen interstitial defects and their deposition temperature dependent concentration must be determined experimentally. However, interstitial defects are very difficult to investigate. Transmission electron microscopy on point defects requires a very sophisticated electron microscope as well as a high level of experience with respect to the interpretation of the data. Furthermore, a large set of samples has to be investigated to identify the oxygen interstitial defects as the origin of the deterioration of the electronic properties, which is not feasible for TEM investigations. One promising technique for the investigation of the interstitial oxygen defects is Rutherford backscattering spectrometry in the channelling configuration.

Especially interstitial defects can be determined element specific with this technique. A collaboration with the institute of solid state physics at the ‘Friedrich-Schiller-Universität Jena’, which has the required equipment and the expertise to perform and interpret such measurements, is being established. Another prospective method for the investigation of the interstitial oxygen defects are cathodoluminescence measurements. Together with the information about the defects by density-functional theory calculations, a reliable statement should be possible. A cooperation with the institute of experimental physics II at the ‘Universität Leipzig’ is being built up to perform cathodoluminescence measurements on selected samples.

Other Compositions of $Zn_{1-x}Mg_xO$

The investigations on $Zn_{1-x}Mg_xO$:Al in this work are limited to films prepared from a target containing 5 at.% Mg. For lower deposition temperatures, this yields a film composition of approximately $x \approx 0.12$. Although the results obtained in this work are of very general nature and can directly be transferred to higher Mg contents, investigations of the structural, electronic, and transport properties of $Zn_{1-x}Mg_xO$ alloys with higher Mg content are necessary to proof and extend the developed models.

List of Figures

8. ZnO:Al and $Zn_{1-x}Mg_xO$:Al in $Cu(In,Ga)S_2$ Solar Cells

9. Conclusions and Outlook

List of Tables

Bibliography

1. D. Ginley, H. Hosono, and D. Paine (editors): Handbook of Transparent Conductors (Springer, New York, 2010).
2. A.J. Freeman, K.R. Poeppelmeier, T.O. Mason, R.P.H. Chang, and T.J. Marks: Chemical and thin-film strategies for new transparent conducting oxides. *MRS Bulletin* **25**, 45-51 (2000).
3. J. Robertson and B. Falabretti: Electronic Structure of Transparent Conducting Oxides, in Handbook of Transparent Conductors, edited by D. Ginley, H. Hosono and D. Paine (Springer, New York, 2010), pp. 27-50.
4. K. Bädeker: Über die elektrische Leitfähigkeit und die thermoelektrische Kraft einiger Schwermetallverbindungen. *Annalen der Physik* **22**, 749 (1907).
5. R.G. Gordon: Criteria for choosing transparent conductors. *MRS Bulletin* **25**, 52-57 (2000).
6. D. Ginley and J. Perkins: Transparent Conductors, in Handbook of Transparent Conductors, edited by D. Ginley, H. Hosono and D. Paine (Springer, New York, 2010), pp. 1-26.
7. K. Ellmer: Transparent Conductive Zinc Oxide and Its Derivatives, in Handbook of Transparent Conductors, edited by D. Ginley, H. Hosono and D. Paine (Springer, New York, 2010), pp. 193-263.
8. C. Klingshirn, M. Grundmann, A. Hoffmann, B. Meyer, and A. Waag: Zinkoxid - ein alter, neuer Halbleiter. *Physik Journal* **5**, 33-38 (2006).
9. K. Ellmer and A. Klein: ZnO and Its Applications, in Transparent Conductive Zinc Oxide: Basics and Applications in Thin Film Solar Cells, edited by K. Ellmer, A. Klein and B. Rech (Springer, Berlin, 2008), pp. 1-33.
10. E. Fortunato, D. Ginley, H. Hosono, and D.C. Paine: Transparent conducting oxides for photovoltaics. *MRS Bulletin* **32**, 242-247 (2007).
11. M. Green: Solar Cells. Operating principles, Technology and System Applications (University of New South Wales, Kensington, 1992).
12. T. Minemoto, T. Negami, S. Nishiwaki, H. Takakura, and Y. Hamakawa: Preparation of $Zn_{1-x}Mg_xO$ films by radio frequency magnetron sputtering. *Thin Solid Films* **372**, 173-176 (2000).
13. K. Ellmer, A. Klein, and B. Rech (editors): Transparent Conductive Zinc Oxide: Basics and Applications in Thin Film Solar Cells (Springer, Berlin, 2008).
14. H. Morkoc and Ü. Özgür: Zinc Oxide: Fundamentals, Materials and Device Technology (Wiley-VCH, Weinheim, 2009).
15. P. Erhart, K. Albe, and A. Klein: First-principles study of intrinsic point defects in ZnO: Role of band structure, volume relaxation, and finite-size effects. *Physical Review B* **73**, 205203 (2006).
16. D.L. Young, T.J. Coutts, V.I. Kaydanov, A.S. Gilmore, and W.P. Mulligan: Direct measurement of density-of-states effective mass and scattering parameter in transparent conducting oxides using second-order transport phenomena. *Journal of Vacuum Science and Technology A* **18**, 2978-2985 (2000).
17. A. Janotti and C.G. Van de Walle: Fundamentals of zinc oxide as a semiconductor. *Reports on Progress in Physics* **72**, 126501 (2009).

18. D.C. Look, J.W. Hemsky, and J.R. Sizelove: Residual native shallow donor in ZnO. *Physical Review Letters* **82**, 2552-2555 (1999).

19. T. Minami, H. Nanto, S. Shooji, and S. Takata: The Stability of Zinc-Oxide Transparent Electrodes Fabricated by RF Magnetron Sputtering. *Thin Solid Films* **111**, 167-174 (1984).

20. T. Minami, H. Sato, H. Nanto, and S. Takata: Group-III Impurity Doped Zinc-Oxide Thin-Films Prepared by RF Magnetron Sputtering. *Japanese Journal of Applied Physics Part 2* **24**, L781-L784 (1985).

21. D.G. Thomas: The Diffusion and Precipitation of Indium in Zinc Oxide. *Journal of Physics and Chemistry of Solids* **9**, 31-42 (1958).

22. K. Ellmer: Electrical Properties, in Transparent Conductive Zinc Oxide: Basics and Applications in Thin Film Solar Cells, edited by K. Ellmer, A. Klein and B. Rech (Springer, Berlin, 2008), pp. 35-78.

23. J. Clatot, G. Campet, A. Zeinert, C. Labrugere, M. Nistor, and A. Rougier: Low temperature Si doped ZnO thin films for transparent conducting oxides. *Solar Energy Materials and Solar Cells* **95**, 2357-2362 (2011).

24. H. Kim, J.S. Horwitz, W.H. Kim, A.J. Makinen, Z.H. Kafafi, and D.B. Chrisey: Doped ZnO thin films as anode materials for organic light-emitting diodes. *Thin Solid Films* **420**, 539-543 (2002).

25. T. Minami: Transparent conducting oxide semiconductors for transparent electrodes. *Semiconductor Science and Technology* **20**, S35-S44 (2005).

26. H. Dixit, N. Tandon, S. Cottenier, R. Saniz, D. Lamoen, B. Partoens, V. Van Speybroeck, and M. Waroquier: Electronic structure and band gap of zinc spinel oxides beyond LDA: $ZnAl_2O_4$, $ZnGa_2O_4$ and $ZnIn_2O_4$. *New Journal of Physics* **13**, 063002 (2011).

27. P. Liley, R. Reid, and E. Buck: Physical and Chemical Data, in CRC Handbook of Chemistry and Physics, edited by R. Weast and M. Astle (CRC Press, Florida, 1981/1982), pp. 147-154.

28. E. Burstein: Anomalous Optical Absorption Limit in InSb. *Physical Review* **93**, 632-633 (1954).

29. T.S. Moss: The Interpretation of the Properties of Indium Antimonide. *Proceedings of the Physical Society of London Section B* **67**, 775-782 (1954).

30. I. Hamberg, C.G. Granqvist, K.F. Berggren, B.E. Sernelius, and L. Engstrom: Band-Gap Widening in Heavily Sn-Doped In_2O_3. *Physical Review B* **30**, 3240-3249 (1984).

31. A.P. Roth, J.B. Webb, and D.F. Williams: Band-Gap Narrowing in Heavily Defect-Doped ZnO. *Physical Review B* **25**, 7836-7839 (1982).

32. B.E. Sernelius, K.F. Berggren, Z.C. Jin, I. Hamberg, and C.G. Granqvist: Band-gap tailoring of ZnO by means of heavy Al doping. *Physical Review B* **37**, 10244-10248 (1988).

33. R.A. Abram, G.N. Childs, and P.A. Saunderson: Band gap narrowing due to many-body effects in silicon and gallium arsenide. *Journal of Physics C - Solid State Physics* **17**, 6105-6125 (1984).

34. K.L. Chopra, S. Major, and D.K. Pandya: Transparent Conductors - a Status Review. *Thin Solid Films* **102**, 1-46 (1983).

35. G. Haacke: Transparent Conducting Coatings. *Annual Review of Materials Science* **7**, 73-93 (1977).

36. S. Adachi: Model dielectric constants of GaP, GaAs, GaSb, InP, InAs, and InSb. *Physical Review B* **35**, 7454-7463 (1987).

37. Y. Ke, J. Berry, P. Parilla, A. Zakutayev, R. O'Hayre, and D. Ginley: The origin of electrical property deterioration with increasing Mg concentration in ZnMgO:Ga. *Thin Solid Films* **520**, 3697-3702 (2012).

38. D. Lide (editor): Ionic Radii in Crystals, in CRC Handbook of Chemistry and Physics (CRC Press, Boca Raton, 2008). pp. 12.11-12.12.

39. W.I. Park, G.C. Yi, and H.M. Jang: Metalorganic vapor-phase epitaxial growth and photoluminescent properties of $Zn_{1-x}Mg_xO$ ($0 <= x <= 0.49$) thin films. *Applied Physics Letters* **79**, 2022-2024 (2001).

40. A. Ohtomo, M. Kawasaki, T. Koida, K. Masubuchi, H. Koinuma, Y. Sakurai, Y. Yoshida, T. Yasuda, and Y. Segawa: $Mg_xZn_{1-x}O$ as a II-VI widegap semiconductor alloy. *Applied Physics Letters* **72**, 2466-2468 (1998).

41. D.J. Cohen, K.C. Ruthe, and S.A. Barnett: Transparent conducting $Zn_{1-x}Mg_xO$:(Al,In) thin films. *Journal of Applied Physics* **96**, 459-467 (2004).

42. K. Ellmer and G. Vollweiler: Electrical transport parameters of heavily-doped zinc oxide and zinc magnesium oxide single and multilayer films heteroepitaxially grown on oxide single crystals. *Thin Solid Films* **496**, 104-111 (2006).

43. T. Glatzel, D.F. Marron, T. Schedel-Niedrig, S. Sadewasser, and M.C. Lux-Steiner: $CuGaSe_2$ solar cell cross section studied by Kelvin probe force microscopy in ultrahigh vacuum. *Applied Physics Letters* **81**, 2017-2019 (2002).

44. T.D. Kang, H. Lee, W.I. Park, and G.C. Yi: Ellipsometry on uniaxial ZnO and $Zn_{1-x}Mg_xO$ thin films grown on (0001) sapphire substrate. *Thin Solid Films* **455**, 609-614 (2004).

45. K. Matsubara, H. Tampo, H. Shibata, A. Yamada, P. Fons, K. Iwata, and S. Niki: Band-gap modified Al-doped $Zn_{1-x}Mg_xO$ transparent conducting films deposited by pulsed laser deposition. *Applied Physics Letters* **85**, 1374-1376 (2004).

46. S. Muthukumar, J. Zhong, Y. Chen, Y. Lu, and T. Siegrist: Growth and structural analysis of metalorganic chemical vapor deposited (11-20) $Mg_xZn_{1-x}O$ ($0 < x < 0.33$) films on (01-12) r-plane Al_2O_3 substrates. *Applied Physics Letters* **82**, 742-744 (2003).

47. R. Schmidt-Grund, M. Schubert, B. Rheinlander, D. Fritsch, H. Schmidt, E.M. Kaidashev, M. Lorenz, C.M. Herzinger, and M. Grundmann: UV-VUV spectroscopic ellipsometry of ternary $Mg_xZn_{1-x}O$ ($0 <= x <= 0.53$) thin films. *Thin Solid Films* **455**, 500-504 (2004).

48. C.W. Teng, J.F. Muth, U. Ozgur, M.J. Bergmann, H.O. Everitt, A.K. Sharma, C. Jin, and J. Narayan: Refractive indices and absorption coefficients of $Mg_xZn_{1-x}O$ alloys. *Applied Physics Letters* **76**, 979-981 (2000).

49. C.X. Wu, Y.M. Lu, D.Z. Shen, and X.W. Fan: Effect of Mg content on the structural and optical properties of $Mg_xZn_{1-x}O$ alloys. *Chinese Science Bulletin* **55**, 90-93 (2010).

50. K. Seeger: Semiconductor Physics, An Introduction (Springer, Berlin, 1991).

51. P. Kireev: Semiconductor Physics (MIR Publishers, Moscow, 1978).

52. B. Askerov: Electron Transport Phenomena in Semiconductors (World Scientific Publishing, Singapore, 1985).

53. N. Ashcroft and D. Mermin: Festkörperphysik (Oldenbourg Wissenschaftsverlag, München, 2007).

54. D. Kleppinger and F. Lindholm: Impurity Concentration Dependence of Density of States in Semiconductors. *Solid-State Electronics* **14**, 199-206 (1971).

55. T.N. Morgan: Broadening of Impurity Bands in Heavily Doped Semiconductors. *Physical Review* **139**, A343-A348 (1965).

56. W. Kuzmicz: Ionization of Impurities in Silicon. *Solid-State Electronics* **29**, 1223-1227 (1986).

57. G.L. Pearson and J. Bardeen: Electrical Properties of Pure Silicon and Silicon Alloys Containing Boron and Phosphorus. *Physical Review* **75**, 865-883 (1949).

58. P.P. Debye and E.M. Conwell: Electrical Properties of N-Type Germanium. *Physical Review* **93**, 693-706 (1954).

59. K.I. Hagemark and L.C. Chacka: Electrical Transport Properties of Zn Doped ZnO. *Journal of Solid State Chemistry* **15**, 261-270 (1975).

60. A.R. Hutson: Hall Effect Studies of Doped Zinc Oxide Single Crystals. *Physical Review* **108**, 222-230 (1957).

61. J.S. Blakemore: The Parameters of Partially Degenerate Semiconductors. *Proceedings of the Physical Society of London Section A* **65**, 460-461 (1952).

62. J.S. Blakemore: Approximations for Fermi-Dirac Integrals, Especially the Function $F_{1/2}$(Eta) used to Describe Electron-Density in a Semiconductor. *Solid-State Electronics* **25**, 1067-1076 (1982).

63. N.G. Nilsson: An Accurate Approximation of the Gerenalized Einstein Relation for Degenerate Semiconductors. *Physica Status Solidi A* **19**, K75-K78 (1973).

64. N.G. Nilsson: Empirical approximations for the Fermi energy in a semiconductor with parabolic bands. *Applied Physics Letters* **33**, 653-654 (1978).

65. S. Kasap, C. Koughia, H. Ruda, and R. Johanson: Electrical Conduction in Metals and Semiconductors, in Handbook of Electronic and Photonic Materials, edited by S. Kasap and P. Capper (Springer, Berlin, 2006), pp. 19-45.

66. D. Look: Electrical Characterization of GaAs Materials and Devices, in Design and Measurement in Electronic Engineering, edited by D. Morgan and H. Grubin (John Wiley & Sons, Chichester, 1989), pp. 1-279.

67. T.C. Damen, S.P.S. Porto, and B. Tell: Raman Effect in Zinc Oxide. *Physical Review* **142**, 570-574 (1966).

68. J. Bardeen and W. Shockley: Deformation Potentials and Mobilities in Non-Polar Crystals. *Physical Review* **80**, 72-80 (1950).

69. D.C. Look, R.C. Scott, K.D. Leedy, and B. Bayraktaroglu: Donor and acceptor concentrations from a single mobility measurement in degenerate semiconductors: ZnO. *Oxide-Based Materials and Devices II* **7940**, 794003 (2011).

70. J.D. Zook: Piezoelectric Scattering in Semiconductors. *Physical Review A* **136**, A869-A878 (1964).

71. D. Rode: Low-Field Electron Transport, in Semiconductors and Semimetals, edited by R. Willardson and A. Beer (Academic Press, New York, 1975), pp. 1-89.

72. P. Wagner and R. Helbig: Halleffekt und Anisotropie der Beweglichkeit der Elektronen in ZnO. *Journal of Physics and Chemistry of Solids* **35**, 327-335 (1974).

73. E. Conwell and V.F. Weisskopf: Theory of Impurity Scattering in Semiconductors. *Physical Review* **77**, 388-390 (1950).

74. H. Brooks: Theroy of the Electrical Properties of Germanium and Silicon. *Advances in Electronics and Electron Physics* **7**, 85-182 (1955).

75. D. Chattopadhyay and H.J. Queisser: Electron-Scattering by Ionized Impurities in Semiconductors. *Reviews of Modern Physics* **53**, 745-768 (1981).

76. W. Shockley: Electrons and Holes in Semiconductors (van Nostrand, Toronto, 1950).

77. R.B. Dingle: Scattering of Electrons and Holes by Charged Donors and Acceptors in Semiconductors. *Philosophical Magazine* **46**, 831-840 (1955).

78. W. Zawadzki: Mechanisms of Electron Scattering in Semiconductors, in Handbook on Semiconductors, edited by T. Moss (North-Holland, Amsterdam, 1982), pp. 713-803.

79. T. Pisarkiewicz, K. Zakrzewska, and E. Leja: Scattering of Charge-Carriers in Transparent and Conducting Thin Oxide-Films with a Non-Parabolic Conduction-Band. *Thin Solid Films* **174**, 217-223 (1989).

80. K. Zakrzewska, T. Pisarkiewicz, and A. Czapla: Scattering of Charge-Carriers in Reactively Sputtered $CdIn_2O_4$ Thin-Films. *Physica Status Solidi A* **99**, 141-149 (1987).

81. D.C. Look, C.E. Stutz, R.J. Molnar, K. Saarinen, and Z. Liliental-Weber: Dislocation-independent mobility in lattice-mismatched epitaxy: application to GaN. *Solid State Communications* **117**, 571-575 (2001).

82. D.B.M. Klaassen: A Unified Mobility Model for Device Simulation. 1. Model-Equations and Concentration-Dependence. *Solid-State Electronics* **35**, 953-959 (1992).

83. J.Y.W. Seto: Electrical Properties of Polycrystalline Silicon Films. *Journal of Applied Physics* **46**, 5247-5254 (1975).

84. R.L. Petritz: Theory of Photoconductivity in Semiconductor Films. *Physical Review* **104**, 1508-1516 (1956).

85. T.I. Kamins: Hall Mobility in Chemically Deposited Polycrystalline Silicon. *Journal of Applied Physics* **42**, 4357-4365 (1971).

86. G. Blatter and F. Greuter: Carrier transport through grain boundaries in semiconductors. *Physical Review B* **33**, 3952-3966 (1986).

87. R. Stratton: Surface Barriers at Semiconductor Contacts. *Proceedings of the Physical Society of London Section B* **69**, 513-527 (1956).

88. G. Baccarani, B. Ricco, and G. Spadini: Transport Properties of Polycrystalline Silicon Films. *Journal of Applied Physics* **49**, 5565-5570 (1978).

89. M.V. Garcia-Cuenca, J.L. Morenza, and J. Esteve: Temperature dependence of intergrain barriers in polycrystalline In-doped CdS films. *Solid-State Electronics* **28**, 1019-1023 (1985).

90. M.V. Garcia-Cuenca, J.L. Morenza, and J.M. Codina: On the Hall effect in polycrystalline semiconductors. *Journal of Applied Physics* **58**, 1080-1082 (1985).

91. R.L. Petritz: Theory of an Experiment for Measuring the Mobility and Density of Carriers in the Space-Charge Region of a Semiconductor Surface. *Physical Review* **110**, 1254-1262 (1958).

92. J. Volger: Note on the Hall Potential across an Inhomogeneous Conductor. *Physical Review* **79**, 1023-1024 (1950).

93. M.V. Garcia-Cuenca and J.L. Morenza: On the electrical conductivity of polycrystalline CdS films. *Journal of Physics D - Applied Physics* **18**, 2081-2086 (1985).

94. M.V. Garcia-Cuenca, J.L. Morenza, and J.M. Codina: Electrical conduction in polycrystalline CdS films. I. Theory. *Journal of Physics D - Applied Physics* **20**, 951-957 (1987).

95. I. Sieber, N. Wanderka, I. Urban, I. Dorfel, E. Schierhorn, F. Fenske, and W. Fuhs: Electron microscopic characterization of reactively sputtered ZnO films with different Al-doping levels. *Thin Solid Films* **330**, 108-113 (1998).

96. J.P. Gambino, W.D. Kingery, G.E. Pike, H.R. Philipp, and L.M. Levinson: Grain-Boundary Electronic States in Some Simple ZnO Varistors. *Journal of Applied Physics* **61**, 2571-2574 (1987).

97. T. Weis, R. Lipperheide, U. Wille, and S. Brehme: Barrier-controlled carrier transport in microcrystalline semiconducting materials: Description within a unified model. *Journal of Applied Physics* **92**, 1411-1418 (2002).

98. L. Nordheim: Zur Elektronentheorie der Metalle II. *Annalen der Physik* **401**, 641-678 (1931).

99. L. Makowski and M. Glicksma: Disorder Scattering in Solid-Solutions of III-V Semiconducting Compounds. *Journal of Physics and Chemistry of Solids* **34**, 487-492 (1973).

100. J.J. Tietjen and L.R. Weisberg: Electron Mobility in $GaAs_{1-x}P_x$ Alloys. *Applied Physics Letters* **7**, 261-263 (1965).

101. D.C. Look, D.K. Lorance, J.R. Sizelove, C.E. Stutz, K.R. Evans, and D.W. Whitson: Alloy Scattering in p-Type $Al_xGa_{1-x}As$. *Journal of Applied Physics* **71**, 260-266 (1992).

102. Collaboration: Authors and editors of the volumes III/17B-22A-41B: Magnesium oxide (MgO) Debye temperature, heat capacity, density, melting and boiling points, hardness, in SpringerMaterials - The Landolt-Börnstein Database (http://www.springermaterials.com), edited by O. Madelung, U. Rössler and M. Schulz, DOI: 10.1007/10681719_215.

103. Y.N. Xu and W.Y. Ching: Self-consistent band structures, charge distributions, and optical-absorption spectra in MgO, Alpha-Al_2O_3, and $MgAl_2O_4$. *Physical Review B* **43**, 4461-4472 (1991).

104. J. Robertson, K. Xiong, and S.J. Clark: Band gaps and defect levels in functional oxides. *Thin Solid Films* **496**, 1-7 (2006).

105. J.W. Harrison and J.R. Hauser: Alloy scattering in ternary III-V compounds. *Physical Review B* **13**, 5347-5350 (1976).

106. J. Kossut: Disorder Scattering in Zincblende Narrow-Gap Semiconducting Mixed-Crystals. *Physica Status Solidi B* **86**, 593-601 (1978).

107. A. Sasaki: Theory for Electron-Mobility in Ternary Mixed Semiconductors. *Japanese Journal of Applied Physics* **17**, 161-166 (1978).

108. A.K. Saxena: Electron-Mobility in $Ga_{1-x}Al_xAs$ Alloys. *Physical Review B* **24**, 3295-3302 (1981).

109. F. Osaka, T. Mikawa, and O. Wada: Effect of Alloy Scattering on Electron and Hole Impact Ionization Rates in $Ga_{1-x}In_xAs_yP_{1-y}$ Alloy System. *Japanese Journal of Applied Physics Part 1* **25**, 568-574 (1986).

110. B. Pödör: Electron Mobility in Plastically Deformed Germanium. *Physica Status Solidi* **16**, K167-K170 (1966).

111. K. Ellmer: Magnetron Discharges for Thin Film Deposition, in Low Temperature Plasmas. Fundamentals, Technologies, and Techniques, edited by R. Hippler, H. Kersten, M. Schmidt and K. Schoenbach (Wiley-VCH, Weinheim, 2008), pp. 675-692.

112. F. Penning: Die Glimmentladung bei niedrigem Druck zwischen koaxialen Zylindern in einem axialen Magnetfeld. *Physica* **3**, 873-894 (1936).

113. K. Ellmer: Magnetron sputtering of transparent conductive zinc oxide: relation between the sputtering parameters and the electronic properties. *Journal of Physics D - Applied Physics* **33**, R17-R32 (2000).

114. B. Szyszka: Magnetron Sputtering of ZnO Films, in Transparent Conductive Zinc Oxide: Basics and Applications in Thin Film Solar Cells, edited by K. Ellmer, A. Klein and B. Rech (Springer, Berlin, 2008), pp. 187-233.

115. J. Vossen and J. Cuomo: Glow Discharge Sputter Deposition, in Thin Film Processes, edited by J. Vossen and W. Kern (Academic Press, San Diego, 1978), pp. 11-73.

116. R. Waits: Planar Magnetron Sputtering, in Thin Film Processes, edited by J. Vossen and W. Kern (Academic Press, San Diego, 1978), pp. 131-173.

117. S. Seeger: Herstellung und Charakterisierung der Schichtgittersulfide MoS_2 und WS_2 für photovoltaische Anwendungen. Dissertation (Technische Universtität Berlin, Berlin, 2006).

118. J.A. Thornton: The Microstructure of Sputter-Deposited Coatings. *Journal of Vacuum Science and Technology A* **4**, 3059-3065 (1986).

119. J.A. Thornton: High-Rate Thick-Film Growth. *Annual Review of Materials Science* **7**, 239-260 (1977).

120. K. Ellmer and T. Welzel: Reactive magnetron sputtering of transparent conductive oxide thin films: Role of energetic particle (ion) bombardment. *Journal of Materials Research* **27**, 765-779 (2012).

121. A. Goetzberger and V. Hoffmann: Photovoltaic Solar Energy Generation (Springer, Berlin, 2005).

122. A. Goetzberger, B. Voß, and J. Knobloch: Sonnenenergie: Photovoltaik (B.G. Teubner, Stuttgart, 1994).

123. R. Scheer and H. Schock: Chalcogenide Photovoltaics. Physics, Technologies, and Thin Film Devices (Wiley-VCH, Weinheim, 2011).

124. S. Siebentritt and U. Rau: Wide-Gap Chalcopyrites (Springer, Berlin, 2006).

125. A. Becquerel: Memoire sur les effects d'electriques produits sous l'influence des rayons solaires. *Comptes Rendus de L'Academie des Sciences* **9**, 561-567 (1839).

126. W. Shockley and H.J. Queisser: Detailed Balance Limit of Efficiency of p-n Junction Solar Cells. *Journal of Applied Physics* **32**, 510-519 (1961).

127. H. Hahn, G. Frank, W. Klingler, A.D. Meyer, and G. Storger: Untersuchungen über ternäre Chalkogenide. 5. Über einige ternare Chalkogenide mit chalkopyritstruktur. *Zeitschrift für anorganische und allgemeine Chemie* **271**, 153-170 (1953).

128. A. Goetzberger, C. Hebling, and H.W. Schock: Photovoltaic materials, history, status and outlook. *Materials Science and Engineering R* **40**, 1-46 (2003).

129. J. Schulte: personal communication (Berlin, 2011).

130. P. Jackson, D. Hariskos, E. Lotter, S. Paetel, R. Wuerz, R. Menner, W. Wischmann, and M. Powalla: New world record efficiency for $Cu(In,Ga)Se_2$ thin-film solar cells beyond 20%. *Progress in Photovoltaics* **19**, 894-897 (2011).

131. A. Yamada, K. Matsubara, K. Sakurai, S. Ishizuka, H. Tampo, P.J. Fons, K. Iwata, and S. Niki: Effect of band offset on the open circuit voltage of heterojunction $CuIn_{1-x}Ga_xSe_2$ solar cells. *Applied Physics Letters* **85**, 5607-5609 (2004).

132. M. Gloeckler and J.R. Sites: Efficiency limitations for wide-band-gap chalcopyrite solar cells. *Thin Solid Films* **480**, 241-245 (2005).

133. T. Minemoto, Y. Hashimoto, T. Satoh, T. Negami, H. Takakura, and Y. Hamakawa: $Cu(In,Ga)Se_2$ solar cells with controlled conduction band offset of window/$Cu(In,Ga)Se_2$ layers. *Journal of Applied Physics* **89**, 8327-8330 (2001).

134. Schott Technical Glass Solutions GmbH: BOROFLOAT 33 Borosilikatglas. Product information (Jena, 2013).

135. L. van der Pauw: A Method of Measuring Specific Resistivity and Hall Effect of Discs of Arbitrary Shape. *Philips Research Reports* **13**, 1-9 (1958).

136. H.J. Juretschke, R. Landauer, and J.A. Swanson: Hall Effect and Conductivity in Porous Media. *Journal of Applied Physics* **27**, 838-839 (1956).

137. H.H. Wieder: Electrical and Galvanomagnetic Measurements on Thin-Films and Epilayers. *Thin Solid Films* **31**, 123-138 (1976).

138. K. Ellmer: Hall Effect and Conductivity Measurements in Semiconductor Crystals and Thin Films, in Characterization of Materials, edited by E. Kaufmann (John Wiley & Sons, Hoboken, 2012), pp. 564-579.

139. C. Bundesmann, R. Schmidt-Grund, and M. Schubert: Optical Properties of ZnO and Related Compounds, in Transparent Conductive Zinc Oxide, edited by K. Ellmer, A. Klein and B. Rech (Springer, Berlin, 2008), pp. 79-124.

140. M. Schubert, T. Hofmann, B. Rheinlander, I. Pietzonka, T. Sass, V. Gottschalch, and J.A. Woollam: Near-band-gap CuPt-order-induced birefringence in $Al_{0.48}Ga_{0.52}InP_2$. *Physical Review B* **60**, 16618-16634 (1999).

141. H. Mayer: Physik Dünner Schichten (Wissenschaftliche Verlagsgesellschaft, Stuttgart, 1950).

142. H. Klug and L. Alexander: X-ray Diffraction Procedures (John Wiley & Sons, New York, 1974).

143. P. Thompson, D.E. Cox, and J.B. Hastings: Rietveld Refinement of Debye-Scherrer Synchrotron X-Ray Data from Al_2O_3. *Journal of Applied Crystallography* **20**, 79-83 (1987).

144. T. Ida: New measures of sharpness for symmetric powder diffraction peak profiles. *Journal of Applied Crystallography* **41**, 393-401 (2008).

145. P. Scherrer: Bestimmung der Grösse und der inneren Struktur von Kolloidteilchen mittels Röntgenstrahlen. *Nachrichten von der Gesellschaft der Wissenschaften zu Göttingen* **2**, 98-100 (1918).

146. J.I. Langford and A.J.C. Wilson: Scherrer after 60 Years - Survey and Some New Results in Determination of Crystallite Size. *Journal of Applied Crystallography* **11**, 102-113 (1978).

147. T.D. Keijser, J. Langford, E. Mittemeijer, and A. Vogels: Use of the Voigt Function in a Single-Line Method for the Analysis of X-ray Diffraction Line Broadening. *Journal of Applied Crystallography* **15**, 308-314 (1982).

148. J. Rodriguez-Carvajal: FULLPROF: A Program for Rietveld Refinement and Pattern Matching Analysis, in Abstracts of the Satellite Meeting on Powder Diffraction of the XV Congress of the IUCr (Toulouse, France, 1990), p. 127.

149. H. Bethge and J. Heydenreich (editors): Electron Microscopy in Solid State Physics (Elsevier, Amsterdam, 1982).

150. Carl Zeiss Microscopy GmbH: In-Column EFTEM Technology with Corrected OMEGA Filter. Product information (Jena, 2012).

151. D. Koningsberger and R. Prins: X-Ray Absorption: Principles, Applications, Techniques of EXAFS, SEXAFS and XANES (John Wiley & Sons, New York, 1988).

152. J.J. Rehr and R.C. Albers: Theoretical approaches to x-ray absorption fine structure. *Reviews of Modern Physics* **72**, 621-654 (2000).

153. A. Thompson (editor): X-Ray Data Booklet (Lawrence Berkeley National Laboratory, Berkeley, 2009).

154. T. Tsong: The Atomic Structure and Atomic Layer Compositional Analysis of Thin Solid Films Using the Time-of-Flight Atom-Probe Field Ion Microscopy, in Analytical Techniques For Thin Films, edited by H. Herman (Academic Press, London, 1988), pp. 449-478.

155. R. Schlesiger, C. Oberdorfer, R. Wurz, G. Greiwe, P. Stender, M. Artmeier, P. Pelka, F. Spaleck, and G. Schmitz: Design of a laser-assisted tomographic atom probe at Münster University. *Review of Scientific Instruments* **81**, 043703 (2010).

156. G. Friedbacher: Atomic Force Microscopy (AFM), in Surface and Thin Film Analysis, edited by H. Bubert and H. Jenett (Wiley-VCH, Weinheim, 2002), pp. 277-284.

157. F.J. Giessibl: Advances in atomic force microscopy. *Reviews of Modern Physics* **75**, 949-983 (2003).

158. T. Finstad and W. Chu: Rutherford Backscattering Spectrometry on Thin Solid Films, in Analytical Techniques for Thin Films, edited by K. Tu and R. Rosenberg (Academic Press, London, 1988), pp. 391-448.

159. H. Bubert and H. Jenett (editors): Surface and Thin Film Analysis (Wiley-VCH, Weinheim, 2002).

160. T. Welzel and K. Ellmer: Negative oxygen ion formation in reactive magnetron sputtering processes for transparent conductive oxides. *Journal of Vacuum Science and Technology A* **30**, 061306 (2012).

161. N. Takahashi, K. Kaiya, K. Omichi, T. Nakamura, S. Okamoto, and H. Yamamoto: Atmospheric pressure vapor-phase growth of ZnO using a chloride source. *Journal of Crystal Growth* **209**, 822-827 (2000).

162. R. Ayouchi, F. Martin, D. Leinen, and J.R. Ramos-Barrado: Growth of pure ZnO thin films prepared by chemical spray pyrolysis on silicon. *Journal of Crystal Growth* **247**, 497-504 (2003).

163. A. Anders, S.H.N. Lim, K.M. Yu, J. Andersson, J. Rosen, M. McFarland, and J. Brown: High quality ZnO:Al transparent conducting oxide films synthesized by pulsed filtered cathodic arc deposition. *Thin Solid Films* **518**, 3313-3319 (2010).

164. M. Lorenz, G. Wagner, A. Rahm, H. Schmidt, H. Hochmuth, H. Schmid, W. Mader, M. Brandt, H. von Wenckstern, and M. Grundmann: Homoepitaxial ZnO thin films by PLD: Structural properties. *Physica Status Solidi C* **5**, 3280-3287 (2008).

165. P. Kuppusami, G. Vollweiler, D. Rafaja, and K. Ellmer: Epitaxial growth of aluminium-doped zinc oxide films by magnetron sputtering on (001), (110), and (012) oriented sapphire substrates. *Applied Physics A* **80**, 183-186 (2005).

166. K. Tominaga, T. Yuasa, M. Kume, and O. Tada: Influence of Energetic Oxygen Bombardment on Conductive ZnO Films. *Japanese Journal of Applied Physics Part 1* **24**, 944-949 (1985).

167. R. Das, K. Adhikary, and S. Ray: Comparison of electrical, optical, and structural properties of RF-sputtered ZnO thin films deposited under different gas ambients. *Japanese Journal of Applied Physics* **47**, 1501-1506 (2008).

168. O. Kluth, G. Schope, B. Rech, R. Menner, M. Oertel, K. Orgassa, and H.W. Schock: Comparative material study on RF and DC magnetron sputtered ZnO:Al films. *Thin Solid Films* **502**, 311-316 (2006).

169. T. Minami, T. Miyata, and Y. Ohtani: Optimization of aluminum-doped ZnO thin-film deposition by magnetron sputtering for liquid crystal display applications. *Physica Status Solidi A* **204**, 3145-3151 (2007).

170. S. Fay and A. Shah: Zinc Oxide Grown by CVD Process as Transparent Contact for Thin Film Solar Cell Applications, in Transparent Conductive Zinc Oxide: Basics and Applications in Thin Film Solar Cells, edited by K. Ellmer, A. Klein and B. Rech (Springer, Berlin, 2008), pp. 235-302.

171. J.A. Thornton: Influence of Apparatus Geometry and Deposition Conditions on Structure and Topography of Thick Sputtered Coatings. *Journal of Vacuum Science and Technology* **11**, 666-670 (1974).

172. H. Windischmann: Intrinsic Stress in Sputter-Deposited Thin-Films. *Critical Reviews in Solid State and Materials Sciences* **17**, 547-596 (1992).

173. K. Tominaga, N. Ueshiba, Y. Shintani, and O. Tada: High-Energy Neutral Atoms in the Sputtering of ZnO. *Japanese Journal of Applied Physics* **20**, 519-526 (1981).

174. R. Dinnebier and S. Billinge: Principles of Powder Diffraction, in Powder Diffraction Theory and Practice, edited by R. Dinnebier and S. Billinge (The Royal Society of Chemistry, Cambridge, 2008).

175. J.E. Ayers: The Measurement of Threading Dislocation Densities in Semiconductor Crystals by X-Ray-Diffraction. *Journal of Crystal Growth* **135**, 71-77 (1994).

176. T. Metzger, R. Hopler, E. Born, O. Ambacher, M. Stutzmann, R. Stommer, M. Schuster, H. Gobel, S. Christiansen, M. Albrecht, and H.P. Strunk: Defect structure of epitaxial GaN films determined by transmission electron microscopy and triple-axis X-ray diffractometry. *Philosophical Magazine A* **77**, 1013-1025 (1998).

177. Z. Chine, A. Rebey, H. Toluati, E. Goovaerts, M. Oueslati, B. El Jani, and S. Laugt: Stress and density of defects in Si-doped GaN. *Physica Status Solidi A* **203**, 1954-1961 (2006).

178. L. Sagalowicz and G.R. Fox: Planar defects in ZnO thin films deposited on optical fibers and flat substrates. *Journal of Materials Research* **14**, 1876-1885 (1999).

179. P.A. Fedders, D.A. Drabold, and S. Nakhmanson: Theoretical study on the nature of band-tail states in amorphous Si. *Physical Review B* **58**, 15624-15631 (1998).

180. J. Mattheis, U. Rau, and J.H. Werner: Light absorption and emission in semiconductors with band gap fluctuations - A study on Cu(In,Ga)Se_2 thin films. *Journal of Applied Physics* **101**, 113519 (2007).

181. F. Urbach: The Long-Wavelength Edge of Photographic Sensitivity and of the Electronic Absorption of Solids. *Physical Review* **92**, 1324-1324 (1953).

182. S. John, C. Soukoulis, M.H. Cohen, and E.N. Economou: Theory of Electron Band Tails and the Urbach Optical-Absorption Edge. *Physical Review Letters* **57**, 1777-1780 (1986).

183. V. Srikant and D.R. Clarke: Optical absorption edge of ZnO thin films: The effect of substrate. *Journal of Applied Physics* **81**, 6357-6364 (1997).

184. D. Dimova-Malinovska, O. Angelov, H. Nichev, M. Kamenova, and J.C. Pivin: Influence of the substrate temperature on the optical and structural properties of magnetron sputtered ZnO thin films doped with Al and Er. *Journal of Optoelectronics and Advanced Materials* **9**, 2512-2515 (2007).

185. G.A. Rozgonyi and W.J. Polito: Epitaxial Thin Films of ZnO on CdS and Sapphire. *Journal of Vacuum Science and Technology* **6**, 115-119 (1969).

186. A. Redondo-Cubero, M. Vinnichenko, M. Krause, A. Mucklich, E. Munoz, A. Kolitsch, and R. Gago: Sublattice-specific ordering of ZnO layers during the heteroepitaxial growth at different temperatures. *Journal of Applied Physics* **110**, 113516 (2011).

187. K. Matsubara, P. Fons, A. Yamada, M. Watanabe, and S. Niki: Epitaxial growth of ZnO thin films on $LiNbO_3$ substrates. *Thin Solid Films* **347**, 238-240 (1999).

188. J. Owen: Growth, Etching, and Stability of Sputtered ZnO:Al for Thin-Film Silicon Solar Cells. Dissertation (Rheinisch-Westfälische Technische Hochschule Aachen, Aachen, 2011).

189. R. Triboulet and J. Perriere: Epitaxial growth of ZnO films. *Progress in Crystal Growth and Characterization of Materials* **47**, 65-138 (2003).

190. F.C. Frank and J.H. van der Merwe: One-Dimensional Dislocations. 2. Misfitting Monolayers and Oriented Overgrowth. *Proceedings of the Royal Society of London Series A* **198**, 216-225 (1949).

191. F.C. Frank and J.H. van der Merwe: One-Dimensional Dislocations. 1. Static Theory. *Proceedings of the Royal Society of London Series A* **198**, 205-216 (1949).

192. R. Cebulla, R. Wendt, and K. Ellmer: Al-doped zinc oxide films deposited by simultaneous rf and dc excitation of a magnetron plasma: Relationships between plasma parameters and structural and electrical film properties. *Journal of Applied Physics* **83**, 1087-1095 (1998).

193. P. Fons, K. Iwata, A. Yamada, K. Matsubara, S. Niki, K. Nakahara, T. Tanabe, and H. Takasu: Uniaxial locked epitaxy of ZnO on the a face of sapphire. *Applied Physics Letters* **77**, 1801-1803 (2000).

194. C.R. Gorla, N.W. Emanetoglu, S. Liang, W.E. Mayo, Y. Lu, M. Wraback, and H. Shen: Structural, optical, and surface acoustic wave properties of epitaxial ZnO films grown on (01-12) sapphire by metalorganic chemical vapor deposition. *Journal of Applied Physics* **85**, 2595-2602 (1999).

195. K. Nakahara, H. Takasu, P. Fons, K. Iwata, A. Yamada, K. Matsubara, R. Hunger, and S. Niki: Growth and characterization of undoped ZnO films for single crystal based device use by radical source molecular beam epitaxy (RS-MBE). *Journal of Crystal Growth* **227**, 923-928 (2001).

196. M. Lorenz, E.M. Kaidashev, H. von Wenckstern, V. Riede, C. Bundesmann, D. Spemann, G. Benndorf, H. Hochmuth, A. Rahm, H.C. Semmelhack, and M. Grundmann: Optical and electrical properties of epitaxial $(Mg,Cd)_xZn_{1-x}O$, ZnO, and ZnO:(Ga,Al) thin films on c-plane sapphire grown by pulsed laser deposition. *Solid-State Electronics* **47**, 2205-2209 (2003).

197. A. Lajn, H. von Wenckstern, G. Benndorf, C.P. Dietrich, M. Brandt, G. Biehne, H. Hochmuth, M. Lorenz, and M. Grundmann: Shallow Donors and Compensation in Homoepitaxial ZnO Thin Films. *Journal of Electronic Materials* **39**, 595-600 (2010).

198. M. Lorenz, M. Brandt, M. Lange, G. Benndorf, H. von Wenckstern, D. Klimm, and M. Grundmann: Homoepitaxial $Mg_xZn_{1-x}O$ ($0 <= x <= 0.22$) thin films grown by pulsed laser deposition. *Thin Solid Films* **518**, 4623-4629 (2010).

199. S.H. Park, T. Minegishi, H.J. Lee, D.C. Oh, H.J. Ko, J.H. Chang, and T. Yao: Growth mechanism of ZnO low-temperature homoepitaxy. *Journal of Applied Physics* **110**, 053520 (2011).

200. W. Pies and A. Weiss: b108, II.1.1 Simple oxides, in Landolt-Börnstein - Group III: Crystal and Solid State Physics, Numerical Data and Functional Relationships in Science and Technology, edited by K. Hellwege and A. Hellwege (Springer, Berlin, 1975), p. 40.

201. T. Yamashita, R. Hansson, and P.C. Hayes: The relationships between microstructure and crystal structure in zincite solid solutions. *Journal of Materials Science* **41**, 5559-5568 (2006).

202. W. Wei, C.M. Jin, J. Narayan, and R.J. Narayan: Optical and electrical properties of gallium-doped $Mg_xZn_{1-x}O$. *Journal of Applied Physics* **107**, 013510 (2010).

203. G. Masetti, M. Severi, and S. Solmi: Modeling of Carrier Mobility against Carrier Concentration in Arsenic-Doped, Phosphorus-Doped, and Boron-Doped Silicon. *IEEE Transactions on Electron Devices* **30**, 764-769 (1983).

204. K. Ellmer: Resistivity of polycrystalline zinc oxide films: current status and physical limit. *Journal of Physics D - Applied Physics* **34**, 3097-3108 (2001).

205. F. Mousty, P. Ostoja, and L. Passari: Relationship between Resistivity and Phosphorus Concentration in Silicon. *Journal of Applied Physics* **45**, 4576-4580 (1974).

206. G. Baccarani and P. Ostoja: Electron-Mobility Empirically Related to Phosphorus Concentration in Silicon. *Solid-State Electronics* **18**, 579-580 (1975).

207. W.R. Thurber, R.L. Mattis, Y.M. Liu, and J.J. Filliben: Resistivity-Dopant Density Relationship for Phosphorus-Doped Silicon. *Journal of the Electrochemical Society* **127**, 1807-1812 (1980).

208. W.R. Thurber, R.L. Mattis, Y.M. Liu, and J.J. Filliben: Resistivity-Dopant Density Relationship for Boron-Doped Silicon. *Journal of the Electrochemical Society* **127**, 2291-2294 (1980).

209. H.D. Chen, M.S. Feng, K.C. Lin, P.A. Chen, C.C. Wu, and J.W. Wu: Anomalous Mobility Enhancement in Heavily Carbon-Doped GaAs. *Journal of Applied Physics* **75**, 5453-5455 (1994).

210. G. Impellizzeri, S. Mirabella, A. Irrera, M.G. Grimaldi, and E. Napolitani: Ga-implantation in Ge: Electrical activation and clustering. *Journal of Applied Physics* **106**, 013518 (2009).

211. F.J. Morin: Lattice-Scattering Mobility in Germanium. *Physical Review* **93**, 62-63 (1954).

212. B. Pödör and N. Nádor: The Lattice Limited Mobility of Electrons in GaAs. *Acta Physica Academiae Scientiarum Hungaricae* **37**, 317-328 (1974).

213. R. Scholz: Stationary lattice mobility of holes in gallium arsenide. *Journal of Applied Physics* **77**, 3232-3242 (1995).

214. D.L. Rode: Electron mobility in II-VI semiconductors. *Physical Review B* **2**, 4036-4044 (1970).

215. S. Sze: Physics of Semiconductor Devices (John Wiley & Sons, New York, 1981).

216. Collaboration: Authors and editors of the volumes III/17B-22A-41B: Zinc oxide (ZnO) electron effective masses, in SpringerMaterials - The Landolt-Börnstein Database (http://www.springermaterials.com), edited by O. Madelung, U. Rössler and M. Schulz, DOI: 10.1007/10681719_268.

217. Collaboration: Authors and editors of the volumes III/17B-22A-41B: Zinc oxide (ZnO) hole effective masses, g-factors, in SpringerMaterials - The Landolt-Börnstein Database (http://www.springermaterials.com), edited by O. Madelung, U. Rössler and M. Schulz, DOI: 10.1007/10681719_269.

218. D. Vasileska-Kafedziska and S. Goodnick: Computational Electronics, in Synthesis Lectures on Computational Electromagnetics, edited by C. Balanis (Morgan & Claypool, USA, 2006), p. 16.

219. Collaboration: Authors and Editors of the LB Volumes III/17A-22A-41A1b: Silicon (Si), reflectance, dielectric constants, in SpringerMaterials - The Landolt-Börnstein Database (http://www.springermaterials.com), edited by O. Madelung, U. Rössler and M. Schulz, DOI: 10.1007/10832182_469.

220. Collaboration: Authors and Editors of the LB Volumes III/17A-22A-41A1b: Germanium (Ge), dielectric constant, in SpringerMaterials - The Landolt-Börnstein Database (http://www.springermaterials.com), edited by O. Madelung, U. Rössler and M. Schulz, DOI: 10.1007/10832182_519.

221. Collaboration: Authors and editors of the volumes III/17A-22A-41A1a: Gallium arsenide (GaAs) dielectric constants, in SpringerMaterials - The Landolt-Börnstein Database (http://www.springermaterials.com), edited by O. Madelung, U. Rössler and M. Schulz, DOI: 10.1007/10551045_113.

222. Collaboration: Authors and editors of the volumes III/17B-22A-41B: Zinc oxide (ZnO) dielectric constants, in SpringerMaterials - The Landolt-Börnstein Database (http://www.springermaterials.com), edited by O. Madelung, U. Rössler and M. Schulz, DOI: 10.1007/10681719_307.

223. M. Berginski, J. Hupkes, M. Schulte, G. Schope, H. Stiebig, B. Rech, and M. Wuttig: The effect of front ZnO:Al surface texture and optical transparency on efficient light trapping in silicon thin-film solar cells. *Journal of Applied Physics* **101**, 074903 (2007).

224. C. Charpentier, P. Prod'homme, and P.R.I. Cabarrocas: Microstructural, optical and electrical properties of annealed ZnO:Al thin films. *Thin Solid Films* **531**, 424-429 (2013).

225. S. Cornelius, M. Vinnichenko, N. Shevchenko, A. Rogozin, A. Kolitsch, and W. Moller: Achieving high free electron mobility in ZnO:Al thin films grown by reactive pulsed magnetron sputtering. *Applied Physics Letters* **94**, 042103 (2009).

226. J.N. Duenow, T.A. Gessert, D.M. Wood, D.L. Young, and T.J. Coutts: Effects of hydrogen content in sputtering ambient on ZnO:Al electrical properties. *Journal of Non-Crystalline Solids* **354**, 2787-2790 (2008).

227. S. Jager, B. Szyszka, J. Szczyrbowski, and G. Brauer: Comparison of transparent conductive oxide thin films prepared by a.c. and d.c. reactive magnetron sputtering. *Surface and Coatings Technology* **98**, 1304-1314 (1998).

228. T. Nakada, Y. Ohkubo, N. Murakami, and A. Kunioka: Transparent Conducting Boron-Doped Zinc-Oxide Films Deposited by DC-Magnetron Sputtering in B_2H_6-Ar Mixtures. *Japanese Journal of Applied Physics Part 1* **34**, 3623-3627 (1995).

229. J. Nomoto, T. Miyata, and T. Minami: Optical and electrical properties of transparent conducting B-doped ZnO thin films prepared by various deposition methods. *Journal of Vacuum Science and Technology A* **29**, 041504 (2011).

230. T. Minami, H. Sato, K. Ohashi, T. Tomofuji, and S. Takata: Conduction Mechanism of Highly Conductive and Transparent Zinc-Oxide Thin-Films Prepared by Magnetron Sputtering. *Journal of Crystal Growth* **117**, 370-374 (1992).

231. A. Suzuki, T. Matsushita, N. Wada, Y. Sakamoto, and M. Okuda: Transparent conducting Al-doped ZnO thin films prepared by pulsed laser deposition. *Japanese Journal of Applied Physics Part 2* **35**, L56-L59 (1996).

232. M. Warzecha, J.I. Owen, M. Wimmer, F. Ruske, J. Hotovy, and J. Hüpkes: High mobility annealing of Transparent Conductive Oxides. *E-MRS 2011 Fall Symposium I: Advances in Transparent Electronics, from Materials to Devices III* **34**, 012004 (2012).

233. T. Yamada, K. Ikeda, S. Kishimoto, H. Makino, and T. Yamamoto: Effects of oxygen partial pressure on doping properties of Ga-doped ZnO films prepared by ion-plating with traveling substrate. *Surface and Coatings Technology* **201**, 4004-4007 (2006).

234. M. Chen, Z.L. Pei, X. Wang, Y.H. Yu, X.H. Liu, C. Sun, and L.S. Wen: Intrinsic limit of electrical properties of transparent conductive oxide films. *Journal of Physics D - Applied Physics* **33**, 2538-2548 (2000).

235. K. Ellmer and R. Mientus: Carrier transport in polycrystalline transparent conductive oxides: A comparative study of zinc oxide and indium oxide. *Thin Solid Films* **516**, 4620-4627 (2008).

236. F. Ruske, M. Roczen, K. Lee, M. Wimmer, S. Gall, J. Hupkes, D. Hrunski, and B. Rech: Improved electrical transport in Al-doped zinc oxide by thermal treatment. *Journal of Applied Physics* **107**, 013708 (2010).

237. K. Nomura, T. Kamiya, H. Ohta, K. Ueda, M. Hirano, and H. Hosono: Carrier transport in transparent oxide semiconductor with intrinsic structural randomness probed using single-crystalline $InGaO_3(ZnO)_5$ films. *Applied Physics Letters* **85**, 1993-1995 (2004).

238. K. Nomura, H. Ohta, A. Takagi, T. Kamiya, M. Hirano, and H. Hosono: Room-temperature fabrication of transparent flexible thin-film transistors using amorphous oxide semiconductors. *Nature* **432**, 488-492 (2004).

239. J. Steinhauser, S. Meyer, M. Schwab, S. Fay, C. Ballif, U. Kroll, and D. Borrello: Humid environment stability of low pressure chemical vapor deposited boron doped zinc oxide used as transparent electrodes in thin film silicon solar cells. *Thin Solid Films* **520**, 558-562 (2011).

240. T. Makino, Y. Segawa, A. Tsukazaki, A. Ohtomo, and M. Kawasaki: Electron transport in ZnO thin films. *Applied Physics Letters* **87**, 022101 (2005).

241. M.W.J. Prins, K.O. Grosse-Holz, J.F.M. Cillessen, and L.F. Feiner: Grain-boundary-limited transport in semiconducting SnO_2 thin films: Model and experiments. *Journal of Applied Physics* **83**, 888-893 (1998).

242. R. Lipperheide, T. Weis, and U. Wille: Generalized Drude model: unification of ballistic and diffusive electron transport. *Journal of Physics - Condensed Matter* **13**, 3347-3363 (2001).

243. Y. Kajikawa, T. Okuzako, S. Takami, and M. Takushima: Electrical properties of polycrystalline GaInAs thin films. *Thin Solid Films* **519**, 136-144 (2010).

244. N. Ashkenov, B.N. Mbenkum, C. Bundesmann, V. Riede, M. Lorenz, D. Spemann, E.M. Kaidashev, A. Kasic, M. Schubert, M. Grundmann, G. Wagner, H. Neumann, V. Darakchieva, H. Arwin, and B. Monemar: Infrared dielectric functions and phonon modes of high-quality ZnO films. *Journal of Applied Physics* **93**, 126-133 (2003).

245. A. Janotti, D. Segev, and C.G. Van de Walle: Effects of cation d states on the structural and electronic properties of III-nitride and II-oxide wide-band-gap semiconductors. *Physical Review B* **74**, 045202 (2006).

246. A. Janotti and C.G. Van de Walle: Absolute deformation potentials and band alignment of wurtzite ZnO, MgO, and CdO. *Physical Review B* **75**, 121201 (2007).

247. S.N. Patra and D.P. Bhattacharya: Piezoelectric interaction in degenerate semiconductors at low lattice temperatures. *Physica B - Condensed Matter* **325**, 17-25 (2003).

248. S. Sahoo, V. Sivasubramanian, S. Dhara, and A.K. Arora: Excitation energy dependence of electron-phonon interaction in ZnO nanoparticles. *Solid State Communications* **147**, 271-273 (2008).

249. C. Solbrig: Das Emissionsspektrum gebundener Excitonen in Zinkoxydkristallen in Abhängigkeit von Temperatur und uniaxialer Verspannung. *Zeitschrift für Physik* **211**, 429-451 (1968).

250. J. Werner: Origin of Curved Arrhenius Plots for the Conductivity of Polycrystalline Semiconductors. *Solid State Phenomena* **37-38**, 213-218 (1994).

251. K. Ellmer and R. Mientus: Carrier transport in polycrystalline ITO and ZnO:Al II: The influence of grain barriers and boundaries. *Thin Solid Films* **516**, 5829-5835 (2008).

252. K. Kishimoto, M. Tsukamoto, and T. Koyanagi: Temperature dependence of the Seebeck coefficient and the potential barrier scattering of n-type PbTe films prepared on heated glass substrates by rf sputtering. *Journal of Applied Physics* **92**, 5331-5339 (2002).

253. Y. Kajikawa: Effects of potential barrier height and its fluctuations at grain boundaries on thermoelectric properties of polycrystalline semiconductors. *Journal of Applied Physics* **114**, 053707 (2013).

254. P. Rhodes: Fermi-Dirac Functions of Integral Order. *Proceedings of the Royal Society of London Series A* **204**, 396-405 (1950).

255. J. Blakemore: Semiconductor Statistics (Dover Publications, Mineola, 1987).

256. Wolfram Research, Inc.: Mathematica Edition: Version 8.0 (Wolfram Research, Inc., Champaign, 2010).

257. J. Jerhot and J. Vlcek: Seebeck Effect in Polycrystalline Semiconductors. *Thin Solid Films* **92**, 259-271 (1982).

258. Y. Sato, T. Yamamoto, and Y. Ikuhara: Atomic structures and electrical properties of ZnO grain boundaries. *Journal of the American Ceramic Society* **90**, 337-357 (2007).

259. C. Agashe, O. Kluth, J. Hupkes, U. Zastrow, B. Rech, and M. Wuttig: Efforts to improve carrier mobility in radio frequency sputtered aluminum doped zinc oxide films. *Journal of Applied Physics* **95**, 1911-1917 (2004).

260. T. Terasako, H. Song, H. Makino, S. Shirakata, and T. Yamamoto: Temperature dependence of electrical properties of Ga-doped ZnO films deposited by ion plating with DC arc discharge. *Thin Solid Films* **528**, 19-25 (2013).

261. R.P. Wang, L.L.H. King, and A.W. Sleight: Highly conducting transparent thin films based on zinc oxide. *Journal of Materials Research* **11**, 1659-1664 (1996).

262. T. Minami, H. Nanto, and S. Takata: Highly Conductive and Transparent Zinc-Oxide Films Prepared by RF Magnetron Sputtering under an Applied External Magnetic-Field. *Applied Physics Letters* **41**, 958-960 (1982).

263. T. Minami, T. Miyata, T. Yamamoto, and H. Toda: Origin of electrical property distribution on the surface of ZnO:Al films prepared by magnetron sputtering. *Journal of Vacuum Science and Technology A* **18**, 1584-1589 (2000).

264. D. Severin, O. Kappertz, T. Nyberg, S. Berg, and M. Wuttig: The effect of target aging on the structure formation of zinc oxide during reactive sputtering. *Thin Solid Films* **515**, 3554-3558 (2007).

265. D.M. Mattox: Particle Bombardment Effects on Thin-Film Deposition - a Review. *Journal of Vacuum Science and Technology A* **7**, 1105-1114 (1989).

266. A. Janotti and C.G. Van de Walle: Native point defects in ZnO. *Physical Review B* **76**, 165202 (2007).

267. E. Wendler, O. Bilani, K. Gartner, W. Wesch, M. Hayes, F.D. Auret, K. Lorenz, and E. Alves: Radiation damage in ZnO ion implanted at 15 K. *Nuclear Instruments and Methods in Physics Research Section B* **267**, 2708-2711 (2009).

268. K. Shirouzu, T. Ohkusa, M. Hotta, N. Enomoto, and J. Hojo: Distribution and solubility limit of Al in Al_2O_3-doped ZnO sintered body. *Journal of the Ceramic Society of Japan* **115**, 254-258 (2007).

269. C.B. Alcock, V.P. Itkin, and M.K. Horrigan: Vapor-Pressure Equations for the Metallic Elements: 298-2500 K. *Canadian Metallurgical Quarterly* **23**, 309-313 (1984).

270. J.P. Han, P.Q. Mantas, and A.M.R. Senos: Densification and grain growth of Al-doped ZnO. *Journal of Materials Research* **16**, 459-468 (2001).

271. Y.M. Sun and H.Z. Wang: The electronic properties of native interstitials in ZnO. *Physica B - Condensed Matter* **325**, 157-163 (2003).

272. S.B. Zhang, S.H. Wei, and A. Zunger: Intrinsic n-type versus p-type doping asymmetry and the defect physics of ZnO. *Physical Review B* **63**, 075205 (2001).

273. A. Audren, A. Hallen, and G. Possnert: Damage recovery in the oxygen sublattice of ZnO by post-implantation annealing. *Nuclear Instruments and Methods in Physics Research Section B* **272**, 418-421 (2012).

274. J.H. Noh, H.S. Jung, J.K. Lee, J.Y. Kim, C.M. Cho, J.S. An, and K.S. Hong: Reversible change in electrical and optical properties in epitaxially grown Al-doped ZnO thin films. *Journal of Applied Physics* **104**, 073706 (2008).

275. N. Roberts, R.P. Wang, A.W. Sleight, and W.W. Warren: ^{27}Al and ^{69}Ga impurity nuclear magnetic resonance in ZnO:Al and ZnO:Ga. *Physical Review B* **57**, 5734-5741 (1998).

276. T. Welzel and K. Ellmer: Comparison of ion energies and fluxes at the substrate during magnetron sputtering of ZnO:Al for dc and rf discharges. *Journal of Physics D - Applied Physics* **46**, 315202 (2013).

277. A. Bogaerts and R. Gijbels: Similarities and differences between direct current and radio-frequency glow discharges: a mathematical simulation. *Journal of Analytical Atomic Spectrometry* **15**, 1191-1201 (2000).

278. D.K. Brice, J.Y. Tsao, and S.T. Picraux: Partitioning of Ion-Induced Surface and Bulk Displacements. *Nuclear Instruments and Methods in Physics Research Section B* **44**, 68-78 (1989).

279. O. Kappertz, R. Drese, and M. Wuttig: Correlation between structure, stress and deposition parameters in direct current sputtered zinc oxide films. *Journal of Vacuum Science and Technology A* **20**, 2084-2095 (2002).

280. D. McLean: Grain Boundaries in Metals (Clarendon, Oxford, 1957).

281. S. Hofmann and P. Lejcek: Solute segregation at grain boundaries. *Interface Science* **3**, 241-267 (1996).

282. F. Morehead and B. Crowder: A Model for the Formation of Amorphous Si by Ion Bombardment. *Radiation effects* **6**, 27-32 (1970).

283. J.F. Ziegler, M.D. Ziegler, and J.P. Biersack: SRIM - The stopping and range of ions in matter (2010). *Nuclear Instruments and Methods in Physics Research Section B* **268**, 1818-1823 (2010).

284. G.W. Tomlins, J.L. Routbort, and T.O. Mason: Oxygen diffusion in single-crystal zinc oxide. *Journal of the American Ceramic Society* **81**, 869-876 (1998).

285. R. Freer: Self-diffusion and impurity diffusion in oxides. *Journal of Materials Science* **15**, 803-824 (1980).

286. L. Vines, R. Schifano, M. Schofield, and B.G. Svensson: Impurity migration in bulk and thin-film ZnO. *Physica Scripta* **T148**, 014005 (2012).

287. H. Haneda, I. Sakaguchi, A. Watanabe, T. Ishigaki, and J. Tanaka: Oxygen Diffusion in Single- and Poly-Crystalline Zinc Oxides. *Journal of Electroceramics* **4**, 41-48 (1999).

288. A. Sabioni, M. Ramos, and W. Ferraz: Oxygen Diffusion in Pure and Doped ZnO. *Materials Research* **6**, 173-178 (2003).

289. D. Marton, J. Fine, and G.P. Chambers: Temperature-dependent radiation-enhanced diffusion in ion-bombarded solids. *Physical Review Letters* **61**, 2697-2700 (1988).

290. H.K. Pappas, B.J. Heuser, and M.M. Strehle: Measurement of radiation-enhanced diffusion of La in single crystal thin film CeO_2. *Journal of Nuclear Materials* **405**, 118-125 (2010).

291. T. Welzel and K. Ellmer: The influence of the target age on laterally resolved ion distributions in reactive planar magnetron sputtering. *Surface and Coatings Technology* **205**, S294-S298 (2011).

292. P.B. Mirkarimi, K.F. McCarty, D.L. Medlin, W.G. Wolfer, T.A. Friedmann, E.J. Klaus, G.F. Cardinale, and D.G. Howitt: On the role of ions in the formation of cubic boron-nitride films by ion-assisted deposition. *Journal of Materials Research* **9**, 2925-2938 (1994).

293. T. Welzel, M. Kellermeier, K. Harbauer, and K. Ellmer: Development of a compact combined plasma sensor for plasma surface engineering processes. *Applied Physics Letters* **102**, 211605 (2013).

294. J. Hinze and K. Ellmer: In situ measurement of mechanical stress in polycrystalline zinc-oxide thin films prepared by magnetron sputtering. *Journal of Applied Physics* **88**, 2443-2450 (2000).

295. A. Segmüller and M. Murakami: X-Ray Diffraction Analysis of Strains and Stresses in Thin Films, in Analytical Techniques For Thin Films, edited by K. Tu and R. Rosenberg (Academic Press, Boston, 1988), pp. 143-200.

296. D. Depla, S. Heirwegh, S. Mahieu, J. Haemers, and R. De Gryse: Understanding the discharge voltage behavior during reactive sputtering of oxides. *Journal of Applied Physics* **101**, 013301 (2007).

297. J.A. Thornton: Magnetron Sputtering - Basic Physics and Application to Cylindrical Magnetrons. *Journal of Vacuum Science and Technology* **15**, 171-177 (1978).

298. Z.L. Petrovic, Z.M. Raspopovic, V.D. Stojanovic, J.V. Jovanovic, G. Malovic, T. Makabe, and J. de Urquijo: Data and modeling of negative ion transport in gases of interest for production of integrated circuits and nanotechnologies. *Applied Surface Science* **253**, 6619-6640 (2007).

299. T. Yamada, H. Makino, N. Yamamoto, and T. Yamamoto: Ingrain and grain boundary scattering effects on electron mobility of transparent conducting polycrystalline Ga-doped ZnO films. *Journal of Applied Physics* **107**, 123534 (2010).

300. C.W. Gorrie, A.K. Sigdel, J.J. Berry, B.J. Reese, M.F.A.M. van Hest, P.H. Holloway, D.S. Ginley, and J.D. Perkins: Effect of deposition distance and temperature on electrical, optical and structural properties of radio-frequency magnetron-sputtered gallium-doped zinc oxide. *Thin Solid Films* **519**, 190-196 (2010).

301. S.E. Park, J.C. Lee, P.K. Song, and J.H. Lee: Properties of Gallium-Doped Zinc-Oxide Films Deposited by RF or DC Magnetron Sputtering with Various GZO Targets. *Journal of the Korean Physical Society* **54**, 1283-1287 (2009).

302. G. Socol, D. Craciun, I.N. Mihailescu, N. Stefan, C. Besleaga, L. Ion, S. Antohe, K.W. Kim, D. Norton, S.J. Pearton, A.C. Galca, and V. Craciun: High quality amorphous indium zinc oxide thin films synthesized by pulsed laser deposition. *Thin Solid Films* **520**, 1274-1277 (2011).

303. K.R. Zhang, F.R. Zhu, C.H.A. Huan, A.T.S. Wee, and T. Osipowicz: Indium-doped zinc oxide films prepared by simultaneous r.f. and d.c. magnetron sputtering. *Surface and Interface Analysis* **28**, 271-274 (1999).

304. L. Zhao, G.J. Shao, S.T. Song, X.J. Qin, and S.H.Z. Han: Development on transparent conductive ZnO thin films doped with various impurity elements. *Rare Metals* **30**, 175-182 (2011).

305. H. Czternastek, A. Brudnik, and M. Jachimowski: Indium-Doped Zinc-Oxide Films Prepared by DC Magnetron Sputtering. *Solid State Communications* **65**, 1025-1029 (1988).

306. C.G. Huang, M.L. Wang, Q.L. Liu, Y.G. Cao, Z.H. Deng, Z. Huang, Y. Liu, Q.F. Huang, and W. Guo: Physical properties and growth kinetics of co-sputtered indium-zinc oxide films. *Semiconductor Science and Technology* **24**, 095019 (2009).

307. S. Cornelius: private communication (Dresden, 2013).

308. R.D. Shannon: Revised Effective Ionic-Radii and Systematic Studies of Interatomic Distances in Halides and Chalcogenides. *Acta Crystallographica Section A* **32**, 751-767 (1976).

309. M. Vinnichenko, R. Gago, S. Cornelius, N. Shevchenko, A. Rogozin, A. Kolitsch, F. Munnik, and W. Moller: Establishing the mechanism of thermally induced degradation of ZnO:Al electrical properties using synchrotron radiation. *Applied Physics Letters* **96**, 141907 (2010).

310. S. Yoshioka, F. Oba, R. Huang, I. Tanaka, T. Mizoguchi, and T. Yamamoto: Atomic structures of supersaturated ZnO-Al_2O_3 solid solutions. *Journal of Applied Physics* **103**, 014309 (2008).

311. T. Suga, S. Kameyama, S. Yoshioka, T. Yamamoto, I. Tanaka, and T. Mizoguchi: Characterization of nanotextured AIN thin films by x-ray absorption near-edge structures. *Applied Physics Letters* **86**, 163113 (2005).

312. D. Ligny, D. Neuville, A. Flank, and P. Lagarde: Structure of spinel at high temperature using *in-situ* XANES study at the Al and Mg K-edge. *Journal of Physics - Conference Series* **190**, 012178 (2009).

313. R. Schuber, P.R. Ganz, F. Wilhelm, A. Rogalev, and D.M. Schaadt: Local electronic structure of Cu-doped GaN investigated by XANES and x-ray linear dichrosim. *Physical Review B* **84**, 155206 (2011).

314. J.W. Chiou, J.C. Jan, H.M. Tsai, W.F. Pong, M.H. Tsai, I.H. Hong, R. Klauser, J.F. Lee, C.W. Hsu, H.M. Lin, C.C. Chen, C.H. Shen, L.C. Chen, and K.H. Chen: Electronic structure of GaN nanowire studied by X-ray-absorption spectroscopy and scanning photoelectron microscopy. *Applied Physics Letters* **82**, 3949-3951 (2003).

315. G. Frank and H. Köstlin: Electrical-Properties and Defect Model of Tin-Doped Indium Oxide Layers. *Applied Physics A* **27**, 197-206 (1982).

316. J. Clatot, G. Campet, M. Jean, M. Nistor, and A. Rougier: Influence of dopant nature on the TCO properties of ZnO:M (M=Al, Ga, Sn, Si, Ge) thin films *MRS Proceedings* **1328**, DOI:10.1557/opl.2011.1308 (2011).

317. H. Makino, Y. Sato, N. Yamamoto, and T. Yamamoto: Changes in electrical and optical properties of polycrystalline Ga-doped ZnO thin films due to thermal desorption of zinc. *Thin Solid Films* **520**, 1407-1410 (2011).

318. S. Ilican, Y. Caglar, M. Caglar, and B. Demirci: Polycrystalline indium-doped ZnO thin films: preparation and characterization. *Journal of Optoelectronics and Advanced Materials* **10**, 2592-2598 (2008).

319. M. Caglar, S. Ilican, and Y. Caglar: Influence of dopant concentration on the optical properties of ZnO:In films by sol-gel method. *Thin Solid Films* **517**, 5023-5028 (2009).

320. N. Aghamalyan, E. Kafadaryan, and R. Hovsepyan: Effect of Lithium and Gallium Impurities on Opto-Electrical Properties of ZnO Films, in Trends in Semiconductor Research, edited by B. Elliot (Nova Science, New York, 2005), pp. 81-110.

321. E. Mollwo: Die Wirkung von Wasserstoff auf die Leitfähigkeit und Lumineszenz von Zinkoxydkristallen. *Zeitschrift für Physik* **138**, 478-488 (1954).

322. D.G. Thomas and J.J. Lander: Hydrogen as a Donor in Zinc Oxide. *Journal of Chemical Physics* **25**, 1136-1142 (1956).

323. C.G. van de Walle: Hydrogen as a Cause of Doping in Zinc Oxide. *Physical Review Letters* **85**, 1012-1015 (2000).

324. Y.-S. Kang, H.-Y. Kim, and J.-Y. Lee: Effects of Hydrogen on the Structural and Electro-optical Properties of Zinc Oxide Thin Films. *Journal of the Electrochemical Society* **147**, 4625-4629 (2000).

325. M.D. McCluskey and S.J. Jokela: Hydrogen Donors in Zinc Oxide, in Zinc Oxide-A Material for Micro- and Optoelectronic Applications, edited by N. H. Nickel and E. Terukov (Springer, Dordrecht, 2005), pp. 125-132.

326. B. Bogdanovic, K. Bohmhammel, B. Christ, A. Reiser, K. Schlichte, R. Vehlen, and U. Wolf: Thermodynamic investigation of the magnesium-hydrogen system. *Journal of Alloys and Compounds* **282**, 84-92 (1999).

327. G.C. Sinke, L.C. Walker, F.L. Oetting, and D.R. Stull: Thermodynamic Properties of Aluminum Hydride. *Journal of Chemical Physics* **47**, 2759-2761 (1967).

328. F. Ruske, V. Sittinger, W. Werner, B. Szyszka, K.U. van Osten, K. Dietrich, and R. Rix: Hydrogen doping of DC sputtered ZnO:Al films from novel target material. *Surface and Coatings Technology* **200**, 236-240 (2005).

329. D.H. Kim, S.H. Lee, G.H. Lee, H.B. Kim, K.H. Kim, Y.G. Lee, and T.H. Yu: Effects of deposition temperature on the effectiveness of hydrogen doping in Ga-doped ZnO thin films. *Journal of Applied Physics* **108**, 023520 (2010).

330. Y.H. Kim, S.Z. Karazhanov, and W.M. Kim: Influence of hydrogen on electrical and optical properties of ZnO films. *Physica Status Solidi B* **248**, 1702-1707 (2011).

331. E.V. Lavrov, F. Herklotz, and J. Weber: Identification of hydrogen molecules in ZnO. *Physical Review Letters* **102**, 185502 (2009).

332. E.V. Lavrov, J. Weber, F. Börrnert, C.G. van de Walle, and R. Helbig: Hydrogen-related defects in ZnO studied by infrared absorption spectrocopy. *Physical Review B* **66**, 165205 (2002).

333. S.H. Lee, T.S. Lee, K.S. Lee, B. Cheong, Y.D. Kim, and W.M. Kim: Characteristics of hydrogen co-doped ZnO:Al thin films. *Journal of Physics D - Applied Physics* **41**, 095303 (2008).

334. E. Fortunato, P. Barquinha, and R. Martins: Oxide semiconductor thin-film transistors: a review of recent advances. *Advanced Materials* **24**, 2945-2986 (2012).

335. M. Orita, H. Ohta, M. Hirano, S. Narushima, and H. Hosono: Amorphous transparent conductive oxide $InGaO_3(ZnO)_m$ (m <= 4): a Zn 4s conductor. *Philosophical Magazine B* **81**, 501-515 (2001).

336. L. Gao, Y. Zhang, J.M. Zhang, and K.W. Xu: Boron doped ZnO thin films fabricated by RF-magnetron sputtering. *Applied Surface Science* **257**, 2498-2502 (2011).

337. B.N. Pawar, S.R. Jadkar, and M.G. Takwale: Deposition and characterization of transparent and conductive sprayed ZnO:B thin films. *Journal of Physics and Chemistry of Solids* **66**, 1779-1782 (2005).

338. T. Minami, H. Sato, H. Nanto, and S. Takata: Highly Conductive and Transparent Silicon Doped Zinc-Oxide Thin-Films Prepared by RF Magnetron Sputtering. *Japanese Journal of Applied Physics Part 2* **25**, L776-L779 (1986).

339. Collaboration: Authors and editors of the volumes III/17B-22A-41B: Zinc oxide (ZnO) Debye temperature, heat capacity, density, melting point, vapor pressure, hardness, in SpringerMaterials - The Landolt-Börnstein Database (http://www.springermaterials.com), edited by O. Madelung, U. Rössler and M. Schulz, DOI: 10.1007/10681719_312.

340. H. Agura, A. Suzuki, T. Matsushita, T. Aoki, and M. Okuda: Low resistivity transparent conducting Al-doped ZnO films prepared by pulsed laser deposition. *Thin Solid Films* **445**, 263-267 (2003).

341. T. Minami, J. Oda, J. Nomoto, and T. Miyata: Effect of target properties on transparent conducting impurity-doped ZnO thin films deposited by DC magnetron sputtering. *Thin Solid Films* **519**, 385-390 (2010).

342. J.H. Hubbell, P.N. Trehan, N. Singh, B. Chand, D. Mehta, M.L. Garg, R.R. Garg, S. Singh, and S. Puri: A Review, Bibliography, and Tabulation of K, L, and Higher Atomic Shell X-Ray-Fluorescence Yields. *Journal of Physical and Chemical Reference Data* **23**, 339-364 (1994).

343. N. Vogel-Schäuble, Y.E. Romanyuk, S. Yoon, K.J. Saji, S. Populoh, S. Pokrant, M.H. Aguirre, and A. Weidenkaff: Thermoelectric properties of nanostructured Al-substituted ZnO thin films. *Thin Solid Films* **520**, 6869-6875 (2012).

344. B.Z. Dong, G.J. Fang, J.F. Wang, W.J. Guan, and X.Z. Zhao: Effect of thickness on structural, electrical, and optical properties of ZnO:Al films deposited by pulsed laser deposition. *Journal of Applied Physics* **101**, 033713 (2007).

345. J.H. Lee: Effects of sputtering pressure and thickness on properties of ZnO:Al films deposited on polymer substrates. *Journal of Electroceramics* **23**, 512-518 (2009).

346. J. Nomoto, J. Oda, T. Miyata, and T. Minami: Effect of inserting a buffer layer on the characteristics of transparent conducting impurity-doped ZnO thin films prepared by dc magnetron sputtering. *Thin Solid Films* **519**, 1587-1593 (2010).

347. L. Holland: Vacuum Deposition of Thin Films (Chapman & Hall, London, 1956).

348. R. Klenk, J. Klaer, R. Scheer, M.C. Lux-Steiner, I. Luck, N. Meyer, and U. Ruhle: Solar cells based on $CuInS_2$ - an overview. *Thin Solid Films* **480**, 509-514 (2005).

349. J. Klaer, I. Luck, A. Boden, R. Klenk, I.G. Perez, and R. Scheer: Mini-modules from a $CuInS_2$ baseline process. *Thin Solid Films* **431**, 534-537 (2003).

350. A. Grimm, R. Klenk, J. Klaer, I. Lauermann, A. Meeder, S. Voigt, and A. Neisser: $CuInS_2$-based thin film solar cells with sputtered (Zn,Mg)O buffer. *Thin Solid Films* **518**, 1157-1159 (2009).

351. R.S. Araoz: Chemical bath deposition of Zn(S,O) buffer layers and application in Cd-free chalcopyrite-based thin-film solar cells and modules. Dissertation (Freie Universität Berlin, Berlin, 2009).

352. R. Hunger, C. Pettenkofer, and R. Scheer: Surface properties of (111), (001), and (110)-oriented epitaxial $CuInS_2$/Si films. *Surface Science* **477**, 76-93 (2001).

353. S. Narushima, M. Orita, M. Hirano, and H. Hosono: Electronic structure and transport properties in the transparent amorphous oxide semiconductor $2CdO\text{-}GeO_2$. *Physical Review B* **66**, 035203 (2002).

Publications

The following list recites the articles which were published in the framework of this thesis.

[A] A. Bikowski and K. Ellmer: Influence of the deposition temperature on electronic transport and structural properties of radio frequency magnetron-sputtered $Zn_{1-x}Mg_xO$:Al and ZnO:Al films. *Journal of Materials Research* **27**, 2249 - 2256 (2012).

[B] A. Bikowski and K. Ellmer: Electrical transport in hydrogen-aluminium co-doped ZnO and $Zn_{1-x}Mg_xO$ films: Relation to film structure and composition. *Journal of Applied Physics* **113**, 053710 (2013).

[C] A. Bikowski, T. Welzel, and K. Ellmer: The impact of negative oxygen ion bombardment on electronic and structural properties of magnetron sputtered ZnO:Al films. *Applied Physics Letters* **102**, 242106 (2013).

[D] A. Bikowski and K. Ellmer: A comparative study of electronic and structural properties of polycrystalline and epitaxial magnetron-sputtered ZnO:Al and $Zn_{1-x}Mg_xO$:Al Films - Origin of the grain barrier traps. *Journal of Applied Physics* **114**, 063709 (2013).

[E] A. Bikowski, T. Welzel, and K. Ellmer: The correlation between the radial distribution of high energetic ions and the structural as well as electrical properties of magnetron sputtered ZnO:Al films. *Journal of Applied Physics*, accepted (2013).

Acknowledgements

At this point, I would like to express my gratitude to all those who supported me in the preparation of this thesis.

First of all, I want to thank Dr. Klaus Ellmer for providing me with the opportunity to prepare my thesis at the ‘Helmholtz-Zentrum Berlin für Materialien und Energie GmbH’. He was always present to answer or help with questions or problems and supported me during the entire thesis. Only through his invaluable expertise, many discussions, and helpful suggestions, the efficient work on this scientific topic became possible.

Further, I am obliged to Prof. Dr. Recardo Manzke from the ‘Humboldt-Universität zu Berlin’ for being the first examiner and Prof. Dr. Marius Grundmann from the ‘Universität Leipzig’ for being the co-examiner in the procedure of the doctoral examination.

I especially want to thank my colleagues, Dr. Thomas Welzel, Karsten Harbauer, Jonas Schulte, and Dr. Dariusz Zajac, for countless fruitful discussions, an always pleasant atmosphere, and the realization of numerous works and experiments for completing my thesis.

Dr. Thomas Welzel’s enormous experience in plasma physics and joint discussions helped me to gain a basic understanding of plasma physics. Furthermore, he performed the plasma process monitor measurements to characterize the high-energetic particle bombardment. Karsten Harbauer carried out numerous engineering tasks, without which some of the experiments could not have been realized. Jonas Schulte did a part of the scanning electron microscopy experiments and was always present to discuss work related or private topics. Dr. Dariusz Zajac introduced me to the X-ray absorption spectroscopy and helped me to perform the experiments.

I would also like to thank Tobias Grund, Dag Riebisch, Dave Plewa, and Patrick Weidner from the ‘Association of Young Volunteers, VJF Berlin’ for their support with the electrical measurements and Man Nie for performing part of the scanning electron microscopy measurements and the atomic force microscopy measurements. Furthermore, I thank Dr. Nelia Wanderka for carrying out the atom probe tomography experiments and analysing the data as well as Ulrike Bloeck for the preparation of the TEM samples. Especially, I want to thank Dr. Markus Wollgarten for his patience when introducing me to the TEM. He was a very organized teacher.

I am indebted to many co-workers not only at the ‘Helmholtz-Zentrum Berlin’, but also to other scientists from different universities and institutes who contributed to the measurements or provided assistance in the analysis of the data. Particularly, I want to thank Richard Wilhelm from the ‘Helmholtz-Zentrum Dresden-Rossendorf’ for his assistance with the Rutherford backscattering spectrometry.

Finally, I want to thank my family, who has been very patient and supportive throughout the whole 3 years even though I was sometimes exclusively focussed on my work.